Stony Brook University

The Census of Warm Debris Disks in the Solar Neighborhood from *WISE* and *Hipparcos*

A Dissertation Presented

by

Rahul Indrakant Patel

to

The Graduate School

in Partial Fulfillment of the Requirements

for the Degree of

Doctor of Philosophy

in

Physics

Stony Brook University

December 2015

Stony Brook University

The Graduate School

Rahul Indrakant Patel

We, the dissertation committee for the above candidate for the

Doctor of Philosophy degree, hereby recommend

acceptance of this dissertation

Stanimir Metchev - Dissertation Advisor
Adjunct Professor, Department of Physics and Astronomy

Michael Zingale - Chairperson of Defense
Associate Professor, Department of Physics and Astronomy

Matthew Dawber - Committee Member
Associate Professor, Department of Physics and Astronomy

Rebecca Oppenheimer - External Member
Curator, Professor, and Chair, American Museum of Natural History

This dissertation is accepted by the Graduate School

Charles Taber
Dean of the Graduate School

Abstract of the Dissertation

The Census of Warm Debris Disks in the Solar Neighborhood from *WISE* and *Hipparcos*

by

Rahul Indrakant Patel

Doctor of Philosophy

in

Physics

Stony Brook University

2015

Debris disks are optically thin circumstellar disks around main-sequence stars, comprised of micron-sized grains. The dust is generated from destructive collisions of planetesimals, induced from gravitational perturbations by large planets. Debris disks can as signposts for planetary systems, through which, a universal picture can be obtained that encompasses the evolution and architecture of the Solar System's own dust disk and planetary system. The dust in these disks can be detected by their thermal infrared flux, measured as an excess above the photospheric emission. Dust at different circumstellar locations, inferred from the peak wavelength of the detected emission, can act as a probe for local dynamical activity in the system. Over the last thirty years, cold disks, analogous to the Kuiper Belt, have constituted the bulk of debris disk detections. Warm disks, analogous to the Main Asteroid belt, can act as signposts for dynamical activity in the terrestrial planet

zone, but are rare in contrast. The Wide-Field Infrared Survey Explorer (*WISE*) space telescope mapped the entire sky in two near-IR and two mid-IR bands in 2012. The two mid-IR bands are well placed to probe dust emission in the terrestrial planet zone of these stars, at sensitivities greater than the last all-sky IR survey in 1983. *WISE* also provides us for the first time an opportunity to contemporaneously measure the photospheric and IR excess wavelengths of the entire sky, increasing sensitivity to fainter levels of dust.

In this thesis, I present an unbiased survey of warm disks around main-sequence Hipparcos stars in the solar neighborhood, detected using data from the *WISE* All-Sky Database. Our series of surveys builds upon each other to find previously undetected faint, warm debris disks by including bright photometrically saturated stars in *WISE*, using empirical photospheric colors, removing several non-trivial false-positive sources, and verifying and validating these detected excesses. This thesis adds a substantial number of new disk targets to the census of debris disks, as well as an assessment of the incidence rate of *WISE* disks in the solar neighborhood. The number and rate of detections can ultimately aid in enhancing our understanding of the formation and evolution of planetary systems.

To my family.

Contents

List of Figures

List of Tables

Acknowledgements

Deshi Basara Basara, Deshi Basara Basara.
— The Dark Knight Rises.

I have determined that I would rather write five more theses than another sentence in the acknowledgements. It has taken me much longer to finish this section — which I started after defending — than to write the entirety of Chapter 5. This is not because I don't want to get sentimental or that I have too many people to thank, though both are true. It's because writing the words "supportive" and "thankful" became repetitive and I started perusing the thesaurus too often. However, I then remembered that Mike Simon once said that "if a fifty cent word works, then don't use a fifty dollar one." So, what you will read here are plain words of the gratitude I feel toward all those who have shared in my triumphs and tribulations these past few years.

First and foremost, I would be ridden with Canadian guilt if I did not thank my advisor, Stanimir Metchev. Stan's guidance, encouragement, patience, and passion for astronomy have sculpted me into the astronomer and scientist I am today — though I know I still have much to learn. He has shown me that there are no shortcuts, and hard work bears its own fruit. At the same time, he has also shown me that it is important to relax, especially when encountering border patrol agents in Arizona after an observing run. I would also like to thank Aren Heinze and Joe Trollo, both of whom have provided insightful ideas, and helped me improve my analytical and statistical skills. Their expertise, insight and constant willingness to help have been invaluable to me throughout this thesis.

I would like to thank all of my committee members for reading my thesis and guiding me to the final product. I want to thank Michael Zingale for acting as chair of my committee, helping me improve in areas where I was weak, for all the fun morning discussions and letting me graduate even though I was not able to discover five new planets. I would also like to thank Rebecca Oppenheimer for serving on my committee, her invaluable guidance, and tremendous amount of encouragement and support over these last few years. I would also like to thank Matthew Dawber for serving on my committee, as well as making first year bearable in the TA labs. I would like to thank Tom Weinacht for his support, and serving on my committee early on. In addition, I would like to especially thank Bruce Macintosh for his support and allowing me to take part

in the outstanding work being done by the Gemini Planet Imager Exoplanet Survey.

The astronomy group at Stony Brook has been especially welcoming and supportive during my time there. This includes Alan Calder for all the helpful life lessons, Mike Simon for all the Yiddish tutorials, and Jin Koda for somehow predicting where I would end up for my first postdoc. I would also like to give many thanks to Josh S. who helped me navigate my way through my first year of research, Brendan who was constantly willing to share his expertise in both academics and sci-fi lore and Chris who kept me on my feet about all the good music of which I had never heard. Without these three, I would have had a much more difficult time staying afloat. My friends in the astronomy group also deserve my appreciation and thanks. Mel, Mathew, Don, Stephka, Adam, Kendra, Max, and Melissa were responsible for making the workplace a lot of fun to be in, and I am grateful for the support they have shown me, and their immeasurable tolerance in dealing with me. This includes all of my office singing, desk drumming (sorry Melissa), and the inane arguments that Max and I would find ourselves in.

Graduate school is a long and arduous road, which is why I am grateful that I did not have to travel it by myself. I would first like to thank Socoro, Sara and the wonderful staff in the physics department. Never again will I have the opportunity nor privilege of working with such a friendly and helpful group of people. To Jeremy, Omer, Josh I., Shawn, and Humed — I could not have asked for a crazier, kinder, and better set of friends/roommates than you guys. I would definitely have lost my mind had it not been for all the late-night homework parties, P90X "parties", and just plain old awkward social parties. I would like to make sure that David knows that had it not been for him I would not have applied to Stony Brook. In a sense, David, all of this is thanks to you. I think that also means that if I mess up, I can blame you for it too. I am also grateful for having met so many wonderful people whom I can continue to call friends and whose support has been unwavering. Among them is my "adopted" cousin Betül, Cip, Karen, Ahsan, Oumarou, Aungshuman, Morgan, Nathan, Heli, Kim, and Wendy.

Of course, thanks to my family and their upbringing and encouragement, I would not have had the courage to undertake this insane yet rewarding endeavor. To my brother Pranav, though we are in different places right now, I want to thank you for showing me the worst is not enough to bring you down. I have also found purpose in my work whenever I see the awe and wonderment in the eyes of Calen, Ella, and Nithya. I want to thank Shaunbhai for all the experienced advice while I was applying for jobs. I would also like to thank Shaunbhai, Roshniben, Sheetalben, Niravjija, Mehuljija, and Mithubhabhi for

their love, support, and being there to talk when I needed it. To my sister and brother-in-law, Vaishali and Suraj, and my parents, Indrakant, Daxa, Ghanshyam and, Jyoshna: no words can describe the heartfelt gratitude I have for all that you have done for me and the unwavering and unconditional love and support you have given me, especially when I didn't want it but totally needed it. Last of all, to Yuki – thank you for being by my side these last two years and for sharing in my joys, childish antics, and absorbing my over-inflated imposter syndrome. They tell me that I'm a scientist now, so I intend to test out how much more of my insanity you can handle in the future.

I would also like to thank the McNair Fellowship program at FIU, in particular to Dr. Simms for the opportunity of pursuing a graduate career. This thesis makes use of data products from the *Wide-field Infrared Survey Explorer*, which is a joint project of the University of California, Los Angeles, and the Jet Propulsion Laboratory/California Institute of Technology, funded by the National Aeronautics and Space Administration. We also use data products from the Two Micron All Sky Survey, which is a joint project of the University of Massachusetts and the Infrared Processing and Analysis Center/California Institute of Technology, funded by the National Aeronautics and Space Administration and the National Science Foundation. This research has also made use of the SIMBAD database, operated at CDS, Strasbourg, France. This research has made use of the Washington Double Star Catalog maintained at the U.S. Naval Observatory. Most of the original figures in this work were created using Matplotlib, a Python graphics environment (Hunter, 2007). This research also made use of APLpy, an open-source plotting package for Python hosted at `http://aplpy.github.com` (Robitaille & Bressert, 2012). This work is partially supported by NASA Origins of Solar Systems through subcontract No. 1467483 to Dr. Stanimir Metchev at Stony Brook University, and by an NSERC Discovery award to Dr. Stanimir Metchev at the University of Western Ontario. I would also like to thank the Astrophysical Journal, Astronomy and Astrophysics Journal, the Journal Science, and the Annual Reviews in Astronomy and Astrophysics for allowing me to reproduce figures from some of their copyrighted publications.

Chapter 1

Introduction

1.1 Solar System Context

Since the discovery of the first extrasolar planets (exoplanets) around a main-sequence star, (HD 114762 b and 51 Pegasi b, Latham et al., 1989; Mayor & Queloz, 1995, respectively), a revolution has occurred in our understanding of planetary formation and evolution. We have seen exoplanets of a variety of flavors: gas giants at fractions of an astronomical unit (AU) from their star, binary planetary systems and even compact multi-planet systems. Giant planets are found with eccentricities ranging from 0–0.9, with sometimes large mutual inclinations. And roughly 50% of solar type stars have a chance of hosting a compact multi-planet system with periods shorter than a year (see review by Winn & Fabrycky, 2015).

In contrast, the planets in our Solar System follow nearly circular, low inclination orbits at distances such that terrestrial and gas giants are separated by the snow-line (see § 1.2.2). Since this Solar System is the only one we know of where a planet can sustain life, perhaps the key to finding another is to search for systems with similar architecture. Of course there are a few exoplanetary systems that may seem architecturally similar to our own. The HR 8799 multi-planet system is an excellent example, where the system's four gas giant planets are at the same equilibrium temperature as our gas giants are to our Sun (Marois et al., 2010).

But this is one in a multitude of over a thousand planets we have uncovered. And if the majority of planets we are finding do not resemble the architecture of the Solar System, we have to ask: Is the existence of another habitable planet likely? If so, how can we identify a system whose interplanetary environment would increase the habitability of an Earth analog?

Over the last thirty years, we have seen that exoplanetary systems can also

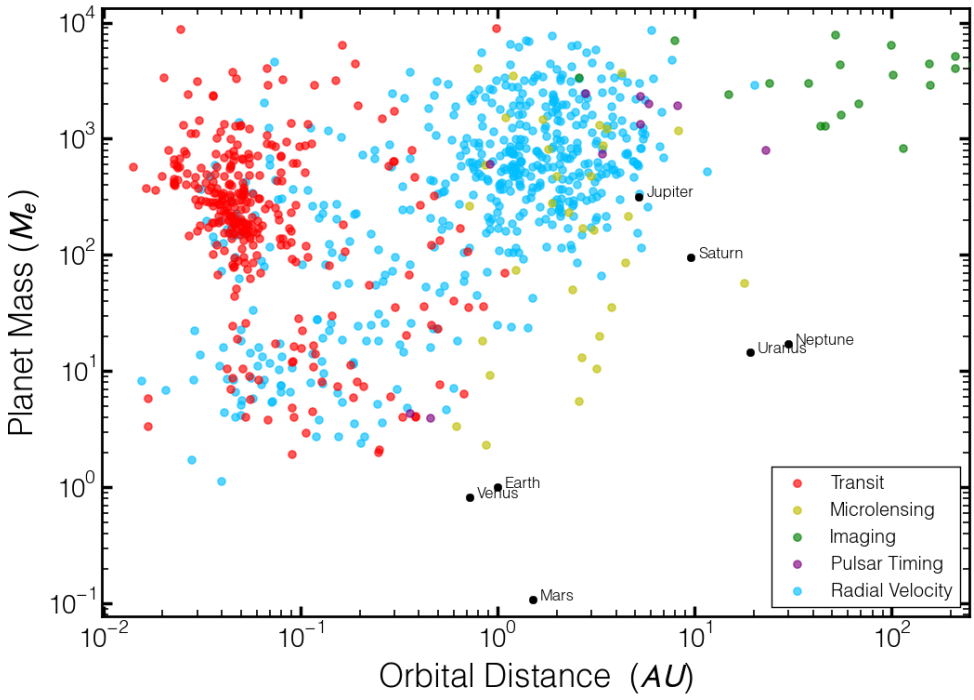

Figure 1.1: Distribution of exoplanet masses vs. their estimated orbital distance and color coded based on the technique used to detect them. This plot only shows exoplanets detected as of June 2015. Only planets with catalogued masses and orbital distances were plotted. $M \sin(i)$ values were used when exact values for the planet mass were unavailable. Solar System data is also plotted. Data was downloaded from `http://exoplanetarchive.ipac.caltech.edu/`. Credit: R. Patel.

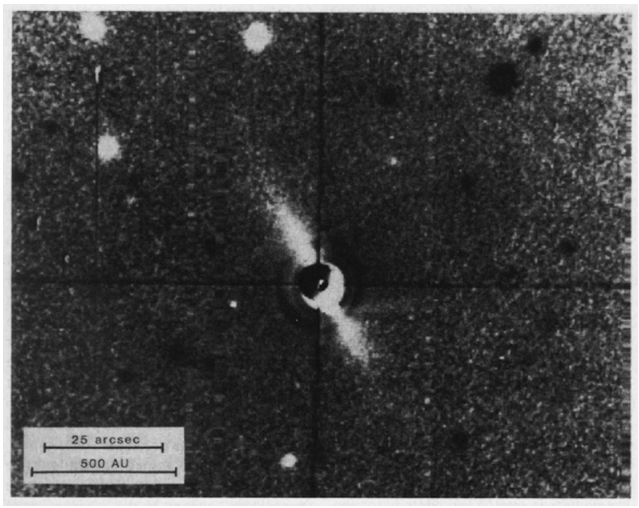

Figure 1.2: Resolved disk emission around the β Pictoris star. First ever resolved image of a debris disk. The image was taken using a coronagraph at the Las Campanas observatory in Chile. The disk is edge-on and composed of solid particles. The flattened shape, rather than a spherical shell of particles is circumstantial evidence of planet formation. The circular shape in the center is due to the coronagraph and imperfect subtraction of the standard star. Image credit: Smith & Terrile (1984). Reprinted with permission from AAAS.

be identified by the presence of any dusty disks orbiting a main-sequence star. The first unresolved detection of extrasolar debris disks was by the *Infrared Astronomical Satellite* (*IRAS*) in 1983 of the Vega debris disk (Aumann et al., 1984). Further evidence from resolved images was taken by Smith & Terrile (1984) of the debris disks around the β Pictoris system and galvanized the idea of these disks, which are created from the collisional grinding of planetesimals, are stirred by large planets (see Figure 1.2). Given that evidence exists that our own Solar System is a result of the concurrent evolution of our circumsolar disk and planets, then perhaps similarities can be drawn between what our circumsolar disk looked like at different stages in its evolution and the extrasolar debris disks astronomers have detected over the last thirty years. Another way to investigate this is to ask: is the likelihood of a system like ours — and hence the possibility of life — linked with the evolution of the disk and planets as a whole?

This thesis takes a step toward investigating these questions by identifying additional systems which have previously been overlooked and may hold a wealth of information with which to place our Solar System in context.

1.2 The Solar System's Debris Disk

1.2.1 Current Configuration

The eight planets in the Solar System follow a relatively ordered configuration. With the exception of Mercury, the orbits are close to circular, and are closely inclined to the invariable plane, where inclination angles range from 0.33°–2.19°. The four rocky planets are located interior to 1.7 AU, while the four gas giant planets are located beyond the snow-line — the point in relation to the Sun beyond which volatile molecules (e.g., H_2O, CH_4) condense — and all the way out to 30 AU.

The inner and outer planets are also segregated by a disk of material known as the Main Asteroid Belt (MAB). Located between the orbits of Mars and Jupiter, the MAB is composed of over a million kilometer-sized objects that can be metallic, stony or even carbon rich in composition.

It has been estimated that the mass of the MAB is $\sim 0.04 M_{\rm moon}$, but was much larger in the early Solar System (see § 1.2.2). Beyond the orbit of Neptune lies a large reservoir or minor planets composed of icy, volatile, cometary material with sizes greater than 1 km. These minor bodies, distributed in a thin belt the width of 20 AU, are known as the Edgeworth-Kuiper Belt (EKB).

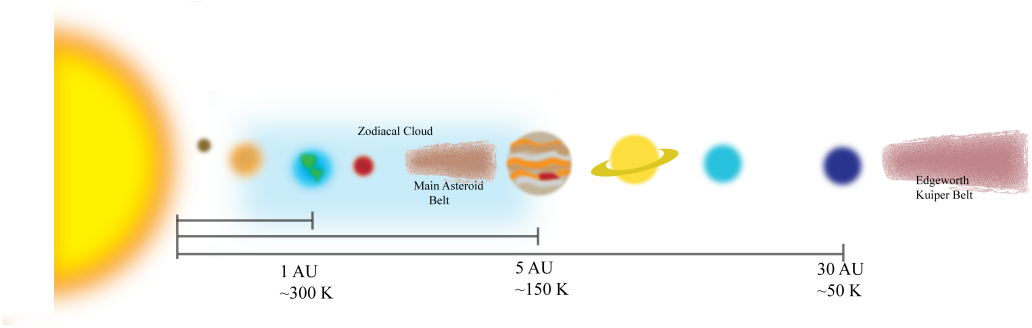

Figure 1.3: An illustration of the Solar System's planets, and major dust belts. Rough equilibrium temperatures are indicated at distances from Earth, Jupiter, and the inner edge of the EKB. The vertical positions of the planets relative to the Earth-Sun plane indicate rough inclinations. Distances and sizes are not to scale. Image credit: R. Patel.

In addition to the rings of large rocky bodies, a population of 10–100μm sized cometary and silicate grains inhabits the Solar System. This disk, known as the Zodiacal Cloud, has been seen in scattered light observations (Hahn et al., 2002), thermal emission from the Planck (Maris et al., 2006; Planck Collaboration et al., 2014), COBE (Kelsall et al., 1998), and the *IRAS* (Sykes,

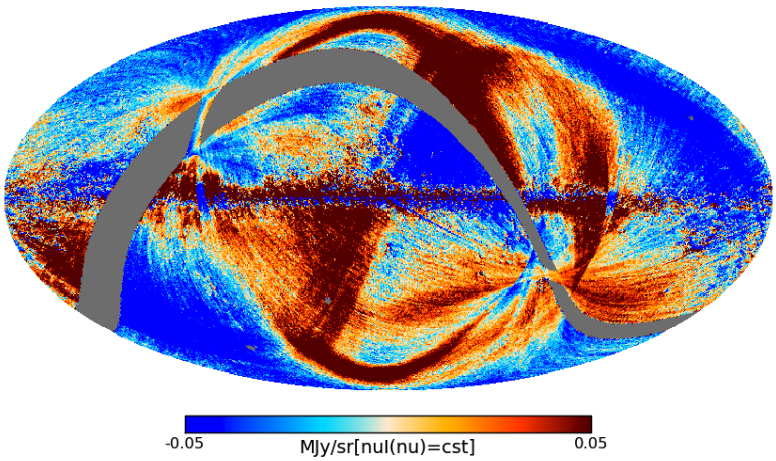

Figure 1.4: Galactic coordinate projection of the sky in the 850 GHz band from the Planck Satellite. The Zodiacal light emission is seen passing diagonally from the lower left to the top right, crossing the middle of the galactic plane. The top and bottom arcs are due to instrumental far side lobes. Image credit: (Planck Collaboration et al., 2014).

Figure 1.5: A faint glow seen along the ecliptic reveals the presence of 100μm sized grains that comprise the Zodiacal Light. Image credit to the European Southern Observatory. Image was taken at Cerro Paranal, Chile `http://www.eso.org/public/unitedkingdom/images/zodiacal-light/`

1990) missions, as well as inferred from spacecraft impact experiments. From the ground, the Zodiacal Cloud can be seen only on the darkest of nights, as a faint glow along the ecliptic (see Figure 1.5). The inner Zodiacal Cloud extends from the orbit of Venus all the way out to Jupiter. From most recent studies, it is thought that mm–cm sized grains are ejected from Jupiter Family Comets (JFC) as they approach the large tidal forces of Jupiter's gravity. The smaller sub-mm sized grains, which comprise the disk are thought to be created from the grinding down of the larger mm–cm sized ejected grains. The overall mass of the inner Zodiacal Cloud has been estimated to be $\sim 1-2\times10^{19}$ g (Nesvorný et al., 2010). The Zodiacal Cloud's density is so low that the overall disk brightness, when compared to the total emission of the Sun at all wavelengths (bolometric luminosity) is $L_{\rm ZODY}/L_{\odot} \sim 2 \times 10^{-7}$ (Nesvorný et al., 2010).

1.2.2 Dynamical Evolution Of Our Planetary System

The combined evolution of the planets, asteroidal and cometary disks are responsible for the current state of the Solar System. It is generally accepted that all the planets formed within the first 100 Myr (upper limit based on the final accretion time to create Earth; Allègre et al., 2008), after the Sun reached its place on the main-sequence. During this time, it has been hypothesized that the planets were in a compact configuration, all of them residing within 15 AU of the Sun (Batygin & Brown, 2010). Roughly 4.0–3.7 Gyr ago, scattering of the planetesimal populations that lay outside the orbit of Neptune at 15 AU resulted in angular momentum exchange between the gas giants and the disk. This led to a period of instability in which Jupiter and Saturn's orbits diverged, and eventually crossed their mutual 1:2 mean motion resonance. From this, Jupiter migrated inward by < 0.5 AU (Morbidelli et al., 2010), and pushed Saturn, Uranus and Neptune further out into the Solar System (Tsiganis et al., 2005).

This migration led to a period known as the Late Heavy Bombardment (LHB). During this time, Jupiter's short migration would have depleted the MAB by a factor or 10, while 97% of the EKB was probably removed as a result of Neptune's outward migration. The scattered comets and asteroids during this period are most likely responsible for the Lunar craters we see today (Gomes et al., 2005). It is also thought that a fraction of Earth's water supply was transported during the LHB either from the EKB or from water rich asteroids. In addition, the depletion of the MAB by Jupiter has implications for the emergence of life on Earth, as a massive MAB today might have resulted in a higher frequency of Terrestrial impacts. In essence, we would like to investigate the relationships a planetary system may have with its environment, similar to the evolution due to dynamical friction in our planet-disk

system, around other star systems.

1.3 Circumstellar Disk Evolution

Understanding the physical nature and processes governing the evolution of circumstellar disks is important if we are to understand the similarities between other systems and our own disk throughout its lifetime. In this section, I briefly outline the properties and characteristics of young gas-rich protoplanetary disks and their evolution into a dusty debris disk.

1.3.1 Protoplanetary Disk Evolution

The paradigm of planet formation begins with a nascent protoplanetary disk (PPD), composed of primordial gas and dust that remains post-star formation. The primordial material forms into a circumstellar disk, as a consequence of angular momentum conservation. The final radial extent of the disk is heavily sensitive to the angular rotation of the central star (Ω^2) and even more sensitive to the infall time of the primordial material ($t^3_{\rm infall}$; Terebey et al., 1984). It is well accepted that 90–99% of a PPD is composed of gas, while the rest is made of micron to millimeter sized-dust grains.

The bulk of the gas is comprised of neutral H_2. Though difficult to measure, mid-IR rotational lines have been observed from hot (> 600 K) H_2 from the ground in systems like AB Aurigae (Bitner et al., 2007). Typically, however, tracers such as CO, and HCN line emissions are observed at sub-mm wavelengths to detect the gas in PPDs (e.g., for stars in young associations such as Ophiuchus and Taurus-Auriga, Andre & Montmerle, 1994; Beckwith et al., 1990, respectively). These observations have shown that the size of these disks can range from 10–100 AU, with masses >0.005 $M_\odot$ (Osterloh & Beckwith, 1995). Dust masses are typically derived from dust thermal emission at mm-wavelengths, which probe the large grain population. The masses are typically derived by assuming an upper limit to the grain size (usually around mm sizes) and some assumed opacity values (Beckwith et al., 1990). Figure 1.6 shows the masses of observed PPDs (ages < 10 Myr), indicating disk masses on the order of a few hundred $M_{\rm earth}$.

The majority of the primordial gas and dust dissipates within the first $\sim$10 Myr. Viscous accretion of gas and dust onto the star has been attributed to the clearing of the inner regions (a few AU) of the star, which is supported by a lack of near-IR flux (2–5μm) and the presence of forbidden line accretion signatures (e.g., OI, SII; Hartigan et al., 1995). Photoevaporation from the central star will also carve out the outer disk. In this process, high-energy UV

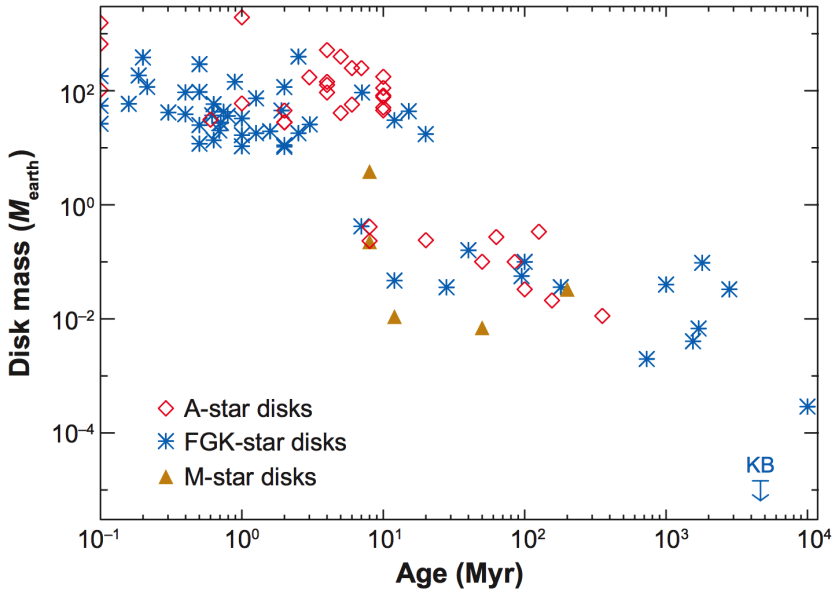

Figure 1.6: Disk masses vs. age taken from Wyatt (2008). Disk masses were derived using sub-mm observations of disks. Different symbols represent different stellar masses (spectral types). The upper limit mass of the Kuiper Belt has also been plotted for contextual purposes. Figure Credit: Wyatt (2008).

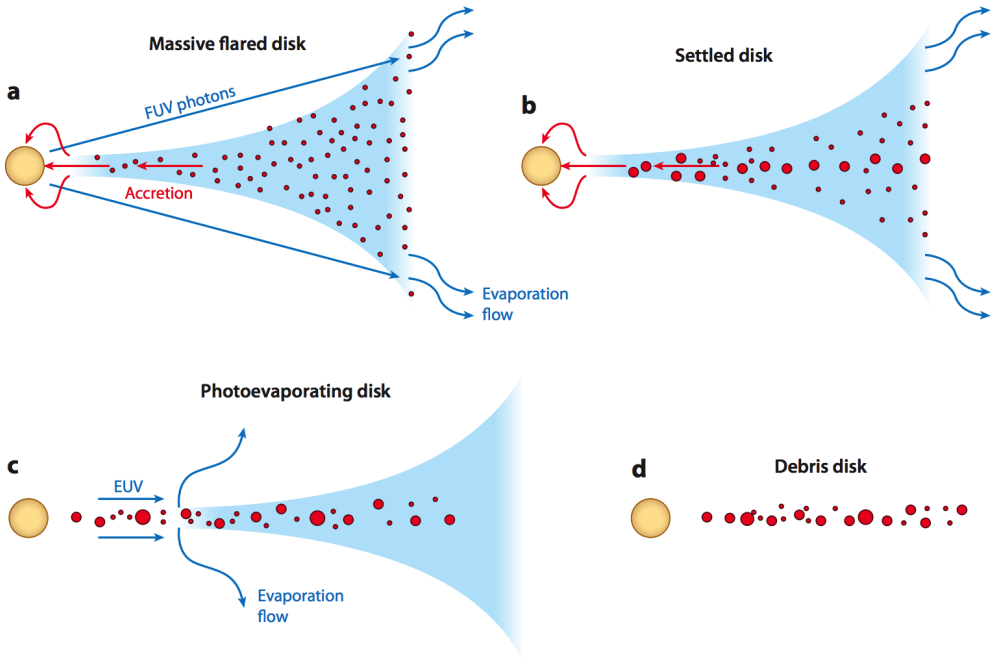

Figure 1.7: Illustration that depicts the evolution of a disk, from a gas-rich PPD to a dust-rich debris disk (from a–d). Blue and red indicate regions of gas and dust, respectively. The different stages indicate the predominant disk dissipation mechanisms, until the debris disk phase. Image credit: (Williams & Cieza, 2011).

and X-Ray photons can excite gas and dust molecules enough so that they are no longer bound to the system, and simply evaporate into interstellar space. The replenishment of material into the inner disk after viscous accretion has halted, is inhibited by extreme-UV photons from the central star. The disk can also be dissipated via external sources. Usually, young stars are found in clusters with thousands of stars. A few of these will be O stars, that irradiate the surrounding environment in intense ionizing UV radiation (Adams et al., 2004). From this, mass loss of the disk will be expedited.

During this entire process, grain growth becomes important, as it not only removes mass from the gas-rich disk, but also provides the seeds for future planetary creation. Micron sized grains will typically feel a pressure gradient, since the gas rotates at sub-Keplerian speeds. As a result, grains will eventually collide, increase in mass and size, and be dragged to the mid-plane of the disk, where they can further grow to form asteroids, comets and even the cores of giant planets. The presence of any fully formed planets within this time can start sculpting the disk. Figure 1.7 illustrates these different processes.

Observations have shown that once the inner disk (<5 AU) is depleted, the outer disk quickly loses the majority of its mass (Williams & Cieza, 2011). Thus, after about 6–10 Myr, most stars have lost their inner disks, as determined from the stars near-IR excess emission (Wyatt, 2008). Figure 1.8 shows the rapid decline in disk fraction as a function of age for a number of different young stellar clusters and associations, illustrating that the fraction of stars with near-IR excesses dwindles down to ∼0%.

1.3.2 Debris Disk Evolution

Dust Removal Mechanims

What remains from the remnant PPD after the bulk of the gas has dissipated, is typically a disk composed of planetesimals and a population of dust (illustrated in Figure 1.7). From studies (e.g., Lisse et al., 2009, 2012; de Vries et al., 2012; Rodigas et al., 2015) we know that the dust in a circumstellar disk can be composed of solid particles, ranging in sizes from $< 100\mu$m to mm in size and heterogeneously composed of various minerals: silicates, other dielectric and refractory particles, and ices (e.g., ice, carbon monoxide). We know from observations of debris disks at sub-mm wavelengths that dust masses are orders of magnitudes lower than in the gas-rich PPD phase; typically on the order of less than an Earth mass (see Figure 1.6).

The motions of grains larger than ∼1 mm (e.g., large grains, small planetesimals), are governed by the gravitational force from the central star. However, the thermal emission seen from these disks is due to smaller grains of order $s < 1$ mm. Since the mass of these disks is low compared to their PPD counterparts, the amount of thermal emission typically observed (further discussed in § 1.4.3) can only be explained by small grains with a surface density great enough to intercept a large cross-section of stellar light. For these smaller grains stellar radiation and stellar wind play an important role in the dynamical behavior of the dust. The force exerted on a particle from radiation pressure $\vec{F}_r$ counteracts the radial gravitational force, giving rise to the photo-gravitational force

$$\left|\vec{F}_{\rm pg}\right| = \frac{GM_\star m_d(1-\beta)}{r_d^2}, \tag{1.1}$$

where β is the ratio of the radiation to gravitational pressure, and is inversely proportional to the stellar luminosity, grain density and size (Burns et al., 1979). In other words, smaller particles will be influenced largely by radiative forces, rather than gravitational ones. Grains whose bulk and optical properties produce $\beta = 0.5$ experience equal gravitational and radiation pressure

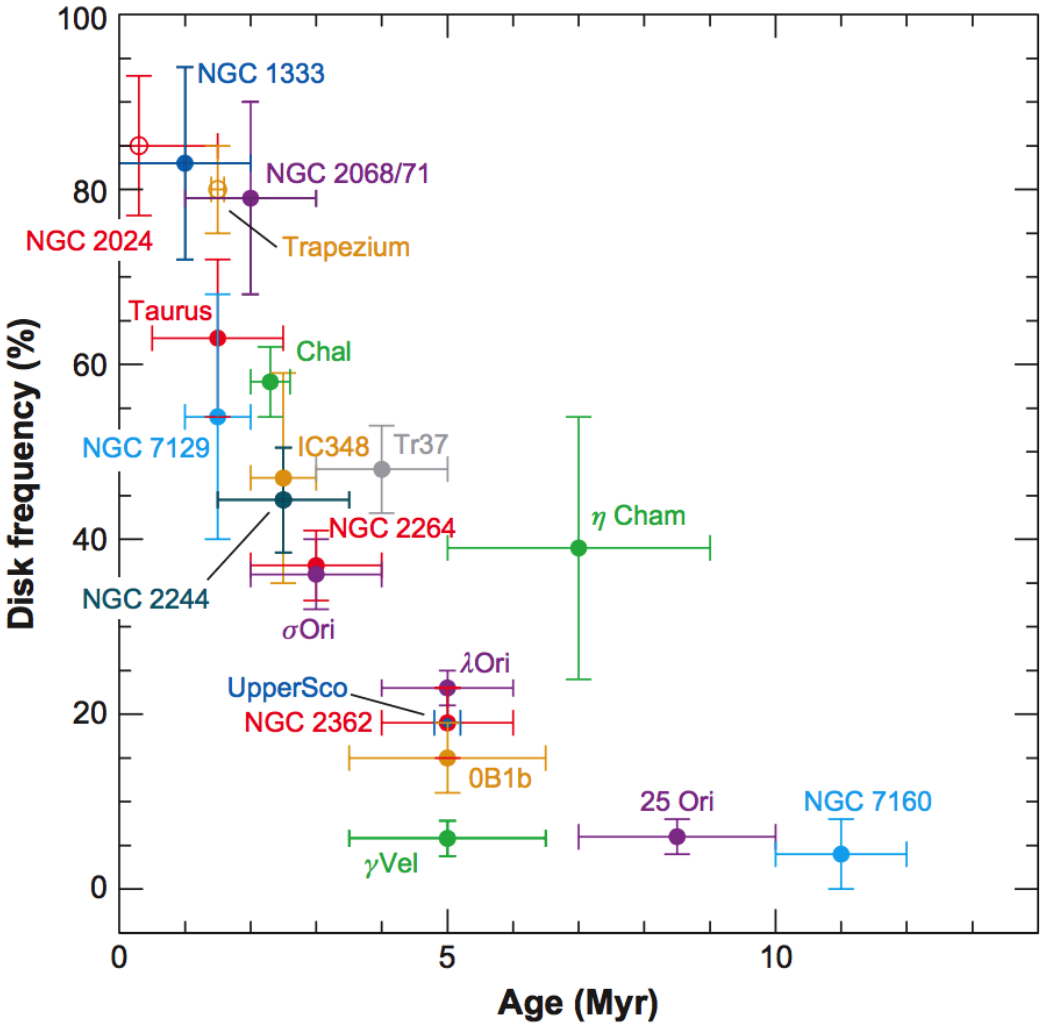

Figure 1.8: Fraction of young stars in different associations, groups, with protoplanetary disks as detected via their near-IR excess flux. By around 6–10 Myr, the fraction of stars with a protoplanetary disk is almost zero. Image credit: Wyatt (2008).

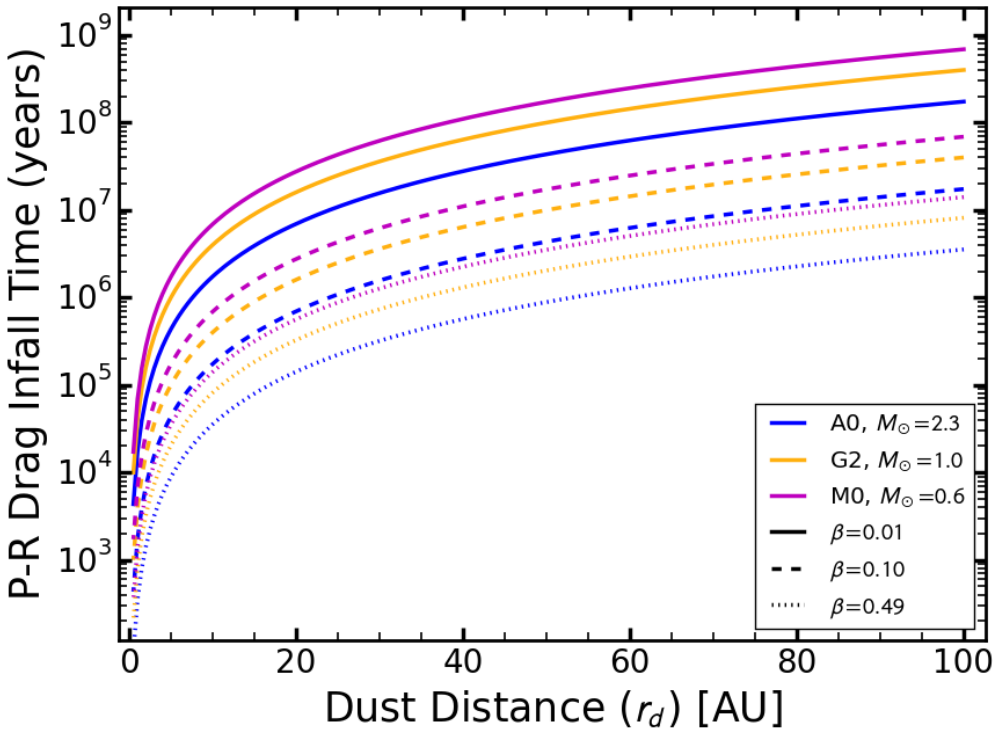

Figure 1.9: A plot of the time it takes for dust at a distance r_d to spiral into the star due to P-R drag. The model for these curves are based on the derivations of Burns et al. (1979): $t_{\rm pr} = 400(r_d^2/M_\star)\beta^{-1}$. This relationship can be derived from Equation 1.2. Large values of β represent smaller particles, and vice-versa. I have plotted the curves for different values of β and for different spectral types (stellar masses).

and represent the minimum size s below which grains will be ejected from the system (blow-out size). In the Solar System, this corresponds to sub-micron sized grains. In addition to radiation pressure, stellar wind pressure created from high velocity plasma, aids in counteracting the gravitational force on the dust grains.

Drag forces will cause the dust to slow down and spiral out of its orbit and eventually into the star. The tangential component (i.e., along the motion vector of the grain), of the stellar wind, or corpuscular drag, is one such drag force. This becomes more important for grains smaller than 0.001μm around Sun-like stars (Burns et al., 1979). The tangential component of the stellar radiation also creates a drag-force on the particle known as Poynting-Robertson (P-R) drag. The P-R drag force is defined as

$$|\vec{F}_{\rm PR}| = \frac{S\pi a^2 Q_{\rm PR} r_d^2 v}{c^2}, \tag{1.2}$$

where S is the stellar flux density, $Q_{\rm PR}$ is the radiation pressure coefficient, and v is the velocity of the grain in the direction normal to the radiation vector, i.e., orbital direction (Burns et al., 1979). P-R drag relies on the change in a particle's momentum due to the acceleration it feels from the stellar radiation perpendicular to its motion vector, and the deceleration it feels from re-radiating the absorbed stellar radiation along the particle's velocity vector.

Figure 1.9 shows that dust around most main-sequence stars at $r_d < 40$ AU will spiral into the star on timescales $\lesssim 100$ Myr. It will take longer for grains at larger distances to spiral into the star, in which case radiation pressure and stellar wind will throw grains out of the system. However, in most detected debris disks (discussed in § 1.6), collisions grind down grains on shorter timescales than P-R drag can remove them from the system (e.g., Wyatt, 2008). Grains, once ground down to smaller sizes can then be removed from the system more easily by radiation pressure and stellar winds. For instance, 100μm grains at 90 AU from the star Vega will spiral into the star within 15 Myr. With collisions, these grains will be removed in roughly 2 Myr (Backman & Paresce, 1993).

Dust Replenishment And Planetary Stirring

We now know that any initial population of dust in a circumstellar environment will not last the lifetime of the star. The larger main-sequence stars, of spectral type (SpT) A2V and later, live for >500 Myr. Dust, on the other hand, is only stable around a star for timescales $\lesssim 1-10$ Myr (dependent on the luminosity of the star; see Figure 1.9). Over the last thirty years, over a thousand debris disks have been discovered. These debris disk systems have been detected around stars of all main-sequence spectral types, as well as ages well beyond the timescale of dust dissipation (see Figure 1.15 in this thesis, and Figure 6 in Wyatt, 2008).

A well accepted explanation for the existence of dust around main-sequence stars is that it is replenished from the destructive collisions of larger oligarchs, planetesimals, asteroids, and comets, where a lot of the dust mass is locked up. These collisions may be governed by a steady state evolution, whereby larger bodies and grains are ground into smaller sizes, eventually being thrown out of the system through one of the dissipative forces described earlier. Thus, a collisional cascade ensues, creating a size distribution of particles. Smaller particles will be removed from the system quickly, while larger particles replenish the smaller grain population. This cycle removes mass from the disk

on timescales $\propto t^{-1}$ (Wyatt et al., 2007). Stochastic evolution may also be responsible for dust replenishment, where dust is ejected into the system from sudden collisions. The LHB event in the early Solar System is an example of this type of dust generation.

Grains and planetesimals must have sufficient kinetic energy for collisions to occur. It is possible that disks evolving from the PPD phase are self-stirred to generate a collisional cascade. Delayed and self-stirring models, whereby the planetesimal disk is stirred from the influence of larger bodies once they have grown to sizes >2000 km, have also been successfully used to explain the presence of dust. As stated by Wyatt (2008), for continuous belts between 1–200 AU, differences between self- and pre-stirred models are insignificant, but are most apparent when there is a clearing in the inner regions.

Though there are a number of collisional models which can adequately explain the dust production in observed systems, the details of each model are beyond the scope of this dissertation. Suffice it to say that the presence of circumstellar dust around main-sequence stars is due to the collisional cascade of planetesimals that ensues from dynamical perturbations.

1.4 Detecting Debris Disks

1.4.1 Dust Thermal Emission

Circumstellar dust immersed in the radiation field of its host star will both scatter and absorb incoming radiation. Though most types of grains are efficient scatterers in the optical and near-IR (see § 1.4.2), a fraction of that light is absorbed and heats the dust. Smaller grains will heat up faster and hence radiate more efficiently than larger grains of the same composition and at the same distance (Krivov, 2010). However, differentiating scattered versus stellar radiation becomes difficult since main-sequence stars at $T_\star > 3000$ K have peak emission in the optical and near-IR (0.4–2.5μm), thus decreasing the contrast between scattered and stellar light in these regimes. Reprocessed thermal emission is easier to detect, as emission from the dust peaks in the mid (10–30μm) and far-IR ($> 30\mu m$) wavelengths — regimes where the stellar photospheric emission can be orders of magnitudes fainter than the observed thermal emission.

Small dust grains, on the order of tens of microns, are largely responsible for thermal emission seen from a star in the mid- and far-IR, given their efficient emission properties. It is typically assumed that the grains are in thermal equilibrium with the stellar radiation field. The amount of energy a grain absorbs (mainly in the UV and optical) $E_{\rm abs}$, is dependent on its size a, radial

distance from the star r_d, stellar luminosity $L_\star$ and the absorption efficiency $Q_{\rm abs}(a,\lambda)$

$$E_{\rm abs} = \left(\frac{\pi a^2}{4\pi r_d^2}\right)\int_0^\infty L_\lambda Q_{\rm abs}(a,\lambda)d\lambda \tag{1.3}$$

$$= \frac{a^2}{4r_d^2}L_\star\langle Q_{\rm abs}\rangle_{\rm UV}. \tag{1.4}$$

The energy emitted by the grain $E_{\rm r}$ depends on the grain size, the radiative efficiency $Q_{\rm r}(a,\lambda)$, and is approximated by

$$E_{\rm r} = 4\pi a^2\int_0^\infty \pi Q_{\rm r}(a,\lambda)B(\lambda,T_d)d\lambda \tag{1.5}$$

$$\approx (2\pi a)^2\,\sigma T_d^4\langle Q_{\rm r}\rangle_{\rm IR}. \tag{1.6}$$

As standard practice, I've assumed an average absorption and emitting efficiency for the grain, which can be derived using Mie Theory. If we assume the grain emits as a blackbody, the expression derived in equation 1.6 naturally falls into place. Conservation of energy dictates that

$$\frac{a^2}{4r_d^2}L_\star\langle Q_{\rm abs}\rangle_{\rm UV} \approx (2\pi a)^2\,\sigma T_d^4\langle Q_{\rm r}\rangle_{\rm IR}, \tag{1.7}$$

which leads to an approximate expression to calculate the dust temperature

$$T_d \approx \left(\frac{\langle Q_{\rm abs}\rangle_{\rm UV}}{\langle Q_{\rm r}\rangle_{\rm IR}}\frac{L_\star}{16\sigma\pi^2 r_d^2}\right)^{1/4}. \tag{1.8}$$

In most cases, the amount of information obtained from the dust emission is only sufficient to satisfy the simplest emission models: grains that emit as blackbodies. In the blackbody assumption, equation 1.8 reduces to

$$T_d = 278\frac{(L_\star/L_\odot)^{1/4}}{\sqrt{r_d}}\ \ [K]. \tag{1.9}$$

assuming that $\langle Q_{\rm abs}\rangle_{\rm UV} \approx \langle Q_{\rm r}\rangle_{\rm IR}$. In a more general sense, the grain equilibrium temperature can vary as it depends on the composition and size of the grain (Draine, 2003). Grains that deviate from the blackbody approximation will have non-zero absorption and emission efficiencies, and moderate the slope of the Wien and Rayleigh-Jeans tails of the grain emission spectrum. Around a Sun-like star, unless the dust orbits at $r_d < 0.1$ AU, the grain temperatures will

typically be $T_d \lesssim 300$ K. Following Wien's approximation, this means that the dust emission spectrum will peak in the mid- and far-IR wavelengths. Thus, astronomers will usually search for the presence of dust at IR wavelengths.

1.4.2 Infrared Excess and Resolved Imaging

The majority of disk systems are identified through unresolved emission via photometric imaging techniques. The IR emission from a star with dust is comprised of both stellar and dust flux. To characterize the dust emission, astronomers must accurately measure and subtract the flux from the star. Fits to stellar models use photometric or spectroscopic data collected in the optical and near-IR ($0.9 - 5\mu$m), where the luminosity of the star is large enough to overwhelm the thermal emission from dust at temperatures < 300 K. The fitted photospheric emission is then extrapolated to the IR. Thus, the excess flux at a particular wavelength is a simple subtraction

$$F_{\mathrm{E},\lambda} = F_{\mathrm{m},\lambda} - F_{\star,\lambda}, \tag{1.10}$$

where $F_{\mathrm{m},\lambda}$ and $F_{\star,\lambda}$ are the measured and photospheric fluxes, respectively. The amount of excess flux at a particular wavelength can be characterized by the measured flux to the photospheric emission, or the relative flux of the excess

$$R_\lambda = F_\lambda / F_{\star,\lambda}. \tag{1.11}$$

The fractional luminosity of the IR excess f_d characterizes the total emission spectrum, or bolometric luminosity, of the dust with respect to the bolometric stellar luminosity

$$f_d = L_{\mathrm{IR}} / L_\star. \tag{1.12}$$

The fractional luminosity can provide a rough estimate of the mass of the dust in the system. This calculation is proportional to f_d as well as the bulk density, grain size, and location from the star (Beckwith et al., 2000). We can see, from Figure 1.10, what a simplified SED looks like for a solar type star that has circumstellar dust with different f_d values.

However, attributing IR excesses based on unresolved fluxes to be circumstellar in nature is not an easy task. There are numerous astrophysical and systematic sources that can contaminate or mimic an IR excess. Background extragalactic sources (e.g., active galactic nuclei, IR bright galaxies), unresolved projected stellar companions and thin patches of infrared bright interstellar clouds of dust are only a few sources that can mimic and bias the

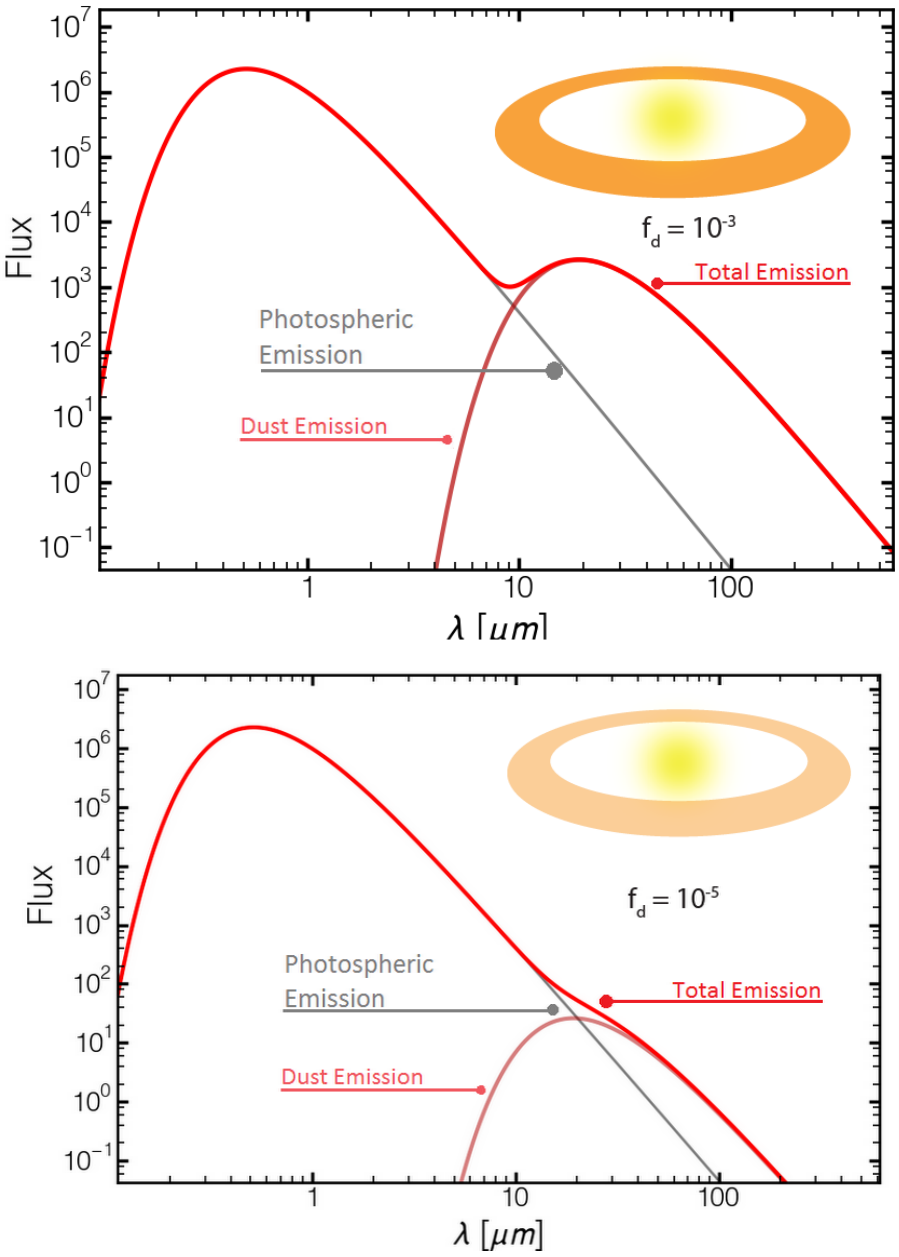

Figure 1.10: Illustrated are the combined SEDs for a star and circumstellar dust thermal emission. The stellar spectrum is approximated by a blackbody with a temperature of 5600 K. In both panels, the dust is assumed to be at a temperature of 150 K, which peaks at $\sim$20μm. The amount of dust in the system is reflected in the 20μm emission amplitude. This directly relates to f_d.

detection of an IR excess. Screening of potential contaminants must be done with great care; follow up studies of potential disk systems are also required to verify the observed thermal excess emission is associated with circumstellar dust.

Resolved images of a debris disk can verify and validate the circumstellar presence of an excess by revealing the structure of the disk. High-contrast optical and near-IR observations trace scattered light, rather than thermal emission, from the dust. It is in these wavelengths that most resolved disks[1] have been imaged. Since the star is orders of magnitudes brighter than the scattered emission from the dust in these wavelength regimes, high-contrast imaging techniques must be employed. This is usually done by using an opaque disk, known as a coronagraph, to attenuate or block the on-axis stellar light. Coronagraphic techniques reduce the glare from the star and allow faint, nearby structure to be imaged. The first resolved image of β Pic (Figure 1.2, taken from Smith & Terrile, 1984) was taken using a coronagraph and imaged in the optical at the Las Campanas Observatory.

Current high-contrast imaging instruments at most ground based observatories also require an adaptive optics (AO) instrument to correct for the refractive distortions imprinted on the stellar wavefront as it passes through our turbulent atmosphere. New extreme-AO systems (e.g., Gemini Planet Imager introduced in Macintosh et al., 2006) are well equipped to image separations as close as 10 AU to some of the closest stars. Information from resolved disks is important as it elucidates degenerate disk parameters obtained from simply analyzing unresolved dust emission. For instance, modelling the SED of the IR excess can be done by either assuming small grains further from the star, or large grains close to the star (Krivov, 2010). Thus, the location of the dust that is causing the emission is important to break the degeneracy (e.g., Figure 13 in Su et al., 2006).

1.4.3 Is It A Protoplanetary Or A Debris Disk?

As illustrated in Figure 1.7, the transition out of a PPD, broadly speaking, occurs with the dissipation of the primordial gas. The remnant circumstellar environment can be composed of planets, minor bodies (asteroids and comets), and micron- to mm-sized dust grains, which may have formed during the PPD phase. This post-PPD, gas-depleted, dust-rich disk is known as a debris disk.

However, there is no clear dividing line between the waning of a PPD and the waxing of a debris disk. Age can act as one metric, though there are examples of PPDs that are older than 30 Myr (De Marchi et al., 2013; Scicluna

[1]See `http://www.circumstellardisks.org` for a compilation of resolved disks.

et al., 2014), and debris disks that have been found in young clusters. The mass of the disk can also be an indicator, as PPDs are usually a couple of orders of magnitudes more massive than a debris disk, as shown in Figure 1.6. A debris disk, unlike a primordial disk, has a smaller gas to dust ratio. Since these disks are primarily optically thin, their IR excesses, and consequently their fractional luminosities, are smaller. Therefore, a debris disk can be characterized by $f_d < 10^{-2}$ (Zuckerman, 2001; Wyatt, 2008).

Although there are clear physical traits that debris disks possess, it is important to note that there can be ambiguities in the disk status of a certain system. Guidelines, like those listed in Wyatt et al. (2015), can aid in clearing such distinctions. However such effort will not be discussed here as it is beyond the scope of this thesis.

1.5 Debris Disks as Signposts for Planets

The self-stirred models, which I briefly touched upon in § 1.3.2, have vast implications for concurrent belt and planetary evolution. Although other mechanisms, such as pre-stirring or close-stellar encounters are possible for generating the necessary perturbations to start a collisional cascade, there is evidence, both theoretical and observational, of dust generation due to the influence of planets (e.g., the HD 141569 system, Wyatt, 2005). With the large number of exoplanets discovered every year, and statistical inferences that almost every star is host to a planetary system (Cassan et al., 2012), dust generation via planetary perturbations is likely a significant phenomenon. This presents an opportunity: if dust in debris disks is generated from collisions due to the influence of larger planetary objects, then the *dust may act as a signpost for undiscovered planetary systems.*

Unresolved debris disk detection can reveal much about the activity in a planetary system. Any excess flux attributed to the star can be used to roughly determine the amount of dust in that system. For stars that are a few hundred million years old, large excess fluxes imply recent collisions, as primordial dust from young systems would have been dissipated millions of years prior (e.g., BD+20 307; Song et al., 2005). In addition, a number of studies have attempted to determine the correlation between systems with known disks and detected planets. The likelihood of a disk being found with known directly imaged systems is relatively high (e.g., systems like β Pic and HR 8799), studies that have tried to find correlations between planet hosts and disk hosts have found conflicting results with strong to no correlation between the two (mainly seen with *Spitzer* studies; Beichman et al., 2005; Bryden et al., 2009). More recent studies with *Herschel* seem to provide more

evidence of a positive correlation between cold disks with the presence of low mass planets (see references in Matthews et al., 2014). In essence, a broader characterization of dust around known planet hosts, or vice versa, is necessary to discern the true correlation of this relationship.

Resolved images can reveal structure in the observed debris disk such as gaps, warps, brightness peaks, etc., which can clarify the dust composition, as well as act as fingerprints for possible planetary activity. For instance the shape of the disk in scattered light can be used to place upper limits on the mass of giant planets sculpting the disk (e.g., Kalas et al., 2005; Rodigas et al., 2014). The warp and secondary dust ring seen in scattered light in the β Pic system was evidence for a possible planet sculpting the ring, as seen in Figure 1.11 (Heap et al., 2000). Later observations in 2010 confirmed the existence of a $9 \pm 2.5 M_J$ planet via direct imaging (Lagrange et al., 2010; Marleau & Cumming, 2014). The recent CO gas clumps seen in this system by the Atacama Large Millimeter/submillimeter Array (ALMA)[2] in Chile are thought to be the result of spiral density waves of dust, created in from the gravitational influence of β Pic b (Nesvold & Kuchner, 2015).

Using multi-wavelength modeling of resolved images from the Herschel Space Observatory of the Fomalhaut debris disk system, Acke et al. (2012) showed that cometary collisions were responsible for the dust seen in the disk. The planet in the Fomalhaut system (Kalas et al., 2008) was discovered from direct imaging observations after the dust ring in the system was thought to have been sculpted by a planet. Although the detected planet is not responsible for the current architecture of the ring (Kalas et al., 2013), it leaves the door open to additional discoveries. And recently, Rodigas et al. (2014) derived an analytical expression to determine the mass of a planet interior to any debris ring scattered light observations.

As discussed in § 1.2.2, the architecture of the circumsolar debris disk also contains clues on the influence the planets have had. Gaps in the MAB, known as the Kirkwood gaps, are the result of the unstable resonant structures due to Jupiter's orbit. Both the MAB and EKB are due to the influence of Jupiter and Neptune, respectively, and also responsible for the interplanetary dust (e.g., Morbidelli et al., 2010). An alien observer looking at our dust disk might infer the presence of Jupiter, Saturn and Neptune in the Solar System. Using the simulation results of the distribution of 24μm dust from Liou & Zook (1999) shown in Figure 1.12, the three giant planets could be identified by observing the non-uniform radial distribution of dust Jupiter and Saturn scatter dust inward from the EKB, ringlike structure along Neptune's orbit, a dark spot that moves along with Neptune, and time varied observations of the

[2] `http://www.almaobservatory.org/`

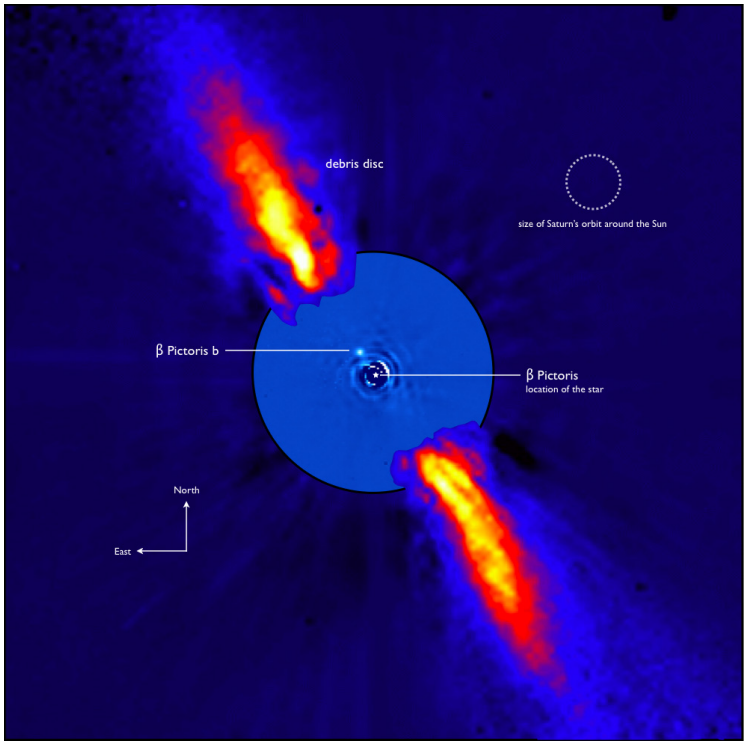

Figure 1.11: A composite image of the β Pic debris disk over plotted with the discovery image of the gas giant planet β Pic b (Lagrange et al., 2010). The warp and secondary inclined disk were evidence of the influence of the planet found in 2008 and later confirmed in 2010. Image credit:European Space Agency.

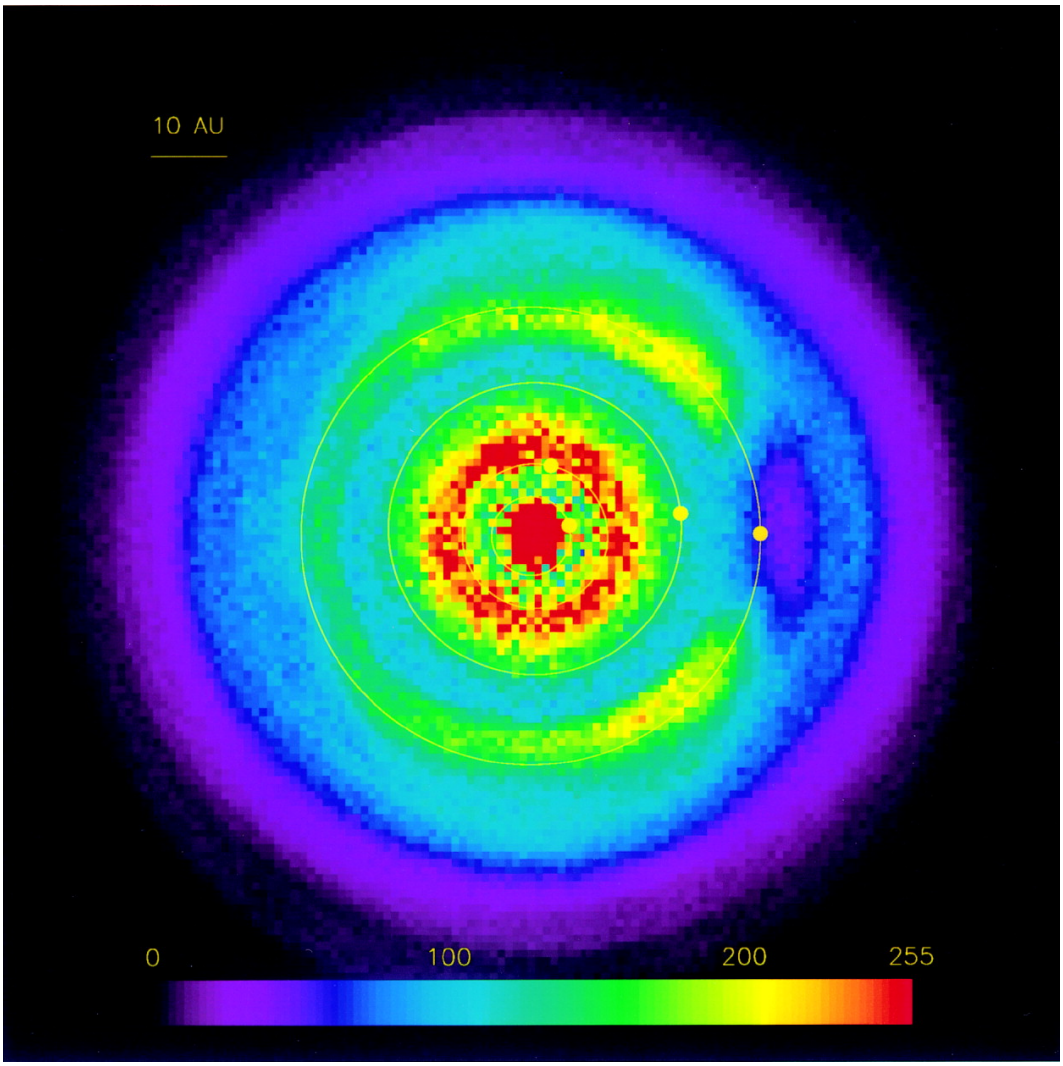

Figure 1.12: Simulation of the brightness distribution due to 23μm interplanetary dust in a face-on view of the Solar System. Shown are the four giant planets in the Solar System, with Neptune's orbit and gravitational influencing the outer architecture of the EKB, and Jupiter and Saturn ejecting particles that are gravitating inwards. From this image, the existence of at least 2 planets can be discerned. Image credit: Liou & Zook (1999).

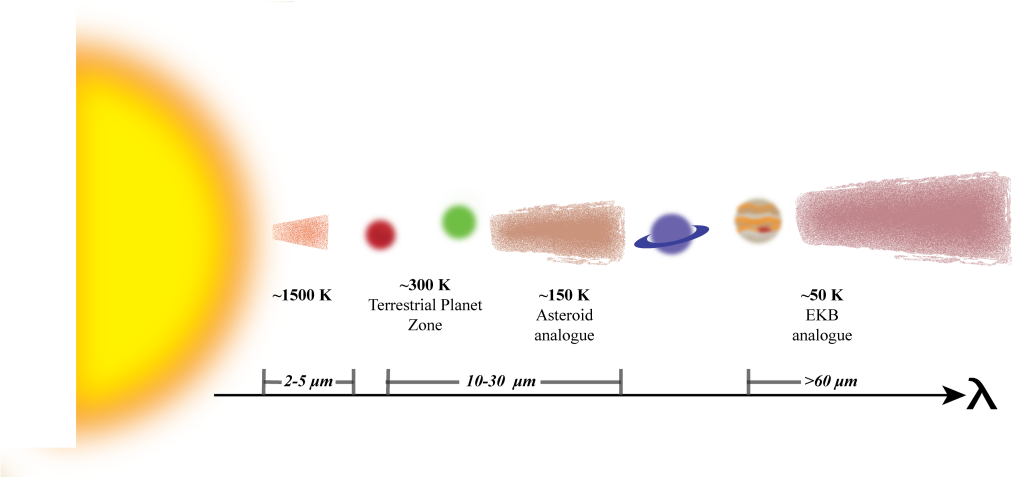

Figure 1.13: Illustration of the various circumstellar regions of interest, the temperature of any dust and the standard wavelengths at which the dust emission may peak. Image credit: R. Patel.

dynamical behavior of the disk structure. What is clear at this is that point once dust is discovered by its unresolved thermal IR excess signature, it can be scrutinized in greater depth with high-contrast and/or high-angular resolution imaging systems to determine the overall architecture of the system.

1.6 Evolving Picture of Debris Disks Over Thirty Years

The majority of debris disks are discovered from the IR excess flux from the star, as opposed to resolved imaging which is typically done as followup to further characterize the disk properties. A number of different surveys have been responsible for the plethora of debris disks discovered to date. Here, I will give a brief summary of what we have learned over last thirty years of debris disk observations, focusing largely on detections from unresolved IR excesses, statistics from various surveys as well as the evolutionary context they provide. The focus will be on detections from space based surveys such as *IRAS*, the *Spitzer Space Telescope*, and *Herschel Space Observatory* — telescope specifications for which can be found in Tables 1.1, 1.2, and 1.3. In addition, I have listed a summary of major studies in Table B.1. Beyond what I discuss here, excellent reviews can be found in Backman & Paresce (1993); Zuckerman (2001); Wyatt (2008); Matthews et al. (2014).

It is useful to keep in mind the relationship between the wavelength of

Table 1.1. *Spitzer* Specifications: 85 cm Primary Mirror.

Instrument	Mode of Observations	Wavelength Range	Band, spectral range (μm)	Beam ($''$) or Spectral Resolution
IRAC	Imaging	near-IR	3.6, 4.5, 5.8, 8.0	1.44, 1.43, 1.49, 1.71
MIPS	Imaging	mid-IR, far-IR	24, 70, 160	6, 18, 40
IRS SL	Spectroscopy	near to mid-IR	5.2–14.5	$60 < R < 128$
IRS SH	Echelle Spectrograph	mid-IR	9.9–19.6	$R \sim 600$
IRS LL	Spectroscopy	mid-IR	14.0–38.0	$57 < R < 126$
IRS LH	Spectroscopy	mid-IR	18.7–37.2	$R \sim 600$

Note. — *Spitzer* Space Telescope Specifications of Relevant Instruments.
IRAC: Infared Array Camera.
IRS: Infrared Spectrograph.
MIPS: Multiband Imaging Photometer for SIRTF.

detected dust emission to where the dust may be located as well as its temperature to first order. Figure 1.13 provides a cartoon picture of these relationships.

1.6.1 Cold Disk Detections

In 1983, the Infrared Astronomical Satellite (*IRAS*) was launched through a joint initiative between NASA in the United States, the Netherlands Agency for Aerospace Programmes and the Science and Engineering Research Council in the United Kingdom. By the end of its 10 month mission, *IRAS* had mapped 96% of the sky at 12, 25, 60 and 100μm. This was the first time the entire sky had been imaged in the IR.

Measurements of a few standard stars revealed a peculiar behavior: where they expected a Rayleigh-Jeans trend in the flux as a function of wavelength, they found instead that the measured fluxes of several stars like Vega (α Lyr), Fomalhaut (HD 216956), β Pic (HD 39060), and ϵ Eridani (HD 22049) revealed an excess of flux several orders of magnitude above the predicted photospheric flux at two or more of the longer wavelength bands. This has since been attributed to "a shell or ring of relatively large particles" at distances and that the grain equilibrium temperatures are $\sim$ 90 K (Aumann et al., 1984; Backman & Paresce, 1993). Figure 1.14 shows the predicted spectral energy distributions (SED) of these four stars in the Rayleigh-Jeans regime, along with the measured fluxes from *IRAS*. Thus, the *IRAS* team identified the first debris disks, aptly named "The Fab Four."

Since the discovery of "The Fab Four", roughly a hundred or so debris disks

Table 1.2. *Herschel Space Observatory* Specifications: 3.5 m Primary Mirror.

Instrument	Mode of Observations	Wavelength Range	Band, spectral range (μm)	Beam ($''$) or Spectral Resolution
PACS	Imaging	Far-IR	70, 100, 160	5.6, 6.8, 11.3
SPIRE	Imaging	far-IR	250, 350, 500	17.6, 23.9, 35.2
SPIRE - SSW	Spectroscopy	far-IR	194-313	$40 < R < 1000$
SPIRE- SLW	Spectroscopy	far-IR	303-671	$40 < R < 1000$

Note. — *Herschel Space Observatory* specifications of relevant instruments.
SPIRE: Spectral and Photometric Imaging Receiver.
SSW: SPIRE Short Wavelength Spectrometer Array.
SLW: SPIRE Long Wavelength Spectrometer Array.
PACS: Photodetector Array Camera and Spectrograph.

Table 1.3. *IRAS* specifications: 0.6 m primary mirror.

Instrument	Mode of Observations	Wavelength Range	Band, spectral range (μm)	Beam ($''$) Resolution
IRAS12	Imaging	mid-IR	12	$30''$–$120''$
IRAS25	Imaging	mid-IR	25	
IRAS60	Imaging	far-IR	60	
IRAS100	Imaging	far-IR	100	

Note. — *IRAS* specifications of relevant instruments.
SPIRE: Spectral and Photometric Imaging Receiver.
SSW: SPIRE Short Wavelength Spectrometer Array.
SLW: SPIRE Long Wavelength Spectrometer Array.
PACS: Photodetector Array Camera and Spectrograph.

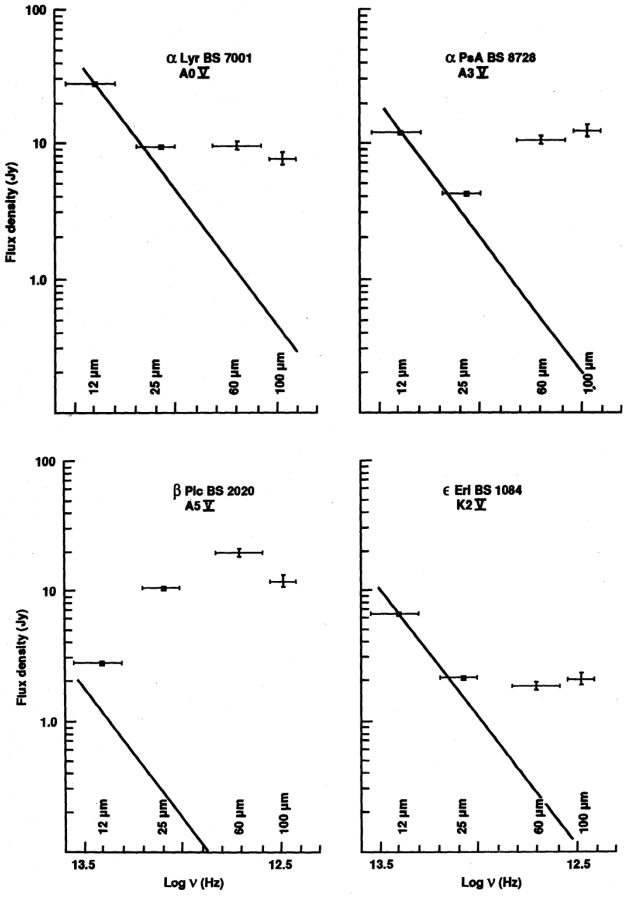

Figure 1.14: The SEDs of *The Fab Four* stars — the first four disks discovered around main-sequence stars — taken from Backman & Paresce (1993). Starting from top-left and moving clockwise: Vega (α Lyr), Fomalhaut (α PsA), ϵ Eridani, and β Pictoris. The *IRAS* fluxes of these stars are shown at 12, 25, 60 and 100μm with the Rayleigh-Jeans photospheric flux over-plotted. The large excess flux measured for these stars indicates optically thin circumstellar disks of cold micron sized grains. Image credit: Backman & Paresce (1993)

using *IRAS* were detected via their far-IR (60–100μm) excesses showed that these systems possess circumstellar dust in optically thin disks at relatively cold temperatures (∼20–100 K). These temperatures, are derived from blackbody fits to the SED of the excess. The dust in these systems is analogous to dust in the EKB ($T_d \sim 50$ K). Hence, the cold dust in these systems are signposts for dynamical planetary activity in the outer regions of these systems, in much the same way the cold dust in our system betrays the existence of Neptune, as it sculpts the cold planetesimal population in the EKB.

The early *IRAS* detections mostly found dust around hotter A and B type stars and that roughly 15% of these main-sequence stars are host to cold dust populations, detected at the *IRAS* 60μm band. Later studies that used improved versions of the original *IRAS* database (Faint Source Catalog), identified a handful of new debris disk host stars, and increased the incidence of cold dust detections to 20% around A stars (Rhee et al., 2007). However, a number of these detections could be false, due to the low resolution of the *IRAS* beam (Moór et al., 2011). The launch of the Spitzer Space Telescope in 2003 commenced a series of surveys to understand the evolution and existence of dust around nearby stars. The Formation and Evolution of Planetary Systems[3] (FEPS; Meyer et al., 2006) surveyed ∼300 stars between FGK spectral types at ages from 3 Myr to 3 Gyr. These studies found that cold dust, or excesses at the Spitzer/MIPS 70μm band, was present around 33% of A stars at all ages, and at relatively bright dust brightnesses (Su et al., 2006). The DEBRIS collaboration[4] recently published their results after conducting a survey for cold dust around 86 main-sequence A stars using the Herschel Space Observatory. They found that roughly 25%±5% of A stars possess far-IR excess emission at 100μm (Thureau et al., 2014).

A similar search for cold dust around solar-type stars (F, G, and K spectral type) revealed something different. The incidence of excesses in the far-IR are lower and a stronger function of the stellar age than for the incidence of excesses around A stars. A number of *Spitzer*/MIPS 70μm surveys (e.g., Trilling et al., 2008; Bryden et al., 2006; Beichman et al., 2006; Hillenbrand et al., 2008) have found that on average, the incidence of 70μm excesses is $\sim$ 15%. Trilling et al. (2008) found $\sim$ 16% of older stars in the field possess far-IR excesses, while these numbers are consistent, but lower (∼10–13%) from other studies of field objects (Beichman et al., 2006; Bryden et al., 2006). The Herschel DUNES[5] survey searched for cold dust around a sample of stars with ages between 100 Myr to 8 Gyr and found that 20% of solar type stars possess

[3] `http://feps.as.arizona.edu/science.html`

[4] Disc Emission via a Bias-free Reconnaissance in the Infrared/Submillimetre

[5] DUst around NEarby Stars

100μm excesses in this age range (Eiroa et al., 2013). Figure 6 in Wyatt (2008) shows a relatively shallow decline for the measured 70μm relative flux (R_{70}; Equation 1.11) of stars at a few Myr up to 800 Myr, in terms of both the number of stars with far-IR excesses, and to the magnitude of the detected excess.

1.6.2 Warm Disk Detections

As depicted, in Figure 1.13, mid-IR excesses from 10–30μm are typically associated with warm dust assuming peak emission at these wavelengths. Though this is not always the case (as the emission at these wavelengths could be due to the Wien tail of colder dust that peaks at longer wavelengths), understanding the IR excess at these wavelengths is still crucial in understanding the evolution of dust in these systems. For the moment, we will assume that these mid-IR excesses are caused by dust in regions analogous to the MAB. This type of dust can act as a signpost for activity in the inner regions of planetary systems, as seen from formation of the Zodiacal cloud in our own system, or the formation of terrestrial planets in others (Song et al., 2005).

The majority of known mid-IR excesses were discovered from surveys using the *Spitzer*/MIPS at 24μm and the *Spitzer*/IRS instruments. Unlike excesses in the far-IR, the incidence of excesses in the mid-IR range were found to be a strong function of age. For B and A stars, the incidence of 24μm excesses from Spitzer/MIPS detections is roughly 1/3 for most ages (Wyatt, 2008) with slight variations. Siegler et al. (2007) found this incidence to be 10^{+17}_{-3}% for A stars in the 50 Myr IC 2391 open cluster. Chen et al. (2012) found this rate to vary slightly between stars in Upper Scorpius Centaurus (11 Myr; 25^{+6}_{-5}%), Upper Centaurus Lupus (15 Myr; 27 ± 4%), and the Lower Centarus Crux (17 Myr; 24 ± 5%) star forming regions. The study performed by Rieke et al. (2005), which combined data from *Spitzer*, *ISO*, and the *IRAS* missions, found that at young ages, roughly 50% of A stars possess mid-IR excesses. They also found that although these excesses persist at later ages, the incidence of stars with strong excesses declines much more rapidly than for excesses with more intermediate excesses[6].

For solar type stars, the incidence of warm excesses is a much stronger function of stellar age. At the youngest ages between 5–50 Myr, the incidence of 24μm excesses has been reported to be between 44% and 22% (Siegler et al., 2007; Chen et al., 2012). At later ages, this incidence rate drops to 10% for stars at ages $\sim$300 Myr (Meyer et al., 2008) and < 4% for stars older than

[6]Rieke et al. (2005) define intermediate and strong excesses as R_{24}=1.25-2 and $R_{24} > 2$ respectively, as defined in Equation 1.11

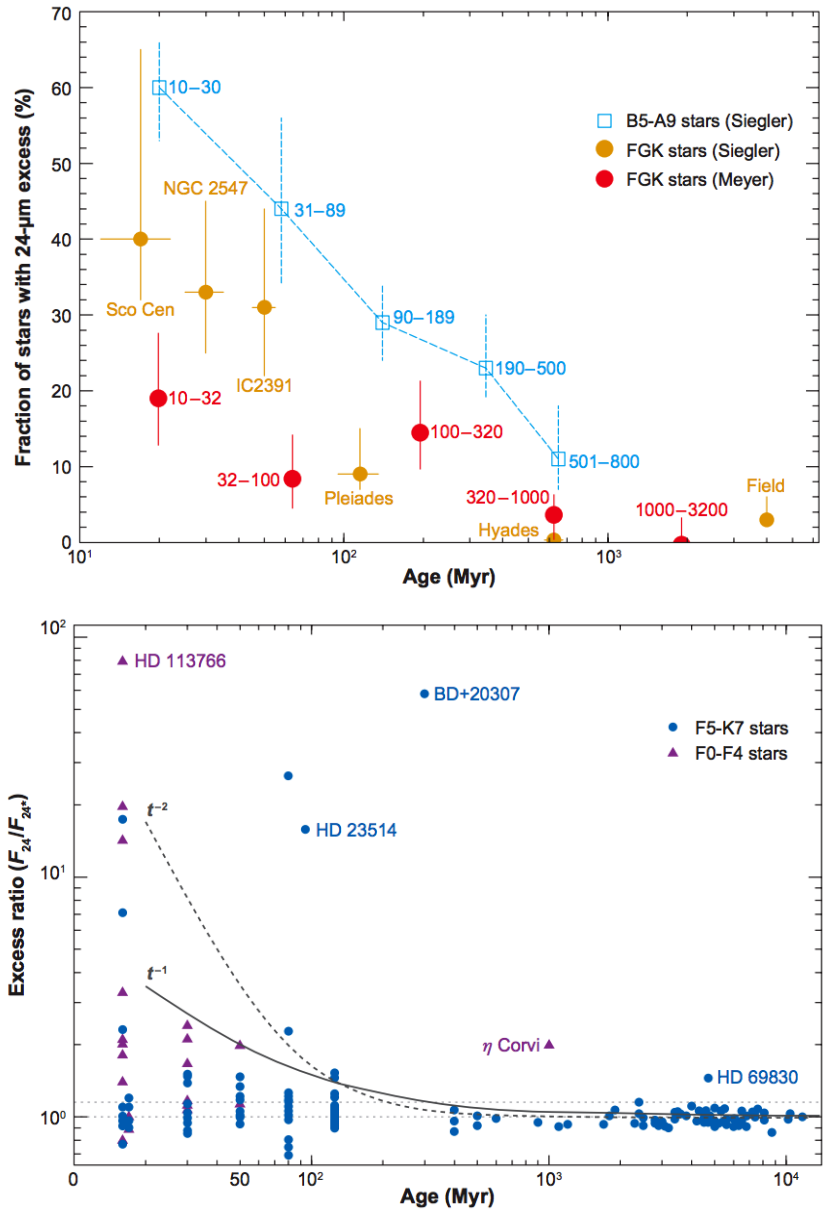

Figure 1.15: Top: Compiled incidence of 24μm excesses from different, spectral types, and ages. Data here was compiled from Meyer et al. (2008) and Siegler et al. (2007). **Bottom:** Relative 24μm ratios for stars plotted against the stellar age for Solar type stars. The horizontal dotted lines show the relative flux thresholds equal to 1 and 1.15. The data were taken from Siegler et al. (2007). Image credit: Wyatt (2008).

1 Gyr (Trilling et al., 2008). A good summary that encompasses most of these statistics can be found in the top panel of Figure 1.15, which shows the fraction of stars with 24μm excesses for different spectral types, stellar clusters and in different age bins. The bottom panel of the same figure shows how the magnitude of the detected 24μm excess evolves for stars at different ages, with the strongest excess at earlier ages, and relatively no detected excess flux at Gyr ages.

If we assume that the detected excess emission corresponds to dust at a particular temperature, and hence a particular radius, as shown in Equation 1.9, then the wavelength dependent decay in excess fraction might be explained by inferring that dust closer to the star would decay more rapidly than dust further away. This is similar to the dust distribution in our own Solar System, where the mass of the MAB is lower than that of the EKB.

1.6.3 Disk Evolution: Stochastic or Steady-State?

One thing that can definitively be inferred from observations is the decrease in excess emission as stars age. In other words, though dust is replenished from collisions, the total disk mass is not conserved due to dissipative forces discussed in § 1.3.2. This trend persists across excesses detected at different wavelengths, although excesses in the far-IR decay slower than those in the mid-IR excesses, and at different rates around different types of stars.

The large spread of mid- and far-IR excesses for A stars of different ages can be explained by a steady state interpretation, where the dust evolves through collisions from a stirred belt (Su et al., 2006; Wyatt, 2008), losing material due to photo-radiative forces. A similar interpretation is typically invoked for the evolution of 24μm and 70μm detected dust for Solar type stars, as the dust persists for billions of years at a steady pace. The collisional evolution of MAB-like dust can explain the steady decay of observed warm dust excesses (Wyatt, 2008). The small number of 70μm (far-IR) excesses detected for FGK stars might be indicative of less massive disks around these type of stars compared to A stars, which would in turn reduce the observed fractional excess (Wyatt, 2008).

However, stochastic evolution cannot be discounted as it can explain the observed excess emission from a number of systems. Stochastic processes must be at work in stars like Vega, where the inferred mass loss rate is too high to be explained from steady state evolution (Su et al., 2006). Massive collisions of large objects and density wave perturbations are likely responsible for the large amount of gas and dust seen in the β Pic system (Telesco et al., 2005; Nesvold & Kuchner, 2015). Stochastic evolution might also be responsible for the observed warm dust excesses around solar type stars, rather than the

steady state MAB evolution. The rapid decay of 24μm excess incidences for FGK stars is circumstantial evidence of terrestrial planet formation as large planetesimals may induce collisions amongst the smaller $\sim$1000 km sized bodies or a destruction of fully grown planetoids (Meyer et al., 2008; Wyatt, 2008).

1.7 What Is Missing?

Unfortunately, the degeneracy of the dominant physical process governing the dust — and subsequent planetary — evolution can only be broken by learning about the presence of dust throughout the system. Characterization of debris disks is not an easy task, as multiple surveys are required to determine the presence of dust at different wavelengths — and hence different temperatures. However, the majority of disk detections have occurred in the far-IR. The cold dust surveys have no doubt pushed the threshold of dust detection and characterization to fainter levels, in some cases as faint as the Solar System's dust disk.

However, the relatively small incidence of warm dust detections, in comparison with cold dust detections needs to be addressed, given the sample sizes and instrument sensitivity of the past surveys (discussed in detail in § 2.1. Recent work using reprocessed *Spitzer*/IRS data has shown that a large number of previously detected cold dust systems also posses a warm dust component (Chen et al., 2014). Whether these are separate disks or different co-located dust populations can be ambiguous. What is certain is that identification and characterization of more warm dust systems will aid in determining the ubiquity of solar system analogs, and perhaps even the prospects of searching for a system whose inner regions are hospitable for conditions seen here on Earth.

In hopes of furthering our understanding of warm dust systems, and their role in understanding our own Solar System's evolution, I conducted a series of surveys to identify and characterize previously undetected warm dust hosts in the solar neighborhood. I continue this thesis in § 2, by introducing the *WISE* space-based telescope, how the data from this survey can be used to identify warm disks, how the *WISE* mission supersedes the last all-sky IR survey, and how it complements the past pointed space based surveys. In Chapter 3, I present a survey to identify disks around *Hipparcos* stars within the solar neighborhood, from their *WISE* color excesses. I show how the *WISE* data can be refined and precisely calibrated to include saturated stars, eliminate major contaminants, and accurately determine the photospheric *WISE* colors, with which to identify faint excesses. In Chapter 4, I enhance the first survey by verifying and validating the excesses we previously found through improved methods to calibrate our confidence levels and the photospheric flux,

as well as remove additional contaminants from high-resolution *WISE* images. In chapter 5, I expand on the first two studies by presenting a preliminary analysis, with which I identify a larger sample of debris disks between 75 and 120 pc. The importance of these three studies are discussed in chapter 6, after which I conclude by outlining how I plan to build upon this work to study the evolution of warm disks in the solar neighborhood.

Chapter 2

Detecting Debris Disks with the Wide-Field Infrared Survey Explorer

2.1 Limitation of Past Surveys

What is apparent from the plethora of debris disk studies over the last three decades is the differences in the reported incidence rate of excesses. Though there is a consensus in terms of typical rates for a given spectral type at various stellar ages, the differences, even within these different bins, require further consideration.

There are a few reasons why these differences exist. The first is instrument sensitivity. Different instruments aboard these satellites are sensitive to different degrees. A good review can be found in Wyatt (2008), where he describes the limiting fractional excess $R_{\lambda,\mathrm{lim}}$ above which a disk is detectable, typically calculated based on the limits of the faintest disk detected in the survey. Equation 11 in Wyatt (2008) defines the lowest fractional luminosity above which a disk is detectable

$$f_{\mathrm{det}} = 6 \times 10^9 X_\lambda \frac{R_{\lambda,\mathrm{lim}} L_\star}{r^2 T_\star^4} \frac{B_\lambda(T_\star)}{B_\lambda(T_d)}. \tag{2.1}$$

Figure 2.1 shows the limiting fractional luminosity from a few different surveys as a function of orbital separation. From *IRAS* to *Spitzer*, improvements in both detector technology and an increase in mirror size have allowed for the detection of fainter and fainter dust populations. Hence, the increase of incidence rates from *IRAS* to *Herschel* does not come as much of a surprise given that *Spitzer* and *Herschel* are sensitive to fainter dust (cold or warm).

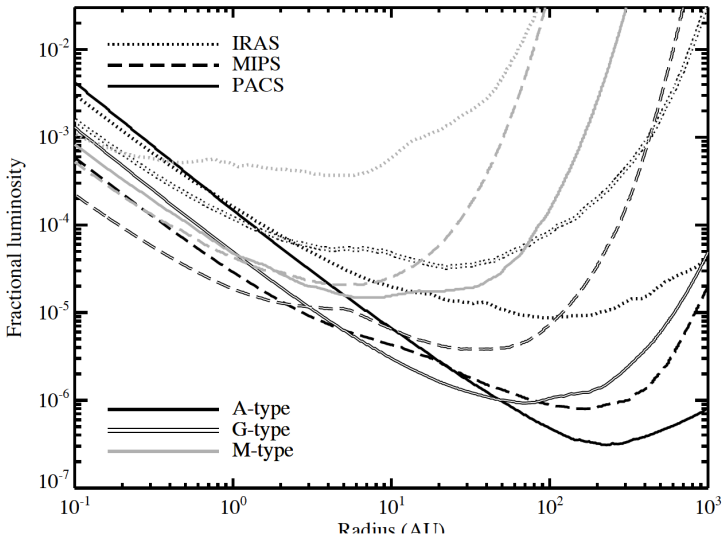

Figure 2.1: This plot shows the limiting fractional luminosity as a function of distance from the star based on data from the DEBRIS survey. Above these lines, 25% of the stars in DEBRIS were detected by surveys conducted by *IRAS*, *Spitzer*/MIPS (24 and 70μm) and Herschel/PACS (100 and 160μm) (Image credit: Grant Kennedy in Matthews et al., 2014)

Differences in incidence rates can also arise due to the threshold of an excess some studies may adopt compared to others. As explained in § 1.4.2, the excess flux is determined from the measured IR flux subtracted from the photospheric flux, which is extrapolated from model fits to optical and near-IR flux measurements. Studies may determine the significance of an excess detection from this subtraction on a case-by-case basis. Other studies may identify excesses based on their statistical significance in a distribution of photospheric-subtracted excesses. However, stellar variability, and more importantly poor calibration of survey systematics of the optical and near-IR data — which is taken over multiple epochs and by various instruments — result in a greater incidence of false detections, as well as a decrease in survey sensitivity.

Studies that used pointed observations with *Herschel* or *Spitzer* were limited to sample sizes of ∼500 stars, due to the pointed nature of the satellite. And although *IRAS* was an all-sky mission, it produced only a couple hundred excess sources, the majority of which were detected at $\lambda \geq 60\mu$m. The study by Rhee et al. (2007) searched for excesses around ∼622 *Hipparcos* main-sequence stars, and produced roughly 50 new excesses, the majority of which were still cold disk detections. We have seen that cold dust is easier to detect due to the large contrast with the photosphere in the far-IR. Low contrast

becomes an issue in the mid-IR, where there are a relatively small number of warm dust detections.

The small number of warm dust detections is due to the small coverage of very sensitive pointed satellites like Spitzer and Herschel, and the relatively low resolution and sensitivity of the last all-sky mission, *IRAS*, where the resolution of the *IRAS* beam was $30''$ at 12μm. To address these limitations, in this thesis, I aim to detect warm dust systems with the latest all-sky infrared mission: the space-based Wide-Field Infrared Survey Explorer.

2.2 The Wide-Field Infrared Survey Explorer Mission

The success of the *IRAS* mission was one of the motivations for launching another new and improved infrared all-sky mission. The goals of the Wide-Field Infrared Survey Explorer mission (*WISE*; Wright et al., 2010) were to observe the entire sky at two near-IR and two mid-IR wavelengths, thus improving and complementing the achievements of *IRAS*. In this section, I discuss the details of the *WISE* mission. Analysis of data from the *WISE* survey constitutes the bulk of my thesis. In the following section, I will summarize the *WISE* mission, explain its purpose and technical specifications, and discuss how data from the mission can be used to identify circumstellar dust.

2.2.1 Mission Overview

WISE is an Earth orbiting observatory, 525 km above the Earth's surface. *WISE* is funded by NASA/JPL and launched on December 14th, 2009. It is a medium-class explorer mission weighing 750 kg. The satellite consists of a 40 cm diameter telescope and four detectors which are cooled by solid hydrogen cryostats. Two of the detectors are designed to image the sky in the near-infrared wavelengths (3.5μm and 4.6μm) and two in the mid-infrared (12μm and 22μm). Figure 2.2 shows an illustration of the physical satellite.

The mission was successful in scanning 99.9% of the entire sky in the aforementioned IR bands. *WISE*'s detector field of view is $47'$ on a side. During its continual orbit around the Earth, overlapping frames were observed at 11 second cadences (8.8 s of integration). The overlap of frames, over multiple orbits, ensures greater depth of coverage. In one day, the satellite performs 15 orbits. Figure 2.3 shows the overlapping frames as the satellite orbits the Earth. Further details of the entire mission can be found online[1] or in Wright

[1] `http://wise2.ipac.caltech.edu/docs/release/allsky/expsup/`

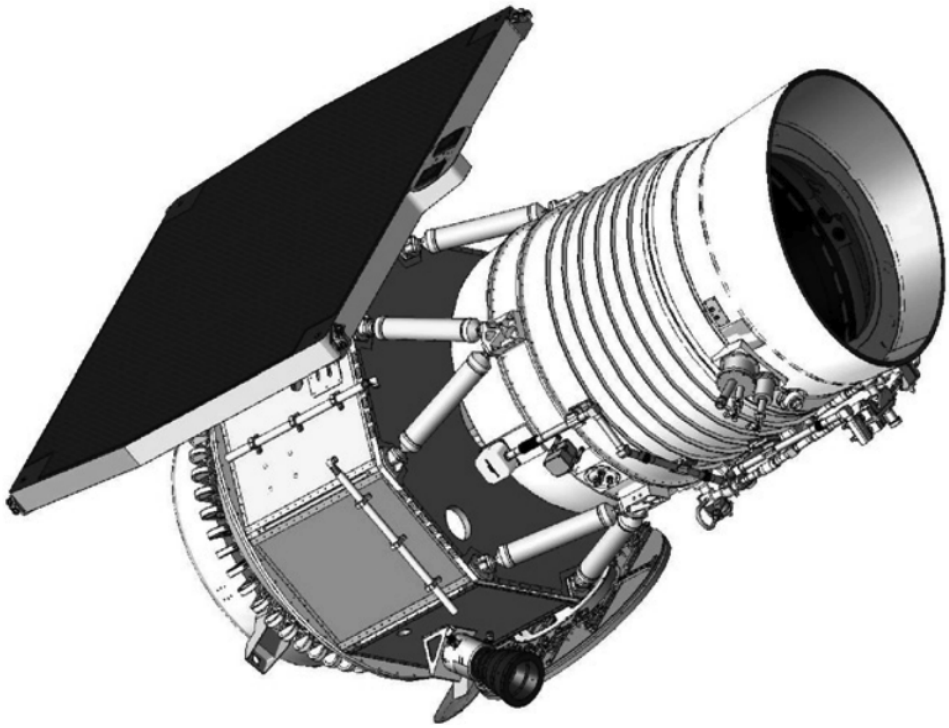

Figure 2.2: Illustration of the *WISE* satellite. Image credit: Wright et al. (2010).

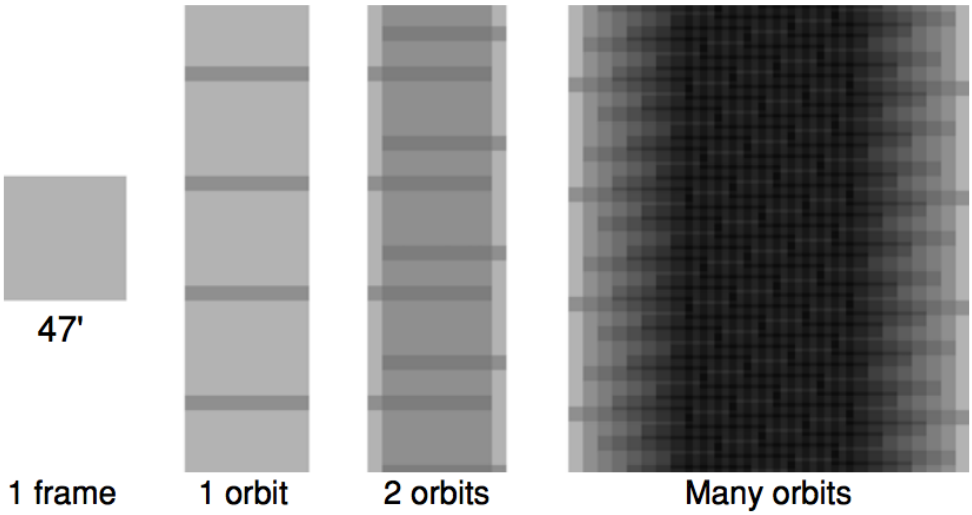

Figure 2.3: *WISE* coverage evolution over many orbits of the satellite around Earth. Each frame is a cadence of 11 s, and subsequent observations provide overlapping regions between frames. Lighter to darker shades of gray indicate increasing depth of coverage. Image credit: Wright et al. (2010).

et al. (2010).

2.2.2 *WISE* Bands

The two near-IR channels image the sky at band centered wavelengths of 3.4μm and 4.6μm using HgCdTe arrays, each with 18μm 1024 $\times$ 1024 pixels. Both of these detectors are cooled to 32 K. The mid-IR channel detectors image the sky at band centered wavelengths of 12μm and 22μm and are made from Si:As BIB arrays of the same structure as the near-IR channels. These arrays are cooled to a temperature of 8.2 K. For the remainder of this thesis, I will refer to each of these bands as $W1$ (3.4μm), $W2$ (4.6μm), $W3$ (12μm) and $W4$ (22μm). Figure 2.4 shows the relative spectral response of each of the detectors.

2.2.3 *WISE* Data Releases

The *WISE* mission has produced several different data releases. The first release, called the *WISE Preliminary Release* was made public on April 14, 2011[3] and contained data that covered only 57% of the sky. The next public release

[3] `http://wise2.ipac.caltech.edu/docs/release/prelim/preview.html`

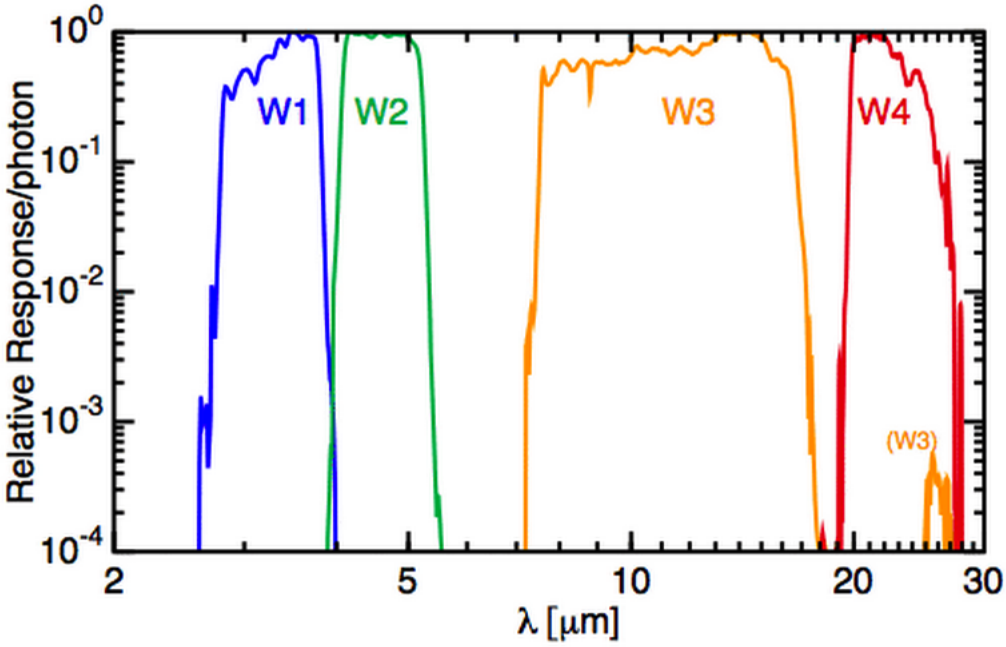

Figure 2.4: Relative spectral response curves for all four *WISE* bands. Plot was taken from the *WISE* Explanatory Supplement[2].

of *WISE* data was made on March 14, 2012. This data set was called the *All-Sky Data Release*[4] and covered the entire sky in all four bands. After the cryostats were depleted, *WISE* began its "warm" mission, and only collected data in the two near-IR $W1$ and $W2$ bands. This commenced the Near-Earth Object *WISE* (NEOWISE) mission. A subsequent all-sky data release by *WISE* came on November 13, 2013 called the *All-WISE Data Release*[5]. For the work I present in the rest of this dissertation, I only use measurements from the *All-Sky Data Release*, except in comparison with other release.

Since the *WISE* data are in the public domain, it can easily be accessed online. The online database consists of measurements for over half a billion objects in all four bands. These measurements consist of photometric data for each band, as well as meta-data pertaining to the quality of the data product. The database also consists of Atlas images of the processed data. The Atlas images were created for each *WISE* band, and are created from the coadded frames, and structured as $1.564^\circ \times 1.564^\circ$ tiles. The Atlas images can be viewed at `http://irsa.ipac.caltech.edu/applications/wise/`.

[4] `http://wise2.ipac.caltech.edu/docs/release/allsky/`
[5] `http://wise2.ipac.caltech.edu/docs/release/allwise/`

2.2.4 Cautionary Tales of *WISE* Data

Before using the *WISE* data products, it is important to understand all the nuances and aspects of what one might encounter. For instance, the *WISE* team implemented profile-fitting algorithms to extract photometric flux measurements and uncertainties. The *WISE* data also provide several meta-data tags for each source to characterize the quality of the measurement. Here I will summarize some of the more important meta-data tags found in the *WISE* database. All of these pertain to identifying sources whose photometry has a high probability of contamination from artificial and astrophysical sources, and hence are likely to bias the presence of an IR excess (i.e., debris disk).

Extended Source Contamination

The Two Micron All-Sky Survey (*2MASS* ; Skrutskie et al., 2006) is a ground based all-sky survey that has mapped the entire sky in three near-IR bands: J (1.25μm), H (1.6μm), and K_s (2.17μm). As a result, the location of known extragalactic extended sources is well known in the near-IR. Stars whose photometry might be contaminated by the flux from a nearby *2MASS* extended source are flagged in *WISE* using `ext_flg` meta-data tag. Figure 2.5 shows clearly how the photometry of one example star, HIP 3293, is contaminated from the isophotal footprint of a nearby *2MASS* galaxy.

Diffraction and Internal Reflection Artifacts from Bright Stars

Source photometry can also be contaminated by optical artifacts. Diffraction spikes from nearby bright sources, scattered light halos from the edge of a bright source's PSF, optical ghosts caused by internal reflections of the telescope optics, and latent images can all contaminate a real source or give rise to a spurious detection. The level of contamination for a source in each of the four *WISE* bands is given the confusion flag `cc_flg` — a four character string. For instance, the star HIP 32362's `cc_flg=hhdd`, implying that the $W1$ and $W2$ bands are predominantly contaminated by halo artifacts from a nearby bright star, while the $W3$ and $W4$ bands are contaminated by diffraction spikes from a nearby bright source. Figure 2.6 shows locations of spurious sources caused by the different artifacts around an example stars, HIP 32362. A full description of these artifacts can be found in Section IV.4.g of the *WISE* Explanatory Supplement[6].

[6] `http://wise2.ipac.caltech.edu/docs/release/allsky/expsup/sec4_4g.html`

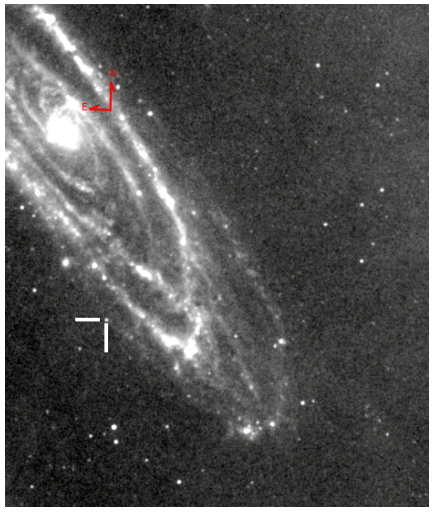

Figure 2.5: An example of a star contaminated due to a *2MASS* extended source object. This $W4$ band image shows the star, HIP 3293, indicated by the blue circle, within the vicinity of a background extragalactic source. The photometry of this star is flagged with *extflg*=2, indicating that it is within the isophotal footprint of this galaxy, and is likely to be contaminated. Image from *WISE* All-Sky Atlas Server.

Moon Contamination

The geocentric orbit of *WISE* unfortunately meant it had to contend with scattered light from the Moon. *WISE*'s observing pattern was such that it attempted to avoid this scattered light. However, complete avoidance was impossible, and the scattered light from the Moon heavily affected a small fraction of the frames in $W3$ and $W4$ relative to the near-IR bands. Figure 2.7 shows the structure of this effect in the $W3$ and $W4$ band images, with the star HIP 114340 marked for reference. The level of the contamination is given by the `moon_flg` and provides the percentage of single frames that are contaminated by the moon for each band. Additional information on Moon contamination in *WISE* can be found at `http://wise2.ipac.caltech.edu/docs/release/allsky/expsup/sec6_2.html`.

Saturated *WISE* Photometry

The detectors aboard the *WISE* spacecraft saturate for relatively bright sources: 8.1 mag, 6.7 mag, 3.8 mag, and -0.4 mag in $W1$, $W2$, $W3$, and $W4$, respectively. It is important to keep these limits in mind, as the photometry for sources brighter than these saturation limits is unreliable. Additional infor-

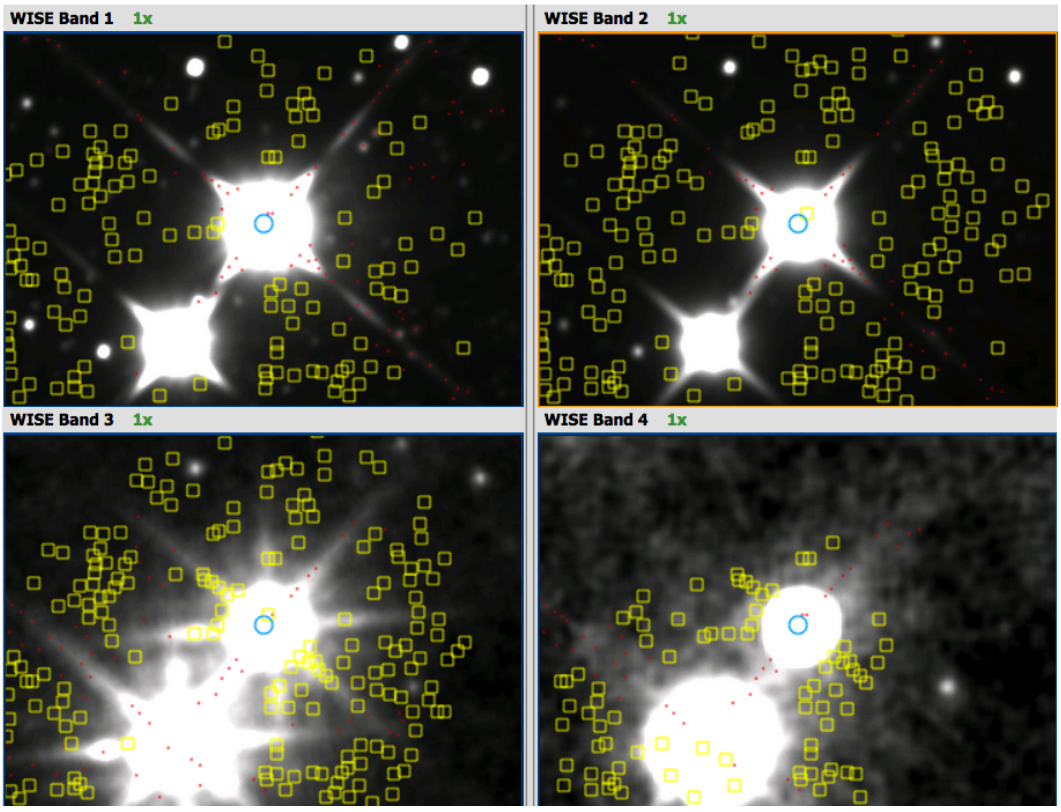

Figure 2.6: *WISE* four band image centered on HIP 32362. The confusion flag for this star is *ccflg=hhdd*. These flags, one character per band, indicate that the source is real but is most likely contaminated spurious sources resulting from diffraction spikes (d) and halo flux (h) from the nearby bright star. Diffraction spikes and halo flux are marked by red circles and yellow squares, respectively. Image from *WISE* All-Sky Atlas Server.

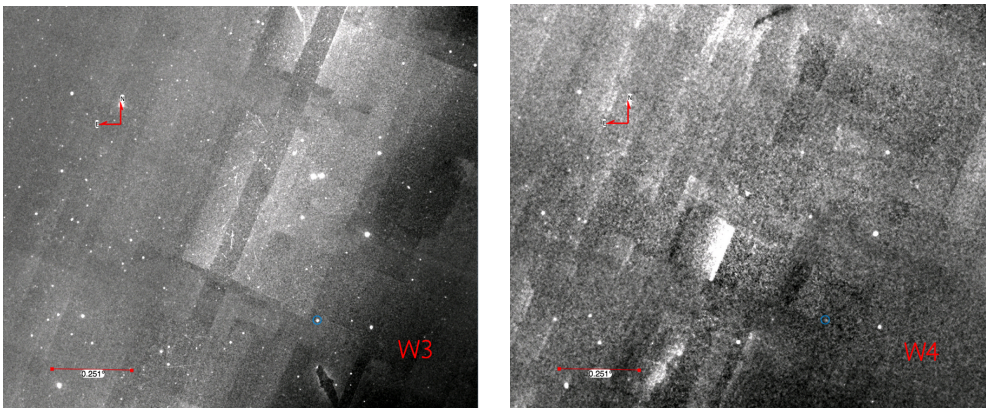

Figure 2.7: *WISE* $W3$ and $W4$ images that show structured scattered light contamination from the Moon. The blue marker indicates the location of the star, HIP 114340. The moon flag for this star indicates that 80% of its frames are heavily affected by scattered Moon light. Image from *WISE* All-Sky Atlas Server.

mation on the saturation of *WISE* sources can be found in Section VI.3.d of the *WISE* Explanatory Supplement[7].

The profile-fitting algorithm attempts to obtain measurements of saturated sources by using non-saturated pixels in the wings of the source's PSF. Figure 17 in Section IV.4.a.vi.1 of the Explanatory Supplement shows the *WISE* magnitudes as a function of their *2MASS* $K_s - WISE$ color. These plots show a different systematic trend for each *WISE* band. This trend is stronger in $W1$ and $W2$, which are the limiting bands in searching for excesses. As I will show in Chapter 3, these trends can be corrected, and thus allow for brighter stars to be used in a large survey.

Internally Inconsistent Variability

The variability flag in the *WISE* database `var_flg` indicates the probability that the flux in a particular band is changes as a function of time. The variability may be due to intrinsic astrophysical processes, as is for example chracteristic of pre-main sequence stars. The variability may also be due to a number of different factors pertaining to instrumental artifacts between subsequent single frame observations by *WISE*, in particular when a star is saturated. Saturation, and other spurious sources may cause variability to arise in one or more, but not all of the *WISE* bands. These *WISE* related variabilities are non-physical and must be addressed before searching for excesses.

[7] `http://wise2.ipac.caltech.edu/docs/release/allsky/expsup/sec6_3d.html`

Additional information for the variability flag can be found at `http://wise2.ipac.caltech.edu/docs/release/allsky/expsup/sec4_4ciii6.html`

Internally Inconsistent Photometry

During the course of this project, we found a peculiar behavior in the *WISE* data. In some very rare cases, the final reported flux measurement in the All-Sky database — after all relevant single frames for that particular star were coadded by the *WISE* internal algorithms — significantly differed from the averaged single-frame measured fluxes for the same star. In other words, there seemed to be internal *WISE* inconsistencies in the measurements of a small percentage of stars, manifesting itself such that the reported coadded photometry was brighter compared to the averaged single frame measurement.

Since we are looking for peculiar (i.e., excesses), we are sensitive to finding these stars. Although there is no reported reason for this phenomenon, we have found a way to deal with this inconsistency and detail it in § 2.3 of Chapter 3.

2.2.5 Advantages Of Using *WISE* Over Other Space Telescopes To Find Debris Disks

IRAS' all-sky design made it ideal to to search for excesses around a large number of stars. And though it found a few hundred excesses, its successor — *WISE* — is capable of advancing this search. This is due to two reasons. The first is that *WISE* is a more sensitive survey compared to *IRAS*. *IRAS* was sensitive down to $\sim$0.2 Jy in its 12 and 25μm bands. In comparison, *WISE* is 160–200$\times$ more sensitive in its $W3$ and $W4$ bands. Figure 2.8 shows the absolute sensitivity of both *IRAS* and *WISE* for each of their IR detectors. The second reason why *WISE* has the ability to outperform *IRAS* in the mid-IR is due to *WISE*'s relatively high resolution compared to *IRAS*. *WISE*'s angular resolution for $W1$–$W4$ is 6.1$''$, 6.4$''$, 6.5$''$, and 12$''$, respectively, with an astrometric accuracy of 0.2$''$. In comparison, the angular resolution of the 12μm detector on *IRAS* is 30$''$ but has a positional accuracy of 20$''$. Figure 2.9 shows the same patch of sky seen by *IRAS* at 25μm and *WISE* at 22μm. The comparison images clearly show that with the superior angular resolution, *WISE* has the ability to identify a plethora of unconfused debris disks from their IR excesses. This is also reflected in the sheer number of point sources catalogued in the *WISE* All-Sky Database ($\sim$600,000,000), compared to those in the *IRAS* database ($\sim$270,000).

The size of the *WISE* All-Sky Database is also important because it provides an advantage over surveys that use Spitzer or Herschel to search for excesses. Figure 2.10 compares the projected sensitivity of instruments on board

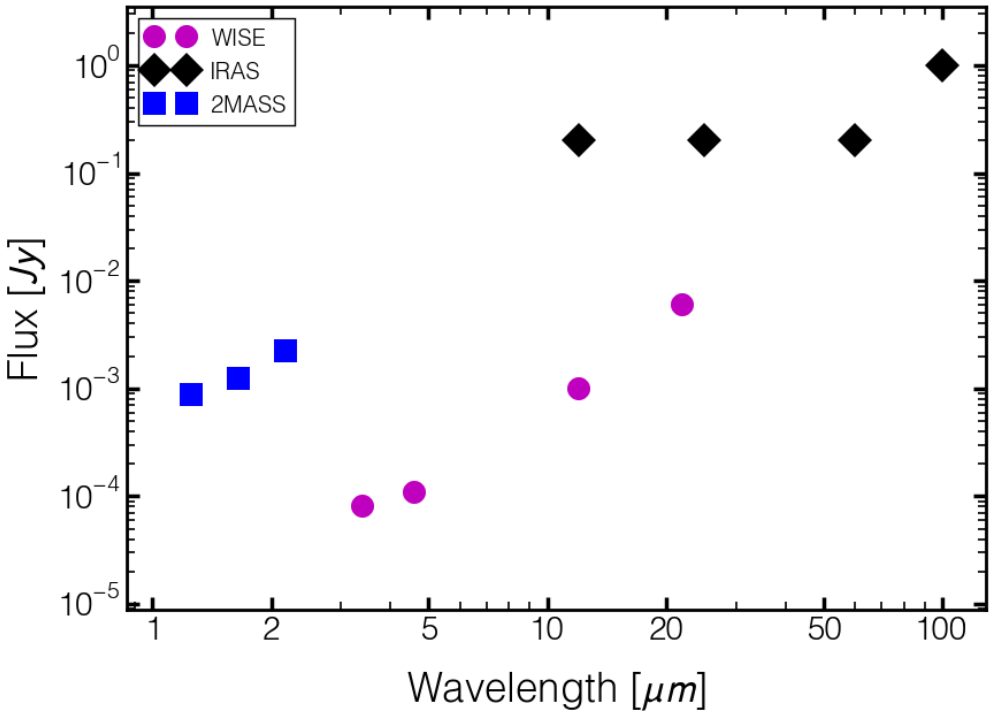

Figure 2.8: Sensitivity of different IR surveys. Plotted are the *WISE*, *IRAS*, and *2MASS*. The plotted *WISE* limits are 5σ point source sensitivities, calculated in unconfused ecliptic regions. These estimates improve at the galactic poles.

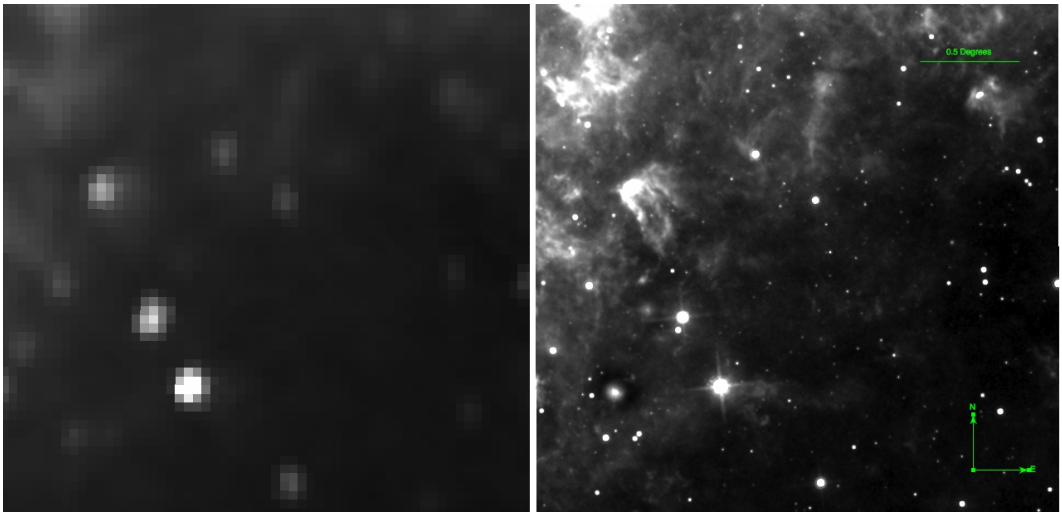

Figure 2.9: Images from *IRAS* at 25μm (left panel) and *WISE* 22μm (right panel), centered on RA=10h 09m 39.5s, DEC=$-60°$ 14' 47" sky coordinates. The difference in resolution and sensitivity is apparent between the two. Image from *WISE* All-Sky Atlas Server and IRAS Atlas Server.

WISE, Spitzer, and *IRAS* in the mid-IR. While it is clear that *WISE* is able to detect fainter dust than *IRAS* at similar wavelengths, the Spitzer/MIPS and IRS instruments have been used to find fainter dust populations. This is no surprise because *Spitzer* is a pointed survey, with higher angular resolution than *WISE* and can hence increase its sensitivity to fainter dust through longer observing times. But, since pointed surveys can only observe a tiny fraction of the sky, the data products from an all-sky survey, like *WISE* can search for excesses around stars which have never been observed.

2.3 Detecting Thermal Emission From Debris Disks with *WISE*

2.3.1 The *WISE* Color Excess Technique and its Advantages

Most debris disks have been found from the subtraction of the measured IR flux from the modelled photospheric flux, as described in § 1.4.2. An alternative to photospheric modelling of individual stars is to derive an estimate of the excess empirically by calculating star's "color excess". The astronomical magnitude system defines the color of a star by the logarithmic ratio of fluxes at two

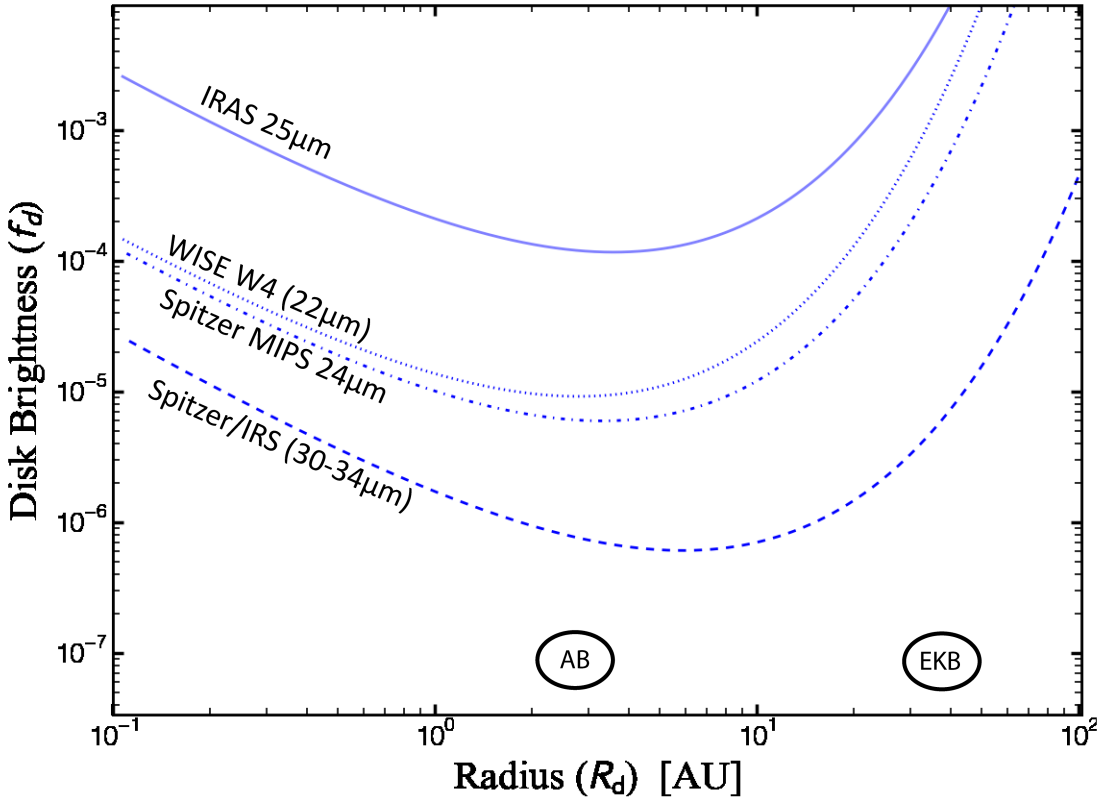

Figure 2.10: Disk brightness sensitivities for dust at different radial locations for various surveys. The curves are calculated by using Equation 2.1, assuming a stellar temperature for an A0 star at $T_\star = 9000$ K. R_λ for Spitzer/IRS is 0.024 (Chen et al., 2006), 0.1 for Spitzer/MIPS 24μm (Rieke et al., 2005) and 0.12 for *WISE* $W4$ (derived from Patel et al., 2014a). Disks can only be detected if they fall above these curves. The location of the Asteroid belt and EKB are plotted for context.

different wavelengths

$$m_{\lambda_1} - m_{\lambda_2} = -2.5 \log F_{\lambda_1}/F_{\lambda_2}, \tag{2.2}$$

where $\lambda_1 < \lambda_2$. For our purposes, we will assume that λ_1 is between $2 - 5\mu$m and $\lambda_2 > 10\mu$m. If we knew the "photospheric color", (i.e., color of the dust-free star) $(m_{\lambda_1} - m_{\lambda_2})_\star$, then we can determine the color excess, by subtracting the photospheric color from the measured color $(m_{\lambda_1} - m_{\lambda_2})_m$

$$\begin{aligned} E\left[m_{\lambda_1} - m_{\lambda_2}\right] &= (m_{\lambda_1} - m_{\lambda_2})_m - (m_{\lambda_1} - m_{\lambda_2})_\star & (2.3) \\ &= m_{\lambda_2 \star} - m_{\lambda_2 m}, & (2.4) \end{aligned}$$

where we assume that $m_{\lambda_1 \star} = m_{\lambda_1 m}$, and that the photospheric color is estimated empirically from the average or median value of a large set of measurements of similar stars. For photospheric colors consistent with a Rayleigh-Jeans slope, $E\left[m_{\lambda_1} - m_{\lambda_2}\right] = 0$. Thus, stars with excesses can be identified by positive, non-zero color excesses such that $E\left[m_{\lambda_1} - m_{\lambda_2}\right] > 0$.

Searching for excesses by using color can be advantageous over searching for excesses from photospheric fitting. The latter technique can introduce inherent biases in measuring the dust emission. The photospheric emission in the IR is estimated from fitting a photospheric model using photometric or spectroscopic data from observations at different epochs. Intrinsic stellar variability will offset any predicted IR flux, subsequently over- or underestimating the amount of IR excess flux. But more importantly, by using data from multiple epochs and different instruments, the relative systematic uncertainties between the flux measurements will reduce the survey sensitivity, and subsequently the significance of the dust emission one is trying to extract.

However, if the photospheric flux is determined by fitting contemporaneously obtained data from the same instrument, the relative systematic uncertainties disappear. For example, Lawler et al. (2009) conducted a study that used Spitzer/IRS spectra, which span shorter near-IR wavelengths, as well as mid-IR wavelengths of interest to detecting excesses. By using the shorter wavelength end of the spectra as an anchor for the photospheric emission, they were then able to predict the photospheric flux at in the mid-IR. Most surveys do not have the capability to simultaneously measure flux in short and long wavelength bands. This limitation makes SED fitting the primary method to identify excesses. The difference in the flux of the detected excess between "color excesses" and "photospheric fitting" is small and only becomes relevant when searching for faint excesses ($f_d < 10^{-4}$–10^{-7}). Though when the goal is to attain greater sensitivity to solar system like dust ($f_d \sim 10^{-7}$),

the additional sensitivity becomes invaluable.

It is in this regime that *WISE* has the largest advantage. For the first time, *WISE* has afforded astronomers the ability to conduct an IR excess search of debris disks through photometric data obtained contemporaneously at both photospheric and dust thermal emission wavelengths *of the entire sky*. Thus, it only makes sense to take advantage of the properties of this data and search for IR excesses using the more sensitive color excess search technique. In this case, equation 2.3 will look like

$$E\left[Wi - Wj\right] = \left(Wi - Wj\right)_m - \left(Wi - Wj\right)_\star, \tag{2.5}$$

where Wi and Wj are the *WISE* bands described in § 2.2.2, such that $Wi = W1$, $W2$, or $W3$ and $Wj = W3$ or $W4$ with the constraint that $Wi < Wj$. The work that I will present in the rest of this thesis is based on the measurements defined in equation 2.5. By using the color excess technique in conjunction with the all-sky coverage data from *WISE*, I will not only be able to identify a large number of excesses but, also gain sensitivity to fainter warm disks around stars that were previously missed due to either lack of resolution or coverage.

2.4 Previous *WISE* Debris Disk Studies

The series of studies that I will be presenting in the subsequent chapters are by no means the first or only studies that have searched for debris disks using data from *WISE*. Here, I will summarize the current literature of *WISE* studies to detect debris disks.

Studies have used data from different data releases on a variety of different data sets to search for debris disks. In particular, a number of studies have searched for excesses around different sets of exoplanet populations to study the relationship between debris disks and planets. Krivov et al. (2011) and Morales et al. (2012) determined that $\sim$2% of known exoplanet transiting hosts possess warm dust based on having *WISE* $W3$ or $W4$ excesses. Kennedy et al. (2012), Ribas et al. (2012), and Lawler & Gladman (2012) searched for excesses around the large number of potential planet host stars in the *Kepler* field. Altogether, roughly two dozen stars with $W3$ or $W4$ excesses were identified.

Other experiments aimed to study the evolution of disks around a younger set of stars. The Scorpius-Centaurus OB association was heavily scrutinized by Rizzuto et al. (2012), Luhman & Mamajek (2012), and Riaz et al. (2012). About 150 stars with excesses were identified from these studies. Other studies focused on *WISE* debris disk searches around subsets of solar neighborhood stars within certain spectral type ranges. Avenhaus et al. (2012) found no

significant *WISE* excess flux around 103 M-dwarfs, while Vican & Schneider (2014) identified 98 excesses from a sample of ∼8800 solar type stars.

Wu et al. (2013) and Kennedy & Wyatt (2013) searched for excesses around a larger, unbiased sample of stars. The latter study searched for $W3$ excesses, around main-sequence *Hipparcos* stars, while the former study searched for $W4$ excesses around the same set of stars. Kennedy & Wyatt (2013) found 7 new $W3$ excesses with an incidence rate of $< 1\%$ for warm dust in the habitable zone of main sequence stars. Wu et al. (2013) identified roughly 70 new bright $W4$ excesses for stars out to 200 pc. In total, roughly 250 new excesses were identified by all these studies using data from *WISE*. These studies have increased our understanding of warm dust, and how it relates to systems of different ages, as well as systems with known planets.

There are a number of biases inherent in all these surveys. The first is that due to the saturation limits of *WISE*, relatively nearby stars were not included in these surveys. A number of these studies have self identified or have since been shown to have reported false excesses. Certain false-excesses were identified by Kennedy & Wyatt (2013) in their own study, while we have identified a number of false-excesses from studies such as Vican & Schneider (2014) in the subsequent chapters. All of these studies used SED fitting or color thresholds without subtracting the photospheric color to identify an excess – both methods which can introduce false excesses (see § 2.3.1). False-positives can also be introduced due to caveats in the *WISE* data (some of which are discussed in § 2.2.4). In fact, none of these past studies have taken a full account of all these false-positive sources. These false-positive sources not only contaminate the literature, but also decrease a survey's sensitivity. Therefore, the full potential of *WISE*'s sensitivity in searching for mid-IR excesses has not been realized.

In the following chapters, I will address these biases and present a set of studies that complements, as well as improves upon the search for warm dust with *WISE*. I utilize the *WISE* data to accurately understand the systematic behavior of the *WISE* data and identify warm dust around nearby main-sequence stars through the use of empirically identified *WISE* colors in addition to incorporating bright, saturated *WISE* photometry. Thus, not only are we able to find faint warm dust in some of these systems, relative to published studies, it will search for undetected excesses around nearby bright stars.

Chapter 3

Identification of Warm Debris Disks Within 75 pc

The study presented here is the first in a series of three to identify mid-IR excesses with WISE at $W3$ and $W4$. This study has been published in the Astrophysical Journal Supplement Series, volume 212, on April 24, 2014. Only a portion of Figure 6 is shown in this paper. The full set can be found in § D.1. In addition, only a portion of Tables 5, 6, and 7 are shown in this article. The complete tables can be found in § B.2.

The Astrophysical Journal Supplement Series, 212:10 (23pp), 2014 May doi:10.1088/0067-0049/212/1/10

A SENSITIVE IDENTIFICATION OF WARM DEBRIS DISKS IN THE SOLAR NEIGHBORHOOD THROUGH PRECISE CALIBRATION OF SATURATED *WISE* PHOTOMETRY

Rahul I. Patel[1], Stanimir A. Metchev[1,2], and Aren Heinze[1]
[1] Department of Physics & Astronomy, Stony Brook University, 100 Nicolls Road, Stony Brook, NY 11794–3800, USA; rahul.patel.1@stonybrook.edu
[2] Department of Physics & Astronomy, The University of Western Ontario, 1151 Richmond Street, London, Ontario N6A 3K7, Canada
Received 2014 January 12; accepted 2014 March 10; published 2014 April 24

ABSTRACT

We present a sensitive search for *WISE* $W3$ (12 μm) and $W4$ (22 μm) excesses from warm optically thin dust around *Hipparcos* main sequence stars within 75 pc from the Sun. We use contemporaneously measured photometry from *WISE*, remove sources of contamination, and derive and apply corrections to saturated fluxes to attain optimal sensitivity to $>10\,\mu$m excesses. We use data from the *WISE* All-Sky Survey Catalog rather than the AllWISE release because we find that its saturated photometry is better behaved, allowing us to detect small excesses even around saturated stars in *WISE*. Our new discoveries increase by 45% the number of stars with warm dusty excesses and expand the number of known debris disks (with excess at any wavelength) within 75 pc by 29%. We identify 220 *Hipparcos* debris disk host stars, 108 of which are new detections at any wavelength. We present the first measurement of a 12 μm and/or 22 μm excess for 10 stars with previously known cold (50–100 K) disks. We also find five new stars with small but significant $W3$ excesses, adding to the small population of known exozodi, and we detect evidence for a $W2$ excess around HIP 96562 (F2V), indicative of tenuous hot (780 K) dust. As a result of our *WISE* study, the number of debris disks with known 10–30 μm excesses within 75 pc (379) has now surpassed the number of disks with known $>30\,\mu$m excesses (289, with 171 in common), even if the latter have been found to have a higher occurrence rate in unbiased samples.

Key words: infrared: planetary systems – planetary systems – protoplanetary disks – stars: statistics – zodiacal dust

Online-only material: color figures, extended figure, machine-readable tables

1. INTRODUCTION

Numerous surveys have been conducted to search for dusty disks around main sequence stars over the last three decades. The all-sky survey performed by the *Infrared Astronomical Satellite* (*IRAS*) was the first to detect infrared (IR) excess emission from circumstellar dust disks at 25 and 60 μm, with ~170 disks identified in all. Subsequent pointed surveys with the *Infrared Space Observatory* (*ISO*), the *Spitzer Space Telescope*, and the *Herschel Space Observatory*, and the recent all-sky survey by the *AKARI* satellite have greatly increased the number of disks discovered. To date, over 350 debris disks are known around main sequence stars within 75 pc (e.g., Su et al. 2006; Moór et al. 2006, 2009, 2011; Bryden et al. 2006; Rhee et al. 2007b; Trilling et al. 2008; Hillenbrand et al. 2008; Carpenter et al. 2009; Mizusawa et al. 2012; Fujiwara et al. 2013; Eiroa et al. 2013; Wu et al. 2013; Cruz-Saenz de Miera et al. 2014, and references therein), and several hundred more around more distant stars, including open cluster members, out to ~1 kpc (e.g., Siegler et al. 2007; Currie et al. 2008a, 2008b).

Most (~85%) of the known debris disks in the solar neighborhood are comprised of cold (<100 K) circumstellar dust. These have been identified through their characteristically strong emission at wavelengths longer than 30 μm, at which the disks are often orders of magnitude brighter than the stellar photosphere. This cold dust is analogous to debris produced from destructive collisions in the solar system Edgeworth–Kuiper Belt (EKB). The dust has to be continually produced in such collisions because its lifetime in the system is short: large grains spiral into the star due to Poynting–Robertson drag, and small grains are blown outward by radiation pressure. Both processes remove dust on characteristic time scale shorter than one million years (Backman & Paresce 1993): much less than the ages of stars in the solar neighborhood. Except in cases of stars with obvious signatures of youth, the detection of cold circumstellar dust demonstrates the presence of a belt of colliding planetesimals which, like the dust, are likely located in the cold outer reaches of the system (i.e., >10 AU from the star).

Most known, faint warm debris disks have been discovered from pointed surveys with *Spitzer* (e.g., Su et al. 2006; Trilling et al. 2008; Carpenter et al. 2009). Deep targeted observations with the *Spitzer* Infrared Spectrograph (IRS; Houck et al. 2004), in particular, have allowed the measurement of excesses peaking in the 10–30 μm range at only 3% of the photospheric flux at the same wavelengths (Carpenter et al. 2009; Lawler et al. 2009). The advantage in using 5–30 μm mid-IR spectroscopy is that it allows an accurate calibration of the stellar photospheric flux—essential for detecting small excesses. However, pointed surveys by design are limited in scope, and the data interpretation is subject to biases in the sample selection.

WISE offers an opportunity to search for warm debris disks over the entire sky in an unbiased fashion. Though not as sensitive as deep, pointed Spitzer observations, *WISE* is 100–600 times more sensitive than *IRAS* and 10–50 times more sensitive than *AKARI* in the mid-IR—making it by far the most sensitive all-sky survey at these wavelengths. Through near-simultaneous and uniform 3–30 μm photometry, *WISE* also enables accurate calibration of the stellar photospheres, and hence good sensitivity to faint mid-IR excesses with <10% of the 10–30 μm photospheric flux.

Numerous searches of the *WISE* catalog have already been conducted to identify debris disks. Krivov et al. (2011), Morales et al. (2012), Ribas et al. (2012), Lawler & Gladman (2012), and Kennedy & Wyatt (2012) sought $W3$ and $W4$ excesses

among known extrasolar planet hosts. Approximately two dozen distinct planet–host stars with possible $W3$ or $W4$ excesses are found among these studies. Rizzuto et al. (2012), Riaz et al. (2012), Luhman & Mamajek (2012), and Dawson et al. (2013) sought *WISE* excesses in the young Scorpius-Centaurus association. The total number of disks identified in these studies is ≈160, with some duplications and/or non-confirmations among the three teams (note that not all of these were debris disks). Finally, Avenhaus et al. (2012), Kennedy & Wyatt (2013), Wu et al. (2013), Cruz-Saenz de Miera et al. (2014), and Vican & Schneider (2014) sought debris disks among solar neighborhood stars. Avenhaus et al. (2012) find no new $W3$ or $W4$ excesses around the 100 nearest M dwarfs. Kennedy & Wyatt (2013) identify 15 known and 7 new $W3$ excesses around *Hipparcos* stars within 150 pc. An excess at such relatively short wavelengths may indicate the presence of an exozodi: a dust population at a similar temperature to the solar system's zodiacal dust.

The recent studies of Wu et al. (2013) and Cruz-Saenz de Miera et al. (2014) are most similar to ours in design. Wu et al. (2013) seek $W4$ excesses around *Hipparcos* stars of all spectral types within 200 pc, while Cruz-Saenz de Miera et al. (2014) seek $W4$ excesses around F2–K0 stars brighter than $V = 15$ mag. As we discuss in Sections 5.2 and 5.3, our results are mostly complementary to the results from these studies. Importantly, through a careful calibration of *WISE* photometric systematics, we are able to detect excesses that are fainter than those reported in Wu et al. (2013) and Cruz-Saenz de Miera et al. (2014). Our newly identified disk host stars are also often either brighter (saturated in *WISE*) than those considered in Wu et al. (2013) and Cruz-Saenz de Miera et al. (2014), or fainter (with $W4$ S/N less than 20) than those considered in Wu et al. (2013).

An accurate understanding of *WISE* photometry systematics is essential to reliable identification of dust excesses. The strongest systematic effect is the over-estimation of the $W2$ fluxes of bright ($W2 < 6.7$ mag) stars from profile-fit photometry (see Section VI.3.c.i.4. of Cutri et al. 2012), but Kennedy & Wyatt (2013) and several additional studies also note remnant offsets in the *WISE* photometry and colors that render some previously reported tenuous excesses uncertain. We address this and other more subtle flux-dependent trends in the *WISE* photometry in Section 2.4.

Other reasons for mis-identifications include confusion with background IR-bright sources seen in projected proximity, contamination from interstellar cirrus, and unknown amounts of interstellar extinction. Various approaches have been adopted to mitigate these effects, including source position comparisons between the short- and long-wavelength *WISE* filters, exclusion of extended IR-bright regions in *IRAS*, confirmation of excesses through spectral energy distribution (SED) fitting, and, importantly, visual inspection of the stellar images (e.g., Kennedy & Wyatt 2013). We have incorporated all of these techniques, and others, in our approach (Section 2.2), and furthermore have only selected candidates at confidence levels greater than 99.5% or 98% at $W4$ or $W3$ respectively, based on the *empirical* scatter in WISE photometry. Importantly, we identify debris disk candidates using only *WISE* colors: the fact that these are homogeneous and simultaneous set of measurements reduces our vulnerability to stellar variability and other sources of error. Our results therefore present an opportunity for an unbiased analysis of the occurrence and evolution of warm circumstellar dusty disks.

We describe the method we used to identify IR excesses in Section 2. We present our cross-match with the entire *Hipparcos* catalog (Perryman et al. 1997; van Leeuwen 2007) with the *WISE* All-Sky Catalog (ASC; Wright et al. 2010) and define our working sample of stars in Sections 2.1 and 2.2, respectively. Section 2.3 addresses a previously unknown issue that we discovered with the reliability of *WISE* ASC photometry on certain stars. In Section 2.4, we outline how we precisely calibrated the *WISE* photometric systematics to produce a set of reliable debris disk detections for stars in our sample. Section 2.5 describes our IR excess identification procedure. Section 2.6 describes our test with identifying IR excesses in the more recent, AllWISE data release, and presents our arguments for the higher reliability of bright-star photometry in the preceding All-Sky data release. In Section 3, we describe our procedure for quantifying basic disk characteristics. Section 4 offers an analysis of the inferred circumstellar locations of the detected excesses: whether they belong to exozodi, asteroid belt analogs, or previously known colder EKB analogs. Section 5 discusses our results in the context of previous surveys with *IRAS*, *Spitzer*, *AKARI*, and *WISE*.

2. INFRARED EXCESS IDENTIFICATION AT $W2$, $W3$, AND $W4$

Our goal is to determine the number of *Hipparcos* stars with circumstellar debris disks, confined to within 75 pc of the Sun and without consideration for youth or the existence of known planets. We search for mid-IR excesses using all *WISE* color combinations, and select stars with significant IR excesses. Here we detail our infrared excess and debris disk candidate selection procedure.

2.1. WISE and Hipparcos Cross-match

We used the *Hipparcos* catalog, which has photometric and parallactic measurements for 117,955 stars, as our starting sample. We updated the stellar positions from the J1991.25 catalog epoch to J2010.54 (the mean epoch of *WISE* observations), using the *Hipparcos* proper motions. We positionally matched the *Hipparcos* stars to detections from the *WISE* ASC using the NASA Infrared Science Archive cross-match service[3] and a 1.″0 matching radius.

Following the cross-match, 159 *Hipparcos* stars remained unmatched in *WISE*. We recovered 116 of these stars in the *WISE* All-Sky Reject Table, which lists objects that were extracted from the *WISE* Atlas images, but were not included in the All-Sky Release Source Catalog because they did not meet the *WISE* Catalog source selection quality criteria (see Cutri et al. 2012). We performed this experiment only to account for unmatched *Hipparcos* stars: we did not include objects with rejected WISE extractions in our final analysis.

The remaining 43 unmatched stars are listed in Table 1 along with reasons for their omission. In the end, a total of 117,912 of the original 117,955 *Hipparcos* stars were positionally matched with *WISE* sources, and no unexplained match-failures remained.

2.2. Sample Definition

We define two samples of stars from *Hipparcos*: a parent sample and a science sample. The parent sample consists of *Hipparcos* stars within 120 pc of the Sun with parallaxes accurate to better than 20%. This provides us with a large enough population of stars to determine the photospheric *WISE* color

[3] http://irsa.ipac.caltech.edu/

Table 1
Unmatched *Hipparcos* Stars in the *WISE* All-Sky Source Catalog

Object	Reason	Object	Reason
HIP 4773	1	HIP 35744	2
HIP 24003	2	HIP 35925	2
HIP 24188	2	HIP 36051	2
HIP 26218	1	HIP 36113	2
HIP 26220	3	HIP 40215	2
HIP 26221	3	HIP 46675	1
HIP 26224	3	HIP 52133	1
HIP 26235	3	HIP 52541	1
HIP 28868	2	HIP 67207	1
HIP 29303	2	HIP 73471	1
HIP 29402	2	HIP 85148	1
HIP 29669	2	HIP 86512	1
HIP 29761	2	HIP 87022	1
HIP 30164	1	HIP 88333	1
HIP 30616	2	HIP 88818	1
HIP 30794	2	HIP 97589	1
HIP 30964	2	HIP 99001	1
HIP 31423	2	HIP 107094	1
HIP 33296	1	HIP 114110	4
HIP 35007	2	HIP 114176	4
HIP 35681	2	HIP 118182	1

Notes. Reasons: 1. Tenuous or no detections in *WISE* $W2$, $W3$, and $W4$ images, and a non-existent entry in the *WISE* All-Sky Source Catalog. 2. Partial or no *WISE* coverage. 3. Extensive $W3$ and $W4$ saturation because of an IR-bright surrounding nebulosity. 4. Not an astrophysical object: a *Hipparcos* object identified as an artifact, produced by scattered light from a nearby star.

dependencies. These stars are mainly within the Local Bubble (Lallement et al. 2003), have little line-of-sight interstellar extinction ($A_V \lesssim 0.5$ mag), and are suitable for correlating optical and infrared colors. The science sample is a subset of the parent sample limited to 75 pc. These are stars with accurate parallaxes, giving a clear volume limit to our study. In this study we report and analyze detections of debris disks only around stars in the 75 pc science sample.

For improved reliability of our debris disk host candidate selection, we applied a number of selection criteria to the parent and science samples. These are described in detail below, and summarized at the end of this section.

2.2.1. Parent Sample: Stars within 120 pc

We first eliminated stars within 5° of the galactic plane. Despite angular resolution 2.5–5 times better than that of *IRAS* at 12 and 25 μm, *WISE* images still face strong contamination from interstellar cirrus close to the plane of the Galaxy. In addition, the local background for *WISE* photometry is estimated from a 50″–70″ annulus around each target, which can result in erroneous flux measurements when the surrounding sky brightness varies on these scales.

We further removed classes of stars in which mid-IR excesses are unlikely to be caused by circumstellar debris disks. We followed a procedure similar to the one described in Rhee et al. (2007b) to remove giant stars from our sample, by placing an absolute magnitude restriction: we retained only stars fainter than $M_V = 6.0(B - V) - 1.5$ mag (Figure 1). We removed stars with SIMBAD luminosity classes of I, II, or III that were missed during the color cut, and other non-main sequence stellar objects: post-asymptotic giant branch stars, white dwarfs,

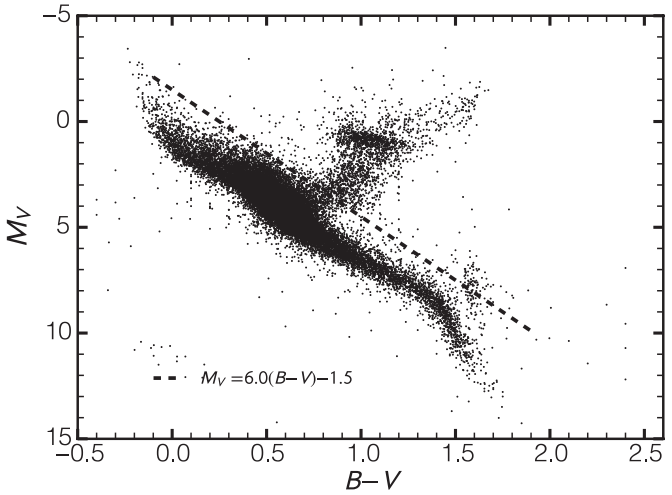

Figure 1. All *Hipparcos* stars in our ⩽120 pc parent sample fall below the prescribed absolute magnitude cut to remove giant stars. The parent sample is restricted to stars with $d \leqslant 120$ pc to reduce the effects of reddening from interstellar cirrus. Stars are also restricted to positions outside the galactic plane ($|b| \geqslant 5°$) to minimize photometric contamination from confusion or interstellar cirrus.

carbon stars, novae, cepheids, cataclysmic variables, high-mass X-ray binaries, planetary nebulae, and Wolf–Rayet stars. Similar to Rhee et al. (2007b), we threw out O–B7 stars ($B_T - V_T \leqslant -0.17$ mag) to avoid contamination in our IR excess selection from free-free emission associated with strong stellar winds. We also removed stars redder than $B_T - V_T = 1.4$ mag. These stars were removed because of the wider dispersion of photospheric *WISE* colors at late spectral types. Some late-type (K and M) stars did possess non-photospherically blue ($B_T - V_T < 1.0$ mag) colors, likely because of chromospheric activity. A star whose $B_T - V_T$ color was >0.3 mag discrepant from the mean of its spectral type (Pecaut & Mamajek 2013) was assigned the mean spectral type color (converted from $B - V$ using the relations in Mamajek et al. 2002).

During the course of this study, we also discovered discrepancies in the photometry between the combined *WISE* Atlas images and the mean of the single-frame images in the $W1$, $W2$ and $W3$ bands. In some cases, these measurements would differ by over a magnitude. Since a definitive solution had not yet been issued by the *WISE* team at the time of this writing, we have removed from our sample stars whose ASC photometry deviates from the mean single exposure measurements by more than 2σ. Our discovery of this problem and removal of affected stars are detailed in Section 2.3.

We further limited our photometric candidate selection to the magnitude ranges where *WISE* photometry is reliable. Aperture photometry is not dependable for stars brighter than $W1 = 8.5$ mag, $W2 = 6.7$ mag, $W3 = 3.8$ mag and $W4 = -0.4$ mag. However, Cutri et al. (2012) show that profile-fitting photometry, which relies on unsaturated pixels in the stellar halo, can consistently extract objects as bright as $W1 \approx 4.5$ mag and $W2 \approx 2.8$ mag. We therefore apply these brighter $W1$ and $W2$ limits in our candidate selection. In Section 2.4 we discuss corrections for systematics in the *WISE* photometry that are particularly pronounced for saturated point sources. We retain the saturation levels in $W3$ and $W4$ as the brightness limits for candidate selection, since profile-fitting is not as well behaved on saturated sources in these bands.

Finally, we applied several additional criteria that ensured good quality photometry—unconfused, uncontaminated, and

Table 2
WISE IR Excess Selection Summary

Color	$\Sigma_{E_{CL}}$	Stars in Parent Sample (<120 pc)	Stars in Science Sample (<75 pc)	Excesses in Science Sample (<75 pc)	Final Disk Candidates (<75 pc)
$W1-W4$	3.19	12942	6294	133	121
$W2-W4$	3.26	13203	6507	164	155
$W3-W4$	3.16	14434	7198	208	198
$W1-W3$	2.82	15017	6788	9	8
$W2-W3$	3.70	15245	6962	4	4
$W1-W2$	2.03	15053	6804	8	6[a]
Total	...	16960	7937	243	220

Notes. Summary of the results from our *WISE* excess and debris disk candidate identification. $\Sigma_{E_{CL}}$ is the confidence level CL threshold adopted for any given color S/N. CL = 99.5% for $W4$ excesses, 98% for $W3$ excesses, and 95% for $W2$ excesses (Section 2.5). The number of stars in the parent and science samples are those that pass the selection criteria in Section 2.2. The excesses in the science sample are for stars that pass the corresponding excess selection criteria at confidence $\geqslant$CL. The final debris disk candidates are the subset of excesses that survive visual inspection. Rejected sources are listed in Table 4. The last row lists the total number of unique stars in each applicable column.
[a] The six stars with detected $W1-W2$ excesses are not included in the total number of disk candidates in this study, as described in Section 4.3.

with adequate S/N—including checking of the detection significance, contamination by nearby resolved companions or extended sources in Two Micron All Sky Survey (2MASS) and consistent variability flagging in $W1$ and $W2$.

In summary, our study samples included only stars with:

1. upper limits to their *Hipparcos* trigonometric distances that place them within 120 pc for the parent sample or within 75 pc for the science sample, and parallax accuracy better than 20%;
2. galactic latitudes $|b| > 5^\circ$;
3. available $B_T - V_T$ colors and $\sigma_{B_T-V_T} < 0.15$ mag from the *Tycho-2* catalog;
4. V-band absolute magnitudes $M_V > 6.0(B-V) - 1.5$ mag and spectral classes excluding I, II, and III;
5. -0.17 mag $< B_T - V_T < 1.4$ mag and spectral type B8 or later;
6. SIMBAD object descriptions excluding non-main sequence stellar objects: post-AGB stars, white dwarfs, carbon stars, novae, cepheids, cataclysmic variables, high-mass X-ray binaries, planetary nebulae, or Wolf–Rayet stars;
7. no $\Delta K_s \leqslant 5$ mag projected companions within $16''$ from 2MASS: applied to exclude unresolved sources in *WISE*;
8. no projected companions within $5''$ from the Visual Double Stars in *Hipparcos* Catalog (Dommanget & Nys 2000): applied to exclude unresolved sources in *WISE*;
9. photometry that is not contaminated by known 2MASS extended sources, i.e., including only stars with *WISE* `ext_flg` = 0 or 1;
10. flux limits of $W1 > 4.5$ mag or $W2 > 2.8$ mag, corresponding to the limits of self-consistent profile-fitting photometry on saturated stars;
11. unsaturated detections in at least one of $W3$ (>3.8 mag) and $W4$ (>−0.4 mag), with S/N $\geqslant 5$;
12. *WISE* confusion flags indicative of unconfused photometry: i.e., only stars with `cc_flg`[Wi] = 0;
13. consistent variability detections in $W1$ and $W2$, where we excluded stars whose `var_flag`[$W1$] > 8 and `var_flag`[$W2$] < 5 or `var_flag`[$W1$] < 5 and `var_flag`[$W2$] > 8.
14. photometry that is not severely contaminated by scattered moonlight in the $W3$ or $W4$ bands, i.e., excluding stars with `moon_lev`[Wi] $\geqslant 8$ corresponding to >80% frames being contaminated by scattered moonlight in these bands;
15. $W1$ or $W2$ ASC profile-fit photometry is $<2\sigma$ discrepant from the mean photometry of the All-Sky Single Exposure (L1b) Source Table. We detail this in Section 2.3.

The total number of *Hipparcos* stars that passed criteria 1–9 was 17,499: 15% of the full *Hipparcos* catalog, but 63% of all *Hipparcos* stars within 120 pc and more than 5° from the galactic plane, and 71% of main-sequence stars within the $-0.17 < B_T - V_T < 1.4$ color range. Our study thus includes the majority of *Hipparcos* main sequence stars in the solar neighborhood.

Criteria 10–15 are band-dependent: the numbers of stars that passed all the criteria in each band with distances less than 120 pc are between 12,942 and 15,245 (Table 2). A total of 16,960 unique stars passed all our selection criteria for a sufficient subset of the *WISE* bands that we could meaningfully probe them for IR excesses at $W3$, $W4$, or (most often) both.

2.2.2. Science Sample: Stars within 75 pc

The science sample is further limited to stars within 75 pc, with a fractional completeness similar to that of the parent sample. It includes 8,370 stars, constituting 67% of *Hipparcos* main sequence stars at $|b| > 5^\circ$ with $-0.17 < B_T - V_T < 1.4$ within 75 pc. Here also, band-dependent constraints cause the total number of stars to vary between *WISE* bands (see Table 2). Since not all the stars in our science sample have valid photometry in all four *WISE* bands, we make use of all possible *WISE* color combinations to probe for excesses. Stars with debris disks reveal themselves by exhibiting anomalously red values for some subset of these colors, depending on the dust temperature—and probing all possible colors allows us to maintain sensitivity to disks at a wide range of plausible temperatures even when one band is missing.

2.3. Discrepancy between WISE Single Exposure and Atlas Photometry

Data in the ASC are created by co-adding frames from the All-Sky Single Exposure (L1b) Source Table, using the individual frame exposures acquired through each pass of the satellite in its orbit on the same part of the sky. The details of this process can be found in Section VI of the *WISE* All-Sky Explanatory Supplement (R. Cutri 2013, private communication). The mean of profile-fit photometric measurements from the

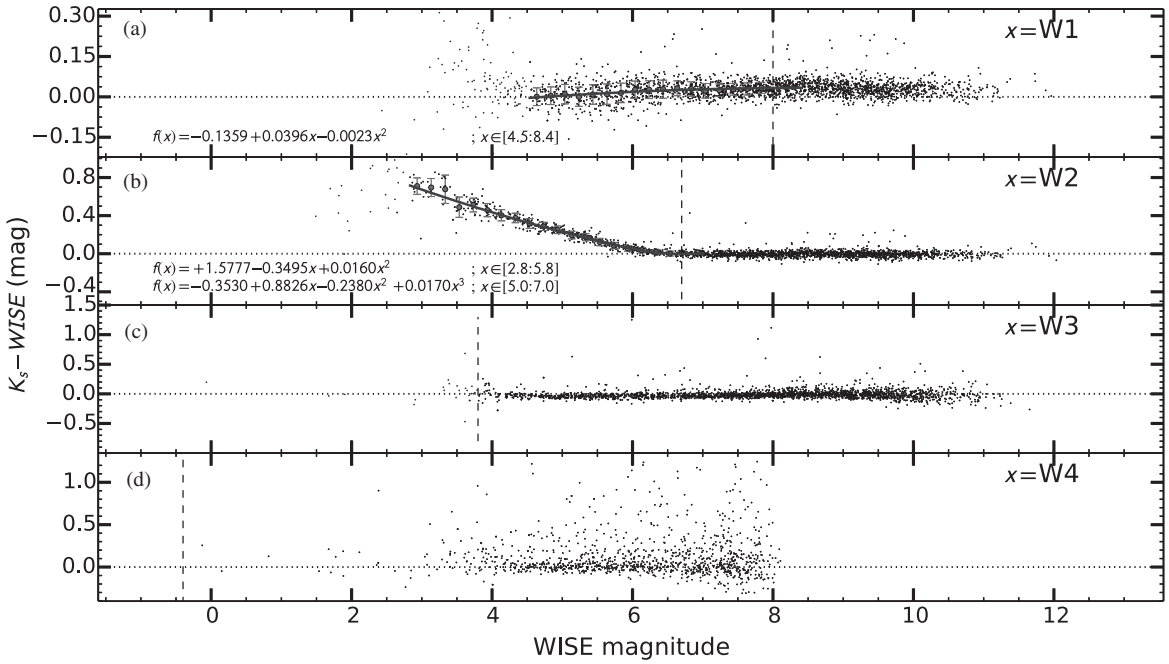

Figure 2. 2MASS K_s − *WISE* vs. *WISE* relations used for correcting systematics in saturated $W1$ (a) and $W2$ (b) photometry. The empirical K_s − *WISE* vs. *WISE* distributions are a combination of bright B8–A9 dwarf stars from our science sample with fainter $B - V < 0.10$ mag A0 stars from the *Tycho-2* Spectral Type Catalog (Wright et al. 2003). Saturation limits for each *WISE* band are shown with vertical dashed lines. Polynomials were fit to the saturated portions of the $K_s - W1$ vs. $W1$ and $K_s - W2$ vs. and $W2$ distributions to model the systematic trends and correct the saturation. Two overlapping polynomials were fit to the saturated $W2$ data to account for the knee between 5.4 mag and 6.7 mag: a quadratic—fit between 2.8 mag $\leqslant W2 \leqslant$ 5.8 mag and applied between 2.8 mag $\leqslant W2 \leqslant$ 5.3 mag—and a cubic—fit between 5.0 mag $\leqslant W2 \leqslant$ 7.0 mag and applied between 5.3 mag $\leqslant W2 \leqslant$ 6.7 mag. The $W3$ (c) and the $W4$ (d) photometry appears self-consistent throughout and does not require correction.

Single Exposure Source Table is generally very consistent with the ASC measurements made from co-adding the same frames.

However, we have found some unexpected instances of large discrepancies between the two values, for individual objects in the $W1$, $W2$ and $W3$ bands. As an example, for HIP 3505, the ASC gives $W1 = 5.118 \pm 0.023$ mag, but the mean magnitude measured from 13 individual exposures is $W1 = 4.3$ mag (this is after clipping any deviant individual measurements). Similarly, ∼0.9 mag discrepancies exist for the $W2$ and $W3$ photometry on the same object. The 2MASS K_s magnitude for this star is 4.359 ± 0.016 mag: consistent with the $W1$ mean Single Exposure measurement but not with the ASC. We note that Mizusawa et al. (2012) did already independently conclude that the *WISE* photometry for HIP 3505 is in error. We found similarly erroneous data for HIP 47007 and HIP 111278. All of these stars are saturated in one or more of the *WISE* bands, but the *WISE* Explanatory Supplement indicates their profile-fitting photometry should still be reliable and consistent. The reason for these occasional discrepancies of up to ∼1 mag is at present unclear. For the *WISE* $W1 - 3$ bands, this issue affects only a tiny fraction of the photometry (∼0.4%–0.9%); it affects ∼10% of the $W4$ photometry.

Since the goal of this study is to search for outlying photometric measurements due to debris disk emission, spurious outliers (even if rare) are a problem that must be addressed. We were faced with the choice of using mean single-exposure fluxes for our analysis, or proceeding with ASC fluxes but removing from our sample all stars with significantly discrepant ASC versus mean single-exposure measurements. We chose to retain the ASC fluxes, since in the vast majority of cases these are reliable. However, we opted to reject from our sample all stars with $>2\sigma$ discrepancies between the two flux estimates.

2.4. Correction of WISE Photometric Systematics on Saturated Stars

WISE photometry on faint (11 mag $\lesssim W1 \lesssim$ 14 mag, 9 mag $\lesssim W2 \lesssim$ 13 mag) stars is highly consistent with *Spitzer* IRAC channels 1 and 2 photometry. However, Cutri et al. (2012, Section VI.3.c.i.4.) note that the *WISE* profile-fitting photometry on bright stars displays systematic trends when compared to the 2MASS K_s magnitudes of the same stars. The effect is strongest for saturated (<6.7 mag) stars in $W2$, and is present at smaller levels in $W1$. While the photometry on saturated stars can a priori be expected to be less reliable, the *WISE* profile-fitting algorithm is designed to produce a flux estimate using the unsaturated pixels around the periphery. Profile fitting indeed produces consistent results without increase in scatter up to 4 magnitudes beyond saturation (8.5 mag) in $W1$ (Figure 2(a)). For $W2$, however, a systematic trend of flux over-estimation starts about 0.5 mag beyond saturation and continues to some of the brightest measured stars (Figure 2(b)).

Cutri et al. (2012) illustrate the *WISE* photometric bias on bright stars using plots of the K_s− *WISE* colors of <10 mag point sources in the *WISE* (ASC). We reproduce this analysis using the B8–A9 stars in our science sample and $B - V <$ 0.10 mag A0 stars from the *Tycho-2* Spectral Type Catalog (Wright et al. 2003). This sample of stars was chosen to reduce any shift of the K_s − *WISE* color locus to the red.

While most of the K_s − Wi colors are close to the 0.0 mag expectation for unextincted main sequence stars of spectral type B8–A9 or earlier, we note the following effects:

1. The $K_s - W1$ colors are systematically offset by +0.031 mag from zero color in unsaturated stars ($W1 > 8$ mag).
2. The $K_s - W2$ colors scatter around −0.004 mag for $W2 > 6.7$ mag; below 6.7 mag the $W2$ magnitudes are

systematically over-estimated, following a well-defined trend with $W2$ magnitude up to $W2 \approx 2.8$ mag.

3. In saturated stars brighter than approximately $W1 = 4.5$ mag or $W2 = 2.8$ mag the scatter in the photometry is very substantial, and there are few data points available to establish reliable trends. We have therefore rejected from our sample all stars brighter than these limits.
4. There are no significant systematic trends in $K_s - W3$ or $K_s - W4$. $W3$ photometry on saturated stars shows a large scatter, and we have excluded these altogether. There is also an increase in scatter toward the faint end of $W4$ because the fluxes of plotted stars approach the $W4 \sim 8$ mag detection limit of *WISE* (Cutri et al. 2012).

To obtain self-consistent *WISE* colors regardless of source brightness, we correct for the biases in the $K_s - Wi$ versus Wi color-magnitude distributions for $W1 > 4.5$ mag and $W2 > 2.8$ mag. We fit polynomials to the two-sigma clipped $K_s - Wi$ versus Wi distributions (these fits are shown in Figure 2), and add the fitted values to correct the Wi measurement for each star. We subtract the respective zero-point offsets (+0.031 mag for $W1$ and −0.004 mag to $W2$) from the corrected saturated photometry to preserve the calibration of the *WISE* photometric system. As an estimate of the uncertainty of the saturation corrections, we use the standard error of the residuals from the fits in 0.2 mag wide bins centered on each data point.

For the remainder of the analysis, we use the corrected *WISE* $W1$ and $W2$ photometry. We do not apply corrections to the $W3$ and $W4$ photometry, which do not display systematic trends with K_s magnitudes (Figures 2(c) and (d)). The $W3$ and $W4$ photometric distributions also show good agreement with *Spitzer* IRAC 8 μm and MIPS 24 μm respectively for bright ($W4 < 9$ mag and $W3 < 12$ mag) point sources (Section VI.3.c.i. of Cutri et al. 2012).

2.5. Debris Disk Candidate Selection

We identified debris disk host candidates by selecting stars with the reddest infrared colors in color–color diagrams. Excesses were sought in the $W2$, $W3$, and $W4$ passbands, so our analysis is sensitive to stars with excesses between 4–28 μm. The excesses were identified based purely on the *WISE* colors, without relying on photospheric fits to the spectral energy distributions. If a star displayed a significant excess in any of the six *WISE* color combinations, it was considered a debris disk candidate. SED fits were used at a later stage to confirm the validity of debris disk candidate identifications, and to determine the dust temperatures of high-probability debris disks.

The photospheric colors of main sequence stars vary over the *WISE* bands, mostly as a function of stellar effective temperature. We calibrated this dependence to avoid mistaking stars with intrinsically red *WISE* colors for debris disks (Figure 3). $B_T - V_T$ color measurements exist for all our sample stars by design, and are not biased by the presence of debris disks. We used a trimmed mean to determine the mean locus of the $Wi - Wj$ versus $B_T - V_T$ relations from the parent sample. We iteratively removed the largest $Wi - Wj$ color outlier in 0.1 mag wide $B_T - V_T$ color bins until half of the data points in the bin were rejected, leaving only the data clustered near the mode of the bin. This removed the dependence of the relation on outliers, most notably mid-IR-excess debris disk hosts. We traced the $Wi - Wj$ versus $B_T - V_T$ relations in step sizes of 0.02 mag in $B_T - V_T$. We refer to the mean $Wi - Wj$ corresponding to a given $B_T - V_T$ color as $W_{ij}(B_T - V_T)$. Table 3 lists the $W_{ij}(B_T - V_T)$ trimmed mean and its standard error (based on the surviving 50% of data points) for all *WISE* color combinations.

We are now in position to determine whether the *WISE* colors of any particular star reveal a significant excess. We define the excess $E[Wi - Wj]$ in the $Wi - Wj$ color of a star with a given value of $B_T - V_T$ as:

$$E[Wi - Wj] = Wi - Wj - W_{ij}(B_T - V_T). \quad (1)$$

We then define the S/N of the excess as the ratio of $E[Wi - Wj]$ to the uncertainty σ_{ij},

$$\Sigma_{E[Wi-Wj]} = \frac{E[Wi - Wj]}{\sigma_{ij}} = \frac{Wi - Wj - W_{ij}(B_T - V_T)}{\sigma_{ij}}, \quad (2)$$

where σ_{ij} combines the Wi and Wj photometric uncertainties, and the standard error on $W_{ij}(B_T - V_T)$:

$$\sigma_{ij} = \sqrt{\sigma_{Wi}^2 + \sigma_{Wj}^2 + \sigma_{W_{ij}}^2}. \quad (3)$$

For shorthand, we use Σ_E throughout the rest of the paper when the discussion does not refer to any specific color. Σ_E is plotted against $B_T - V_T$ for each color in the bottom halves of the panels in Figure 3.

Figure 4 shows the Σ_E distributions for each set of *WISE* colors with solid histograms. The distributions are characterized by sharp cores and long tails to higher S/Ns. The cores of the histograms represent the random scatter around zero excess (black data points in the lower halves of the panels of Figure 3), corresponding to measurement and calibration uncertainties. We estimate the rate of low-S/N false-positive excesses by mirroring (dashed histograms) the distribution of negative excesses into the positive wing. We thus empirically construct a distribution that represents the measurement uncertainties, both random and systematic.

Using the empirically determined uncertainty distribution, we can calculate the false-positive rate (FPR) for detecting excesses as a function of the threshold beyond which red outliers are designated as bona fide excesses. The FPR is simply the number of outliers beyond the threshold in the uncertainty distribution divided by the number of red excesses beyond the threshold. For example, based on the histogram of our $W1 - W4$ uncertainty distribution (see top left panel of Figure 3), we expect only two false positives beyond our chosen threshold of $\Sigma_{E[W1-W4]} = 3.19$ (vertical dashed line in the figure). As there are 429 excesses in the actual $W1 - W4$ color distribution redward of the same limit, the empirical FPR is $2/429 = 0.47\%$. Choosing a lower threshold for excess identification would produce more excesses but would increase the FPR, while choosing a higher threshold would reduce the FPR further. Our objective in general is to obtain FPR $< 0.5\%$.

Empirically, however, we can not determine the FPR beyond the threshold value at which the number of false positives drops to zero. This sets an upper bound to our ability to empirically set the confidence level for excess identification. For color distributions involving $W4$ this upper bound is between 99.8%–99.9%. However, the $W1-W2$, $W1-W3$, and $W2-W3$ distributions do not possess >200 excesses with even a single false positive (such that FPR $\leqslant 0.5\%$) at any value for Σ_E. Our empirical confidence level for the $W1 - W3$ and $W2 - W3$ excess selection in $\gtrsim$98%, and for $W1-W2$ it is $\gtrsim$95%. We note that these confidence thresholds do not assume Gaussian error statistics, only that the distribution of uncertainties is symmetric around zero.

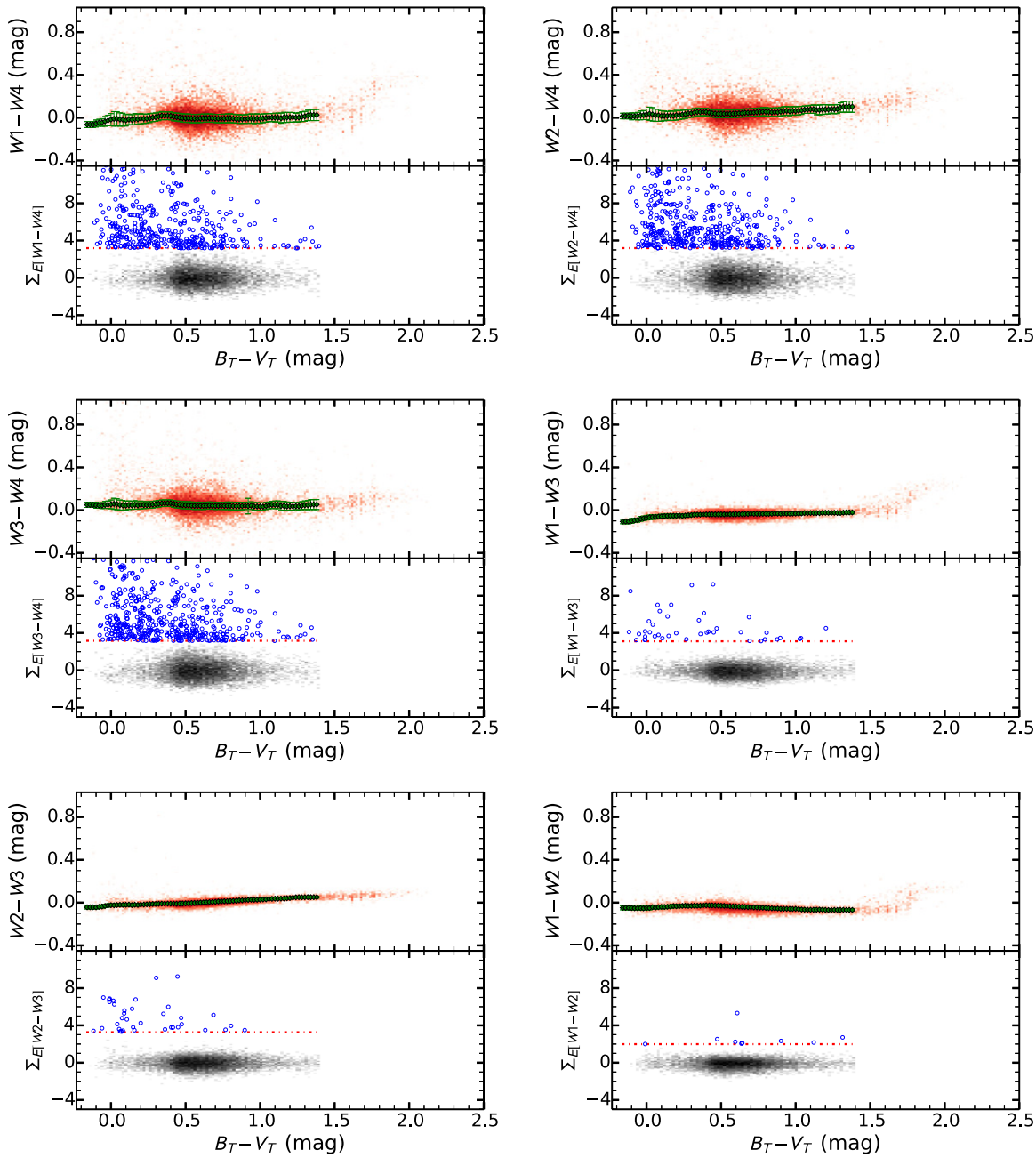

Figure 3. Top half of each panel: *WISE* vs. *Tycho-2* $B_T - V_T$ color–color diagrams of our parent sample stars (red). The green diamonds in each panel follow the running mean of the parent sample. We eliminated stars outside the -0.17 mag $< B_T - V_T <$ 1.4 mag range from all of our analysis. Bottom half of each panel: Plots of the significance Σ_E of the color excess as a function of $B_T - V_T$. These are residuals of the subtraction of the photospheric running mean, normalized to the 1σ scatter. The stars selected as debris disk candidates in the parent sample are denoted by open blue circles. These are more significant than the confidence limit CL thresholds shown by the dashed purple lines. CL = 99.5% for $W4$ excesses, 98% for $W3$ excesses, and 95% for $W2$ excesses.

(A color version of this figure is available in the online journal.)

We denote the minimum excess S/N Σ_E at the 99.5% confidence level for the $Wi - W4$ colors as $\Sigma_{E_{\rm CL}} = \Sigma_{E_{99.5}}$. Accordingly, the 98% Σ_E confidence threshold for the $Wi - W3$ colors is $= \Sigma_{E_{98}}$, and the 95% confidence threshold for $W1 - W2$ is $= \Sigma_{E_{95}}$. All $\Sigma_{E_{\rm CL}}$ thresholds are listed in Table 2 and are marked with vertical dotted lines in Figure 4.

We note that our definition of the empirical FPR and the associated confidence level CL $= 1 -$ FPR are not identical to the definition of a Gaussian confidence level. In the context of our data the latter would be defined as the ratio of the number of outliers beyond the threshold in the uncertainty distribution and the total number of stars in the uncertainty distribution. In our case, the uncertainty distributions total between 12,300–15,000 stars in each of the WISE colors (equal to twice the number of stars with negative Σ_E values for each color). With $\leqslant$2 false-positive outliers in any of our color excess distributions, the effective Gaussian confidence level is $\geqslant 1 - 2/12{,}300 = 99.98\%$, or nearly 4σ (one-tailed). It is the latter threshold, in units of Gaussian σ, that is directly comparable to our empirical $\Sigma_{E_{\rm CL}}$ thresholds.

We observe that for all of our color distributions the empirical $\Sigma_{E_{\rm CL}}$ thresholds are $\lesssim$4 even if the effective Gaussian confidence level is $\geqslant$99.98%. We conclude that the strategies that we employed to mitigate systematics (Sections 2.3–2.5) have been

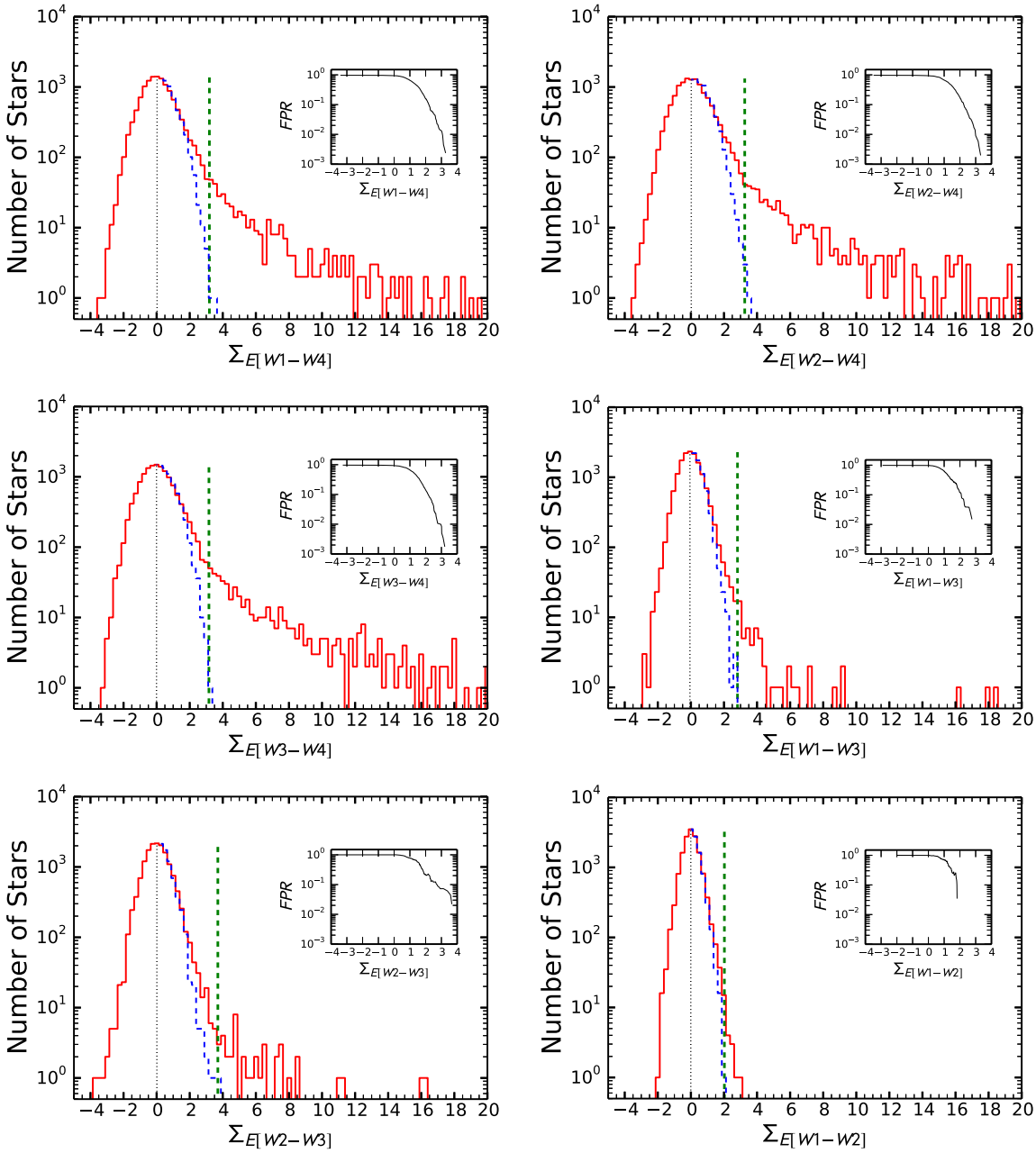

Figure 4. Distributions of the significance of the color excess Σ_E for the stars in our parent sample for each *WISE* color. We assume that the negative excesses, where $\Sigma_E < 0$, are representative of the intrinsic random and systematic noise in the data. A reflection of the negative excess histogram around 0 (dashed histogram) is thus representative of the false positive excess expectation. We define the FPR at a given Σ_E as the ratio of the cumulative numbers of $>\Sigma_E$ excesses in the positive tails of the dashed and solid histograms. The vertical dashed lines indicate the FPR thresholds for each $Wi - Wj$ color, above which we identify all stars as probable debris disk hosts. The insets show the FPR for each distribution.

(A color version of this figure is available in the online journal.)

successful to the point where the uncertainty distributions can be explained entirely by random photometric errors. In particular, judging by the low $\Sigma_{E_{\rm CL}} = 2.03$ threshold for the $W1-W2$ distribution, we believe that our clean sample of single *Hipparcos* stars has a factor of ∼2 better internal photometric consistency in $W1$ and $W2$ than the ASC photometric errors indicate.

We identified 243 stars with significant excesses within 75 pc of the Sun, the vast majority (231) of which are in $W4$. Among which we expect only $0.5\% \times 231 = 1.2$ false excesses. However, IR excesses can in principle be caused by contamination from other IR sources in the *WISE* beam (mainly IR cirrus and unresolved late-type binary companions) rather than circumstellar dust. We screen our excesses for these types of contamination, and eliminate 23 of them (mostly due to line-of-sight IR cirrus visible in the *WISE* images), leaving 220 candidate debris disks with excesses at $W2$, $W3$, or $W4$ within 75 pc of the Sun.

A summary of the number of identified mid-IR excesses, contaminated sources, and candidate debris disks for each color selection criterion is given in Table 2. Stars that were rejected after being identified as candidate debris disk hosts are listed in Table 4. The host star properties of all our identified debris disk systems are shown in Table 5. Table 6 lists the information on

Table 3
Photospheric *WISE* Colors of -0.15 mag $< B_T - V_T <$ 1.4 mag Main Sequence Stars

$B_T - V_T$ (mag)	$W1 - W4$ (mag)	$W2 - W4$ (mag)	$W3 - W4$ (mag)	$W1 - W3$ (mag)	$W2 - W3$ (mag)	$W1 - W2$ (mag)
−0.16	−0.070 ± 0.006	−0.001 ± 0.005	0.050 ± 0.004	−0.117 ± 0.004	−0.059 ± 0.003	−0.045 ± 0.004
−0.14	−0.070 ± 0.006	−0.001 ± 0.005	0.050 ± 0.004	−0.117 ± 0.004	−0.059 ± 0.003	−0.045 ± 0.004
−0.12	−0.070 ± 0.006	−0.001 ± 0.005	0.050 ± 0.004	−0.117 ± 0.004	−0.059 ± 0.003	−0.045 ± 0.004
−0.10	−0.065 ± 0.005	−0.006 ± 0.004	0.046 ± 0.004	−0.115 ± 0.003	−0.059 ± 0.002	−0.047 ± 0.003
−0.08	−0.056 ± 0.004	−0.003 ± 0.004	0.044 ± 0.003	−0.105 ± 0.002	−0.056 ± 0.002	−0.049 ± 0.002
−0.06	−0.054 ± 0.004	−0.001 ± 0.004	0.043 ± 0.003	−0.104 ± 0.002	−0.051 ± 0.002	−0.050 ± 0.002
−0.04	−0.043 ± 0.005	0.009 ± 0.004	0.049 ± 0.003	−0.091 ± 0.002	−0.044 ± 0.001	−0.044 ± 0.002
−0.02	−0.035 ± 0.005	0.011 ± 0.004	0.051 ± 0.003	−0.087 ± 0.002	−0.041 ± 0.001	−0.047 ± 0.002
−0.00	−0.026 ± 0.005	0.018 ± 0.004	0.054 ± 0.003	−0.078 ± 0.002	−0.037 ± 0.001	−0.042 ± 0.001
0.02	−0.019 ± 0.005	0.023 ± 0.005	0.059 ± 0.004	−0.071 ± 0.002	−0.038 ± 0.001	−0.041 ± 0.001
0.04	−0.019 ± 0.005	0.018 ± 0.004	0.056 ± 0.003	−0.070 ± 0.002	−0.036 ± 0.001	−0.035 ± 0.001
0.06	−0.024 ± 0.005	0.009 ± 0.004	0.049 ± 0.003	−0.067 ± 0.002	−0.036 ± 0.001	−0.036 ± 0.001
0.08	−0.026 ± 0.004	0.009 ± 0.004	0.045 ± 0.003	−0.068 ± 0.001	−0.034 ± 0.001	−0.035 ± 0.001
0.10	−0.032 ± 0.004	0.002 ± 0.003	0.043 ± 0.003	−0.067 ± 0.001	−0.034 ± 0.001	−0.034 ± 0.001
0.12	−0.026 ± 0.003	0.003 ± 0.003	0.047 ± 0.003	−0.064 ± 0.001	−0.034 ± 0.001	−0.032 ± 0.001
0.14	−0.027 ± 0.003	0.005 ± 0.003	0.045 ± 0.002	−0.060 ± 0.001	−0.032 ± 0.001	−0.033 ± 0.001
0.16	−0.021 ± 0.003	0.006 ± 0.003	0.049 ± 0.002	−0.059 ± 0.001	−0.035 ± 0.001	−0.031 ± 0.001
0.18	−0.022 ± 0.003	0.004 ± 0.003	0.045 ± 0.002	−0.058 ± 0.001	−0.032 ± 0.001	−0.030 ± 0.001
0.20	−0.017 ± 0.003	0.012 ± 0.003	0.049 ± 0.002	−0.056 ± 0.001	−0.031 ± 0.001	−0.030 ± 0.001
0.22	−0.018 ± 0.002	0.011 ± 0.002	0.048 ± 0.002	−0.055 ± 0.001	−0.030 ± 0.001	−0.031 ± 0.001
0.24	−0.017 ± 0.002	0.015 ± 0.002	0.048 ± 0.002	−0.057 ± 0.001	−0.030 ± 0.001	−0.030 ± 0.001
0.26	−0.012 ± 0.002	0.019 ± 0.002	0.049 ± 0.002	−0.056 ± 0.001	−0.028 ± 0.001	−0.029 ± 0.001
0.28	−0.007 ± 0.002	0.025 ± 0.002	0.052 ± 0.002	−0.055 ± 0.001	−0.027 ± 0.001	−0.028 ± 0.001
0.30	−0.004 ± 0.002	0.025 ± 0.002	0.056 ± 0.001	−0.054 ± 0.001	−0.026 ± 0.000	−0.027 ± 0.001
0.32	0.004 ± 0.002	0.033 ± 0.002	0.061 ± 0.001	−0.049 ± 0.001	−0.025 ± 0.000	−0.026 ± 0.001
0.34	0.009 ± 0.002	0.037 ± 0.002	0.065 ± 0.001	−0.047 ± 0.001	−0.023 ± 0.000	−0.026 ± 0.000
0.36	0.009 ± 0.001	0.038 ± 0.001	0.065 ± 0.001	−0.047 ± 0.001	−0.021 ± 0.000	−0.027 ± 0.000
0.38	0.012 ± 0.001	0.039 ± 0.001	0.066 ± 0.001	−0.046 ± 0.000	−0.020 ± 0.000	−0.027 ± 0.000
0.40	0.010 ± 0.001	0.039 ± 0.001	0.065 ± 0.001	−0.046 ± 0.000	−0.020 ± 0.000	−0.028 ± 0.000
0.42	0.001 ± 0.001	0.034 ± 0.001	0.059 ± 0.001	−0.046 ± 0.000	−0.019 ± 0.000	−0.029 ± 0.000
0.44	−0.002 ± 0.001	0.030 ± 0.001	0.054 ± 0.001	−0.045 ± 0.000	−0.019 ± 0.000	−0.029 ± 0.000
0.46	−0.005 ± 0.001	0.028 ± 0.001	0.051 ± 0.001	−0.045 ± 0.000	−0.018 ± 0.000	−0.030 ± 0.000
0.48	−0.010 ± 0.001	0.024 ± 0.001	0.047 ± 0.001	−0.045 ± 0.000	−0.016 ± 0.000	−0.032 ± 0.000
0.50	−0.012 ± 0.001	0.023 ± 0.001	0.046 ± 0.001	−0.045 ± 0.000	−0.015 ± 0.000	−0.033 ± 0.000
0.52	−0.012 ± 0.001	0.023 ± 0.001	0.045 ± 0.001	−0.046 ± 0.000	−0.014 ± 0.000	−0.035 ± 0.000
0.54	−0.014 ± 0.001	0.024 ± 0.001	0.043 ± 0.001	−0.044 ± 0.000	−0.012 ± 0.000	−0.037 ± 0.000
0.56	−0.016 ± 0.001	0.023 ± 0.001	0.041 ± 0.001	−0.044 ± 0.000	−0.011 ± 0.000	−0.039 ± 0.000
0.58	−0.015 ± 0.001	0.025 ± 0.001	0.042 ± 0.001	−0.044 ± 0.000	−0.009 ± 0.000	−0.040 ± 0.000
0.60	−0.013 ± 0.001	0.027 ± 0.001	0.042 ± 0.001	−0.043 ± 0.000	−0.007 ± 0.000	−0.042 ± 0.000
0.62	−0.011 ± 0.001	0.029 ± 0.001	0.041 ± 0.001	−0.043 ± 0.000	−0.005 ± 0.000	−0.042 ± 0.000
0.64	−0.010 ± 0.001	0.029 ± 0.001	0.042 ± 0.001	−0.043 ± 0.000	−0.004 ± 0.000	−0.043 ± 0.000
0.66	−0.010 ± 0.001	0.034 ± 0.001	0.044 ± 0.001	−0.042 ± 0.000	−0.002 ± 0.000	−0.044 ± 0.000
0.68	−0.011 ± 0.001	0.034 ± 0.001	0.042 ± 0.001	−0.042 ± 0.000	0.000 ± 0.000	−0.046 ± 0.000
0.70	−0.015 ± 0.001	0.035 ± 0.001	0.041 ± 0.001	−0.041 ± 0.000	0.002 ± 0.000	−0.047 ± 0.000
0.72	−0.016 ± 0.001	0.036 ± 0.001	0.041 ± 0.001	−0.040 ± 0.000	0.003 ± 0.000	−0.050 ± 0.000
0.74	−0.014 ± 0.001	0.039 ± 0.001	0.042 ± 0.001	−0.040 ± 0.000	0.005 ± 0.000	−0.050 ± 0.000
0.76	−0.014 ± 0.001	0.040 ± 0.001	0.041 ± 0.001	−0.041 ± 0.000	0.005 ± 0.000	−0.052 ± 0.000
0.78	−0.012 ± 0.001	0.043 ± 0.001	0.041 ± 0.001	−0.040 ± 0.000	0.006 ± 0.000	−0.053 ± 0.000
0.80	−0.012 ± 0.001	0.044 ± 0.001	0.041 ± 0.001	−0.040 ± 0.000	0.008 ± 0.000	−0.053 ± 0.000
0.82	−0.014 ± 0.002	0.042 ± 0.001	0.039 ± 0.001	−0.040 ± 0.000	0.010 ± 0.000	−0.055 ± 0.000
0.84	−0.018 ± 0.002	0.040 ± 0.002	0.038 ± 0.001	−0.039 ± 0.000	0.012 ± 0.000	−0.057 ± 0.000
0.86	−0.019 ± 0.002	0.041 ± 0.002	0.039 ± 0.001	−0.038 ± 0.000	0.014 ± 0.000	−0.058 ± 0.000
0.88	−0.019 ± 0.002	0.042 ± 0.002	0.040 ± 0.002	−0.038 ± 0.001	0.017 ± 0.000	−0.059 ± 0.000
0.90	−0.018 ± 0.002	0.045 ± 0.002	0.041 ± 0.002	−0.038 ± 0.001	0.020 ± 0.000	−0.061 ± 0.000
0.92	−0.018 ± 0.002	0.048 ± 0.002	0.038 ± 0.003	−0.037 ± 0.001	0.020 ± 0.000	−0.062 ± 0.000
0.94	−0.014 ± 0.002	0.054 ± 0.002	0.043 ± 0.002	−0.037 ± 0.001	0.023 ± 0.000	−0.063 ± 0.000
0.96	−0.019 ± 0.002	0.047 ± 0.002	0.035 ± 0.002	−0.038 ± 0.001	0.022 ± 0.000	−0.064 ± 0.000
0.98	−0.013 ± 0.002	0.054 ± 0.002	0.035 ± 0.002	−0.038 ± 0.001	0.022 ± 0.001	−0.064 ± 0.000
1.00	−0.016 ± 0.002	0.051 ± 0.002	0.034 ± 0.002	−0.037 ± 0.001	0.024 ± 0.001	−0.063 ± 0.000
1.02	−0.011 ± 0.003	0.056 ± 0.002	0.033 ± 0.002	−0.038 ± 0.001	0.025 ± 0.001	−0.065 ± 0.001
1.04	−0.008 ± 0.003	0.060 ± 0.002	0.040 ± 0.002	−0.036 ± 0.001	0.026 ± 0.001	−0.067 ± 0.001
1.06	−0.005 ± 0.003	0.064 ± 0.002	0.045 ± 0.002	−0.033 ± 0.001	0.026 ± 0.001	−0.070 ± 0.001
1.08	−0.005 ± 0.003	0.066 ± 0.003	0.050 ± 0.002	−0.032 ± 0.001	0.030 ± 0.001	−0.070 ± 0.001
1.10	−0.006 ± 0.003	0.067 ± 0.003	0.050 ± 0.002	−0.032 ± 0.001	0.031 ± 0.001	−0.071 ± 0.001
1.12	−0.005 ± 0.003	0.063 ± 0.003	0.050 ± 0.003	−0.031 ± 0.001	0.031 ± 0.001	−0.072 ± 0.001

Table 3
(Continued)

$B_T - V_T$ (mag)	$W1 - W4$ (mag)	$W2 - W4$ (mag)	$W3 - W4$ (mag)	$W1 - W3$ (mag)	$W2 - W3$ (mag)	$W1 - W2$ (mag)
1.14	-0.011 ± 0.004	0.060 ± 0.003	0.040 ± 0.003	-0.031 ± 0.001	0.032 ± 0.001	-0.071 ± 0.001
1.16	-0.005 ± 0.004	0.063 ± 0.004	0.041 ± 0.003	-0.031 ± 0.001	0.032 ± 0.001	-0.071 ± 0.001
1.18	-0.002 ± 0.004	0.062 ± 0.004	0.035 ± 0.003	-0.030 ± 0.001	0.034 ± 0.001	-0.071 ± 0.001
1.20	-0.003 ± 0.004	0.065 ± 0.004	0.037 ± 0.003	-0.030 ± 0.001	0.037 ± 0.001	-0.073 ± 0.001
1.22	-0.003 ± 0.004	0.067 ± 0.004	0.036 ± 0.003	-0.030 ± 0.001	0.038 ± 0.001	-0.073 ± 0.001
1.24	-0.005 ± 0.004	0.069 ± 0.003	0.038 ± 0.003	-0.031 ± 0.001	0.043 ± 0.001	-0.074 ± 0.001
1.26	-0.004 ± 0.004	0.069 ± 0.004	0.037 ± 0.003	-0.030 ± 0.001	0.046 ± 0.001	-0.073 ± 0.001
1.28	0.003 ± 0.004	0.073 ± 0.004	0.042 ± 0.003	-0.032 ± 0.001	0.044 ± 0.001	-0.073 ± 0.001
1.30	0.006 ± 0.004	0.073 ± 0.004	0.046 ± 0.004	-0.032 ± 0.001	0.047 ± 0.001	-0.073 ± 0.001
1.32	0.015 ± 0.005	0.085 ± 0.005	0.048 ± 0.004	-0.030 ± 0.001	0.048 ± 0.001	-0.073 ± 0.001
1.34	0.019 ± 0.005	0.098 ± 0.005	0.053 ± 0.004	-0.029 ± 0.001	0.046 ± 0.001	-0.073 ± 0.001
1.36	0.019 ± 0.005	0.098 ± 0.005	0.053 ± 0.004	-0.029 ± 0.001	0.046 ± 0.001	-0.073 ± 0.001
1.38	0.019 ± 0.005	0.098 ± 0.005	0.053 ± 0.004	-0.029 ± 0.001	0.046 ± 0.001	-0.073 ± 0.001

Notes. Empirically determined *WISE* vs. $B_T - V_T$ photospheric color-color trends for all six *WISE* colors obtained from the parent sample as described in Section 2.5 and shown in Figure 3. The standard error of the mean for the distribution of stars in each *WISE* vs. $B_T - V_T$ bin is listed. These trends were used to correct for the photospheric color variation over the *WISE* bands and to obtain a population of colors independent of stellar temperature. Bold values denote stars with a significant detection of both $W3$ and $W4$ excess. Dust parameters are exact calculations.

Table 4
Rejected *WISE* Excesses

HIP ID	*WISE* ID	Rejection Reason
HIP 999	J001230.54+143348.0	2
HIP 3121	J003942.53+103911.7	2
HIP 3729	J004752.96−324520.6	2
HIP 4016	J005129.22+563005.5	1
HIP 13631	J025532.50+184624.2	1
HIP 27114	J054500.36−023534.3	1
HIP 40122	J081144.04−440200.9	1
HIP 60689	J122617.82−512146.6	1
HIP 71262	J143426.35−541637.8	1
HIP 74045	J150755.93+761204.2	2
HIP 76907	J154214.76−404922.9	1
HIP 79741	J161628.20−364453.2	1
HIP 79969	J161922.47−254538.9	1
HIP 81181	J163453.29−253445.3	1
HIP 82384	J165003.66−152534.0	1
HIP 83251	J170055.98−314640.2	1
HIP 83875	J170833.23−231338.7	1
HIP 99542	J201205.89+461804.8	1

Notes. Rejection reasons: 1. Contamination by nearby infrared source. 2. Contamination by spectroscopic secondary component.

the significance of the excess Σ_E for each color. Since debris disk-bearing stars often have an excess in multiple *WISE* color combinations, a six character flag indicating the color excess each star has also been provided. The dust properties determined from SED fitting (Section 3) are given in Table 7.

2.6. All-Sky versus AllWISE Data Release

Since the inception of this study, *WISE* has released an updated version of the all-sky survey, called the AllWISE Data Release[4] (AWR). The AWR incorporates data products taken during the NEOWISE Post-Cryo phase of the mission, and is a significant improvement over the *WISE* ASC. We incorporated the *WISE* AWR into our IR excess search in an attempt at more reliable debris disk identification.

However, we identified two issues that make the AWR less suitable than the ASC for precise identification of IR excesses. First, the $W1$ and $W2$ AWR photometry behaves less well in the saturated regimes of these bands. In particular, we find that the behavior of the $K_s - WISE$ versus *WISE* relations for saturated $W1$ and $W2$ AWR photometry is not monotonic, unlike in the ASC. This is indeed seen in Figures 10(a) and (b) in Section II.1.d.i of the AWR explanatory supplement, which compares the ASC data to the AWR for $W1$ and $W2$. Consistent with these observations, the AWR explanatory supplement states that "The *WISE* ASC may provide better photometry than in the AWR for objects brighter than [$W1 < 8$ mag and $W2 < 7$ mag]." Therefore, we abandon using the AWR $W1$ and $W2$ photometry for our analysis.

We noticed a similar issue when we attempted to identify excesses using only $W3 - W4$ colors constructed from the AWR data products. Here, we found more stars with negative $\Sigma_{E[W3-W4]}$ values, that widened the Σ_E distribution and pushed the 99.5% confidence threshold for $W4$ excesses to $\Sigma_{E[W3-W4]_{\rm CL}} = 9.4$. This is in stark contrast with the much tighter distribution we found using the ASC data ($\Sigma_{E[W3-W4]_{\rm CL}} = 3.2$). After closer inspection of the negative Σ_E valued stars, we found that the AWR $W3$ photometry was intrinsically brighter than the same ASC photometric measurement for the same star. HIP 51933 is one such example, where its AWR $W3$ profile fit photometric measurement is 0.25 mag brighter than the corresponding ASC photometry. This intrinsic brightening is seen in the majority of our negative Σ_E stars. We can see similar brightening of the AWR $W3$ photometry relative to the ASC in Figure 10(c) in Section II.1.d.i of the AWR explanatory supplement between AllWISE $W3$ magnitude at 7.5 mag $< W3 <$ 9 mag. The surplus of stars with negative Σ_E incurs a non-Gaussian component to the $\Sigma_{E[W3-W4]}$ distribution, and makes the AWR $W3$ photometry less reliable in searching for IR excesses.

Hence, after performing the same set of procedures outlined in Sections 2–2.5 on data from the AWR, we determined that the ASC data are better suited for identifying IR excesses through the method outlined in the preceding sections.

[4] http://wise2.ipac.caltech.edu/docs/release/allwise/expsup/index.html

Table 5
Stellar Parameters of Stars with IR Excesses

HIP ID	WISE ID	SpT[a]	Dist.[b] (pc)	T_* (K)	R_* ($R_\odot$)	χ^2_*	F_{W3} (mJy)	$F_{W3,*}$ (mJy)	F_{W4} (mJy)	$F_{W4,*}$ (mJy)	$\Delta_{F_{W3}}/F_{W3}$[d]	$\Delta_{F_{W4}}/F_{W4}$[d]	$W1_{\rm corr}$[e] (mag)	$W2_{\rm corr}$[e] (mag)
544	J000637.09+290115.4	K0V	14	5493	0.86	3.3	536 ± 7	550	186 ± 4	153	−0.026	0.178	4.260 ± 0.082	4.290 ± 0.051
560	J000650.16−230627.5	F2IV	39	6789	1.5	0.38	234 ± 3	234	130 ± 3	64.7	−0.001	0.501	5.220 ± 0.072	5.240 ± 0.037
682	J000825.79+063700.6	G2V	39	5845	1.1	1.2	106 ± 1	108	41.6 ± 2	29.9	−0.019	0.281	6.050 ± 0.051	6.100 ± 0.022
1473	J001819.60+364706.3	A2V	41	8987	2	0.62	527 ± 7	524	182 ± 3	144	0.006	0.208	4.260 ± 0.097	4.330 ± 0.050
1481	J001826.25−632839.6	F8/G0V	42	6138	1.1	0.73	102 ± 1	102	41.7 ± 1	28.4	−0.003	0.319	6.130 ± 0.048	6.150 ± 0.023
1866	J002338.01−034548.9	K:	47	4527	0.65	1.7	21.1 ± 0.4	21.4	9.22 ± 1	5.99	−0.012	0.350	7.830 ± 0.022	7.910 ± 0.021
2472	J003125.12−484812.7	A0V	53	9489	2.1	1.2	377 ± 6	374	130 ± 4	103	0.010	0.209	4.760 ± 0.075	4.790 ± 0.046
2710	J003427.10−063014.9	F2	41	6428	1.2	1.2	142 ± 2	145	48.3 ± 2	40.0	−0.019	0.171	5.680 ± 0.061	5.740 ± 0.027
3210	J004051.69−531236.1	F7V	45	6197	1.2	1.4	107 ± 1	107	37 ± 1	29.6	0.006	0.200	6.070 ± 0.050	6.090 ± 0.022
3279	J004147.56+554056.2	G5	69	5807	1.2	1.3	41.4 ± 0.6	42.1	14.4 ± 0.6	11.7	−0.015	0.188	7.070 ± 0.030	7.120 ± 0.020

Notes. *Hipparcos* stars with detected mid-IR excesses at either $W2$, $W3$ and/or $W4$. Unless otherwise noted, the stellar temperature and radius were obtained from photometric fits as described in Section 3. The χ^2_* column gives the goodness of the photospheric fit.
[a] Spectral types for stars downloaded from *Hipparcos* database. Stars marked with asterisks had their spectral types estimated from their $B_T - V_T$ colors using empirical color relations from Pecaut & Mamajek (2013).
[b] Parallactic distances from *Hipparcos*.
[c] Stellar temperature and radius were estimated from empirical color relations from Pecaut & Mamajek (2013) using the listed *Hipparcos* spectral type.
[d] The quoted fractional excesses in $W3$ and $W4$ represent the ratios of the measured excess and the estimated stellar photospheric flux in these bands. They have not been color-corrected for the filter response, although such corrections have been applied to the estimates of the fractional bolometric luminosities f_d of the dust (Section 3, Table 7).
[e] Saturation corrected $W1$ and $W2$ photometry (see Section 2.4).

(This table is available in its entirety in a machine-readable form in the online journal. A portion is shown here for guidance regarding its form and content.)

Table 6
IR Excess Information

HIP ID	Excess Flag	New? (12|22 μm)	Excess Significance (Σ_E)					
			$W1-W4$	$W2-W4$	$W3-W4$	$W1-W3$	$W2-W3$	$W1-W2$
544	UNYUNU	–N	...	2.26	6.47	...	−1.16	...
560	YYYNNN	–N	9.22	15.98	24.30	0.47	0.77	0.08
682	YYYNNN	–N	4.67	6.46	6.81	−0.24	−0.18	−0.06
1473	UYYUNU	–N	...	3.29	6.70	...	0.20	...
1481	YYYNNN	–N	6.97	9.63	10.17	0.72	0.57	0.48
1866	YYYNNN	–Y	3.43	3.48	3.16	0.43	1.03	−0.27
2472	YYYNNN	–Y	3.29	4.64	4.17	1.46	2.24	0.12
2710	NNYNNN	–N	1.51	2.96	3.61	−0.78	−0.54	−0.43
3210	YYYNNN	–Y	3.28	4.43	4.05	0.53	0.83	0.20
3279	NYYNNN	–Y	3.19	3.61	3.43	−0.27	0.27	−0.26

Notes. Summary of the properties of the IR excesses attributed to circumstellar excess disks at $W2$, $W3$ and/or $W4$ for the stars in our science sample. The *WISE* Excess Flag indicates the combination of detections from the various colors. Each flag is a six character string that identifies whether the star has a statistically probable (Y) or insignificant (N) excess based on the order of the color analyses: $W1-W4$, $W2-W4$, $W3-W4$, $W1-W3$, $W2-W3$ and $W1-W2$. Any stars can have unlisted (U) values, indicating that the star was rejected by the selection criteria for that particular color (Section 2.2). "U" entries correspond to null entries in the corresponding $Wi-Wj$ Σ_E column. Column 3 lists whether or not the star is a new detection at the $W3$ and/or $W4$ bands (12 or 22 μm). The last six columns lists the significance of the excess Σ_E for each color.

(This table is available in its entirety in a machine-readable form in the online journal. A portion is shown here for guidance regarding its form and content.)

3. DEBRIS DISK BRIGHTNESS AND TEMPERATURE DETERMINATION

We fit the photometry of our debris disk candidates using model photospheres for the stellar contribution and single-temperature blackbodies for the dust. To constrain the photospheric fits, we use optical B & V Johnson photometry taken from the *Hipparcos* catalog, JHK_s photometry from 2MASS, $W1$, and in the lack of significant excesses ($\Sigma_E < \Sigma_{E_{\rm CL}}$), also $W2$ and $W3$ photometry from *WISE*. The photometry was converted from magnitudes to erg s^{-1} cm^{-2} Å^{-1} using the Johnson, 2MASS and *WISE* zero-point fluxes (Johnson & Morgan 1953; Cohen et al. 2003; Wright et al. 2010). The isophotal wavelength was adopted as the central wavelength for each bandpass.

We used NextGen (Hauschildt et al. 1999) photospheric models for stars of A–K spectral types, and Kurucz (1993) models for the few late-B stars in our candidate list. The models were fit to the calculated integrated fluxes over the bandpasses using χ^2 minimization with MPFIT (Markwardt 2009). The photospheric temperature (T_*), and flux scaling (i.e., stellar radius) were kept as free parameters. The surface gravity

Table 7
Debris Disk Parameters from Single-Temperature Blackbody Fits

HIP ID	T_{BB} (K)	$T_{BB_{lim}}$ (K)	R_{BB} (AU)	$R_{BB_{lim}}$ (AU)	θ ($''$)	f_d (10^{-5})	$f_{d_{lim}}$ (10^{-5})	Notes
544	...	<162	...	>2.3	>0.17	6.0	>0.23	b, e
560	...	<138	...	>8.1	>0.21	16	>0.57	b, e
682	...	<160	...	>3.2	>0.083	9.1	>0.35	b, e
1473	112	<263	28	>5.1	0.12–0.68	2.5	>0.064	c, e
1481	...	<185	...	>2.7	>0.065	9.6	>0.36	b, e
1866	...	<177	...	>0.99	>0.021	27	>1.0	b, e
2472	137	<311	22	>4.2	0.08–0.42	1.7	>0.055	c, e
2710	...	<208	...	>2.7	>0.065	3.9	>0.14	b, e
3210	117	<276	7.6	>1.3	0.03–0.17	6.3	>0.19	c, e
3279	...	<215	...	>1.9	>0.028	6.0	>0.21	b, e

Notes. A summary of the calculated disk properties of stars with $W2$, $W3$ and $W4$ excesses. Blackbody temperatures for the dust are listed alongside the calculated circumstellar location, projected angular extent of the dust and the fractional bolometric luminosity.
a. $W4$-only excess: The $W3$ excess flux in this case was either saturated or $>3\sigma$ below the photosphere. A limiting temperature and radius for the dust cannot be determined.
b. $W4$-only excess: The $W3$ excess flux is formally negative and an upper limit to the excess flux is used to place a 3σ limit to the dust temperature and radius.
c. $W4$-only excess: The $W3$ positive excess flux in this case was used to calculate a dust temperature and radius. An upper limit to the $W3$ excess flux was used to calculate a 3σ limit to the dust temperature and radius.
d. $W3$-only excess: The $W4$ positive excess flux in this case was used to calculate a dust temperature and radius. An upper limit to the $W4$ excess flux was used to calculate a 3σ limit to the dust temperature and radius.
e. Lower limit to the fractional luminosity was calculated for a blackbody with peak emission at $\lambda = 12\,\mu$m as described in Section 3.
f. Lower limit to the fractional luminosity was calculated for a blackbody with peak emission at $\lambda = 22\,\mu$m as described in Section 3.
g. Significant $W3$ and $W4$ excess found in these stars. Dust parameters are exact calculations.
h. $W3$-only excess: The $W4$ excess significance in this case was undetermined as the measurement was ignored in all $W4$ analyses as its ASC measurement was $>2\sigma$ discrepant from the mean Single Frame measurement.

(This table is available in its entirety in a machine-readable form in the online journal. A portion is shown here for guidance regarding its form and content.)

was kept constant at empirically determined values for main sequence stars from Schmidt-Kaler (1982).[5]

In some cases our fits produced poor matches to the stellar photosphere ($\chi^2 > 4$). In each of these cases, the 2MASS measurements were systematically offset compared to *WISE* $W1$ and $W2$. In such situations we used only $W1$ and $W2$ to fit the Raleigh-Jeans tail of the stellar photosphere; the stellar temperature was estimated from the SIMBAD spectral type listing and comparing it to Table 5 from Pecaut & Mamajek (2013).

We calculate the dust excess fluxes in each *WISE* band by subtracting the photospheric flux integrated over that band ($F_*(\lambda_{iso})$) from the measured values ($F_{obs}(\lambda_{iso})$), thereby obtaining a value for the dust flux at λ_{iso}, the isophotal wavelength of the band in question:

$$F_d^o(\lambda_{iso}) = F_{obs}(\lambda_{iso}) - F_*(\lambda_{iso}). \quad (4)$$

Where a significant excess is detected in both $W3$ and $W4$, we fit the measured flux excesses using a single-temperature (T_{BB}) blackbody model of the dust. While the dust is not expected to be actually concentrated in a thin ring at uniform temperature and radius from the star, the calculated temperature and circumstellar radius constitute useful estimates of the debris disk's average properties.

Most of our excess detections are at $W4$ only. In these cases, we use the upper limit on the $W3$ excess flux to set a 3σ upper limit on the dust temperature. In many of these cases, the $W3$ excess, though formally insignificant, is positive. We use these marginal $W3$ excesses to calculate a unique temperature for the dust, in addition to the upper limit already mentioned. The data in these cases are formally consistent with arbitrarily low temperatures, but nevertheless the calculated temperature is of some value, especially when the $W3$ excess has a significance more than 2σ and is only just below our threshold. Both the calculated and upper-limit temperatures are given in Table 7, and the reader should bear in mind that only the latter are guaranteed to be physically meaningful.

We proceed in an exactly analogous way for the few disks where we have significant detections only in $W3$. Here, we use upper limits on the $W4$ flux to set 3σ *lower* limits on the temperatures. In every case, the nominal $W4$ excess is positive though not significant. Thus, just as for the $W4$-only excesses with positive non-significant $W3$ excesses, we calculate unique temperatures in addition to the limits. These values and the limits are given in Table 7.

In addition to dust temperatures, we derive and tabulate the values of f_d, the ratio of the bolometric luminosity of the dust to that of the star—and also the circumstellar radii corresponding to dust temperatures. We will now describe how we use measured flux excesses (or limits) in $W4$ and $W3$, obtained using Equation (4), to calculate the dust temperature (or limit), the value of f_d, and the circumstellar radius of the dust (or limit thereon).

The *WISE* magnitude-to-flux conversion assumes that the spectral slope of the excess is akin to a Vega-like spectrum (i.e., a Rayleigh–Jeans slope) at the *WISE* wavelengths. The excess monochromatic flux from Equation (4) therefore needs to be color-corrected for the response of *WISE* to an emission from a cool blackbody source:

$$F_d(\lambda_{iso}) = \frac{F_d^o(\lambda_{iso})}{f_c(Wi; T_{BB})}, \quad (5)$$

where $f_c(Wi; T_{BB})$ are the flux correction factors like those found in Table 6 in Section IV.3.g.vi of the *WISE* Explanatory Supplement. We have duplicated the calculations that produced these and created a lookup table of $f_c(Wi; T_{BB})$ that spans a wider and much more finely sampled range of temperatures than that in the Explanatory Supplement.

Since we do not know a priori the temperature of the dust, we use this lookup table to perform a grid search to find the blackbody temperature that matches our observed fluxes. This gives us the spectrum of the dust. As we already have the photospheric model of the star, the bolometric luminosity ratio f_d may easily be found:

$$f_d = \frac{\int F_{\lambda,d} d\lambda}{\int F_{\lambda,*} d\lambda}. \quad (6)$$

The disk radius is then calculated assuming that the dust ring is in thermal equilibrium with the stellar radiation:

$$R_{BB} = (278.3/T_{BB})^2 \sqrt{L_*}\ (\mathrm{AU}). \quad (7)$$

Where one of the fluxes is an upper limit, the temperature will also be a limit (upper limit for a $W4$-only excess; lower limit

[5] Available on-line at the STScI Calibration Database System, http://www.stsci.edu/hst/observatory/cdbs/castelli_kurucz_atlas.html.

for a $W3$-only excess). A temperature limit converts easily into a limit on $R_{\rm BB}$, but not into a limit on f_d: in general, the value of f_d obtained using the equations above in the case where one of the fluxes is an upper limit will be neither the lowest nor the highest value of f_d permitted by the data.

However, we can set a meaningful lower limit on f_d in every case of single-band excess. This is because the lowest value of f_d consistent with the data corresponds to the case where the largest possible fraction of the disk luminosity comes out in the one band we have measured—in other words, where the blackbody emission peaks at the band's isophotal wavelength. This corresponds to a temperature of 131 K in the case of $W4$-only excesses or 272 K for $W3$-only excesses. We can therefore adopt as our dust model a blackbody having whichever of these temperatures is appropriate, normalized to match the measured excess in the relevant band. Equation (6) then gives the *minimum* f_d that is consistent with the data. This limit is given in Table 7 for all of our single-band excesses.

For some $W4$-only excesses, the $W3$ flux measurement fails to pass our selection criteria. For these, we cannot place any constraints on the dust temperature, but we can still place a lower limit on f_d as described in the preceding paragraph. For these cases, the temperature given in Table 7 is the one corresponding to the lower-limit f_d (131 K) and has no independent physical meaning.

For disks with excesses at both $W3$ and $W4$, Table 7 gives values for the dust temperature, its circumstellar radius, and its bolometric flux fraction f_d. For single-band disks, the table gives limiting values for all these quantities, as well as tentative calculated values in cases where the formally non-detected band showed a positive though non-significant excess. The SEDs of all stars with *WISE* $W3$ or $W4$ excesses, including our blackbody fits to the dust emission, are plotted in Figure 5.

4. ANALYSIS OF EXCESSES AND LOCATION OF THE DUST

We divide the analysis of our candidate debris disks according to the wavelengths at which they were detected. We first discuss our $W4$-only detections, which in most cases represent the short-wavelength tail of blackbody emission from cold dust peaking at longer wavelengths, although in a few cases we find evidence of multi-temperature dust. We then discuss detections of excesses at both $W3$ and $W4$ bands that may be explained by warm dust alone. Finally, we discuss the likelihood of hot dust orbiting a few stars that show significant excesses at $W2$.

4.1. W4-only Excesses: Kuiper Belt Analogs and Multi-temperature Dust Disks

Stars with dust emission detected at $W4$, but not in any of the three colors that do not include $W4$, make up 96% of our total detections, or 211 of 220. Of these 211 stars, just over 50% have been previously published as excess detections, and 36% have published dust temperatures, mostly based on IR excess measurements at multiple wavelengths including $\lambda \gtrsim 60\,\mu$m. None exhibits an excess detected at shorter wavelengths comparable to the $W3$ band (12 μm).

However, the dust in these systems must necessarily emit some flux at shorter wavelengths, even though it is not above our $W3$ detection threshold. The existence of such flux, undetectable from any individual star, can nonetheless be divined from the distributions of $E[W1-W3]$ and $E[W2-W3]$ (defined in Equation (1)). If there were no $W3$ flux from the dust, these distributions would be symmetric around zero, with the numbers of positive and negative values equal to within statistical uncertainties. Instead, we find that they are strongly skewed toward positive values. This observation suggests that we can measure the $W3$ excess flux, in aggregate, for these nominally $W4$-only systems. Such measurements allow us to determine the averaged dust temperature of various subsets of the $W4$-only systems, even though only an upper limit can be placed on the temperature of each dust-disk individually.

Because the distances and dust-luminosities of stars in our sample vary widely, we perform such analyses by calculating the $W3/W4$ excess flux ratios, rather than simply the $W3$ excess flux. We have a $W3$ measurement that meets the selection criteria given in Section 2.2 for 183 of our 211 $W4$-only detections. The weighted mean of the uncorrected $W3/W4$ flux ratio for all 183 stars is 0.174 ± 0.026. Thus we have a highly significant detection of the aggregate $W3$ excess, even though none of these stars had individual $W3$ excesses above our detection threshold. This calculation can be repeated for specific subsets of these 183 stars, with interesting implications for the characteristic dust temperatures. We perform these calculations below in Sections 4.1.1 and 4.1.2.

4.1.1. W4-only Excesses with Prior Longer Wavelength Detections

Of our 183 stars with $W4$-only excesses and $W3$ fluxes passing our selection criteria, 95 were previously known to exhibit IR flux excess, in many cases due to measurements at wavelengths longer than 30 μm. Of these 95 stars, 46 have published dust temperatures below 130 K, 20 have published dust temperatures of 130 K or higher, and 29 have no previously published dust temperatures. For convenience, in this section we will refer to these three samples of stars as the "known cold disks," the "known warm disks," and the "published disks of unknown temperature."

The published dust temperatures of the 46 known cold disks, by construction, all correspond to dust colder than the asteroid belt in our own solar system. They range down to 50 K, just slightly warmer than the solar system's EKB. For these 46 stars, we find an aggregate $W3/W4$ excess flux ratio of 0.122 ± 0.028. The fact that this ratio is not statistically consistent with zero means that we have detected a statistically significant $W3$ excess in the aggregate of these systems, though not in any one individually. This is the first indication of excess flux at wavelengths shorter than 18 μm for any of these systems.

We convert this aggregate $W3/W4$ excess flux ratio to a blackbody temperature, which will approximate the flux-weighted mean temperature of dust in the known cold disks. The correction factors $f_c(Wi; T_{\rm BB})$ must be taken into account in this conversion, and we do not know their values a priori since they depend on the temperature we seek to determine. Since it is easy to solve the inverse problem of predicting the uncorrected $W3/W4$ excess flux ratio for dust at a given blackbody temperature, we perform the conversion by a simple grid search in temperature space, finding that the uncorrected excess flux ratio $W3/W4 = 0.122 \pm 0.028$ corresponds to a blackbody temperature of 90 ± 6 K. For comparison, the median published dust temperature for these disks is 85 K (see Section 5 and Figure 6 references). Our 90 ± 6 K aggregate temperature, which was measured using shorter wavelengths than any of the published temperatures, is consistent with this result: it appears that at $W4$ and $W3$, we are measuring the Wien tail of blackbody emission from the same cold dust seen at longer wavelengths.

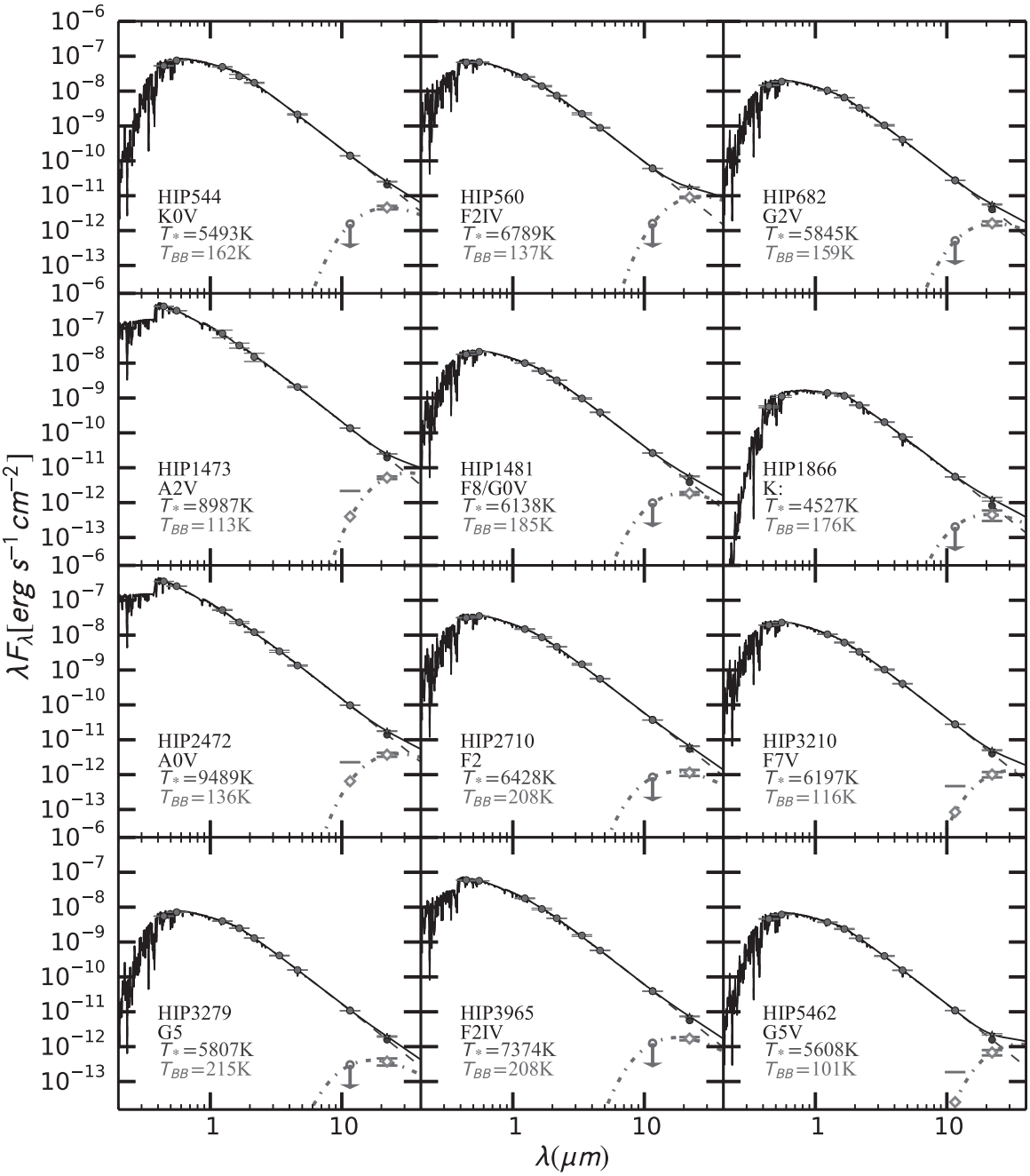

Figure 5. SEDs of probable debris disk host stars in our science sample. The dashed lines and solid data points correspond to the fitted model NextGen photosphere and to $BVJHK_s$ photometry from the *Hipparcos* Catalogue and 2MASS Point Source Catalog. Fluxes plotted as closed circles were used in the fit, and fluxes plotted as stars—excesses above the photosphere—were not used in the fit. Cool blackbody curves (dash-dotted line) were fitted to the excess fluxes (open diamonds) at the $W3$ and/or $W4$ wavelengths. The combined photosphere and excess emission for each star is plotted as a solid black line.

(An extended version of this figure is available in the online journal.)

The known warm disks have published temperatures ranging from 130 K to 276 K (with one outlier at 1700 K; Matranga et al. 2010). This dust could be analogous to the asteroid belt and even the zodiacal dust in our solar system. Our aggregate $W3/W4$ excess flux ratio from these 20 stars is 0.68 ± 0.21. This much higher result relative to the known cold disks is expected given that the warm dust will emit more at shorter wavelengths. Our $W3/W4$ excess flux ratio corresponds to an aggregate dust temperature of 154 ± 19 K. This is consistent with the median published dust temperature of 178 K for these disks,corresponding to a disk brightness of $f_d = 3.93 \times 10^{-5}$. This aggregate temperature also indicates a weak contribution from any exozodi (300 K) dust emission in these systems. We calculate the contribution of any such exozodiacal dust in the aggregate by assuming the $W3$ excess aggregate flux is arises from 300 K dust. Using the 2σ upper limit on the $W3$ excess aggregate flux, we calculate an upper limit dust brightness $f_d = 2.48 \times 10^{-5}$. This is 37% smaller than the actual disk brightness for the aggregate. Consequently, the $W4$ excess produced from this dust emission is 80% fainter than that of the derived aggregate, evidence of non exozodi dust emission in the aggregate.

For the 29 previously published disks of unknown temperature, we find an aggregate $W3/W4$ excess flux ratio of

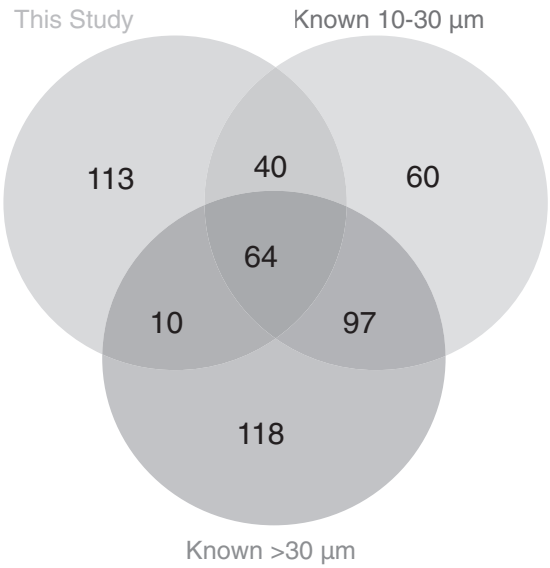

Figure 6. Comparison between excess detections in this study and previously reported excesses at mid-IR (10–30 μm) and far-IR ($\lambda \geqslant 30\,\mu$m) wavelengths. Only stars that are within 75 pc of the Sun with galactic latitudes 5° above or below the galactic plane are included in this comparison. Our study is focused on *Hipparcos* stars, while the previous studies include non-*Hipparcos* stars, too. Data for these stars was obtained from the following sources: Sylvester & Mannings (2000), Habing et al. (2001), Metchev et al. (2004), Beichman et al. (2005), Chen et al. (2005a), Chen et al. (2005b), Low et al. (2005), Beichman et al. (2006a), Beichman et al. (2006b), Chen et al. (2006), Moór et al. (2006), Smith et al. (2006), Su et al. (2006), Rhee et al. (2007b), Rhee et al. (2007a), Trilling et al. (2007), Wyatt et al. (2007), Hillenbrand et al. (2008), Meyer et al. (2008), Rebull et al. (2008), Rhee et al. (2008), Roberge & Weinberger (2008), Trilling et al. (2008), Bryden et al. (2009), Carpenter et al. (2009), Dahm & Carpenter (2009), Kóspál et al. (2009), Lawler et al. (2009), Moór et al. (2009), Morales et al. (2009), Plavchan et al. (2009), Su et al. (2009), Koerner et al. (2010), Moerchen et al. (2010), Smith & Wyatt (2010), Dodson-Robinson et al. (2011), Eiroa et al. (2011), Moór et al. (2011), Morales et al. (2011), Zuckerman et al. (2011), Kennedy et al. (2012), Urban et al. (2012) and Wu et al. (2013).

0.30 ± 0.14. As this value is too uncertain to be useful, we combine the published disks of unknown temperature with our own newly discovered disks in Section 4.1.2 below.

4.1.2. New W4-only Excesses

Of our 183 stars with $W4$-only excesses and $W3$ fluxes passing our selection criteria, 88 have not been previously published as IR excesses at any wavelength. These excesses are too tenuous (<10%) to have been accurately measured with *IRAS* or *AKARI*, and the stars have not been targeted with *Spitzer* or *Herschel*. They have not been identified as excesses in previous analyses of the *WISE* data.

Calculating the aggregate $W3/W4$ excess flux ratio is of particular importance for these systems, because if the systems correspond to real dust disks at physically plausible temperatures, a detectable aggregate $W3$ excess must be present. Lack of such a detection would falsify the $W4$ excesses, suggesting that they were due to imperfectly understood systematics in $W4$ rather than to genuine dusty disks.

The aggregate $W3/W4$ excess flux ratio for these is 0.508 ± 0.082, corresponding to a highly significant detection of the aggregate $W3$ excess flux. This ratio maps to an aggregate temperature of 139 ± 8 K. These significant, consistent, and physically reasonable results constitute a useful check, and confirm that our new $W4$-only excesses are real dust disks not identified by previous studies.

We can also add the sample of previously published disks of unknown temperature, mentioned in Section 4.1.1 above, to the sample of 88 new disks, and calculate the aggregate ratio of the combined samples. This is interesting because most of the 29 previously published disks of unknown temperature were also identified using *WISE* and thus the result will yield an estimate of the characteristic dust temperature of disks that were not detected in previous surveys (*ISO*, *IRAS*, *AKARI*), but have recently been identified using *WISE*. The aggregate $W3/W4$ excess flux ratio for this combined sample of 117 disks is 0.458 ± 0.071, which corresponds to a temperature of 134 ± 8 K. This temperature is comparable to the outer edge of our own asteroid belt.

4.1.3. Summary

We have found conclusive evidence for an aggregate $W3$ excess from stars that individually have significant excesses only at $W4$. Known cold disks have aggregate $W3/W4$ excess flux ratios implying cold dust and known warm disks have aggregate excess flux ratios consistent with warm dust. Disks recently discovered in this work and other studies using *WISE* $W4$ photometry show intermediate flux ratios that correspond, interestingly, to the temperature of dust located near the frost line and emitting its peak blackbody flux in the $W4$ bandpass. This aggregate temperature is only the mean of a potentially very wide distribution, but it is nonetheless possible that most of the newly discovered disks are warm (i.e., >100 K): if the $W4$ excesses measured for these systems were all merely the Wien tails of cold-dust emission, the cold dust in at least some cases would likely have already have been detected at 60 μm by *IRAS*.

4.2. W3 and W4 Excesses: Asteroid Belts and Exozodi

We find four stars with significant excesses in both $W3$ and $W4$ but not in $W2$: HIP 7345 (49 Cet), HIP 24528 (HD 34324), HIP 41081 (HD 71043) and HIP 95261 (η Tel). Their blackbody dust temperatures can be determined exactly and reliably, and are given in bold in Table 7. All of these are known debris disk host stars with 24 μm excesses from *Spitzer*, 25 μm excesses from *IRAS*, or 22 μm excesses from the recent *WISE* study by Wu et al. (2013), and with longer-wavelength detections at either 60 μm (*IRAS*), or 70 μm (*Spitzer*). Their published dust temperatures based on the longer-wavelength results range 80 K to 150 K. Our measured dust temperatures are higher in every case, ranging from 133 K to 199 K. These temperatures are well-matched to the 130–190 K temperature range corresponding to the asteroid belt in our own solar system; by contrast, the published temperatures mostly correspond to dust much colder than our asteroid belt, though not at the 30–55 K temperatures characteristic of solar system Kuiper Belt objects.

The discrepancies between our dust temperatures for these objects and the published ones based on longer-wavelength excesses demonstrates the existence of dust at multiple temperatures. HIP 95261 has the lowest discrepancy (177 K versus 150 K) and HIP 41081 the greatest (199 K versus 91 K). Even for HIP 95261, the discrepancy is likely real and points to a dust distribution spanning a wide range in circumstellar radius. The much larger discrepancy seen for HIP 41081 could even indicate two distinct dust populations at different radii and temperatures, separated by a gap—however, detailed modeling to distinguish this possibility from a single dust distribution spanning a wide range in circumstellar radius and temperature is beyond the scope of this work. In any case, all of these objects

are extremely interesting as targets for further study and observations, both to map the dust in more detail and to search for possible associated planets.

We also find five stars with excesses that are significant only at $W3$: HIP 19610, HIP 51793, HIP 80781, HIP 102238 and HIP 109656. All are new discoveries of our survey, with no previously published IR excess detection at any wavelength. All five have positive though formally non-significant $W4$ excesses, a statistical result which strongly suggests that the dust is emitting flux at $W4$, even though it is below our detection threshold.

We use upper limits on the $W4$ excess in these systems to calculate 3σ lower limits on the temperatures. These range from 174 K (HIP 80781) to 274 K (HIP 19610), although we caution that for HIP 80781 and HIP 109656 the $W4$ fluxes are suspect due to the discrepancy between the ASC and single-exposure photometry discussed in Section 2.3, and were therefore not used in our search for excesses within the science sample. Nevertheless, the fluxes may be accurate for these objects, and certainly are for the other three stars. Thus our 3σ lower limits on the dust temperatures conclusively demonstrate (at least for the three stars with good $W4$ photometry) that we are not merely measuring the Wien tail of blackbody emission from cold dust. Rather, dust exists at asteroidal (130–190 K) or, more likely, even warmer temperatures in these systems.

It is highly likely that the dust in these systems overlaps the habitable zone, which corresponds to temperatures of 230–330 K. This dust is likely produced by mutual collisions between asteroidal objects warmer and far more abundant than those in our solar system—objects that could be leftovers from the formation of one or more potentially habitable planets. Interestingly, however, the lack of significant excess detections at wavelengths greater than 12 μm suggests there is no Kuiper Belt analog in these systems, and therefore the overall system architecture may be very different from that of our own solar system. Such systems could serve as a probe of the diverse evolutionary pathways the process of planet formation can follow.

4.3. *W2 Excesses: Hot Dust or Signs of Chromospheric Activity*

Our $W3$ and $W4$ analyses are naturally extendable to $W2$, and we sought hot-dust excesses from the $W1 - W2$ color distribution. We found eight stars within 75 pc with significant $W2$ excesses. As discussed in Section 2.5, our empirical calibration of false positives does not allow us to push our confidence threshold beyond 95% for the $W1 - W2$ excesses. Nonetheless, this still implies that among the eight $W2$ excesses we expect less than one to be caused by random error.

We exclude two of the excesses from further consideration, as they are associated with unresolved binary stars with disparate spectral types: HIP 999 (G8V+K5; composite spectral type of K0 in *Hipparcos*) and HIP 3121 (K5V+M3V). That is, in these two cases an inaccurate estimate of the joint photospheric $W1 - W2$ color of the binaries is indeed the likely cause for the small $W2$ excesses. This conclusion is supported by the fact that these stars also possess small, sometimes significant, $W1 - W3$ and $W1 - W4$ excesses: that is, a blackbody slightly cooler than the $BVJHK_sW1$ photospheric fit—the secondary component—is needed to explain the *WISE* SED. A third $W2$ excess star, HIP 3729 (K2Ve), is a suspected double-lined spectroscopic binary, although according to Torres et al. (2006) that classification is uncertain because of the star's large $v \sin i$ (75 km s^{-1}). We observe that this star shows marginal excesses at all *WISE* wavelengths, including $W1$: a signature of variability between the 2MASS and *WISE* epochs, rather than a bona-fide excess. It is possible that the *WISE* excesses are caused by geometric factors affecting the combined flux from an unresolved close binary: e.g., grazing eclipses or ellipsoidal variations. Therefore, we also exclude HIP 3729.

The remaining five stars are not known to be in binary systems: HIP 30893 (K2V), HIP 74235 (K2V), HIP 74926 (K5Vp), HIP 96562 (F2V), and HIP 109941 (K5V). Their SEDs stars are shown in Figure 7. Four of the five stars show small, sometimes significant $W1 - W3$ and $W1 - W4$ excesses (Table 6), and for three of them the $W1$ data point is also marginally above the fitted photosphere. Previously unknown close companions could account for these, in much the same way as for HIP 999, HIP 3121, and HIP 3729. However, being within 75 pc and relatively cool, these stars have been prime targets for radial velocity monitoring and planet searches. Therefore, we assume that the excesses from these four stars are not caused by unknown stellar companions. The remaining $W2$ excess star, HIP 74235 (K2V), exhibits no excess at any other wavelength. All of its non-$W1-W2$ excesses are negative—most marginally, except for $W2 - W3$—indicating that the apparent excess is localized to the $W2$ band.

A potential clue to the nature of the detected $W2$ excesses is the fact that four of the five stars have K spectral types, and only one is hotter (F type). This may suggest that an inaccurate photospheric correction of the $W1 - W2$ color may be to blame for the large fraction of K-star $W2$ excesses in our science (75 pc) sample. However, the larger parent (120 pc) sample selection also contains A through G-type $W2$-excess stars, with no additional $W2$ excesses from K stars. This is evident from the distribution of $W1 - W2$ excesses as a function of $B_T - V_T$ in the bottom right panel of Figure 3: the $W1 - W2$ excesses do not cluster at red $B_T - V_T$ colors. The dominance of K star excesses in the 75 pc sample may therefore be attributable to the higher photometric precision that can be attained on faint K dwarfs near the Sun. We conclude that these excesses are real.

All five of the detected $W2$-excess systems may possess small amounts of hot dust, between ~400 K–900 K. Such dust would be in close proximity to the star, and would be expected to be very short-lived: potentially indicative of the recent planetesimal activity in the innermost reaches of these systems. The excess from the one F star (HIP 96562) is fully consistent with a $T_{\rm eff} = 780$ K black body. The remainder of the excesses, around the four K stars, require steeper than Raleigh-Jeans SEDs to fit the lower $W3$ and $W4$ excesses. Such SEDs would be representative of sub-micron dust grains with low emissivity at >5 μm wavelengths. We use modified blackbodies to model these:

$$B_\lambda(T_{\rm BB})_m = B_\lambda(T_{\rm BB}) \left(\frac{\lambda_0}{\lambda}\right)^\beta, \quad (8)$$

where β is the power index of the grain emissivity: typically between 0 and 3 for ideal dielectric materials (Helou 1989). In two of the cases (HIP 74235 and HIP 74926) we have set the excesses to peak at $W2$, since the information from the other *WISE* bands is not sufficient to constrain the temperatures. For the other two stars we have sought fits that satisfy all of the *WISE* excesses and upper limits.

HIP 30893 and HIP 109941 are the only stars for which β falls between 0 and 3, in agreement with thermal emission from dust with low emissivity. HIP 74235 and HIP 74926 have grain emissivity indices $\beta > 3$ that exceed physical values and

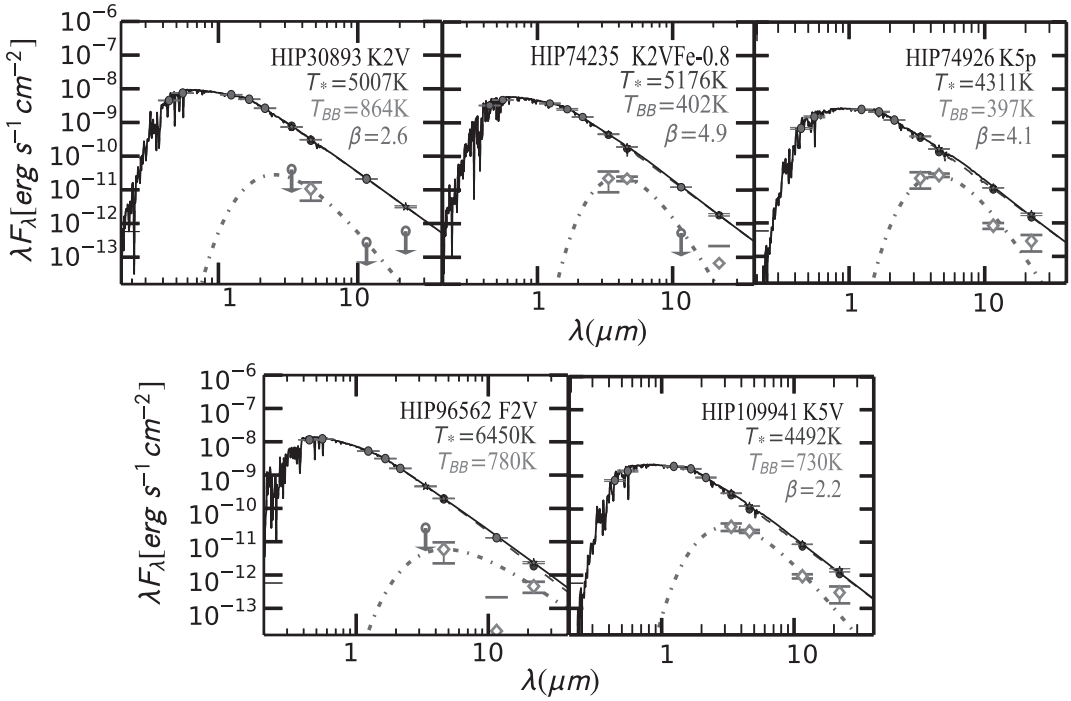

Figure 7. SEDs of stars with $W2$ excesses above the 95% confidence level. The stellar photosphere (dashed line) was fit to the $BVJHK_s$ photometry only. A blackbody was fit to the excess around the F star HIP 96562. In the cases of the four K stars, we fit modified blackbody functions (dot-dashed lines) to the *WISE* excess fluxes (diamonds), or to the *WISE* 3σ upper limit fluxes (open circles with downward arrows) when the excesses were negative. The K-star SEDs require a wide range of grain-emissivity index values (β), some of which are unphysical. The nature of these excesses remains uncertain at this time.

are difficult to interpret. We therefore can not conclude with confidence that dust is at the origin of any of the four K-star $W2$ excesses.

It is possible that the $W2$ excesses from the four K stars are related to their late spectral types, but not for reasons of inaccurate calibration of the photospheric $W1 - W2$ color. Instead, the responsible mechanism may be chromospheric activity. One of the stars, HIP 109941, is included in the *ROSAT* Bright Survey catalog (Fischer et al. 1998) and possesses Hα in emission. More generally, K stars have relatively active chromospheres compared to earlier-type stars, driven by deep convection. $W2$ spans the CO fundamental vibration-rotation bands, which are prominent in K stars. CO could conceivably be observed in emission under the right circumstances. CO emission at 4.7 μm is indeed observed in the Sun's lower chromosphere, within 1000 km of the Sun's limb, at gas temperatures of 3000–3500 K (Solanki et al. 1994). However, the emission does not contribute a significant portion of the Sun's bolometric flux. K dwarfs are more chromospherically active than the Sun, although it remains to be seen whether their entire $W2$-band fluxes can be raised by 5%–8% through CO line emission.

Because the nature of the $W2$ excesses remains speculative, and because the confidence threshold for the detections is lower ($\gtrsim$95%), we do not count the five stars discussed in this section toward the overall number of debris disks detected in our study. We single out only the F2V star HIP 96562 as a potential host of hot (780 K) circumstellar dust. If this excess is real, it would be among the most tenuous debris disks detected around any star.

4.4. Circumbinary Dust

The majority of studies looking for IR excesses from circumstellar disk material limit themselves to single stars, as the possibility of photometric confusion or contamination from closely separated stars is a concern. This is also the case in our study, as we aimed to remove all visual binary systems in which a companion may affect the photometry in the different *WISE* bands differently (see Section 2.2). However, a small number of stars, mostly in very wide binary or multiple systems passed all of our contamination checks and have bona-fide IR excesses. Only a few close binaries were allowed: those for which the component spectral types were very similar and so the composite $B_T - V_T$ color of the system is representative of the component's colors.

Using information from the Washington Double Star Catalog[6] (Mason et al. 2013) and from the literature, we identified 25 stars from our debris disk candidates that are part of binary or multiple star systems. Projected orbital separations are listed in Table 8. Three of these stars have companions projected separations $<12''$—HIP 9141, HIP 16908 and HIP 95261—placing them within the $W4$ beam. Thus the flux from these companions might mimic and IR excess attributed to the primary target. However we find this is not the case: HIP 9141 has an equal mass companion (Biller et al. 2007) and the SED for this star does not show an excess attributed to a binary component. HIP 95261 has an M7/8 spectral type companion, but the $W4$ flux for this star is $\sim$20% above the photosphere and does not possess a significant $W3$ excess. The inferred dust temperature is thus inconsistent with this star's companion. HIP 16908 has an M1/3V companion but the inferred dust temperature, along with the slope of the SED and an insignificant $W3$ excess is inconsistent with the IR flux of an M-type stellar companion.

We compare the calculated circumstellar dust radius (Table 7) and the binary separation to infer the location of the dust with respect to the stellar components.

Most (23) of the projected separations between the stellar binary components are larger than the inferred dust orbital radius, and the dust is therefore circumstellar. Given sufficiently wide angular separations between the stellar components in

[6] http://ad.usno.navy.mil/wds/

Table 8
Excesses Detected in Binary Systems

Star	Dist. (pc)	Binary Separation (″)	Binary Separation (AU)	Dust Radius (AU)	Dust State[a]
HIP 544	42	189.7	7900	2.7	cs
HIP 1481	47	12.6	590	36	cs
HIP 2472	60	SB	...	2.7	cb
HIP 4016	44	40	1800	2.9	cs
HIP 6679	29	132.9	3900	5.5	cs
HIP 7576	53	612	32000	22	cs
HIP 9141	61	0.15	9.2	3.4	cs
HIP 9902	29	52.4	1500	2.8	cs
HIP 11477	43	391.2	17000	10	cs
HIP 12489	71	29	2100	11	cs
HIP 13209	47	15.2	710	33	cs
HIP 16908	71	0.8	57	8.2	cs
HIP 21547	49	28.9	1400	4.3	cs
HIP 22394	41	SB	...	1.5	cb
HIP 25183	51	17.2	870	14	cs
HIP 61960	40	12.7	500	0.71	cs
HIP 65728	24	181.7	4400	2.4	cs
HIP 69281	50	12.6	630	5.9	cs
HIP 82587	72	74.7	5300	4.2	cs
HIP 94184	14	50.5	690	2.3	cs
HIP 95261	36	4.2	150	15	cs
HIP 102655	54	391.4	21000	2.7	cs
HIP 105388	53	13.6	730	6.3	cs
HIP 113477	48	21.6	1000	11	cs
HIP 115738	41	176.8	7200	1.1	cs

Notes. Science sample stars with debris disks in known binary systems. The binary separation was calculated using the parallactic distance and angular separations from the Washington Double Star Catalog. Spectroscopic binaries are listed as SB with no known projected separation information available.
[a] Orbital state of the dust: "cs" means the dust is in a circumstellar location around the primary star; "cb" means the dust is in a circumbinary configuration.

most of these systems, we are confident that the debris disk is co-located with the component identified in the *Hipparcos* catalog.

The remaining two stars, HIP 2472 (A0V) and HIP 22394 (K3V) are part of spectroscopic binary systems. There is no information in the literature for the orbital elements or spectral type for the binary component of HIP 2472. The binary component for HIP 22394 has a published orbital period of 11.9 days. The average separation of the stars would ∼0.″1. The radius for the dust in both these systems is estimated to be at 2.7 and 1.5 AU respectively. Since our assumption of blackbody dust properties is simplistic, and in reality circumstellar dust grains have poorer emissivity, our inferred dust orbital radii may be too small by a factor of up to two. Therefore, in these two cases, we conclude that the dust is in circumbinary configuration.

5. DISCUSSION

5.1. Comparison to Previous Work

We compare our sample of *Hipparcos* debris disks discovered in *WISE* to those previously reported in published work. The literature sample consists of excesses detected at multiple reference wavelengths, from IR surveys with *IRAS*, *ISO*, *Spitzer*, *AKARI*, *WISE*, and *Herschel* and includes stars not in *Hipparcos*. Our compilation of published results contains a total of 449 bona-fide debris disks within 75 pc, most (389) of which satisfy the spatial and color constraints that we placed on our science sample: i.e., $|b| > 5^\circ$ and $-0.17 < B_T - V_T \leqslant 1.40$. Among these, 261 have known warm component excess emission (10–30 μm).

We have identified 220 debris disks within 75 pc, 108 of which are new detections, and 114 have previously reported mid-IR and/or far-IR excesses ($\lambda > 10\,\mu$m). That is, our study has expanded the overall 75 pc debris disk census by 108/388 = 28%. Ten of the 114 previously known disks were not known to possess excesses at $\lambda < 30\,\mu$m, so the total number of new 10–30 μm disk identifications from our study is 108+10 = 118: a 118/262 = 45% increase. The third column of Table 6 lists whether our *WISE*-detected debris disks have previous detections at wavelengths similar to 12 μm or 22 μm. The Venn diagram in Figure 5 compares the number of detections in our survey to those stars with IR excesses discovered from past surveys at 10–30 μm and at $\lambda \geqslant 30\,\mu$m.

Our very strict photometric selection criteria and binarity checks have excluded a significant fraction (33%) of the overall 75 pc *Hipparcos* sample. The fact that over half of our 220 debris disk identifications are new indicates that previous searches for debris disks in all-sky surveys are only $\lesssim$50% complete to the precision limits of *WISE*. Hence, there is a potential to further double the number of known warm debris disks outside of the 75 pc *Hipparcos* sample.

We can also estimate the completeness of our own debris disk identification method by comparing the fraction of *Hipparcos* stars included in our science sample to the fraction of known 10–30 μm debris disks that we recover. As discussed in Section 2.2.2, our science sample includes 67% of $|b| > 5^\circ$ *Hipparcos* 75 pc main sequence stars with $-0.17 < B_T - V_T < 1.4$.

Within the same constraints we confirm 78% of the disks known from *WISE* and *AKARI*, and 38% of the disks known from *Spitzer*. We do miss most (14/23) of the few known 10–30 μm debris disks from *IRAS* and *ISO*, only because these stars exceed our $W2 > 2.8$ mag brightness threshold.

Therefore, our selection is at least as, or more sensitive than any of the previously published work that uses data from all-sky infrared survey telescopes. We achieve this without compromising confidence in our reported detections, as our overall $W4$ excess selection has 99.5% reliability. The reason for the lower fraction of recovered *Spitzer* 10–30 μm excesses is the greater sensitivity of targeted *Spitzer* observations, and the improved ability to remove the stellar photospheric contribution in *Spitzer* IRS observations. The missed warm excesses known from *Spitzer* are indeed all tenuous, below the sensitivity or precision limits of *WISE*.

Our search for 5–22 μm excesses from warm debris disks in the solar neighborhood is the most comprehensive and sensitive one to date, with a sample of nearly 8000 stars within 75 pc. Nevertheless, several recent $W4$-only studies have reported substantial numbers of new debris disk identifications in *WISE*, with samples that in some cases have significant overlap with ours. In the following, we compare our findings to these particular ones, and identify areas in which our work represents an improvement.

5.2. Comparison to the WISE W4 Debris Disk Study of Wu et al. (2013)

Wu et al. (2013) performed a search for $W4$ excesses from bright ($V < 10.27$ mag) *Hipparcos* stars, identifying 112 excesses, 70 of which were considered new candidate debris disks. While similar to ours, their analysis differs in ways that make the two studies complementary, with ours being sensitive to excesses around brighter stars (saturated in *WISE*), and to altogether fainter excesses around stars within 75 pc.

Wu et al. (2013) use a sample of 7624 stars within 200 pc, comprised of sources detected at S/N > 20 in $W4$, parallactic precision better than 10%, photometric precision better than 2.5% in $B - V$ colors, 2MASS $\sigma_{K_s} < 0.1$ mag, and unsaturated photometry in K_s, $W3$, and $W4$. Their excess candidates are defined as stars with $K_s - W4$ colors at least 4σ redward of the mean, where the mean and σ are calculated in four bins based on the $J - H$ colors of stars. This is analogous to our analysis using $B_T - V_T$ rather than $J - H$, and a running mean rather than four bins. Wu et al. (2013) removed sources contaminated by IR cirrus or confusion after their excess candidates were selected.

The Wu et al. (2013) approach results in several important differences in the results. First, Wu et al. (2013) probe stars out to much larger distances than we do, but they confine their analysis to the brightest unsaturated objects, with high-significance $W4$ detections and precise optical photometry. This allows the detection of disks with low fractional luminosity around any star in their sample, but at the same time rejects both the brightest saturated stars and fainter stars with G or K spectral types, around which we have detected significant excesses. If we compare the $W4$-excess disks in our science sample (<75 pc) to their selection criteria, we find that $180/220 = 82\%$ of our science sample disks are removed from their study: mostly because of saturation in K_s or because their $B - V$ color errors are >2.5%.

Second, Wu et al. (2013) choose to eliminate some sources of contamination *after* performing their color selection. On the one hand, this allows them to retain a larger statistical sample of stars to characterize the full $K_s - W4$ distribution. On the other hand, it results in a higher probability of missing faint excesses: including stars with *WISE* photometry contaminated by line-of-sight IR cirrus systematically increases the width of the $K_s - W4$ distribution. Our stricter selection criteria result in a cleaner sample, with $Wi - Wj$ distribution widths almost entirely accounted for by the photometric uncertainties (Section 2.5).

Our use of *WISE*-only colors and our treatment of the photometric systematics (Sections 2.3–2.5) also allows us to potentially detect fainter excesses. Wu et al. (2013) use 2MASS K_s photometry where the observations were conducted years prior to the launch of *WISE*. 2MASS minus *WISE* photometry is vulnerable to precision limitations induced by stellar variability or cross-platform systematics. These also increase the width of the $K_s - W4$ color distribution and can result in missed excesses.

Finally, we note that the tenuous excesses reported in Wu et al. (2013) from six F stars within 75 pc— HIP 22531, HIP 29888, HIP 42753, HIP 67953, HIP 70386, and HIP 72138—are likely not caused by circumstellar dust, but are the result of the stars' known binary companions. Wu et al. (2013) do note the presence of known companions in all of these cases, although do not rule out debris disks. We observe that the $K_s - W4$ excesses for these stars are similar to their respective $K_s - W1$, $K_s - W2$, and $K_s - W3$ excesses. In most of these cases the wider *WISE* beam has not resolved close visual binaries that are otherwise partially resolved in the seeing-limited 2MASS observations. In the case of the eclipsing binary HIP 72138 the 2MASS and *WISE* observations have likely seen the system at different orbital phases, such that the measurements are discrepant and a small excess appears to exist at *WISE* wavelengths.

While we do not address M stars in our study, we also note that two of the three M stars within 75 pc, HIP 21765 and HIP 63942, identified as candidate debris disk hosts in Wu et al. (2013) are also close (1.″4–2.″0) visual binaries. These are partially resolved in 2MASS and their $K_s - W4$ excesses are similar to those at the rest of the $K_s - WISE$ colors. That is, the excesses are most likely not from dust.

We do not recover every single reported debris disk in Wu et al. (2013). Within 75 pc we recover 37 of the 47 bona-fide debris disks reported in Wu et al. (2013), where we have excluded the eight F- and M-star binaries discussed above. The remaining 10 stars did not pass our selection criteria (Section 2.5), designed to remove objects for which the photospheric calibration of *WISE* colors is uncertain, and which may produce false-positive detections. HIP 12351 is an M star, excluded by our $B_T - V_T < 1.4$ mag criterion. HIP 11360 has contaminated *WISE* photometry (*WISE* confusion flag set to "dddd," indicative of contamination from a diffraction spike in each band by a closely separated star[7]), although the $W4$ excess does appear real. HIP 20713 has a companion within 5″ listed in the *Hipparcos* Visual Double Database. Lastly, seven of the stars within 75 pc in Wu et al. (2013) are giants (HIP 12361, HIP 15039, HIP 26309, HIP 43970, HIP 53824, HIP 55700, and HIP 100787), whereas we have focused only on main sequence stars.

Altogether, because of the greater emphasis on uncontaminated photometry, our analysis has resulted in greater sensitivity to debris disks and a larger detection rate within 75 pc. We have missed only one of the bona-fide main sequence B–K star debris disks from Wu et al. (2013)—HIP 11360, excluded because of contamination flagging in *WISE*. That is, we are 100% complete

[7] http://wise2.ipac.caltech.edu/docs/release/allsky/expsup/sec2_2a.html

to debris disks within our overall set of constraints. Conversely, the Wu et al. (2013) study encompasses a larger volume and identifies more distant debris disk systems. However, it does not include stars brighter than the $K_s \approx 4.2$ mag saturation limit in 2MASS, whereas we are able to. In addition, extra scrutiny is required to remove spurious excess identifications associated with double star systems.

5.3. Comparison to WISE W4 Debris Disk Study of Cruz-Saenz de Miera et al. (2014)

Cruz-Saenz de Miera et al. (2014, henceforth CS14) also carried out a search to find $W4$ excesses around main-sequence stars, finding 197 disk candidates. Their method to search for excesses is similar to ours, in that they relied solely on *WISE* photometry (the $W2 - W4$ color) to identify excesses while avoiding external systematics and stellar variability. CS14 focused on unsaturated F2-K0 stars with $V < 15$mag that were free of contamination in *WISE*.

Because of the elimination of saturated stars in CS14 and our focus on stars within 75 pc, the two studies are almost entirely complementary. In particular, there is no overlap in the reported detections. This is because their parent sample is generated from SIMBAD, and most of their stars are not in the *Hipparcos* database: only 68 of their 197 disk host stars have *Hipparcos* parallaxes. Only three of these are within <75 pc. We confirm two of these: HIP 5462 and HIP 93412. The remaining star, HIP 63880, is within 5° of the galactic plane, and so is not included in our selection, although the excess reported in CS14 is likely real.

5.4. Comparison to Vican & Schneider (2014)

Recently, a study of the age dependence of $W4$ excesses was published by Vican & Schneider (2014). In a sample of 2820 *Hipparcos* field FGK stars with ages estimated from chromospheric activity, Vican & Schneider (2014) report 98 excesses, 74 of which are identified as new, for a detection rate of 3.5%. The authors use photospheric fitting of the stellar SED, from the $BVJHK_s$ photometry, which they then compare to the measured $W4$ flux and error. The quality of the photospheric fits is inspected visually, and in the absence of nearby contamination evident from the *WISE* images, excesses with S/N > 5 are deemed significant.

Eighty-one of the 98 excesses reported in Vican & Schneider (2014) are from stars within 75 pc from the Sun, and would therefore be expected to be within our science sample, modulo the set of constraints that we impose to retain stars with clean *WISE* photometry. Among these we recover 24 of the reported excesses, we miss 11 stars because of our selection criteria, and do not confirm the remaining 46 excesses, even though those stars are included in our analysis.

We find that the 46 unconfirmed excesses from Vican & Schneider (2014) have Σ_E values that are often well below the 99.5% confidence threshold in our $W1 - W4$, $W2 - W4$, and $W3 - W4$ color distributions. A select few are even negative: e.g., HIP 117247, identified as a 6σ $W4$ excess in Vican & Schneider (2014), or HIP 10977, which has a negative $\Sigma_{E[W1-W4]}$ and $\Sigma_{E[W2-W4]}$ along with a positive but insignificant $\Sigma_{E[W3-W4]} = 0.49$.

We believe that our empirically determined 99.5% confidence threshold in $W4$ is robust, and is as aggressive as the data allow: evidenced by our 100% recovery rate of B–K main sequence star debris disks within 75 pc reported in Wu et al. (2013). Conversely, it is likely that the excess selection technique employed by Vican & Schneider (2014) is subject to unrecognized stellar variability between the multiple epochs that span the collection of the $BVJHK_s$ and *WISE* photometry. The fitting of stellar photospheres from the $BVJHK_s$ photometry, independently of any of the *WISE* measurements, and the subsequent selection of $W4$ excesses above the fitted photosphere, biases the excess candidate selection toward stars that are overall slightly brighter during the *WISE* epoch. In addition, such an approach should incorporate the overall 1.5% uncertainty in the *WISE* $W4$ calibration (Wright et al. 2010). Our empirical calibration of the stellar photospheric colors in *WISE* and our use of *WISE*-only photometry for excess selection allows us to calibrate both of these sources of systematic error.

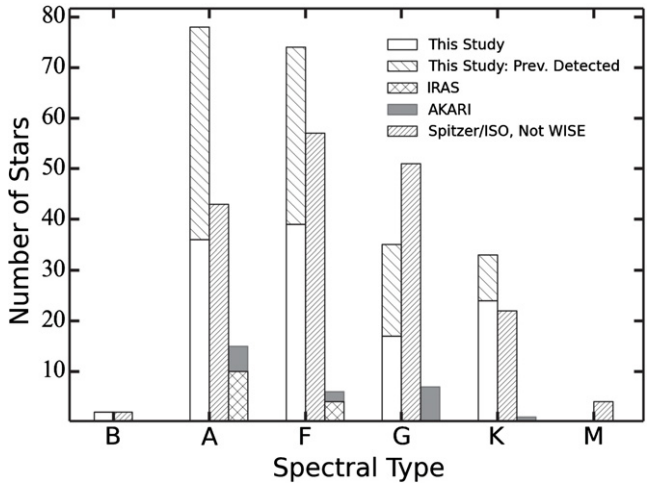

Figure 8. Distribution of excesses detected as a function of spectral type using *WISE* (this paper) compared to IR excess stars detected by pointed surveys and other all-sky surveys. All the excesses are compared at wavelengths between 10–30 μm, for stars that are outside the galactic plane $|b| \geqslant 5°$ and within 75 pc of the Sun.

Overall, we find that the 10–30 μm excess rate for field FGK stars in the Vican & Schneider (2014) study is approximately 1/3 of their reported one, and so more in agreement with the rate that we estimate in Section 5.5 below.

5.5. Stellar Spectral Type and Warm Disk Fraction

As detailed in Sections 5.1–5.3, because of our strict selection criteria, our study is not complete to all warm debris disks around *Hipparcos* stars within 75 pc. Nonetheless, within our carefully selected and unbiased science sample, we have performed the most sensitive and complete photometric identification of 10–30 μm excesses around main sequence stars using *WISE*. In the following, we use this result to study the relative occurrence of warm debris disks in the solar neighborhood.

Figure 8 plots the distribution of detected 10–30 μm excesses from *WISE* and previous surveys as a function of spectral type, within the spatial and color constraints of our science sample. We find that *WISE* detects approximately five times as many warm debris disks as *IRAS* and *AKARI* combined. Our particular study also increases by 45% the number of known warm dust excesses within 75 pc. Notably, we detect a substantial number of disks around cool stars, where the disks are intrinsically fainter. The discovery of these fainter disks is a consequence of both the increased sensitivity of *WISE* compared to *IRAS* and *AKARI*, and of our careful calibration of *WISE* systematics.

We present the distribution of *WISE* excess occurrence rate as a function of stellar $B_T - V_T$ color and spectral type in Figure 9. We find that B8–A9 stars show a 21.6% ± 2.5% incidence

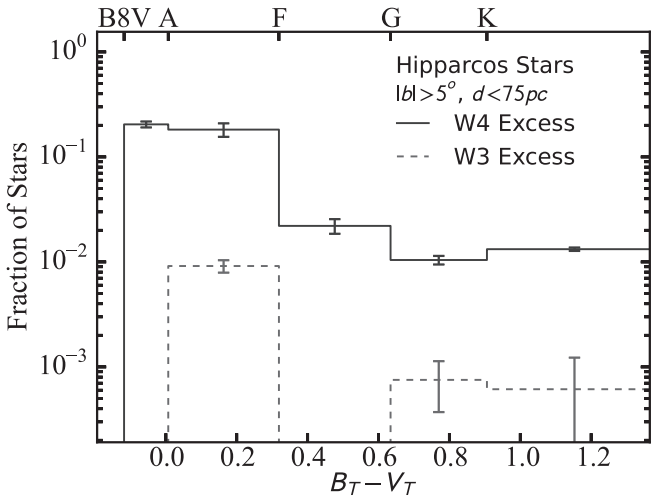

Figure 9. Fraction of *WISE* excesses detected in this survey as a function of spectral type from our science sample. To determine the excess fraction at each wavelength, we chose the most sensitive color combination.

of significant $W4$ excesses, and a $1.0\% \pm 0.5\%$ incidence of $W3$ excesses. Solar-type FGK stars have much lower excess occurrence rates: $1.8\% \pm 0.2\%$ at $W4$ and $0.08\% \pm 0.04\%$ at $W3$. The occurrence rates represent the results for the most sensitive among the different color combinations.

Our findings are in broad agreement with previous searches for $W4$ excesses on *WISE*, although we have had to point out several caveats with previous such studies. Thus, Wu et al. (2013) report that 6.9% of main-sequence FGK stars possess $W4$ excesses detected at the 3σ level. However, without detailed attention to photometric systematics they have adopted a higher working threshold for excess detection—4σ–at which level only 2.2% of their FGK stars have $W4$ excesses. We also discussed that a fraction (≈25%; Section 5.2) of the excesses identified in Wu et al. (2013) do not originate from dust, or are not associated with main sequence stars. That is, the actual rate of identifications of main sequence debris disks in Wu et al. (2013) is ≈1.6%. Similarly, CS14 report that 2% of all their FKG main-sequence stars possess 3σ $W4$ excesses, while our correction to the FGK debris disk rate found in Vican & Schneider (2014) is 1.2%. All of these warm-disk ($\lesssim$150 K) excess rates are consistent with our own findings for incidence of $W4$ excesses around FGK stars.

Compared to previous unbiased studies of warm debris disks with *Spitzer* our *WISE* analysis produces a factor of 1.5–3 lower detection rates. Su et al. (2006) determine a 32% rate of debris disks among A stars at 24 μm, while Carpenter et al. (2009) find debris disks with 10–70 μm excesses around 3% of >300 Myr old FGK stars. The discrepancies with the *Spitzer* studies are attributable to the higher sensitivity of pointed *Spitzer* observations.

Finally, our 0.08%–1.0% 12 μm excess rate from exozodi (∼300 K) among field stars is in agreement with an estimate from *WISE* in Kennedy & Wyatt (0.01%; 2013) and with findings from *Spitzer* (1%; Lawler et al. 2009). We note that our calibration and sample selection approach have enabled a somewhat better sensitivity to exozodi than the previous *WISE* study. In addition, our large-scale study has now for the first time provided a sufficient sample size to establish the relative frequency of exozodi between A and FGK stars: bright ($f_d > 10^{-4}$) exozodi are a factor of ∼10 more common around hot stars than around solar analogs.

6. CONCLUSION

We identify a volume-limited sample of *Hipparcos* stars within 75 pc that show infrared excess fluxes based on photometry contained in the *WISE* All-Sky Data Release. We carefully screen the *WISE* photometry for various sources of false-positives both astrophysical and instrumental. One such issue, newly identified in our work, is that in a tiny fraction of *WISE* photometry, the median of single-exposure fluxes is inconsistent with the *WISE* All Sky Catalog flux, and neither is reliable. We reject photometry compromised by this and other issues; precisely calibrate flux-dependent systematic effects in saturated photometry; and correct for the dependence of *WISE* colors on photospheric temperature. Using the blue wing of the resulting color distributions to empirically evaluate our FPR for the red outliers that correspond to dusty circumstellar disks, we robustly detect 215 such disks at 22 μm with FPR < 0.5% and 5 additional disks at 12 μm with FPR < 2%.

Our careful screening and precise calibration of the *WISE* photometry enables us to identify faint circumstellar dust disks that had gone unnoticed in previous analyses, in addition to confirming disks that had been previously detected using photometry from *WISE* and other missions. Our new detections represent, in total, an increase of 45% in the number of stars within 75 pc known to have flux excesses at mid-IR wavelengths. In contrast to *IRAS* and *ISO*, which produced many detections of cold circumstellar dust, the *WISE* mid-infrared bands have enhanced sensitivity to warmer dust in regions analogous to our own solar system's asteroid belt and zodiacal cloud—regions most likely responsible for terrestrial planet formation. We report the following detections:

1. 220 stars with FPR < 0.5% mid-IR excesses at 22 μm and/or FPR < 2% excesses at 12 μm. For 113 of these we present the first detection of a debris disk at any wavelength, and for a further 10 that have known longer-wavelength excesses, we present the first measurement of an excess at 12 μm and/or 22 μm.
2. A subset of 211 of our disks are detected with significant excesses in 22 μm only. Aggregate 12 μm excesses can be detected by weighted averages of the 12/22 μm excess flux ratio over different subsets of this sample, and these aggregate 12 μm detections are highly significant. The subset with previously published low (50–120 K) dust temperatures has an aggregate 12/22 μm excess flux ratio consistent with low-temperature dust, while the aggregate flux ratio for the previously unknown disks indicates that many of them have dust at asteroidal temperatures (>130 K).
3. A subset of four stars possess significant excess detections at both 12 and 22 μm, with a flux ratio indicative of dust temperatures ranging from ∼130 K to ∼200 K. All of these systems are known to possess long-wavelength (>60 μm) excesses well fit by colder dust, and none were suspected to have >100 K dust. Hence, our results indicate the presence of dust at multiple temperatures in these systems.
4. A subset of five disks are detected with significant excesses only at 12 μm. Upper limits to the 22 μm excesses in these systems yield 3σ lower limits on the temperature ranging from ∼175 K to ∼275 K. While the coolest of these limits would permit asteroidal-temperature dust, the data are more consistent with warmer dust. Such dust would overlap with the habitable zones in these systems and could come from

planetesimals left over from the formation of terrestrial planets.

5. Five additional stars, not included in our count of 220 detected dust disks, possess shorter-wavelength excesses at 4.6 μm with FPR $< 5\%$. One of these excesses, around the F2V star HIP 96562, is suspected to be caused by hot (780 K) dust. The origin of the remaining four excesses, all associated with K dwarfs, remains speculative. It is possible that in two of the cases the thermal emission is caused by tenuous amounts of hot, short-lived, sub-micron-sized dust. However, this scenario can not account for all four cases of $W2$ emission from K stars. We therefore suggest an alternate explanation involving chromospheric activity.
6. $1.8\% \pm 0.2\%$ of solar type (FGK) stars and $21.6\% \pm 2.5\%$ of A stars possess mid-infrared excesses at 22 μm, and the median lower limit to the fractional dust luminosity is $L_{\rm dust}/L_* \gtrsim 1.2 \times 10^{-6}$ for the A stars. At 12 μm, the occurrence rate of excesses is $0.08\% \pm 0.04\%$ for solar type stars and $1.0\% \pm 0.5\%$ for A stars.
7. As a result of our study, the number of debris disks with known 10–30 μm excesses within 75 pc (379) has now surpassed the number of disks with known >30 μm excesses (289, with 171 in common), even if the latter are known to have a higher occurrence rate in unbiased samples.

In addition to the scientific results, notable numerical and tabular references from the present study include:

1. the determination of photospheric *WISE* colors from $-0.15 < B_T - V_T < 1.4$ mag main sequence stars (Table 3)
2. polynomial relations for correcting saturated *WISE* $4.5 < W1 < 8.4$ mag and $2.8 < W2 < 7.0$ mag photometry (Figure 2)

WISE has rekindled the search for new disk bearing stars due to its enhanced resolving power compared to previous all-sky surveys like *IRAS*, combined with its wider coverage relative to pointed surveys using *Spitzer*. Although *WISE* cannot detect disks as faint as *Spitzer*, for that very reason the brighter, *WISE*-selected systems are excellent targets for resolved imaging observations, e.g., with the Gemini Planet Imager, ALMA, the LBTI nuller, or the *James Webb Space Telescope*. Such observations would further constrain the structure of the disks and the properties of the dust grains that reside in them, expanding our knowledge of the range of planetary system architectures in the galaxy.

This publication makes use of data products from the *Wide-field Infrared Survey Explorer*, which is a joint project of the University of California, Los Angeles, and the Jet Propulsion Laboratory/California Institute of Technology, funded by the National Aeronautics and Space Administration. We also use data products from the Two Micron All Sky Survey, which is a joint project of the University of Massachusetts and the Infrared Processing and Analysis Center/California Institute of Technology, funded by the National Aeronautics and Space Administration and the National Science Foundation. This research has also made use of the SIMBAD database, operated at CDS, Strasbourg, France. This research has made use of the Washington Double Star Catalog maintained at the U.S. Naval Observatory. We would also like to thank Kendra Kellogg for her help in visually inspecting the *WISE* images in the initial stages of this study as well as Joe Trollo for his help in the development phase of the SED plotting algorithm. Most of the figures in this work were created using Matplotlib, a Python graphics environment (Hunter 2007). This work is partially supported by NASA Origins of Solar Systems through subcontract No. 1467483.

REFERENCES

Avenhaus, H., Schmid, H. M., & Meyer, M. R. 2012, A&A, 548, A105
Backman, D. E., & Paresce, F. 1993, in Protostars and Planets III, ed. V. Mannings, A. P. Boss, & S. S. Russell (Tucson, AZ: Univ. Arizona Press), 1253
Beichman, C. A., Bryden, G., Rieke, G. H., et al. 2005, ApJ, 622, 1160
Beichman, C. A., Bryden, G., Stapelfeldt, K. R., et al. 2006a, ApJ, 652, 1674
Beichman, C. A., Tanner, A., Bryden, G., et al. 2006b, ApJ, 639, 1166
Biller, B. A., Close, L. M., Masciadri, E., et al. 2007, ApJS, 173, 143
Bryden, G., Beichman, C. A., Carpenter, J. M., et al. 2009, ApJ, 705, 1226
Bryden, G., Beichman, C. A., Trilling, D. E., et al. 2006, ApJ, 636, 1098
Carpenter, J. M., Bouwman, J., Mamajek, E. E., et al. 2009, ApJS, 181, 197
Chen, C. H., Jura, M., Gordon, K. D., & Blaylock, M. 2005a, ApJ, 623, 493
Chen, C. H., Patten, B. M., Werner, M. W., et al. 2005b, ApJ, 634, 1372
Chen, C. H., Sargent, B. A., Bohac, C., et al. 2006, ApJS, 166, 351
Cohen, M., Wheaton, W. A., & Megeath, S. T. 2003, AJ, 126, 1090
Cruz-Saenz de Miera, F., Chavez, M., Bertone, E., & Vega, O. 2014, MNRAS, 437, 391
Currie, T., Kenyon, S. J., Balog, Z., et al. 2008a, ApJ, 672, 558
Currie, T., Plavchan, P., & Kenyon, S. J. 2008b, ApJ, 688, 597
Cutri, R. M., Wright, E. L., Conrow, T., et al. 2012, Explanatory Supplement to the WISE All-Sky Data Release Products, Tech. Rep., NASA-IPAC
Dahm, S. E., & Carpenter, J. M. 2009, AJ, 137, 4024
Dawson, P., Scholz, A., Ray, T. P., et al. 2013, MNRAS, 429, 903
Dodson-Robinson, S. E., Beichman, C. A., Carpenter, J. M., & Bryden, G. 2011, AJ, 141, 11
Dommanget, J., & Nys, O. 2000, A&A, 363, 991
Eiroa, C., Marshall, J. P., Mora, A., et al. 2011, A&A, 536, L4
Eiroa, C., Marshall, J. P., Mora, A., et al. 2013, A&A, 555, A11
Fischer, J.-U., Hasinger, G., Schwope, A. D., et al. 1998, AN, 319, 347
Fujiwara, H., Ishihara, D., Onaka, T., et al. 2013, A&A, 550, A45
Habing, H. J., Dominik, C., Jourdain de Muizon, M., et al. 2001, A&A, 365, 545
Hauschildt, P. H., Allard, F., & Baron, E. 1999, ApJ, 512, 377
Helou, G. 1989, in IAU Symp. 135, Interstellar Dust, ed. L. J. Allamandola & A. G. G. M. Tielens (Dordrecht: Kluwer), 285
Hillenbrand, L. A., Carpenter, J. M., Kim, J. S., et al. 2008, ApJ, 677, 630
Houck, J. R., Roellig, T. L., van Cleve, J., et al. 2004, ApJS, 154, 18
Hunter, J. D. 2007, CSE, 9, 90
Johnson, H. L., & Morgan, W. W. 1953, ApJ, 117, 313
Kennedy, G. M., & Wyatt, M. C. 2012, MNRAS, 426, 91
Kennedy, G. M., & Wyatt, M. C. 2013, MNRAS, 433, 2334
Kennedy, G. M., Wyatt, M. C., Sibthorpe, B., et al. 2012, MNRAS, 426, 2115
Koerner, D. W., Kim, S., Trilling, D. E., et al. 2010, ApJL, 710, L26
Kóspál, Á., Ardila, D. R., Moór, A., & Ábrahám, P. 2009, ApJL, 700, L73
Krivov, A. V., Reidemeister, M., Fiedler, S., Löhne, T., & Neuhäuser, R. 2011, MNRAS, 418, L15
Kurucz, R. L. 1993, yCat, 6039, 0
Lallement, R., Welsh, B. Y., Vergely, J. L., Crifo, F., & Sfeir, D. 2003, A&A, 411, 447
Lawler, S. M., Beichman, C. A., Bryden, G., et al. 2009, ApJ, 705, 89
Lawler, S. M., & Gladman, B. 2012, ApJ, 752, 53
Low, F. J., Smith, P. S., Werner, M., et al. 2005, ApJ, 631, 1170
Luhman, K. L., & Mamajek, E. E. 2012, ApJ, 758, 31
Mamajek, E. E., Meyer, M. R., & Liebert, J. 2002, AJ, 124, 1670
Markwardt, C. B. 2009, in ASP Conf. Ser. 411, Astronomical Data Analysis Software and Systems XVIII, ed. D. A. Bohlender, D. Durand, & P. Dowler (San Francisco, CA: ASP), 251
Mason, B. D., Wycoff, G. L., Hartkopf, W. I., Douglass, G. G., & Worley, C. E. 2013, yCat, 1, 2026
Matranga, M., Drake, J. J., Kashyap, V. L., Marengo, M., & Kuchner, M. J. 2010, ApJL, 720, L164
Metchev, S. A., Hillenbrand, L. A., & Meyer, M. R. 2004, ApJ, 600, 435
Meyer, M. R., Carpenter, J. M., Mamajek, E. E., et al. 2008, ApJL, 673, L181
Mizusawa, T. F., Rebull, L. M., Stauffer, J. R., et al. 2012, AJ, 144, 135
Moerchen, M. M., Telesco, C. M., & Packham, C. 2010, ApJ, 723, 1418
Moór, A., Ábrahám, P., Derekas, A., et al. 2006, ApJ, 644, 525
Moór, A., Apai, D., Pascucci, I., et al. 2009, ApJL, 700, L25
Moór, A., Pascucci, I., Kóspál, Á., et al. 2011, ApJS, 193, 4
Morales, F. Y., Padgett, D. L., Bryden, G., Werner, M. W., & Furlan, E. 2012, ApJ, 757, 7

Morales, F. Y., Rieke, G. H., Werner, M. W., et al. 2011, ApJL, 730, L29
Morales, F. Y., Werner, M. W., Bryden, G., et al. 2009, ApJ, 699, 1067
Pecaut, M. J., & Mamajek, E. E. 2013, ApJS, 208, 9
Perryman, M. A. C., Lindegren, L., Kovalevsky, J., et al. 1997, A&A, 323, L49
Plavchan, P., Werner, M. W., Chen, C. H., et al. 2009, ApJ, 698, 1068
Rebull, L. M., Stapelfeldt, K. R., Werner, M. W., et al. 2008, ApJ, 681, 1484
Rhee, J. H., Song, I., & Zuckerman, B. 2007a, ApJ, 671, 616
Rhee, J. H., Song, I., & Zuckerman, B. 2008, ApJ, 675, 777
Rhee, J. H., Song, I., Zuckerman, B., & McElwain, M. 2007b, ApJ, 660, 1556
Riaz, B., Lodieu, N., Goodwin, S., Stamatellos, D., & Thompson, M. 2012, MNRAS, 420, 2497
Ribas, Á., Merín, B., Ardila, D. R., & Bouy, H. 2012, A&A, 541, A38
Rizzuto, A. C., Ireland, M. J., & Zucker, D. B. 2012, MNRAS, 421, L97
Roberge, A., & Weinberger, A. J. 2008, ApJ, 676, 509
Schmidt-Kaler, T. 1982, BICDS, 23, 2
Siegler, N., Muzerolle, J., Young, E. T., et al. 2007, ApJ, 654, 580
Smith, P. S., Hines, D. C., Low, F. J., et al. 2006, ApJL, 644, L125
Smith, R., & Wyatt, M. C. 2010, A&A, 515, A95
Solanki, S. K., Livingston, W., & Ayres, T. 1994, Sci, 263, 64
Su, K. Y. L., Rieke, G. H., Stansberry, J. A., et al. 2006, ApJ, 653, 675
Su, K. Y. L., Rieke, G. H., Stapelfeldt, K. R., et al. 2009, ApJ, 705, 314
Sylvester, R. J., & Mannings, V. 2000, MNRAS, 313, 73
Torres, C. A. O., Quast, G. R., da Silva, L., et al. 2006, A&A, 460, 695
Trilling, D. E., Bryden, G., Beichman, C. A., et al. 2008, ApJ, 674, 1086
Trilling, D. E., Stansberry, J. A., Stapelfeldt, K. R., et al. 2007, ApJ, 658, 1289
Urban, L. E., Rieke, G., Su, K., & Trilling, D. E. 2012, ApJ, 750, 98
van Leeuwen, F. 2007, A&A, 474, 653
Vican, L., & Schneider, A. 2014, ApJ, 780, 154
Wright, C. O., Egan, M. P., Kraemer, K. E., & Price, S. D. 2003, AJ, 125, 359
Wright, E. L., Eisenhardt, P. R. M., Mainzer, A. K., et al. 2010, AJ, 140, 1868
Wu, C.-J., Wu, H., Lam, M.-I., et al. 2013, ApJS, 208, 29
Wyatt, M. C., Smith, R., Su, K. Y. L., et al. 2007, ApJ, 663, 365
Zuckerman, B., Rhee, J. H., Song, I., & Bessell, M. S. 2011, ApJ, 732, 61

The Astrophysical Journal Supplement Series, 214:14 (2pp), 2014 September doi:10.1088/0067-0049/214/1/14

ERRATUM: "A SENSITIVE IDENTIFICATION OF WARM DEBRIS DISKS IN THE SOLAR NEIGHBORHOOD THROUGH PRECISE CALIBRATION OF SATURATED *WISE* PHOTOMETRY" (2014, ApJS, 212, 10)

Rahul I. Patel[1], Stanimir A. Metchev[1,2], and Aren Heinze[1]
[1] Department of Physics and Astronomy, Stony Brook University, 100 Nicolls Road, Stony Brook, NY 11794–3800, USA
[2] Department of Physics and Astronomy, The University of Western Ontario, 1151 Richmond Street, London, Ontario N6A 3K7, Canada
Received 2014 July 30; published 2014 September 3

In Section 2.5, we used the surviving 2/3 of data points in the trimmed mean to calculate the $W_{ij}(B_T - V_T)$ relations instead of the stated 50% of data points. The uncertainties in the $W_{ij}(B_T - V_T)$ relations in Table 3 were underestimated because we did not include a systematic component. The systematic errors for the relations are calculated by rms-deviation of trimmed means from a combination of three $B_T - V_T$ bin sizes (0.05 mag, 0.1 mag, and 0.2 mag) and three data rejection fractions (30%, 40%, and 50%), and are added in quadrature to the standard error. A corrected version of Table 3 is included below.

Table 3
Photospheric *WISE* Colors of $-0.17 < B_T - V_T < 1.4$ mag Main Sequence Stars

$B_T - V_T$ (mag)	$W1 - W4$ (mag)	$W2 - W4$ (mag)	$W3 - W4$ (mag)	$W1 - W3$ (mag)	$W2 - W3$ (mag)	$W1 - W2$ (mag)
−0.16	−0.070 ± 0.013	−0.001 ± 0.010	0.050 ± 0.007	−0.117 ± 0.011	−0.059 ± 0.011	−0.045 ± 0.007
−0.14	−0.070 ± 0.013	−0.001 ± 0.010	0.050 ± 0.007	−0.117 ± 0.011	−0.059 ± 0.011	−0.045 ± 0.007
−0.12	−0.070 ± 0.014	−0.001 ± 0.007	0.050 ± 0.007	−0.117 ± 0.011	−0.059 ± 0.010	−0.045 ± 0.007
−0.10	−0.065 ± 0.011	−0.006 ± 0.008	0.046 ± 0.006	−0.115 ± 0.010	−0.059 ± 0.009	−0.047 ± 0.007
−0.08	−0.056 ± 0.012	−0.003 ± 0.006	0.044 ± 0.006	−0.105 ± 0.009	−0.056 ± 0.007	−0.049 ± 0.003
−0.06	−0.054 ± 0.010	−0.001 ± 0.008	0.043 ± 0.007	−0.104 ± 0.008	−0.051 ± 0.006	−0.050 ± 0.004
−0.04	−0.043 ± 0.009	0.009 ± 0.010	0.049 ± 0.008	−0.091 ± 0.008	−0.044 ± 0.005	−0.044 ± 0.007
−0.02	−0.035 ± 0.008	0.011 ± 0.010	0.051 ± 0.008	−0.087 ± 0.007	−0.041 ± 0.002	−0.047 ± 0.005
0.00	−0.026 ± 0.011	0.018 ± 0.012	0.054 ± 0.009	−0.078 ± 0.009	−0.037 ± 0.002	−0.042 ± 0.003
0.02	−0.019 ± 0.013	0.023 ± 0.014	0.059 ± 0.010	−0.071 ± 0.005	−0.038 ± 0.002	−0.041 ± 0.003
0.04	−0.019 ± 0.012	0.018 ± 0.011	0.056 ± 0.008	−0.070 ± 0.006	−0.036 ± 0.002	−0.035 ± 0.003
0.06	−0.024 ± 0.013	0.009 ± 0.011	0.049 ± 0.009	−0.067 ± 0.005	−0.036 ± 0.002	−0.036 ± 0.004
0.08	−0.026 ± 0.008	0.009 ± 0.007	0.045 ± 0.006	−0.068 ± 0.006	−0.034 ± 0.002	−0.035 ± 0.002
0.10	−0.032 ± 0.005	0.002 ± 0.005	0.043 ± 0.004	−0.067 ± 0.004	−0.034 ± 0.002	−0.034 ± 0.002
0.12	−0.026 ± 0.006	0.003 ± 0.005	0.047 ± 0.004	−0.064 ± 0.003	−0.034 ± 0.001	−0.032 ± 0.003
0.14	−0.027 ± 0.005	0.005 ± 0.005	0.045 ± 0.004	−0.060 ± 0.003	−0.032 ± 0.002	−0.033 ± 0.002
0.16	−0.021 ± 0.005	0.006 ± 0.006	0.049 ± 0.005	−0.059 ± 0.002	−0.035 ± 0.002	−0.031 ± 0.002
0.18	−0.022 ± 0.005	0.004 ± 0.007	0.045 ± 0.005	−0.058 ± 0.002	−0.032 ± 0.002	−0.030 ± 0.002
0.20	−0.017 ± 0.004	0.012 ± 0.004	0.049 ± 0.003	−0.056 ± 0.002	−0.031 ± 0.002	−0.030 ± 0.001
0.22	−0.018 ± 0.005	0.011 ± 0.003	0.048 ± 0.003	−0.055 ± 0.002	−0.030 ± 0.002	−0.031 ± 0.002
0.24	−0.017 ± 0.006	0.015 ± 0.004	0.048 ± 0.003	−0.057 ± 0.002	−0.030 ± 0.001	−0.030 ± 0.002
0.26	−0.012 ± 0.004	0.019 ± 0.003	0.049 ± 0.003	−0.056 ± 0.002	−0.028 ± 0.001	−0.029 ± 0.002
0.28	−0.007 ± 0.006	0.025 ± 0.005	0.052 ± 0.003	−0.055 ± 0.004	−0.027 ± 0.001	−0.028 ± 0.002
0.30	−0.004 ± 0.003	0.025 ± 0.003	0.056 ± 0.003	−0.054 ± 0.002	−0.026 ± 0.001	−0.027 ± 0.001
0.32	0.004 ± 0.004	0.033 ± 0.003	0.061 ± 0.002	−0.049 ± 0.002	−0.025 ± 0.001	−0.026 ± 0.001
0.34	0.009 ± 0.005	0.037 ± 0.004	0.065 ± 0.002	−0.047 ± 0.001	−0.023 ± 0.001	−0.026 ± 0.001
0.36	0.009 ± 0.006	0.038 ± 0.005	0.065 ± 0.003	−0.047 ± 0.001	−0.021 ± 0.001	−0.027 ± 0.001
0.38	0.012 ± 0.006	0.039 ± 0.005	0.066 ± 0.003	−0.046 ± 0.001	−0.020 ± 0.001	−0.027 ± 0.001
0.40	0.010 ± 0.005	0.039 ± 0.004	0.065 ± 0.003	−0.046 ± 0.001	−0.020 ± 0.001	−0.028 ± 0.001
0.42	0.001 ± 0.003	0.034 ± 0.002	0.059 ± 0.003	−0.046 ± 0.001	−0.019 ± 0.001	−0.029 ± 0.001
0.44	−0.002 ± 0.002	0.030 ± 0.002	0.054 ± 0.002	−0.045 ± 0.001	−0.019 ± 0.001	−0.029 ± 0.001
0.46	−0.005 ± 0.003	0.028 ± 0.002	0.051 ± 0.002	−0.045 ± 0.001	−0.018 ± 0.001	−0.030 ± 0.001
0.48	−0.010 ± 0.002	0.024 ± 0.002	0.047 ± 0.002	−0.045 ± 0.002	−0.016 ± 0.001	−0.032 ± 0.001
0.50	−0.012 ± 0.002	0.023 ± 0.002	0.046 ± 0.002	−0.045 ± 0.002	−0.015 ± 0.000	−0.033 ± 0.001
0.52	−0.012 ± 0.002	0.023 ± 0.001	0.045 ± 0.001	−0.046 ± 0.002	−0.014 ± 0.001	−0.035 ± 0.000
0.54	−0.014 ± 0.003	0.024 ± 0.002	0.043 ± 0.001	−0.044 ± 0.002	−0.012 ± 0.001	−0.037 ± 0.000
0.56	−0.016 ± 0.003	0.023 ± 0.002	0.041 ± 0.002	−0.044 ± 0.002	−0.011 ± 0.000	−0.039 ± 0.001
0.58	−0.015 ± 0.003	0.025 ± 0.002	0.042 ± 0.002	−0.044 ± 0.001	−0.009 ± 0.001	−0.040 ± 0.001
0.60	−0.013 ± 0.002	0.027 ± 0.001	0.042 ± 0.002	−0.043 ± 0.001	−0.007 ± 0.001	−0.042 ± 0.001
0.62	−0.011 ± 0.002	0.029 ± 0.002	0.041 ± 0.001	−0.043 ± 0.002	−0.005 ± 0.001	−0.042 ± 0.001
0.64	−0.010 ± 0.004	0.029 ± 0.003	0.042 ± 0.001	−0.043 ± 0.002	−0.004 ± 0.001	−0.043 ± 0.001
0.66	−0.010 ± 0.003	0.034 ± 0.003	0.044 ± 0.001	−0.042 ± 0.002	−0.002 ± 0.001	−0.044 ± 0.000
0.68	−0.011 ± 0.002	0.034 ± 0.003	0.042 ± 0.001	−0.042 ± 0.001	0.000 ± 0.001	−0.046 ± 0.001

Table 3
(Continued)

$B_T - V_T$ (mag)	$W1 - W4$ (mag)	$W2 - W4$ (mag)	$W3 - W4$ (mag)	$W1 - W3$ (mag)	$W2 - W3$ (mag)	$W1 - W2$ (mag)
0.70	-0.015 ± 0.002	0.035 ± 0.002	0.041 ± 0.001	-0.041 ± 0.001	0.002 ± 0.001	-0.047 ± 0.001
0.72	-0.016 ± 0.004	0.036 ± 0.001	0.041 ± 0.001	-0.040 ± 0.001	0.003 ± 0.001	-0.050 ± 0.001
0.74	-0.014 ± 0.003	0.039 ± 0.002	0.042 ± 0.002	-0.040 ± 0.001	0.005 ± 0.001	-0.050 ± 0.002
0.76	-0.014 ± 0.002	0.040 ± 0.003	0.041 ± 0.001	-0.041 ± 0.001	0.005 ± 0.001	-0.052 ± 0.001
0.78	-0.012 ± 0.004	0.043 ± 0.004	0.041 ± 0.002	-0.040 ± 0.001	0.006 ± 0.001	-0.053 ± 0.001
0.80	-0.012 ± 0.005	0.044 ± 0.004	0.041 ± 0.003	-0.040 ± 0.001	0.008 ± 0.001	-0.053 ± 0.001
0.82	-0.014 ± 0.003	0.042 ± 0.003	0.039 ± 0.005	-0.040 ± 0.001	0.010 ± 0.001	-0.055 ± 0.001
0.84	-0.018 ± 0.004	0.040 ± 0.003	0.038 ± 0.002	-0.039 ± 0.001	0.012 ± 0.001	-0.057 ± 0.001
0.86	-0.019 ± 0.005	0.041 ± 0.004	0.039 ± 0.003	-0.038 ± 0.001	0.014 ± 0.002	-0.058 ± 0.001
0.88	-0.019 ± 0.004	0.042 ± 0.004	0.040 ± 0.003	-0.038 ± 0.001	0.017 ± 0.002	-0.059 ± 0.001
0.90	-0.018 ± 0.002	0.045 ± 0.003	0.041 ± 0.002	-0.038 ± 0.001	0.020 ± 0.002	-0.061 ± 0.001
0.92	-0.018 ± 0.005	0.048 ± 0.005	0.038 ± 0.003	-0.037 ± 0.002	0.020 ± 0.004	-0.062 ± 0.001
0.94	-0.014 ± 0.006	0.054 ± 0.005	0.043 ± 0.002	-0.037 ± 0.001	0.023 ± 0.002	-0.063 ± 0.001
0.96	-0.019 ± 0.008	0.047 ± 0.007	0.035 ± 0.004	-0.038 ± 0.002	0.022 ± 0.001	-0.064 ± 0.001
0.98	-0.013 ± 0.004	0.054 ± 0.004	0.035 ± 0.003	-0.038 ± 0.001	0.022 ± 0.001	-0.064 ± 0.001
1.00	-0.016 ± 0.005	0.051 ± 0.005	0.034 ± 0.006	-0.037 ± 0.003	0.024 ± 0.001	-0.063 ± 0.001
1.02	-0.011 ± 0.005	0.056 ± 0.006	0.033 ± 0.006	-0.038 ± 0.002	0.025 ± 0.001	-0.065 ± 0.001
1.04	-0.008 ± 0.006	0.060 ± 0.006	0.040 ± 0.006	-0.036 ± 0.001	0.026 ± 0.002	-0.067 ± 0.002
1.06	-0.005 ± 0.004	0.064 ± 0.007	0.045 ± 0.004	-0.033 ± 0.001	0.026 ± 0.001	-0.070 ± 0.002
1.08	-0.005 ± 0.005	0.066 ± 0.007	0.050 ± 0.005	-0.032 ± 0.002	0.030 ± 0.002	-0.070 ± 0.002
1.10	-0.006 ± 0.008	0.067 ± 0.008	0.050 ± 0.005	-0.032 ± 0.002	0.031 ± 0.002	-0.071 ± 0.003
1.12	-0.005 ± 0.008	0.063 ± 0.006	0.050 ± 0.006	-0.031 ± 0.001	0.031 ± 0.001	-0.072 ± 0.002
1.14	-0.011 ± 0.007	0.060 ± 0.005	0.040 ± 0.007	-0.031 ± 0.001	0.032 ± 0.001	-0.071 ± 0.002
1.16	-0.005 ± 0.008	0.063 ± 0.008	0.041 ± 0.007	-0.031 ± 0.002	0.032 ± 0.001	-0.071 ± 0.003
1.18	-0.002 ± 0.006	0.062 ± 0.006	0.035 ± 0.007	-0.030 ± 0.002	0.034 ± 0.001	-0.071 ± 0.004
1.20	-0.003 ± 0.006	0.065 ± 0.005	0.037 ± 0.007	-0.030 ± 0.002	0.037 ± 0.001	-0.073 ± 0.004
1.22	-0.003 ± 0.006	0.067 ± 0.005	0.036 ± 0.004	-0.030 ± 0.002	0.038 ± 0.002	-0.073 ± 0.002
1.24	-0.005 ± 0.007	0.069 ± 0.005	0.038 ± 0.004	-0.031 ± 0.003	0.043 ± 0.002	-0.074 ± 0.002
1.26	-0.004 ± 0.007	0.069 ± 0.005	0.037 ± 0.006	-0.030 ± 0.002	0.046 ± 0.004	-0.073 ± 0.002
1.28	0.003 ± 0.008	0.073 ± 0.005	0.042 ± 0.005	-0.032 ± 0.002	0.044 ± 0.004	-0.073 ± 0.002
1.30	0.006 ± 0.008	0.073 ± 0.005	0.046 ± 0.005	-0.032 ± 0.002	0.047 ± 0.004	-0.073 ± 0.002
1.32	0.015 ± 0.008	0.085 ± 0.006	0.048 ± 0.005	-0.030 ± 0.002	0.048 ± 0.003	-0.073 ± 0.002
1.34	0.019 ± 0.013	0.098 ± 0.011	0.053 ± 0.011	-0.029 ± 0.003	0.046 ± 0.003	-0.073 ± 0.002
1.36	0.019 ± 0.011	0.098 ± 0.010	0.053 ± 0.009	-0.029 ± 0.003	0.046 ± 0.002	-0.073 ± 0.002
1.38	0.019 ± 0.011	0.098 ± 0.010	0.053 ± 0.009	-0.029 ± 0.003	0.046 ± 0.002	-0.073 ± 0.002

Note. Empirically determined *WISE* versus $B_T - V_T$ photospheric color–color trends for all six *WISE* colors obtained from the parent sample as described in Section 2.5 and shown in Figure 3.

We apply these corrected $W_{ij}(B_T - V_T)$ relations to our analysis, and find that six stars drop slightly below the formal excess thresholds: HIP 6490, HIP 8987, HIP 47792, HIP 66257, HIP 82887, and HIP 105891. However, we find 13 additional excesses. Six of these have 10–30 μm excesses reported in the literature: HIP 2072, HIP 12198, HIP 21091, HIP 42438, HIP 92024, HIP 115527. The remaining seven are new detections: HIP 2852, HIP 18837, HIP 20094, HIP 39947, HIP 50191, HIP 66322, HIP 110365. These 13 stars are not included in the final tally in this paper here but will be discussed in a later study.

In addition, there were several minor numerical inconsistencies in the counting statistics in the abstract, Section 5, and conclusion of the paper. The total number of excesses detected is 214, not 220. The total number of new excesses never previously reported at any wavelength is 106, not 108. Among the 214 detections, 108 have previously reported mid to far-IR excess emission instead of the stated 114. An additional 10 out of the 214 detections are for the first time found to possess 10–30 μm excesses, although they were already known to have excess emission at longer wavelengths. Therefore, the total number of new 10–30 μm disk identifications is $106 + 10 = 116$, instead of $108 + 10 = 118$.

The overall scientific conclusions in the original manuscript are unaffected by any changes reported here.

The Astrophysical Journal Supplement Series, 220:21 (1pp), 2015 September doi:10.1088/0067-0049/220/1/21

ERRATUM 2: "A SENSITIVE IDENTIFICATION OF WARM DEBRIS DISKS IN THE SOLAR NEIGHBORHOOD THROUGH PRECISE CALIBRATION OF SATURATED *WISE* PHOTOMETRY" (2014, ApJS, 212, 10)

Rahul I. Patel[1], Stanimir A. Metchev[1,2,3], and Aren Heinze[1]
[1] Department of Physics & Astronomy, Stony Brook University, 100 Nicolls Road, Stony Brook, New York 11794–3800
[2] Department of Physics & Astronomy, The University of Western Ontario, 1151 Richmond Street, London, Ontario, N6A 3K7, Canada
[3] Centre for Planetary Science and Exploration, 1151 Richmond Street, London, Ontario, N6A 5B8, Canada
Received 2015 July 26; accepted 2015 July 28; published 2015 September 28

Five stars were erroneously identified as infrared excess sources at 12 μm and 22 μm. The new excess associated with HIP 85523 was overestimated because its $B_T - V_T$ color was corrected according to empirical tables based on its *Hipparcos* spectral type of K7. Multiple references however have confirmed its spectral type to be M2.5/3 V (e.g., Riaz et al. 2006; Cushing et al. 2006; Torres et al. 2006). Therefore our photospheric color was underestimated, and the excess was overestimated. The *W*4 photometry for HIP 69281 is likely contaminated by nearby projected companions with a similar assessment provided by Wu et al. (2013). HIP 32435 is likely contaminated by a star ~15″ away and a galaxy that is 25″ away, as noted by Donaldson et al. (2012). HIP 106914 might be a false-positive star based on MIPS 24 μm measurements reported in Moór et al. (2011), and the presence of a bright nearby source seen in MIPS 70 μm images. HIP 69682 was reported to have an excess at 60 μm by Rhee et al. (2007), and identified by us as a *W*4 excess. However, the presence of a red companion 21.″4 from the primary is likely responsible for the 60 μm excess, as the two would be blended in the 60″ IRAS beam. We remove HIP 69682 from our list of excesses as the PSF tail of the red companion is also most likely responsible for the *W*4 excess flux of HIP 69682.

The above reduction brings the total number of detected excesses to 209 instead of 214, and the total number of new 10–30 μm excesses to 113 instead of 116. Our tally of new excesses constitutes a 25% increase in the census of debris disks within 75 pc and a 35% increase of debris disks with 10–30 μm excesses within this volume.

In Section 4.4, we discuss the state of circumbinary dust in 26 binary systems. Several of these systems were erroneously identified as binary systems. We have removed HIP 544, HIP 1481, HIP 2472, HIP 61960, HIP 95261, and HIP 115738 from our list of binaries. In addition, we have revised Table 8, the entries in which were inadvertently scrambled during submission. The new Table 8 reflects the true characteristics of these binary excess hosts.

The overall scientific conclusions in the original manuscript are unaffected by the changes reported here.

Table 8
Excesses Detected in Binary Systems

Star	Dist. (pc)	Binary Separation (")	Binary Separation (AU)	Dust Radius (AU)	Dust State[a]
HIP4016	61	40.0	2456	3.4	cs
HIP6679	49	132.9	6512	4.3	cs
HIP7576	24	612.0	14688	2.4	cs
HIP9141	41	0.2	6	1.5	cs
HIP9902	44	52.4	2316	2.9	cs
HIP11477	47	391.2	18230	32.8	cs
HIP12489	71	29.0	2059	8.2	cs
HIP13209	51	0.3	15	13.9	cs
HIP16908	40	0.8	32	0.7	cs
HIP21547	29	66.7	1961	5.5	cs
HIP22394	50	SB	…	5.9	cb
HIP25183	72	17.2	1232	4.2	cs
HIP65728	71	181.7	12973	11.1	cs
HIP69281	61	12.6	762	2.7	cs
HIP82587	29	74.7	2181	2.8	cs
HIP94184	53	50.5	2697	6.3	cs
HIP95261	48	4.2	202	10.6	cs
HIP102655	54	391.4	21057	2.7	cs
HIP105388	43	13.6	585	10.2	cs
HIP113477	41	21.6	886	1.1	cs

Notes. Science sample stars with debris disks in known binary systems. The binary separation was calculated using the parallactic distance and angular separations from the Washington Double Star Catalog.
[a] Orbital state of the dust: "cs" means the dust is in a circumstellar location around the primary star, "cb" means the dust is in a circumbinary configuration

REFERENCES

Cushing, M. C., Roellig, T. L., Marley, M. S., et al. 2006, ApJ, 648, 614
Donaldson, J. K., Roberge, A., Chen, C. H., et al. 2012, ApJ, 753, 147
Moór, A., Pascucci, I., Kóspál, Á., et al. 2011, ApJS, 193, 4
Rhee, J. H., Song, I., Zuckerman, B., & McElwain, M. 2007, ApJ, 660, 1556
Riaz, B., Gizis, J. E., & Harvin, J. 2006, AJ, 132, 866
Torres, C. A. O., Quast, G. R., da Silva, L., et al. 2006, A&A, 460, 695
Wu, C.-J., Wu, H., Lam, M.-I., et al. 2013, ApJS, 208, 29

Chapter 4

Improved Methods to Verify *WISE* Debris Disks With Weighted Colors and unWISE Images

The work presented in this chapter is to be submitted to the Astrophysical Journal. This study is the second in a series of three, and was done in collaboration with Dr. Stanimir Metchev, Dr. Aren Heinze, and Joseph Trollo, where I will be the primary author.

4.1 Introduction

Dust orbiting within several tens of AU around main sequence stars is unstable: the combination of radiative and gravitational effects eliminate it on timescales of a hundred to a few million years. The presence of such dust implies its continual generation by collisions among larger bodies (e.g., asteroids or comets) that may be dynamically stirred by unseen planets. Identifying stars with dusty disks helps us probe the diversity of planetary system architectures and choose targets for future planet-imaging campaigns.

Main sequence stars with debris disks are typically identified first by their infrared (IR) dust excesses: their IR fluxes at $\lambda \gtrsim 5\mu$m are significantly higher than would be expected from photospheric emission alone. A debris disk can be detected by fitting a photospheric model to the shorter-wavelength (visible and near-IR) photometry, and subtracting the fitted photosphere to check for a $\gtrsim 5\mu$m excess. A large number of stars with IR excesses have been found this way, using data from *IRAS* (e.g., Moór et al., 2006; Rhee et al.,

2007; Zuckerman, 2001, and references therein), Spitzer (e.g., Su et al., 2006; Bryden et al., 2006; Trilling et al., 2008; Carpenter et al., 2009a), AKARI (e.g., Fujiwara et al., 2013), and *WISE* (e.g., Cruz-Saenz de Miera et al., 2014; McDonald et al., 2012).

A limitation of this approach is the normalization of the underlying stellar photosphere. Flux comparisons across wide wavelength ranges—optical/near-IR for the photosphere and mid-IR for the excess—can be uncertain by several per cent. The combination of photometric data from different surveys (e.g., Tycho–2, SDSS, 2MASS, *WISE*, *IRAS*) incorporates often unknown systematic uncertainties in the photometric calibration of the survey filters. Any stellar variability between the various epochs of the observations also adds an unknown contribution. Thus, while the systematic color uncertainties of photospheric models are generally very small, the accurate normalization of the model in the mid-IR can be uncertain by a few per cent. Adding to these factors other potential data systematics, most common of which can be uncertainties in the mid-IR filter profiles and the corresponding color corrections, the precision of mid-IR excess determination is generally limited to 10% (1 σ).

Notable exceptions are the Spitzer/IRS surveys of Carpenter et al. (2009a), Lawler et al. (2009), and Dodson-Robinson et al. (2011), who demonstrate that the IRS has been the most sensitive instrument ever for detecting 10–40μm photometric excesses from debris disks, with nearly twice as many detections as MIPS at 24μm. The advantage of the IRS lies in the ability to locally calibrate the stellar photospheric model over a spectral range that is close to the excess wavelengths, and in the fact that the entire 5–40μm spectrum can be obtained nearly simultaneously.

With its better sensitivity than *IRAS*, a wavelength range that samples both the 3–5μm stellar photosphere and potential 10–30μm excesses simultaneously, and with the advantage of full-sky coverage over *Spitzer*, *WISE* (Wright et al., 2010) presents an opportunity to find unprecedentedly faint mid-IR excesses over the entire sky. In particular, greatest sensitivity to faint mid-IR excesses is obtained by analyzing the distributions of stellar colors formed from combinations of short- and long-wavelength *WISE* bands: e.g., $W1 - W3$ or $W2 - W4$.

For the reasons detailed above, using broader-wavelength coverage to fit stellar photospheric models can introduce contaminants. During this post-processing phase of the analysis, contaminants can arise from an inaccurate estimate of the photospheric emission. This usually occurs when determining the photospheric flux by photospheric modelling. The fitting approach is limited in that it can be affected by non-simultaneity of the various photometric observations and by discrepancies among the zero-points of the various photo-

metric systems. This problem is avoided when all of the data used to estimate the photospheric and the excess emission are measured concurrently. But for most bright stars there is no contemporaneous, precise photometry that spans a wide enough range in wavelength to produce a well-constrained photospheric fit. Contaminants introduced during the acquisition phase, in contrast, can arise from a number of astrophysical and instrumental sources: imaging artifacts (ghosts, halos, etc.), large patches of non-uniformly distributed infrared cirrus, scattered light from the Moon, closely separated projected extragalactic sources, projected optical companions blended into the *WISE* beam, and undiscovered Active Galactic Nuclei or Luminous Infrared Galaxies.

There are, however, methods to address contaminants introduced at both phases. For instance, the photospheric emission can be calibrated empirically, rather than using a model fit that will introduce additional post-processing contamination. This approach has been applied successfully to the *WISE* data: Rizzuto et al. (2012) used it to search for excesses around Sco-Cen stars based on their $W1 - W3$ and $W1 - W4$ colors from the *WISE* Preliminary Release Data Release[1] and Theissen & West (2014) applied a similar approach to search for excesses around M dwarfs using the Sloan Digital Sky Survey Data Release 7 and the AllWISE Data Release[2]. In Patel et al. (2014a, henceforth as PMH14), we used the *WISE* All-Sky Survey Data Release[3] and the *Hipparcos* catalog (Perryman et al., 1997) to determine the frequency of debris disk hosts stars within 75 pc of the Sun. To reduce contaminants accumulated from the acquisition phase, one can take advantage of survey meta-data to place filters or use crowd-sourced citizen science tools[4] to remove contaminated stars.

In PMH14, we identified stars with infrared excesses in the $W3$ and $W4$ bands by first filtering out 15 major sources of contaminants, seeking anomalously red *WISE* colors ($W1-W3, W2-W3, W1-W4$, $W2-W4$ or $W3-W4$) compared to the mean photospheric values for stars with the same Tycho $B_T - V_T$ colors, and finally removing any contaminated excess by checking their *WISE* images for background IR cirrus. We evaluated the statistical distributions of each of these *WISE* colors independently. This approach was effective, and had the advantage of not excluding stars without valid measurements in some of the *WISE* bands: for example, if $W1$ was excessively saturated, a star could still be determined to have an excess based on its $W2 - W4$ or $W3 - W4$ color. However, where valid measurements exist for all *WISE* bands – the majority of cases – an optimally weighted combination of colors should have lower noise and potentially deliver greater sensitivity to

[1] `http://wise2.ipac.caltech.edu/docs/release/prelim/`

[2] `http://wise2.ipac.caltech.edu/docs/release/allwise/`

[3] `http://wise2.ipac.caltech.edu/docs/release/allsky/`

[4] Check out `http://www.diskdetective.org/`

faint excesses.

In this study we seek to identify high-fidelity faint IR excesses around main sequence *Hipparcos* stars within 75 pc by 1) using the combined weight of multiple *WISE* colors to assess a star's $W3$ or $W4$ excess, and 2) by rejecting excesses that may be contaminated from unrelated IR sources at small angular separations from our stars. We motivate the selection of our sample of stars in Section 4.2. In Section 4.3, we describe techniques for improved accuracy in the confidence threshold determination and for seeking IR excesses using weighted combinations of *WISE* colors. In Section 4.4, we describe and apply our method for rejecting contaminated sources based on their relative positional offsets. We use these techniques to confirm previously discovered IR excesses and to find new ones. We summarize the results of the excesses we have newly identified, verified and rejected in Section 4.5. In Section 4.6, we discuss our interpretation of the weighted color excess search results and compare them to the single-color approach in *WISE*.

4.2 Sample Definition

Our sample consists of main-sequence *Hipparcos* stars with reliable *WISE* All-Sky Catalog photometry in all four *WISE* bands. The details of the selection process are outlined in PMH14. In short, we first created a parent sample of *Hipparcos* stars within 120 pc, outside the galactic plane ($|b| > 5^\circ$), and constrained to the -0.17 mag $< B_T - V_T < 1.4$ mag *Tycho* color range. We performed additional automated screening to ensure photometric quality, consistency, and minimal contamination. We then corrected saturated photometry in the $W1$ and $W2$ bands using relations derived in PMH14. Unlike in PMH14, however, we included only stars that had valid photometry in $W1$, $W2$ and $W3$ bands when seeking weighted $W3$ excesses and valid photometry in all four bands when seeking weighted $W4$ excesses.

The parent (120 pc) sample provides us with a large population of stars to calibrate the photospheric *WISE* colors as a function of $B_T - V_T$ (PMH14; Patel et al., 2014b). These stars are mostly within the Local Bubble (Lallement et al., 2003), and have little line-of-sight interstellar extinction ($A_V <$ 0.05 mag). The science sample is a 75 pc sub-sample of the parent sample, whose stars stars have accurate parallaxes. As in PMH14, we only report and analyze detections of IR excesses from stars in the science sample. However we iterate on the excess selection and contamination checking approaches for better detection sensitivity and fidelity.

4.3 Single-Color and Weighted Color Excesses

4.3.1 Improved Detection of Single-Color Excesses

We identify single-color *WISE* excesses based on the significance of their color excess as defined in Equation 2 of PMH14

$$\Sigma_{E[Wi-Wj]} = \frac{Wi - Wj - W_{ij}(B_T - V_T)}{\sigma_{ij}}, \tag{4.1}$$

where the numerator determines the excess in the measured $Wi - Wj$ color by subtracting the mean $Wi - Wj$ color of the photosphere. We denote the photospheric $Wi - Wj$ color by $W_{ij}(B_T - V_T)$, as it is a function of the optical $B_T - V_T$ color of the star. We use the tabulated photospheric $W_{ij}(B_T - V_T)$ relations for $-0.17\text{mag} < B_T - V_T < 1.4$ mag from Patel et al. (2014b). Throughout the rest of this paper, the significance of a single-color excess is denoted with Σ_E.

The single-color *WISE* excesses are selected by seeking stars with Σ_E values above a certain confidence threshold. We denote the Σ_E value at the confidence threshold CL as $\Sigma_{E_{CL}}$: CL=98% at $W3$ and CL=99.5% at $W4$. In PMH14 we used the excess and the uncertainty distributions as a function of Σ_E to determine the values $\Sigma_{E_{CL}}$ for the various colors. Given a set false-discovery rate (FDR), and that CL = 1−FDR, we seek the value of Σ_E, where the FDR drops below 2% for $W3$ excesses, or below 0.5% for $W4$ excesses[5]. The FDR can be determined directly from the ratio of the counts of stars in the uncertainty and excess distributions. To form the uncertainty distribution for a given color, we assume that the effect of random errors on Σ_E is symmetric with respect to $\Sigma_E = 0$. The various Σ_E distributions do indeed peak close to zero (PMH14), which supports this supposition. We hence assume that the negative sides of the Σ_E distributions are representative of the negative halves of the uncertainty distributions, and so we mirror the negative Σ_E values around the distribution peaks to obtain the full uncertainty distributions. The shapes of the combined uncertainty distributions are consistent with a Gaussian of standard deviation ~ 1, as we might expect in the absence of unknown systematics when we have weighted each color measurement by its error. This indicates that our analysis is not limited by residual calibration systematics. We show an illustration of the above method in Figure 4.1, albeit not for the single-color excess Σ_E metrics discussed here and in PMH14, but for the weighted color $\Sigma_{\overline{E}}$ metrics introduced in Section 4.3.2.

[5]in PMH14, we incorrectly called the FDR the false-positive rate. See Figure 4 in Wahhaj et al. (2015), which illustrates the difference between the two terms.

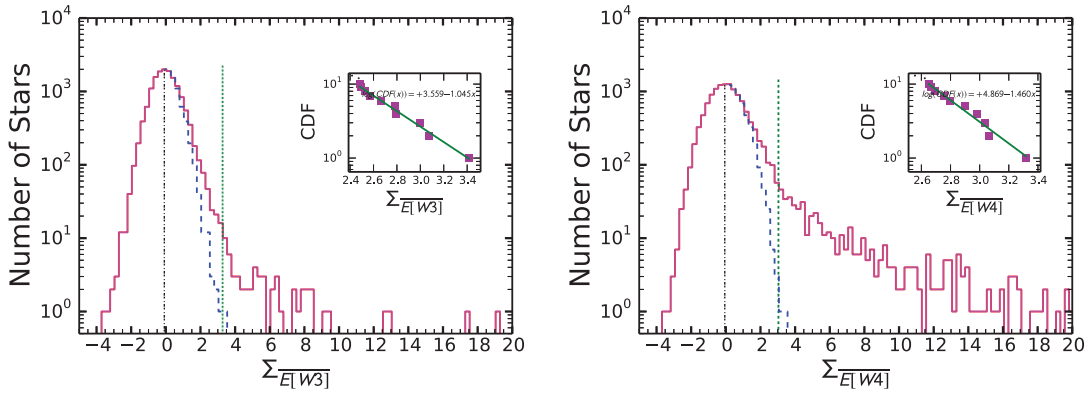

Figure 4.1: Distributions of the weighted excess metrics, $\Sigma_{\overline{E[W3]}}$ (left) and $\Sigma_{\overline{E[W4]}}$ (right) for all stars in our parent sample. We have assumed that the negative portion of each $\Sigma_{\overline{E}}$ distribution is representative of the intrinsic random and systematic noise in the data (Section 4.3.1). The mode of the full distribution is shown by a vertical black dashed-dot line. A reflection (dashed histogram) of the negative portion of the $\Sigma_{\overline{E}}$ histogram around the mode is thus representative of the false positive excess expectation. We define the FDR at a given $\Sigma_{\overline{E}}$ as the ratio of the cumulative numbers of $>\Sigma_{\overline{E}}$ excesses in the positive tails of the dashed and solid histograms. The vertical dotted lines indicate the FDR thresholds for each weighted Wj excess, 2% for $W3$ and 0.5% for $W4$, above which we identify all stars as probable debris disk hosts. Each inset shows a log-log fit of a line to the last ten points in the reverse cumulative distribution function of the uncertainties (see Section 4.3.1). Assuming exponential behavior in the tail of the uncertainty distribution, this fit smoothes over the stochasticity in this sparsely populated region of the uncertainty distribution to attain a more accurate estimate of the FDR threshold.

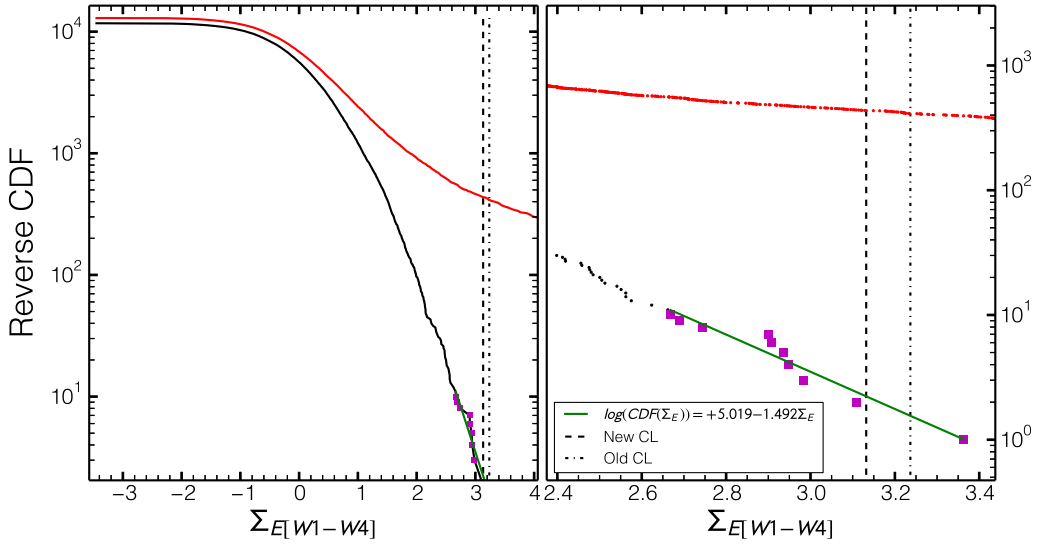

Figure 4.2: A reverse cumulative distribution function (rCDF, Section 4.3.1) of the uncertainty (black) and excess (red) distributions of $\Sigma_{E[W1-W4]}$. We use the rCDF to estimate the FDR at any Σ_E: as the ratio of the black and red rCDFs. The vertical dash-dotted line shows the more conservative $\Sigma_{E_{99.5}}$ estimate of the confidence threshold from PMH14, set half-way between the last two points. The vertical dashed line shows the present, more accurate, $\Sigma_{E_{99.5}}$ estimate, based on a fit (solid green line) to the last ten data points in the tail of the rCDF (magenta squares). The left panel shows the full rCDFs, while the right panel zooms in near the $\Sigma_{E_{CL}}$ threshold.

The empirical estimate of the FDR described above and adopted in PMH14 offers a straightforward method to assess the reliability of candidate excesses. However, the exact value of the $\Sigma_{E_{CL}}$ threshold tends to rely only on the one or two most-outlying stars in the (negative wing of the) Σ_E distribution (Figure 4.1), and so is uncertain. In PMH14 we purposefully overestimated $\Sigma_{E_{CL}}$ by the half distance to the star prior to the one that satisfied the FDR threshold. Our estimate of the $\Sigma_{E_{CL}}$ was conservative, not very accurate, and may have excluded potentially significant excesses.

Here we iterate on this approach by taking advantage of the near-Gaussian behavior of each uncertainty distribution. To circumvent the small-number sampling in the tail, we average the functional behavior by fitting an exponential curve to the last ten points in the rCDF of the uncertainty distribution (Figure 4.2). This continuous form of the tail of the uncertainty distribution enables a more accurate estimate of the FDR.

We used the improved confidence threshold determination procedure to search for additional single-color excesses using the same set of stars and colors ($W1-W4$, $W2-W4$, $W3-W4$, $W1-W3$ and $W2-W3$) as in PMH14. $W3$ and $W4$ excesses were again identified at the 98% and 99.5% confidence levels, respectively. In addition to the excesses already identified in PMH14, we found 39 additional single-color excess candidates. After inspecting and removing stars that seemed to be contaminated by background cirrus emission, we were left with 27 single-color excess candidates, 19 of which do not have IR excess detections reported in the literature. Of these 19, 18 are newly detected single-color excesses at $W4$, and one has a significant single-color excess only at $W3$, with a marginal excess at $W4$. The excess detection statistics are summarized in Table 4.1. The newly detected excesses and their significances are listed individually in Table 4.2.

4.3.2 Defining A New Weighted IR Excess Metric

In PMH14 and Section 4.3.1, we identified debris disk-host candidates by selecting stars with individual anomalously red *WISE* $Wi-Wj$ colors, where $i=1,2,3$, $j=3,4$, and $i<j$. However, it may be possible to attain more reliable excess detections at Wj by combining all relevant $Wi-Wj$ colors. Herein we define this new "weighted excess" Wj metric.

As in Equation 4.1, we first remove the contribution from the photospheric emission. Thus the single-color excess is:

$$E[Wi-Wj] = Wi - Wj - W_{ij}(B_T - V_T). \tag{4.2}$$

Since we want to use the strength of all possible *WISE* color combinations for band Wj, we constructed the weighted average of the color excesses as

$$\overline{E[Wj]} = \frac{1}{A}\sum_{i=1}^{j-1}\frac{E[Wi-Wj]}{{\sigma_{Wi}}^2}, \tag{4.3}$$

where σ_{Wi} is the photometric uncertainity of Wi and $j \in [3,4]$. Here, $A = \sum_{i=1}^{j-1}\frac{1}{\sigma_i^2}$ is a normalization constant. Our definition for the significance $\left(\Sigma_{\overline{E[Wj]}}\right)$ of the weighted excess at Wj is the ratio of the weighted average of all color excesses (Equation 4.3) to the uncertainty in the weighted average ($\sigma_{\overline{E[Wj]}}$):

$$\Sigma_{\overline{E[Wj]}} = \overline{E[Wj]}/\sigma_{\overline{E[Wj]}} \quad (4.4)$$

$$= \frac{\frac{1}{A}\sum_{i=1}^{j-1}\frac{E[Wi-Wj]}{\sigma_i^2}}{\sqrt{\sigma_j^2 + 1/A}}. \quad (4.5)$$

The full derivation of this metric can be found in Appendix C.1. We use $\Sigma_{\overline{E}}$ through the rest of the paper as shorthand for the significance of the weighted excess for either $W3$ or $W4$, as appropriate, and Σ_E as shorthand for the significance of the single-color excess when the discussion does not refer to any specific color.

4.3.3 Weighted Color Excesses

We extend the same procedure used to identify stars with single-color excesses in Section 4.3.1 to search for optimally weighted excesses in $W3$ or $W4$ using Equation 4.4. When discussing weighted excesses, we denote the confidence threshold as $\Sigma_{\overline{E_{CL}}}$. In Figure 4.1, we plot the $\Sigma_{\overline{E}}$ distributions as solid red histograms for both $W3$ and $W4$. The positive wings of the uncertainty distributions, defined analogously to those for the single-color uncertainty distributions, are shown as dashed blue histograms. The $\Sigma_{\overline{E_{CL}}}$ threshold is shown as the vertical dotted green line. We claim that a star has a significant weighted excess if its $\Sigma_{\overline{E}} \geq \Sigma_{\overline{E_{CL}}}$.

We identify 6 stars with 98% significant weighted $W3$ excesses within 75 pc of the Sun, among which we expect $2\% \times 6 = 0.12$ to be false positives. We identify 184 stars with 99.5% significant weighted $W4$ excesses within 75 pc of the Sun, among which we expect $0.5\% \times 184 = 0.92$ to be false positives. However, these FDRs do not account for spurious excesses caused by contamination from IR cirrus or unresolved binary companions. Hence, we checked the four-band *WISE* images for this type of contamination for all of our detections. We removed 11 of the 184 weighted $W4$ excess sources that were deemed to be contaminated. Ten of these 11 have single-color excess detections, which we rejected as debris disk candidates in PMH14. The other one, HIP 111136, is a new candidate; however, its $W4$ images reveal line-of-sight IR cirrus contamination, for which we reject this stars. All 11 rejected sources are listed in Table 4.3. We were then left with 173 $W4$ excess stars. None of our weighted $W3$ excesses seem to be contaminated based on their *WISE* images. A summary of these detections can be found in Tables 4.1 and 4.2.

4.4 Automated Rejection of Contaminated Stars Using Reprocessed WISE Images

WISE offers higher angular resolution than IRAS. However, source photometry it is still prone to contamination by unrelated astrophysical sources seen in projection. Possible contaminants may include nearby point sources, at angular separations comparable to the *WISE* $W3$ and $W4$ PSFs. Even if the All-Sky Catalogue provides resolved photometry for such objects, the deblending algorithm may introduce systematic offsets in the flux that are not characteristic of isolated point sources. Other possible contamination can be caused by nearby extended emission: e.g., from interstellar cirrus or from the PSF wings of a nearby bright source. We expect that both types of contamination may manifest themselves in discrepant source positions: either between the $W3$ and $W4$ images, or among $W4$ positional measurements that use different centering region sizes.

The All-Sky and the AllWISE Catalogues do not list individual positions in each of the filters. Therefore, we downloaded individual $W3$ and $W4$-band images for all stars in our parent sample. As we describe below, we also used the higher angular resolution raw WISE images, rather than the smoothed ones accessible directly from the WISE All-Sky or AllWISE Data Releases.

4.4.1 Checking for Contaminants In unWISE Images

Instead of using the All-Sky Atlas images, we used the higher angular resolution unWISE images, which can be retrieved from the unWISE image service[6] (Lang, 2014). Images from the All-Sky and AllWISE catalog were created by stacking individual exposures and then convolving each stack with a model of the detector's point-spread function (PSF). By not including this last step to create the unWISE images, Lang (2014) preserves the nominal resolution of the original stacked images. Hence, the unWISE PSF is a factor of $\sqrt{2}$ narrower than for the All-Sky Catalog images ($6''$ for $W1$, $W2$, and $W3$ and $12''$ for $W4$). We downloaded $150'' \times 150''$ $W3$ and $W4$ images from the unWISE website for all of our excess stars, each centered on the stellar coordinates at the mean *WISE* observational epoch. We also downloaded images for the vast majority of our 16960 parent (120 pc) sample stars. These stars are the union of all the stars that comprised the parent samples for the five different color excess searches in PMH14: $W1 - W3$, $W2 - W3$, $W1 - W4$, $W2 - W4$, and $W3 - W4$. This amalgamated sample will be used as a statistical basis for

[6] `http://unwise.me`

determining significant outliers amongst our excesses based on their relative positional offsets.

We use the unWISE $W3$ and $W4$ images of the parent sample stars to test for astrometric contamination by line-of-sight neighbors. We hypothesized that point-source contaminants can be identified through large relative positional offsets between the centroids of the $W3$ and $W4$-band unWISE images. Thus, for all our stars, we extracted centroid positions for our $W3$ and $W4$ images ($\vec{r}_{W3}$ and $\vec{r}_{W4}$ respectively). The vectors $\vec{r}_{W3}$ and $\vec{r}_{W4}$ were calculated using Gaussian centroiding in a 3.06 pixel radius aperture using a Gaussian of $\sigma = 1.02$ pixels. This value of σ was chosen to yield a full width at half maximum (FWHM) of 2.4 pixels, thus matching the FWHM of the $W3$ images. We also hypothesized that extended source contaminants could be identified by comparing the $W4$ centroid calculated in an $r = 3.06$ pixel aperture to a $W4$ centroid calculated in a wider $r = 10$ pixel aperture. The $W4$ centroid calculated using the wide aperture radius is denoted as $\vec{r}_{W4,wide}$. The 10 pixel radius ($\sim 25''$) extends to roughly twice the FWHM of the $W4$ PSF, and incorporates the radial distance of the first Airy ring. This ensures that any flux from the wings of the PSF from a nearby source will be flagged as a contamination source.

The density clouds in Figures 4.3 and 4.4 show the distributions of our stars' $W4$ SNRs as a function of the $W3$ to $W4$ relative centroid offsets ($\Delta r_{W3,W4} = |\vec{r}_{W3} - \vec{r}_{W4}|$) as well as a function of the $W4$ to wide-$W4$ centroid offsets ($\Delta r_{W4} = |\vec{r}_{W4} - \vec{r}_{W4,wide}|$). Contaminated stars will therefore be located at larger separations compared to the majority of the (uncontaminated) stars that populate the cores of the centroid offset distributions.

4.4.2 Rejecting Astrometric Contaminants

We aimed to find the separation threshold beyond which stars can be considered contaminated. Since the spread of separations varies as a function of $W4$ SNR, we performed this analysis using logarithmically spaced bins in $W4$ SNR space. Assuming that the core of the j^{th} SNR bin was normally distributed, we defined the maximum allowed separation in each bin $\Delta r_{j,max}$ such that

$$\Delta r_{j,max} = 3\sigma_j, \tag{4.6}$$

where σ_j is the standard deviation of the azimuthally symmetric 2D Gaussian Δx vs. Δy distribution in the j^{th} $W4$ SNR bin (i.e., $\sigma_j = \sigma_{\Delta x} = \sigma_{\Delta y}$). To calculate σ_j, we assumed first that the Δx and Δy offsets (used to create Δr) are distributed as a circular 2-dimensional Gaussian. A fit to this multi-variate

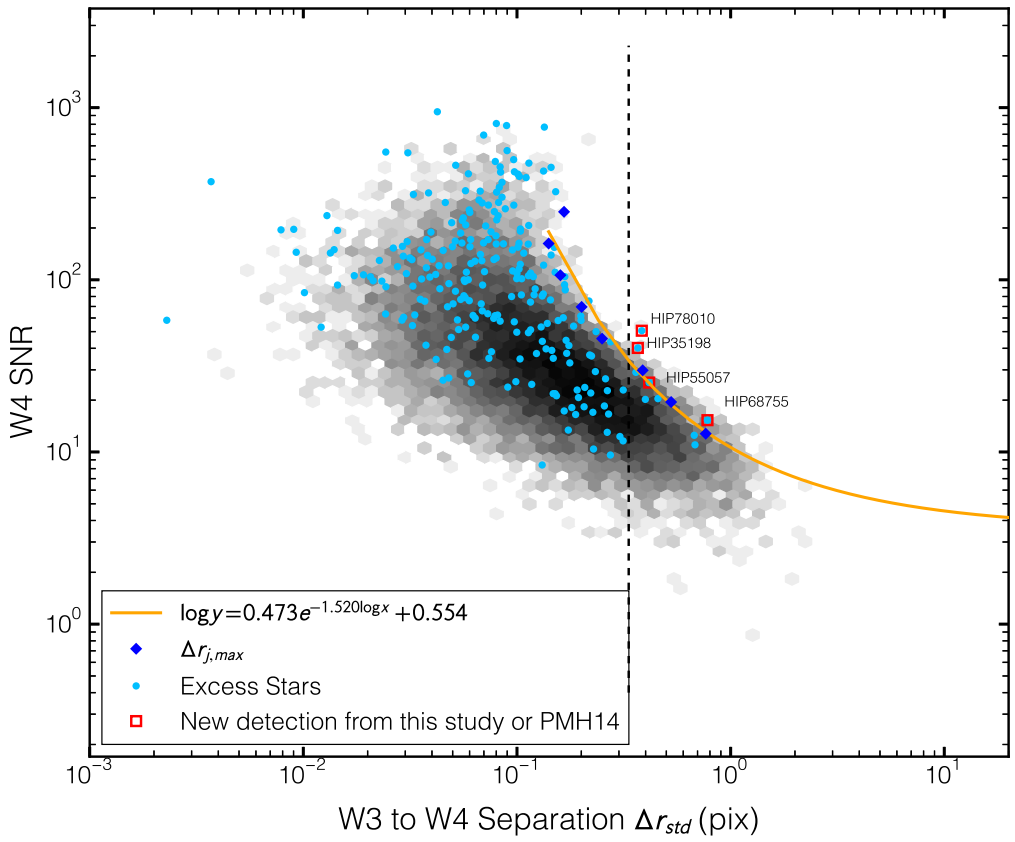

Figure 4.3: Distribution of relative positional offsets of stellar centroids between $W3$ and $W4$ using images from the unWISE image service, plotted with respect to the $W4$ SNR calculated from the unWISE images. The black/gray density cloud represents the density of 16927 Hipparcos stars from the parent 120 pc sample, while the light-blue dots show the locations of our excess stars. The black-dotted line represents our separation cut-off (1/3 pixels) below which stars are not rejected. Our rejection threshold (solid orange line) was fit to $\{\Delta r_{j,max}\}$ (dark-blue diamonds), calculated as described in Section 4.4.2. Stars to the right of the vertical dotted black line and above the orange line (red squares) are deemed to be contaminated by an unrelated nearby point or extended source. The contaminated objects include four candidate debris disk excesses identified in this study or in PMH14.

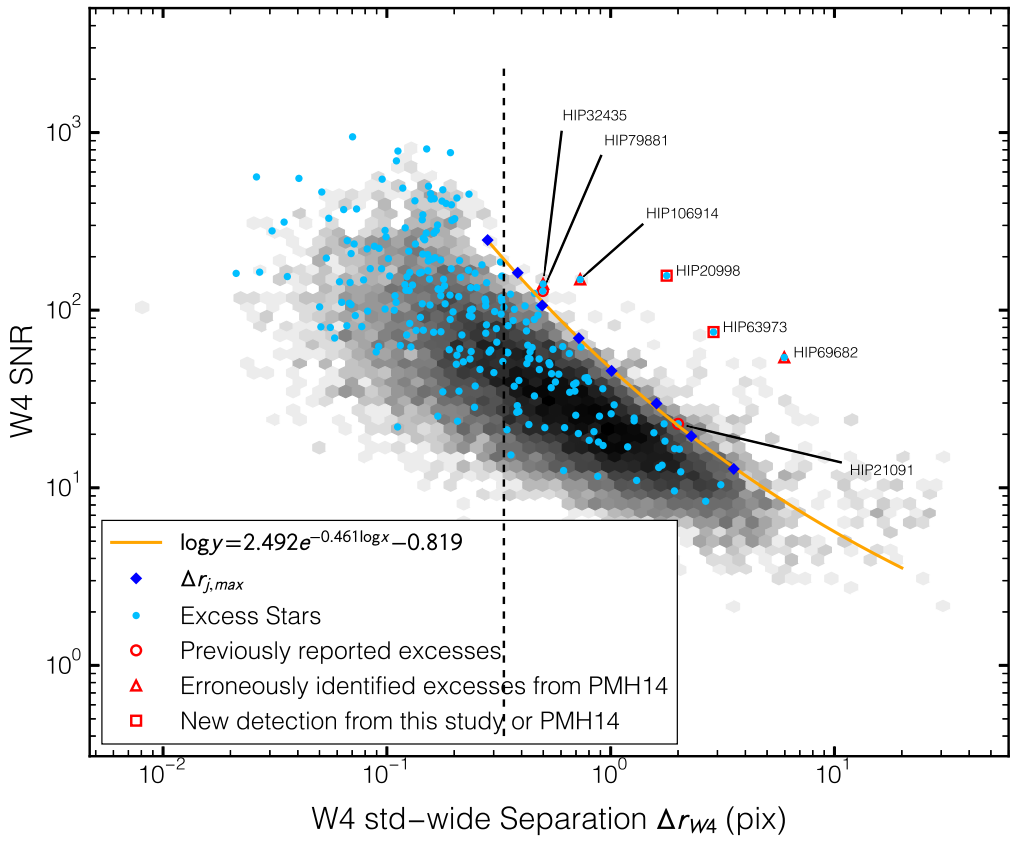

Figure 4.4: Distribution of relative positional offsets of stellar centroids between a narrow 2.5 pixel radius and wide 10 pixel radius apertures, as described in Section 4.4.1. The plot elements are the same as those described in Figure 4.3. Stars to the right of the vertical dotted black line and above the orange line (red squares, circles, and triangles) are deemed to be contaminated by an unrelated nearby point or extended source.

Gaussian would then yield σ_j.

According to the WISE Explanatory Supplement, however, the major and minor axes of the WISE PSF differ: FWHMs of 7.4″ and 6.1″ for the major and minor axes for $W3$, and 12.0″ and 11.7″ for $W4$. Therefore, the morphologies of the 2-D Δx vs. Δy distributions are also elliptical. To simplify calculations, we opted to circularize the elliptically distributed data: by scaling the major axis by the ratio of the standard deviations along the minor to major-axes of the Δx vs. Δy distributions.
We then fit a circular 2-D Gaussian to a 2σ-clipped portion of the circularized data to obtain the standard deviations of the sample in Δx ($\sigma_{\Delta x}$) and Δy ($\sigma_{\Delta y}$). This central part of the offset distribution was expected to be representative of the random positional scatter among point source coordinates for sources that were not contaminated. Since $\sigma_{\Delta x} = \sigma_{\Delta y}$, the final form of the Gaussian has only radial dependence, such that:

$$\exp\left[-\left(\frac{\Delta x^2}{2\sigma_{\Delta x}^2} + \frac{\Delta y^2}{2\sigma_{\Delta y}^2}\right)\right] = \exp\frac{\Delta r^2}{2\sigma_j^2}. \tag{4.7}$$

The radial form in Equation 4.7 allows us to use σ_j and place the rejection threshold in Δr space.

The above procedure is used for every j^{th} SNR bin to calculate $\Delta r_{j,max}$. We then fit an exponential curve to the $\Delta r_{j,max}$ points in log-log space, as seen in Figures 4.3 and 4.4. The exponential form was selected as it fit the $\Delta r_{j,max}$ data adequately with the smallest number of parameters. The fit averages out the small-scale deviations between the SNR bins and provides a smooth upper envelope. We also added a fixed lower limit at 1/3 pixel, for both the point- and extended source analyses. We do not reject any stars below this separation, as we do not trust pixel centroids to better than 1/3 pixel accuracy in the unWISE images, which are barely Nyquist-sampled. Stars with measured offsets shown in Figure 4.4 are susceptible to flux variations in the first Airy ring of the PSF, as the wider 10 pixel radius (25″) centroiding region is sufficiently large to encompass the Airy ring.

4.4.3 Rejection Fidelity

We would like to determine whether stars rejected based on the unWISE analyses are indeed contaminated. The hypothesis is that if a point-source or extended emission can randomly offset the centroid positions (and hence contaminate the photometry) of a star, then the fraction of rejected (hence contaminated) stars among our candidate excesses should be higher than the fraction of rejected stars in the parent sample. This is because if a contaminat-

ing source is bright enough to influence the photocenter of the star, it is likely to increase the flux of the star as well. We compared the percentage of rejected excesses (which include all stars identified as excesses, prior to rejection by visual inspection of the *WISE* images) to the percentage of rejected science sample stars (d<75 pc). We limited the comparison to the science sample because all our reported excesses are within this volume. The total number of stars in the science sample is 8179. Figures 4.3 and 4.4 show that the majority of rejected stars are at low SNR values (W4 SNR< 30), while the majority of our excesses (∼85%) have $W4$ SNR values > 30. Therefore, we limited our comparison to stars with $W4$ SNR> 30. This SNR cut further reduced the science sample to 4973 stars. We found that 3.10% ± 0.25% (=154/4973) of the SNR>30 parent sample stars and 5.14% ± 1.54% (=11/214) of stars with excesses were rejected. The fraction of rejected excesses is marginally larger than the fraction of rejected science sample stars. The precision of the comparison is likely hindered by the small number of rejected candidate excesses. Nonetheless, it suggests that we are likely correctly rejecting contaminated stars.

Another indication that our astrometric analysis is rejecting contaminated sources are shown in Figure 4.4. This plot shows three stars that we had previously rejected based on contaminating sources that we identified using *WISE* and Herschel data (Donaldson et al., 2012; Patel et al., 2015): HIP 32435, HIP 69682, and HIP 106914. Nearby bright sources to these stars are clearly responsible for the $\Delta r_{W4} > 0.5$ pixel offsets. Postage stamp images of these three stars can be seen in Figures 4.5 and 4.6. Aside from these three, our astrometric unWISE analysis rejected eight other excesses. From our $W3$ vs. $W4$ centroid astrometric analysis, we rejected four contaminated excesses: HIP 35198, HIP 78010, HIP 68755, and HIP 55057. Figure 4.5 shows elongated and irregular images for the first three stars, indicative of a blended contaminant. From our extended emission contamination identification analysis, we rejected four excesses which are most likely contaminated: HIP 63973, HIP 21091, HIP 79881, HIP 20998. In total, we rejected a total of eight excesses based on the relative positions of their centroids.

For the majority of these stars, the contaminating source can be easily identified from visual inspection. In other cases, the contamination is subtle. For instance, the contaminating source is difficult to pinpoint based on the shape of the PSFs for HIP 68755 and HIP 21091. HIP 21091 was also previously identified as a $W4$ excess by Vican & Schneider (2014) and we have identified HIP 21091 as a new $W3-W4$ and weighted $W4$ excess, though we cannot say to what level a background object may be affecting the excess flux for this star. However, if a contaminant is truly blended with the star, the positional offset is

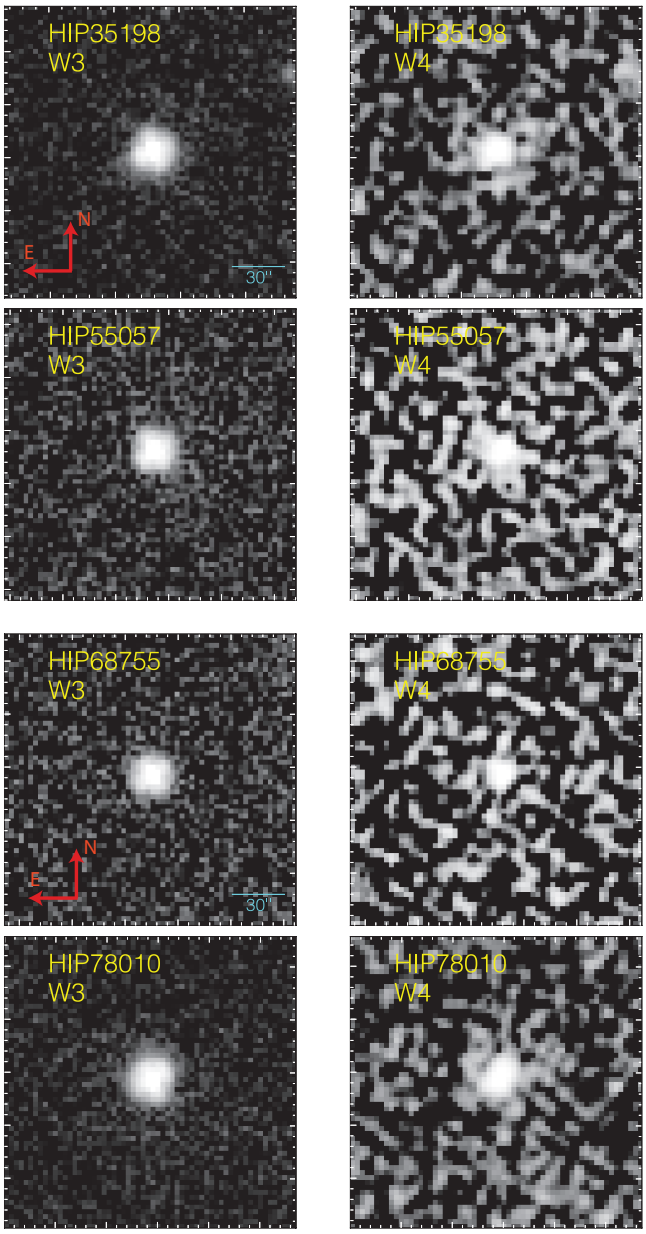

Figure 4.5: 150″ ×150″ unWISE $W3$ and $W4$ postage stamp images of stars rejected by our point-source contamination (Δr_{W4} vs. $W4$ SNR) analysis. The images are displayed using an ArcSinh scale.

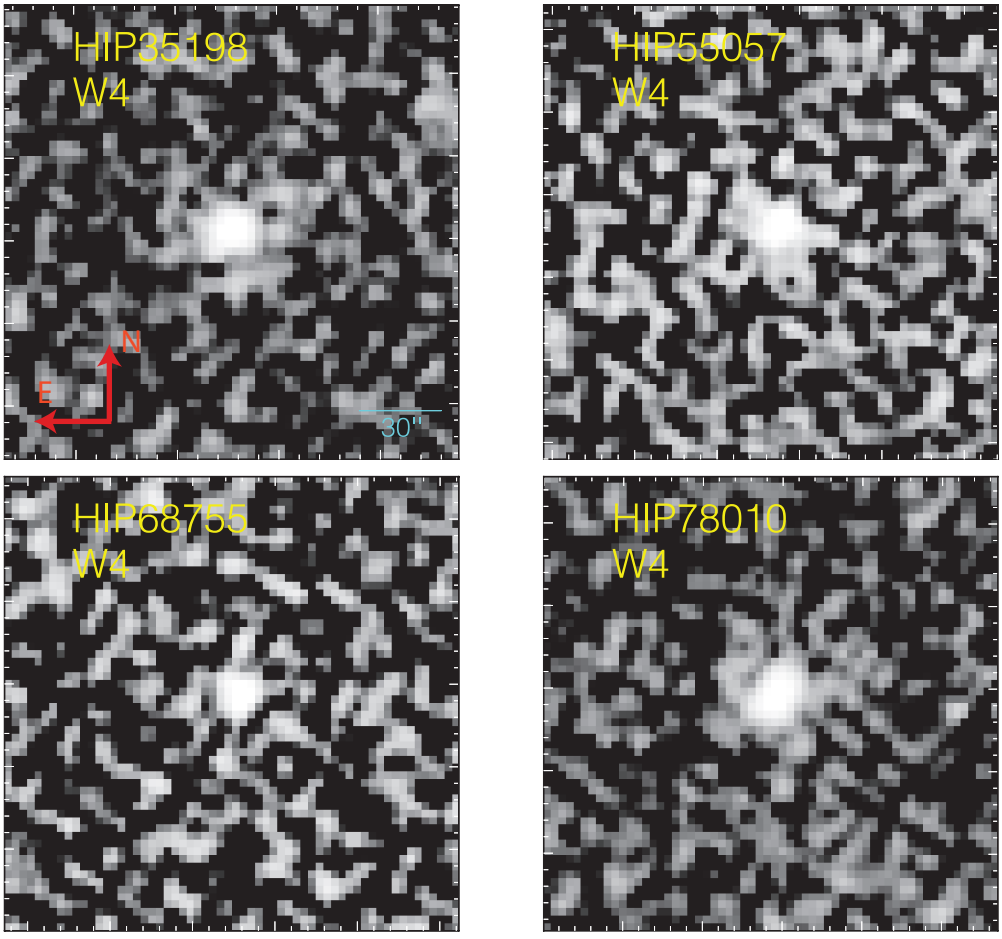

Figure 4.6: 150″ × 150″ unWISE $W4$ postage stamp images of stars rejected from our extended emission contamination (Δr_{W4} vs. $W4$ SNR) analysis. The images are displayed using an ArcSinh scale.

the only objective way to identify it. For instance, the profiles of HIP 68755 in Figure 4.5 do not "appear" to be contaminated. But subtle astrometric shifts due to blended contamination will not be apparent from visual inspection. Thus it is important to incorporate such checks, in addition to visual checks for contamination.

4.5 Results

Our improved *WISE* IR excess identification procedure has uncovered 28 excesses that we did not report in PMH14. In Section 4.5.1 we argue that one of the new excesses, associated with HIP 910, is likely spurious, which leaves 27 new excess identifications. The 27 new excesses include new single-color only excesses (12 at $W4$ and one at $W3$), new weighted color only excesses (one at $W3$ and one at $W4$), and excesses that have both new single-color and weighted color detections (12 at $W4$). The specifics of the new excesses detections and their significance in the different *WISE* color combinations are given in Table 4.2. An inspection of the single-color excess significances Σ_E for each star shows that all of the new detections are fainter than those found in PMH14: mainly because of the decrease of $\Sigma_{E_{CL}}$ in our updated determination of the FDR thresholds.

The stellar and dust properties of the newly discovered IR excesses are listed in Tables 4.4 and 4.5. These parameters are derived from photospheric model fits to the optical and near-IR photometry from *Hipparcos* and the Two Micron All-Sky Sky Survey (2MASS) using a similar procedure as outlined in PMH14. The only update with respect to PMH14 is that after fitting the optical/IR SED with a photospheric model to determine the best stellar effective temperature, we then scale the model to the weighted mean of the $W1$, and $W2$ fluxes for consistency with our weighted excess search methodology. In most cases we used the $W4$ excess and the 3-σ upper limits to the $W3$ excess to calculate upper limits to the blackbody dust temperatures. In cases with significant or marginal $W3$ excesses, we calculated the actual blackbody dust temperatures. However, we note that without additional longer-wavelength observations, our estimates of the circumstellar dust temperatures are only approximate.

In Section 4.6 we discuss the new excesses in the context of the published literature to assess their reliability and, wherever possible, to elucidate their nature.

4.5.1 New Candidate Debris Disks

Out of the 27 *WISE* excesses discovered since PMH14, 19 are completely new detections, with no previously reported excesses at any wavelength. Eighteen of these are $W4$ excesses, and are indicated with 'Y-' in the column labeled 'New?' in Table 4.2. These are new excesses at 22μm, but have no significant 12μm excesses. Seventeen are detected through the single-color excess search, although they are often independently confirmed in several single-color combinations. Eight of the 17 also display a weighted color $W4$ excess, while nine do not. In Section 4.6.1 we discuss two reasons for which a single-color excess may not be confirmed through the weighted color excess metric, even if the single-color excess is real. Only one new $W4$ excess, HIP 13932, is revealed only through its weighted color combination, without showing any significant single-color excesses.

One of the new excesses, from HIP 117972, is significant only at $W3$. The excess is present in the $W1-W3$ color at $\Sigma_{E[W1-W3]} = 2.73$, just above the $\Sigma_{E[W1-W3]_{98}} = 2.66$ 98% confidence level threshold. It is not confirmed as a weighted excess at $W3$ because the weighted $W3$ excess confidence threshold is higher: at $\Sigma_{\overline{E[W3]_{98}}} = 3.28$. Given our adoption of a lower confidence level (98%) for detecting $W3$ excesses, it is possible that the excess from HIP 117792 may be spurious. Nonetheless, the star does show a marginal excess also in the $W1-W4$ and $W2-W4$ colors. The combined evidence for faint $W3$ and $W4$ excesses suggests that they may be real, and that HIP 117972 may host a warm zodiacal dust-like debris disk. A joint SED fit to the shorter-wavelength and WISE photometry indicates a ∼530 K dust excess (third panel, Figure 4.7) at $f_d = 1.92 \times 10^{-4}$ of the stellar bolometric luminosity (Table 4.5).

New Disk Candidates with Archival IR Observations

While none of the 19 stars with new excess detections discussed here have been previously identified as debris disk hosts in the literature, perusal of archival observations from *Spitzer* and *Herschel* reveals data for HIP 21783 and HIP 67837. The SED for HIP 20507 can be seen in the fourth panel of Figure 4.7. HIP 20507 has an *IRAS* 25μm detection, although it is too noisy to place useful constraints. Finally, one of our initially identified excesses, HIP 910, has extensive *Spitzer* and *Herschel* observations discussed in the published literature, in addition to detections by *IRAS* at 25μm and by *AKARI* at 18μm. Our consideration of the ensemble of these data shows that the small HIP 910 *WISE* $W4$ excess is likely spurious. Hence, the total number of new *WISE* excesses is 18.

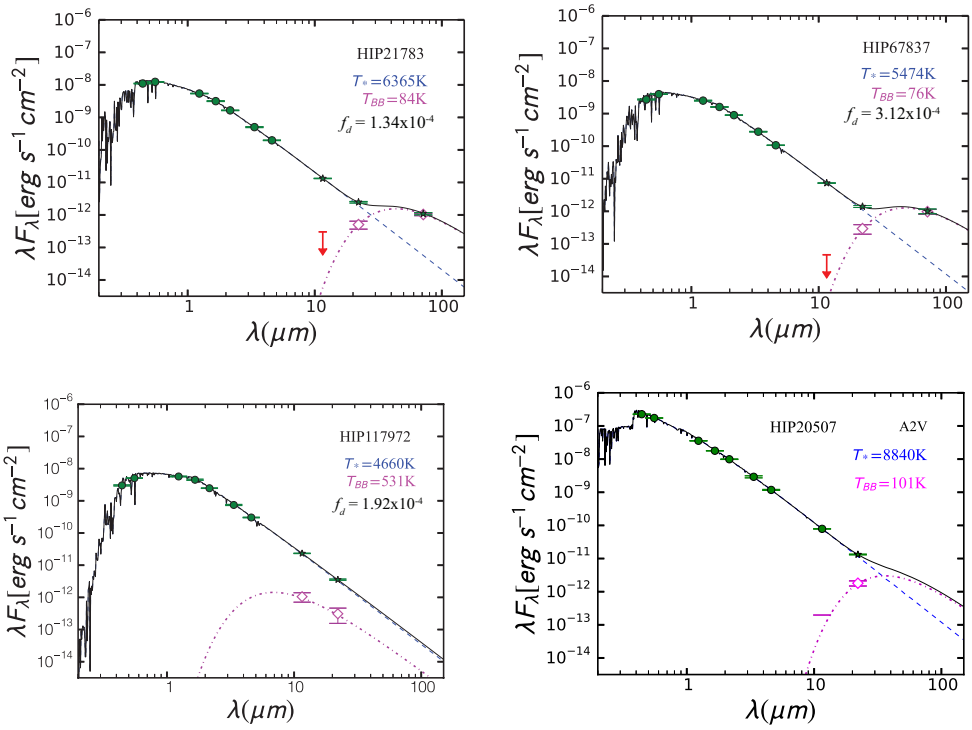

Figure 4.7: Example SEDs representative of newly detected excesses from this study. In each plot, the blue dashed lines correspond to the fitted NextGen photosphere models using photometry indicated by the green circles. The photospheric fit was performed using the BVJHKs photometry from the Hipparcos Catalogue and the *2MASS* Point Source Catalog, as well as the $W1$ and $W2$ fluxes. After fitting, the photosphere was scaled to the weighted average of the $W1$ and $W2$ fluxes. The $W1$ and $W2$ photometry were corrected using saturation correction trends derived in PMH14. $W3$ and $W4$ All-Sky photometry are green stars at 12 and 22μm in each plot. We fit blackbody curves (magenta dashed-dot curves) to excess fluxes (open magenta diamonds) and 3σ upper limits (red arrows) red-ward of $W3$. The combined photosphere and excess emission for each star is plotted as solid black line. HIP 21783 and HIP 67837 are new $W4$ excesses we identified from the significance of their $W2-W4$ and $W3-W4$ color, respectively. We also use archival Spitzer/MIPS 70μm and Herschel/PACS 70μm fluxes to further constrain the dust temperature fits for HIP 21783 and HIP 67837, respectively. The Spitzer and Herschel fluxes were obtained as described in Section 4.5.1. In addition, HIP 117972 is a new $W3$-only excess which we identified from the significance of its $W1-W3$ color, while HIP 20507 is a new weighted $W4$ excess.

HIP 21783. This star is serendipitously included in a single MIPS 70μm pointing in *Spitzer* program GO 54777 (PI: T. Bourke). We measure a flux of 26 ± 2 mJy by performing $r = 16''$ aperture photometry on the post-basic calibrated data (PBCD) images, and apply an aperture correction of 2.04, according to Table 4.14 of the MIPS Instrument Handbook v. 3.0.[7] The MIPS70 measurement confirms the presence of a thermal excess. A fit to the optical–IR SED (panel 1, Figure 4.7) reveals that the associated circumstellar dust has a temperature of 84 K and a fractional luminosity of $f_d = 1.34 \times 10^{-4}$.

HIP 67837. HIP 67837 is included in a *Herschel*/PACS 70μm and 160μm Open Time program (PI: D. Padgett). Its 70μm flux is 24 ± 4 mJy, where we have performed $r = 5''$ aperture photometry on the Level 2.5-processed images, and applied an aperture correction of $1/0.577 = 1.733$, according to Table 2 of Balog et al. (2014). The PACS 70μm measurement also confirms the presence of a thermal excess (panel 2, Figure 4.7). The star is not detected at 160 μm. The inferred dust temperature is 76 K and the fractional dust luminosity is $f_d = 3.12 \times 10^{-4}$.

HIP 910. Among the four stars for which archival mid-IR data exist, only HIP 910 has been discussed in the debris disk literature, where it has received considerable scrutiny as a nearby (19 pc; van Leeuwen, 2007) near-solar analog (F8V; Gray et al., 2006). Independent analyses of *Spitzer*/IRS low-resolution spectra (Beichman et al., 2006), MIPS 24μm and 70μm photometry (Trilling et al., 2008), and *Herschel* PACS 100μm and 160μm photometry (Eiroa et al., 2013) all conclude that HIP 910 does not possess an excess. We find that HIP 910 has a small $W2 - W4$ excess (0.19 ± 0.06 mag) and $W2 - W3$ excess (0.15 ± 0.04 mag) excesses above the photosphere. As such, it would be a candidate for an exozodiacal debris disk. A 19% excess at W4 would have only been $\sim 2\sigma$ significant in the MIPS24 observations of Trilling et al. (2008), hence the non-confirmation in MIPS is not surprising. However, a 15%–19% excess at 10–30μm would have been detected at $\sim 10\sigma$ significance in the *Spitzer*/IRS analysis of Beichman et al. (2006). Their low-resolution *Spitzer*/IRS observations cover a wide wavelength range, 6–38μm, and have superior sensitivity to faint excesses compared to *WISE* photometry: because of the better stellar photospheric estimation possible from the larger number of independent short-wavelength data points. Given the lack of confirmation from the *Spitzer*/IRS observations, we conclude that the candidate $W4$ excess from HIP 910 is probably spurious: representative of the very few false-positive excesses beyond our 99.5% confidence threshold.

[7] http://irsa.ipac.caltech.edu/data/SPITZER/docs/mips/mipsinstrumenthandbook/

It is worth noting that HIP 910 is the only newly-identified excess candidate in the present study for which published mid-IR observations exist. Because it is also unique in that it is not confirmed as a debris disk in the more sensitive *Spitzer*/IRS data, this raises the question whether some of our other candidates discussed here and in PMH14 may also be spurious. To determine whether the non-confirmation of *WISE* excesses from *Spitzer*/IRS observations is a common occurrence for any of our reported excesses, we searched the recent literature for all of the new excess stars discovered in PMH14. Nineteen of these have had *Spitzer*/IRS observations published since, all in Chen et al. (2014).

All are confirmed to have *Spitzer*/IRS excesses.[8] Hence, we can conclude that the non-confirmation of HIP 910 is not typical of our *WISE* excess detections, and that the remaining 19 new candidate debris disks reported here and the 104 new candidates in PMH14 remain viable.

New Disk Candidates in Binary Systems

Two of our new excess stars, HIP 2852 and HIP 70022, have recently discovered M-dwarf companions (De Rosa et al., 2014). This may be a cause for concern, as these companions might be responsible for the $W4$ excesses from these two stars. HIP 2852 has a physical $0.30 M_{\odot}$ companion, which corresponds to an M3/4 spectral type, at a separation of $0.93'' \pm 0.01''$ (45.6 ± 0.49 AU). HIP 70022 has a 0.18 $M_{\odot}$ (M5/6) companion which is likely physical (De Rosa et al., 2014), separated by $1.84''$ (116 AU) from the central star. Given $\Delta K_s \geq 5$ mag contrasts between the primary and the companion in each case, the flux from each of the M-dwarf companions is not enough to produce the observed 13%–16% excesses at $W4$. Therefore, we conclude that both stars possess real mid-IR excesses that are likely associated with debris disks. After factoring the companion separation for both of these stars, the dust in each system is expected to be circumstellar and not circumbinary.

4.5.2 Confirmations of Previously Known 22μm Faint Debris Disks

Out of our 27 additional $W3$ or $W4$ excess detections not reported in PMH14, 19 represent completely new discoveries: 18 at $W4$ and one at $W3$. An additional star (HIP 26395) was found to possess a $W4$ excess in PMH14, but we

[8] After the publication of PMH14 we recognized that some of the excesses that we reported as new had already been identified as candidate debris disks from *Spitzer*/IRS spectra by Ballering et al. (2013). There are 14 such excesses: a subsample of the 19 new PMH14 $W4$ excesses that are confirmed in Chen et al. (2014).

now report a new excess detection at $W3$. The remaining eight have previously reported excess in the literature. We detected $W4$ excesses associated with seven of these eight stars, while one possesses a $W3$ excess. Here we examine the literature data on the nine previously reported excesses—form PMH14 or elsewhere— in context of our *WISE* detections.

Five of our eight $W4$ excesses were previously reported as *WISE* $W4$ excesses. Vican & Schneider (2014) reported 200 K upper limit blackbody temperatures based on non-detections of excesses at $W3$ for four of these stars: HIP 12198, HIP 21091, HIP 78466 and HIP 115527. We use the 3-σ upper limits on the $W3$ excess fluxes of these four stars to determine dust temperature the upper limits. The dust temperature upper limits are between 131 K and 203 K, consistent with the estimates found by Vican & Schneider (2014). The fifth star (HIP 92270) was reported as a $W4$ excess by Mizusawa et al. (2012), although no other relevant information exists for this star.

The remaining three $W4$ excess hosts (HIP 42333, HIP 42438, and HIP 100469) have published mid- and far-IR excess detections from Spitzer, thus providing greater constraint on the dust properties in these systems. Plavchan et al. (2009) reported 24μm and 70μm excess detections for HIP 42333 and calculated the dust temperature of the excess to be $T < 91$ K. Our estimates to the blackbody temperature from the $W4$ excesses and the $W3$ 3-σ upper limits yield a hotter, yet consistent result ($T_{BB} < 344$ K). HIP 42438 and HIP 100469 are stars with previously detected Spitzer/IRS excesses between 8–30μm and Spitzer/MIPS excesses at 70μm. Chen et al. (2014) report multi-temperature debris disks for both these stars, where the cold dust component is $\sim$ 70–80 K while the hot dust component is constrained to 499 K for each system. Our single-population dust temperatures for HIP 42438 ($T_{BB} < 432$ K) and HIP 100469 (T_{BB} =131 K) are consistent with the estimates from Chen et al. (2014).

Our last new excess detection, from HIP 26395, was already included in PMH14 as a $W4$ excess. In this study, we report the detection of a weighted $W3$ excess. A 10–30μm excess for this star was also reported by Chen et al. (2014), using Spitzer/IRS data. Chen et al. (2014) found that HIP 26395 has a multi-temperature debris disk, similar to HIP 42438 and HIP 100469; a cold component at T=94 K and a hot component at T=399 K. Again, our single-population dust temperature (146 K) is consistent with the two-population dust model of Chen et al. (2014). Notably, our detection of the weighted $W3$ excess shows that our improved technique can detect as faint a population of excesses as detectable by *Spitzer*/IRS thanks to our increased precision in pinpointing the level of the photosphere.

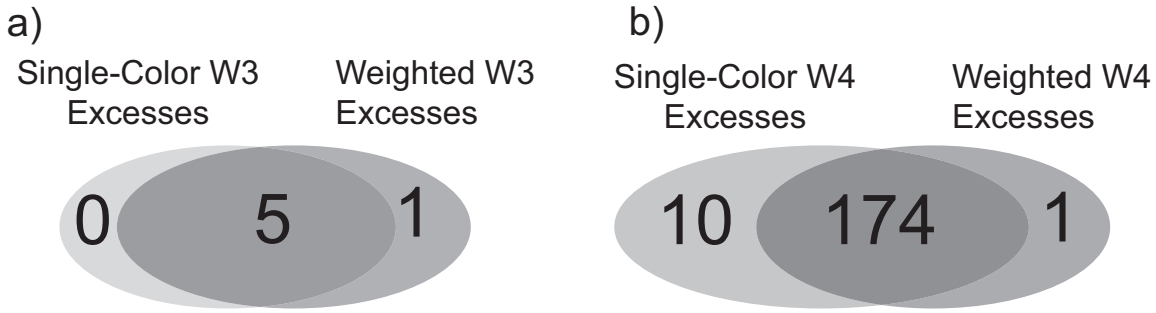

Figure 4.8: Venn diagrams comparing the candidate excesses from our weighted excess analysis (right circles) and from our single-color excess (left circles). Stars from the single-color excess sets were selected only if they had good quality photometry in $W1$, $W2$ and $W3$ for our $W3$ excesses (a) and good quality photometry in all four bands for our $W4$ excesses (b).

4.6 Discussion

4.6.1 Single vs. Weighted Color Excess Search

We compare the number of IR-excess stars detected from the weighted $W3$ and $W4$ searches to the corresponding single-color excess detections from PMH14 and to the additional single-color excesses from the improved detection procedures outlined in Sections 4.3.1 and 4.3.2. For consistency, we limit the comparison set of the single-color excess sample only to stars with valid *WISE* photometry in all four bands. The Venn diagrams in Figure 4.8 show the comparison of stars detected from the weighted $W3$ and weighted $W4$ searches to their respective samples of single-color excess detections. The weighted excess metrics confirm all five of the single-color $W3$ excesses, and 174/184 (=94.6%) of the single-color $W4$ excesses from PMH14 and from Section 4.3.1. Surprisingly, we only find one new weighted $W3$ and one new weighted $W4$ excess that had not been reported in our single-color analysis (PMH14).

Our initial expectation was that by averaging down the photometric uncertainties, with a weighted color search we might have been able to detect at higher significance previously marginal single-excesses. In reality, all of the individual color components in our weighted excess measure are correlated through their common use of the same longer-wavelength filter. For example, the three individual $Wi - W4$ colors are correlated, and do not give independent assessments of the presence of a $W4$ excess. Consequently, the *averaging* in the weighted color combination does not substantially improve our sensitivity. Moreover, a consideration of the *WISE* photometric uncertainty distributions (Figure 4.9) shows that the $W4$ photometric errors dominate. As a

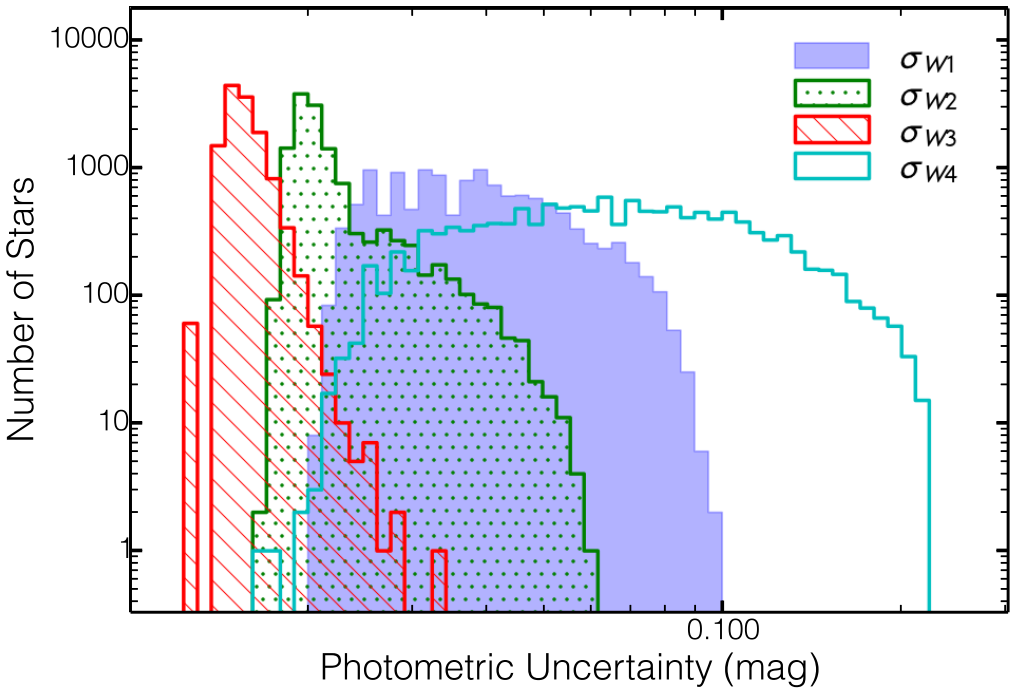

Figure 4.9: Distributions of photometric uncertainties for all four *WISE* bands for 12654 stars in the weighted $W4$ parent sample, including stars with saturated and then corrected $W1$ and $W2$ photometry. The large spread in σ_{W4} is expected because of the lower absolute flux levels in $W4$. It is evident that the mean σ_{W1} is larger than the means of σ_{W2} or σ_{W3}. This systematic trend of increasing photometric uncertainty from $W3$ down to $W1$ dominates the determination of a significant excess when the $E[Wi-Wj]$ are comparable.

result of the large $W4$ photometric errors, the weighted color combination only marginally improves the accuracy of our $W4$ excess measurement. Hence, the weighted excess metric produces somewhat higher-fidelity excesses, but only slightly so.

Conversely, if a star's excess is not detected from its weighted color, then any excess identified from individual colors might be considered suspect. Thus, the 10 stars that were not detected in our weighted $W4$ excess search (Figure 4.8b), might be false detections. There are two reasons, however, that a star may not have a weighted $W4$ excess but still be a bona-fide detection based on its single-color excess.

The first is that the presence of a small but positive $W3$ excess can decrease

the overall significance $\Sigma_{\overline{E[W4]}}$ of the $W4$ three-color-weighted excess. Five out of ten unrecovered stars in the weighted $W4$ search have small but positive $W1-W3$ or $W2-W3$ excesses (HIP 8987, HIP 13932, HIP 21918, HIP 43273, HIP 82887, and HIP 85354). In view of potentially increasing the number of new detections, we then ran a two-color weighted search by excluding the $W3-W4$ color and only using $W1-W4$ and $W2-W4$ in the weighted metric (equation 4.4). However, the two-color weighted $W4$ excess search did not bear any new fruit; it produced just as many new stars when compared to the set of single-color detections as the three-color weighted search produced. We attribute the lack of an increase in detections from the two-color weighted search to the fact that the $W3$ photometric errors are on average smaller than the $W1$ and $W2$ photometric errors (Figure 4.9). That is, the removal of the contribution of some marginally significant $W3$ excesses by eliminating $W3-W4$ from the weighted excess calculation is offset by the greater uncertainty in the $W1$ and $W2$ photometry. In other words, by excluding $W3-W4$ we are excluding more of the "excess signal", and leaving more of the noise (Figure 4.10).

The fact that the $W3$ photometric errors are on average the smallest indicates that some bona-fide faint $W3-W4$ excesses may not be confirmed in $W1-W4$ and $W2-W4$, and even in the weighted $W4$ excess. This is the second reason for which some of the single-color candidate $W3-W4$ excesses are probably caused by real debris disks, even if they are not confirmed in the weighted $W4$ analysis. Such is the case for the remaining four of the ten unrecovered stars (HIP 1893, HIP 70022, HIP 92270, and HIP 100469), all of which are $W3-W4$-only single-color excess detections, and have much larger photometric uncertainties in $W1$ and $W2$ than in $W3$: not surprising as all four stars are saturated in $W1$ and $W2$. Even though we correct the saturated photometry of these stars, the resulting photometric uncertainties will always be larger than those of unsaturated stars.

4.7 Conclusion

We have presented a series of techniques that improve upon our *WISE* debris disk-search methods in PMH14 to 1) identify new *WISE* excesses within 75 pc, 2) verify single-color *WISE* excesses, and 3) reject contaminated excesses.

In Section 4.3, we implemented an improved assessment of the confidence threshold beyond which we select candidate excesses, which reveals 19 previously unreported candidate *WISE* single-color $W3$ and $W4$ excesses associated with main-sequence Hipparcos stars within 75 pc. We also presented a method that uses an optimally-weighted average of multiple *WISE* colors to identify

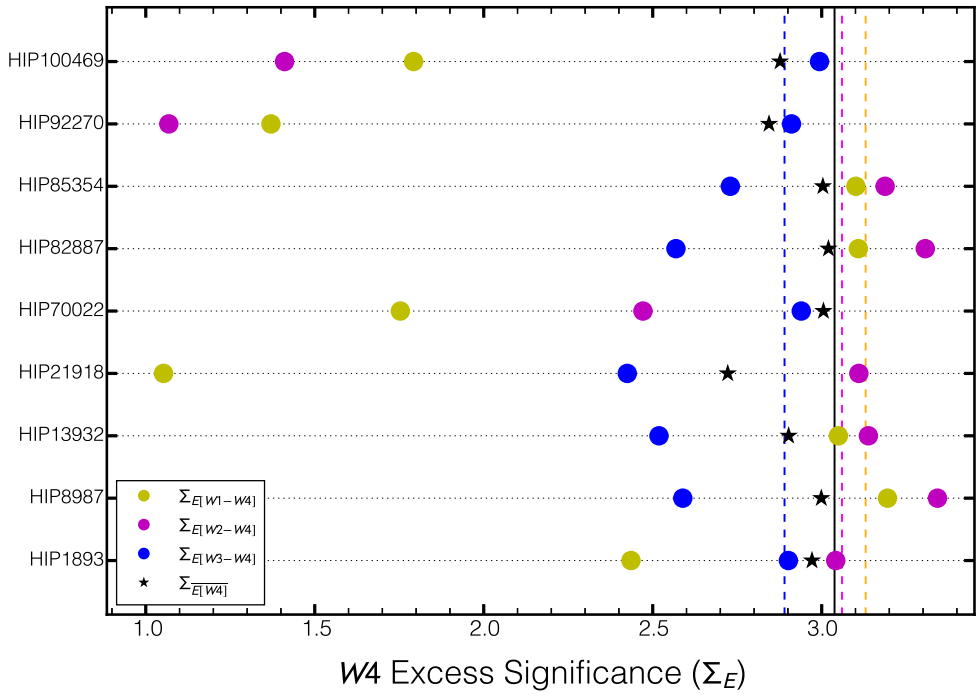

Figure 4.10: The excess significances for the nine stars with single-color $W4$ excesses in PMH14 that were not recovered with the weighted $W4$ excess metric in this study (see Figure 4.8b). Each vertical colored line corresponds to the current 99.5% detection threshold for each color listed in the legend. We see that the weighted $W4$ excess threshold ($\Sigma_{\overline{E[W4]}}$) effectively averages the individual single-color detection thresholds.

$W3$ and $W4$ excesses from main sequence stars in the attempt to attain greater accuracy compared to using individual *WISE* colors (PMH14). While the color weighting approach also has the potential to identify fainter IR excesses, most of the excesses are expressed only at $W4$, and the $W4$ photometric uncertainties are the largest. Hence, we are unable to uncover a substantial new population of debris disks. Instead we mostly confirm the already identified single-color excesses, and add only two new weighted-excess detections. Both of these, one at $W3$ and one at $W4$, were already known as debris disk hosts from previously published longer-wavelength observations.

None of the candidate $W4$ excess stars found on the same sample as in the same 75 pc sample as in PMH14, plus one new single-color $W4$ excess found in this study, are not confirmed in the weighted $W4$ analysis. In six of the cases, the reason can be traced to the presence of a marginal $W3$ excess, which diminishes the overall significance of the weighted $W4$ excess. All six of these are detected as excesses in $W1 - W4$ or in $W2 - W4$ in PMH14, but not in $W3 - W4$. Hence, their $W4$ excesses are likely real. The non-confirmation of the remaining four is linked to their poor $W1$ and $W2$ photometry and to having $W3 - W4$ excesses that are only marginally above the significance threshold. These are also possibly real, although we can not confirm this with the present analysis.

In addition, we further refined our sample of excesses by removing stars which are likely contaminated by blended point-sources or by extended emission. We rejected eight excess-bearing stars by assessing their $W3$ and $W4$ centroids in the higher-resolution unWISE image data set. Though we perform "by-eye" checks of the *WISE* All-Sky images post excess selection, the automated assessment of the stellar centroid offsets provides a sensitive and objective metric to assess contamination from unrelated objects.

Overall, the use of a weighted combination of *WISE* colors improves the reliability of candidate IR excess detections from individual *WISE* colors at the cost of potentially overlooking a small population of faint W4 excesses. In addition, an objective assessment of contamination from unWISE centroid offsets complements visual inspection of *WISE* images. And even though the fraction of debris disk-bearing stars within 75 pc does not change significantly from the findings in our previous study, the verification through weighted colors and the positional checks using higher angular resolution images provide confidence that the 19 new disks discovered here are real, and not spurious or contaminated. Thus, combined with the PMH14 results, we find a total of 9 $W3$ and 229 significant $W4$ excesses from $<$75 pc *Hipparcos* stars in *WISE*. As of the current study, 107 of these represent previously unreported 10–30μm excesses from stars known to host debris disks.

Table 4.1. Single- and Weighted-Color Excess Selection Summary

Color	$\Sigma_{E_{\rm CL}}$[a] or $\Sigma_{\overline{E_{\rm CL}}}$	Stars in Parent Sample(<120 pc)	Stars in Science sample (<75 pc)	Excesses in Science Sample	Debris Disk Candidates	New Excesses
$W1-W4$	3.13	12942	6294	135	120	0
$W2-W4$	3.06	13203	6507	192	177	13
$W3-W4$	2.89	14434	7198	239	222	18
$W1-W3$	2.66	15017	6788	13	9	1
$W2-W3$	3.83	15245	6962	3	3	0
Weighted $W4$	3.04	12654	6140	188	175	1
Weighted $W3$	3.28	14808	6684	6	6	1
Total	···	16960	7937	282	245	27

Note. — Summary of the results from our *WISE* single-color and weighted $W3$ and $W4$ excess identification, using the more accurate determination of the $\Sigma_{E_{CL}}$ outlined in Section 4.3.1. $\Sigma_{E_{CL}}$ is the threshold Σ_E above which we select an excess at a confidence level higher than CL. $CL = 99.5\%$ for $W4$ excesses and 98% for $W3$ excesses. The number of stars in the parent and science samples are those that pass the sample selection criteria of PMH14 (see also Section 4.2). The final debris disk candidates are the subset of excesses that survive visual inspection for contamination. The last column indicates the number of new detections from the sample of stars over the ones already reported in PMH14.

[a]Excess significance threshold for single-color excesses ($\Sigma_{E_{CL}}$) or weighted color excesses ($\Sigma_{\overline{E_{\rm CL}}}$).

Table 4.2. IR Excess Information for Newly Identified Debris Disk Candidates from *WISE*

				Σ_E					$\Sigma_{\overline{E}}$	
HIP ID	Single Color Excess Flag	Weighted Excess Flag	New? (22|12μm)	$W1-W4$	$W2-W4$	$W3-W4$	$W1-W3$	$W2-W3$	Weighted $W4$	Weighted $W3$
1893	NNYNN	NN	Y-	2.44	3.04	2.90	-0.87	0.35	2.97	-0.16
2852	NNYNN	YN	Y-	0.72	2.28	3.07	-0.97	-0.21	3.05	-0.60
12198	NYYNN	YN	N-	2.87	3.24	3.06	-0.41	0.28	3.18	0.06
13932	NYNNN	NN	Y-	3.05	3.14	2.52	1.83	2.54	2.90	2.61
18837	NYYNN	YN	Y-	2.67	3.16	3.03	-0.24	0.15	3.15	0.04
20094	NYYNN	YN	Y-	2.86	3.13	3.03	-0.07	0.15	3.14	0.10
20507	NNNNN	YN	Y-	1.63	2.21	2.85	0.57	0.46	3.08	0.66
21783	NYUUU	UU	Y-	2.86	3.21	...	...	...	...	...
21918	NYNNN	NN	Y-	1.05	3.11	2.42	-0.86	1.07	2.72	0.58
26395	YYYNN	YY	NN	13.08	21.07	20.61	1.00	3.31	23.18	3.28
39947	NNYNN	YN	Y-	0.83	2.55	3.07	-0.55	0.29	3.20	0.04
42333	NYNNN	YN	N-	0.96	3.12	2.89	-0.40	1.02	3.15	0.77
42438	UNYUN	UU	N-	...	2.02	3.07	...	0.71	...	...
43273	NYNNN	NN	Y-	2.69	3.09	2.63	0.08	1.28	2.82	0.96
58083	NYYNN	YN	Y-	3.08	3.23	3.05	-0.05	0.46	3.17	0.32
66322	NNYNN	YN	Y-	1.95	2.72	3.10	-0.12	-0.19	3.19	-0.21
67837	UUYUU	UU	Y-	...	...	2.99	...	...	...	...
70022	NNYNN	NN	Y-	1.75	2.47	2.94	-0.02	-0.30	3.01	-0.27
72066	UUYUU	UU	Y-	...	...	2.92	...	...	...	...
73772	NYYNN	YN	Y-	3.03	3.14	2.99	0.17	0.18	3.14	0.21
78466	NYYNN	YN	N-	2.94	3.15	2.92	0.71	0.40	3.15	0.59
85354	NYNNN	NN	Y-	3.10	3.19	2.73	1.01	1.74	3.00	1.70
92270	NNYNN	NN	N-	1.37	1.07	2.91	-0.02	-1.02	2.84	-0.86
100469	NNYNN	NN	NN	1.79	1.41	2.99	0.10	-1.60	2.88	-1.38
110365	NYYNN	YN	Y-	3.08	3.17	3.01	0.04	0.41	3.12	0.29
115527	NNYNN	YN	N-	1.88	2.86	3.13	-0.24	-0.10	3.20	-0.18
117972	NNNYN	NN	-Y	2.64	1.78	0.50	2.73	2.21	1.20	2.87

Note. — Summary of the properties of the single-color and weighted-color IR excesses attributed to debris disks at $W3$ and/or $W4$ for the stars in our science sample. The second column indicates the combination of detections from individual colors. Each flag is a five character string that identifies whether the star has a statistically probable (Y) or insignificant (N) single-color excess in the following order: $W1-W4$, $W2-W4$, $W3-W4$, $W1-W3$ and $W2-W3$. Any star can have an unlisted (U) value, indicating that the star was rejected by the selection criteria for that particular color (Section 2.2 in PMH14). "U" entries correspond to null entries in the corresponding $Wi-Wj$ Σ_E column. Column 3 shows a two-character flag to indicate whether the star has a significant weighted excess in the following order: weighted $W4$ excess and weighted $W3$ excess. Column 4 lists whether or not the star has a new excess detection in the $W4$ or $W3$ bands (22 or 12μm), or not. Dashed entries ("-") indicate no detected excess in that band. The last seven columns list the significance of the excess for each color or weighted metric.

Table 4.3. Rejected *WISE* Excesses

HIP ID	WISE ID	Rejection Reason
New Single-Color and Weighted Excesses		
HIP910	J001115.82-152807.2	2
HIP13631	J025532.50+184624.2	1
HIP27114	J054500.36-023534.3	1
HIP21091	J043111.09+111439.9	3
HIP55057	J111616.56-034541.8	4
HIP60689	J122617.82-512146.6	1
HIP79741	J161628.20-364453.2	1
HIP79969	J161922.47-254538.9	1
HIP81181	J163453.29-253445.3	1
HIP82384	J165003.66-152534.0	1
HIP83221	J170028.63+150935.1	1
HIP83251	J170055.98-314640.2	1
HIP99542	J201205.89+461804.8	1
HIP111136	J223049.77+404319.8	1
Previouly Identified Single-Color Excesses from PMH14		
HIP79881	J161817.88-283651.5	3
HIP20998	J043011.60-675234.8	3
HIP68755	J140422.92-032804.6	4
HIP35198	J071625.22+350102.8	4
HIP78010	J155546.22-150933.9	4
HIP63973	J130634.58-494111.0	3

Note. — Rejection reasons:
1. Contamination by line-of-sight interstellar cirrus based on visual "by-eye" inspection.
2. Spurious excess. See Section 4.5.1.
3.Contaminated by extended emission contaminants based on Δr_{W4} vs. $W4$ SNR analysis.
4. Contaminated by point-source contaminants based on $\Delta r_{W3,W4}$ vs. $W4$ SNR analysis.

Table 4.4. Stellar Parameters of New Excess Stars from Improved Methods

HIP ID	WISE ID	SpT[a]	Dist.[b] (pc)	T_* (K)	R_* ($R_\odot$)	χ^2_*	F_{W3} (mJy)	$F_{W3,*}$ (mJy)	F_{W4} (mJy)	$F_{W4,*}$ (mJy)	$\Delta_{F_{W3}}/F_{W3}$[c]	$\Delta_{F_{W4}}/F_{W4}$[c]	$W1_{corr}$[d] (mag)	$W2_{corr}$[d] (mag)
1893	J002356.52-142047.4	G6V	53	5468	1.0	1.9	48.6±0.8	50.4	17.3±1	14	-0.036	0.188	6.868±0.032	6.958±0.023
2852	J003606.78-225032.9	A5m...	49	7448	1.6	1.4	194±3	202	64.3±2	55.7	-0.040	0.133	5.321±0.062	5.403±0.033
12198	J023705.64+125406.0	G5	71	5834	1.2	2.1	39.4±0.6	40.3	14.3±0.9	11.2	-0.021	0.215	7.113±0.032	7.178±0.019
13932	J025930.69+062022.5	G0	65	5950	0.8	1.1	21.5±0.4	20.9	8.48±1	5.81	0.028	0.315	7.838±0.023	7.886±0.020
18837	J040217.21-013757.9	F5	68	6472	1.4	1.0	64.7±1	66	23±1	18.2	-0.019	0.206	6.575±0.039	6.619±0.020
20094	J041829.43+355926.6	F5	43	5550	0.9	2.5	63±1	66.5	23.2±2	18.4	-0.055	0.207	6.611±0.038	6.645±0.021
20507	J042340.81-034444.0	A2V	64	8842	2.3	5.8	303±4	306	97.6±2	84.4	-0.009	0.135	4.930±0.077	4.939±0.041
21783	J044046.82+301728.9	F5	64	6365	1.2	0.3	51.1±0.8	52	18.1±1	14.4	-0.018	0.207	6.843±0.038	6.879±0.021
21918	J044248.88+121233.0	G5	56	5642	1.8	3.7	138±2	138	44.7±2	38.5	-0.002	0.139	5.720±0.054	5.855±0.028
26395	J053708.78-114632.0	A2V	63	9099	1.4	0.5	124±2	120	73.4±2	33	0.036	0.551	5.910±0.051	5.978±0.022
39947	J080930.03-515033.6	G0V	57	5959	2.4	2.0	259±4	264	84.1±2	73.5	-0.019	0.126	5.040±0.074	5.132±0.036
42333	J083750.09-064824.2	G0	24	5817	1.0	0.9	235±3	234	76.2±2	65.1	0.004	0.145	5.156±0.079	5.271±0.035
42438	J083911.67+650116.5	G1.5Vb	14	5902	0.9	0.8	626±8	614	199±4	171	0.019	0.142	4.098±0.106	4.210±0.059
43273	J084855.82+724034.7	G0	67	5997	1.1	1.5	38.1±0.5	38.2	13.8±1	10.6	-0.002	0.229	7.163±0.028	7.231±0.022
58083	J115442.60+030837.0	K2	40	4728	0.7	1.5	34.2±0.5	36.2	13.2±1	10.1	-0.059	0.238	7.284±0.029	7.359±0.020
66322	J133531.56-220128.7	F7/F8V	49	6374	1.4	1.4	122±2	125	40.3±1	34.8	-0.028	0.137	5.892±0.053	5.924±0.026
67837	J135343.46-782450.1	G5V	56	5474	0.8	3.5	28.4±0.4	29.2	10.3±0.7	8.13	-0.029	0.214	7.485±0.025	7.546±0.019
70022	J141940.92+002303.6	A7V	63	7950	1.7	0.6	147±2	153	48.9±2	42.1	-0.035	0.138	5.680±0.061	5.697±0.028
72066	J144428.29+451109.4	F0	62	7233	1.6	0.3	118±2	119	39.1±1	32.8	-0.007	0.160	5.930±0.051	5.972±0.024
73772	J150447.01-511505.2	G3V	71	5966	1.1	0.5	35.9±0.6	36.7	13.1±0.9	10.2	-0.022	0.221	7.233±0.030	7.271±0.021
78466	J160105.03-324145.9	G3V	47	5652	1.1	1.8	84.6±1	86.4	28.7±1	24	-0.021	0.162	6.332±0.046	6.351±0.021
85354	J172630.24-130924.7	K2*	57	4708	0.8	0.7	23±0.4	23.5	9.38±1	6.54	-0.020	0.303	7.752±0.024	7.832±0.020
92270	J184816.42+233053.0	F8V	29	6318	1.2	0.9	294±4	312	94.9±2	86.7	-0.060	0.086	4.940±0.069	4.929±0.041
100469	J202227.53-420259.2	A0V	66	9641	1.7	2.1	164±2	177	55.4±2	48.7	-0.078	0.121	5.550±0.066	5.528±0.032
110365	J222112.66+084051.9	G0	71	5843	0.9	1.6	24.2±0.4	24.8	9.61±0.9	6.89	-0.024	0.282	7.656±0.023	7.704±0.020
115527	J232406.43-073302.6	G5	30	5654	0.9	1.3	116±2	120	38.9±1	33.4	-0.032	0.140	5.939±0.056	5.998±0.024
117972	J235541.67+250838.8	G5	50	4653	1.4	4.6	85.6±1	87.8	26±1	24.5	-0.026	0.057	6.418±0.045	6.391±0.021

Note. — *Hipparcos* stars with detected mid-IR excesses at either $W3$ or $W4$. Unless otherwise noted, the stellar temperature and radius were obtained from photospheric model fits ot the optical through 4.5μm photometry, as described in Section 3 of PMH14.

[a]Spectral types are from the *Hipparcos* database. Stars marked with asterisks have had their spectral types estimated from their $B_T - V_T$ colors using empirical color relations from Pecaut & Mamajek (2013).

[b]Parallactic distances from *Hipparcos*.

[c]The quoted fractional excesses in $W3$ and $W4$ represent the ratios of the measured excess and the total fluxes in these bands. They have not been color-corrected for the filter response, although such corrections have been applied to the estimates of the fractional bolometric luminosities f_d of the dust (Table 4.2; see Section 3 of PMH14).

[d]Saturation corrected $W1$ and $W2$ photometry (see Section 2.4 in PMH14)

Table 4.5. Disk Parameters from Blackbody Fits of Excesses from Improved Methods in 75 pc.

HIP ID	T_{BB} (K)	$T_{BB_{lim}}$ (K)	R_{BB} (AU)	$R_{BB_{lim}}$ (AU)	θ (")	f_d (10^{-5})	$f_{d_{lim}}$ (10^{-5})	Notes
1893	···	<145	···	>3.4	>0.063	6.6	>0.25	b,f
2852	···	<99	···	>21	>0.43	3.1	>0.066	b,f
12198	···	<185	···	>2.7	>0.038	6.3	>0.25	b,f
13932	166	<264	2.3	>0.9	0.014–0.035	10	>0.39	c,f
18837	···	<197	···	>3.4	>0.05	4.5	>0.17	b,f
20094	131	···	3.9	···	0.091	7.6	>0.27	a,f
20507	···	<279	···	>5.3	>0.083	1.6	>0.04	b,f
21783	···	<202	···	>2.7	>0.042	4.8	>0.18	b,f
21918	···	<339	···	>1.1	>0.02	7.9	>0.16	b,f
26395	146	···	13	···	0.2	8.5	···	g
39947	···	<248	···	>3.2	>0.057	3.9	>0.12	b,f
42333	117	<344	5.5	>0.64	0.027–0.23	5	>0.15	c,f
42438	219	<432	1.6	>0.4	0.028–0.11	4	>0.14	c,f
43273	···	<229	···	>1.7	>0.025	7.1	>0.24	b,f
58083	131	···	2.1	···	0.053	15	>0.53	a,f
66322	···	<188	···	>3.6	>0.074	2.8	>0.11	b,f
67837	···	<145	···	>2.7	>0.048	7.8	>0.3	b,f
70022	···	<140	···	>13	>0.2	1.6	>0.057	b,f
72066	···	<258	···	>2.9	>0.046	3	>0.089	b,f
73772	···	<199	···	>2.3	>0.033	6.3	>0.24	b,f
78466	···	<204	···	>2.1	>0.044	5.1	>0.19	b,f
85354	···	<170	···	>1.4	>0.025	19	>0.74	b,f
92270	131	···	6.9	···	0.24	1.9	>0.067	a,f
100469	131	···	21	···	0.32	0.88	>0.027	a,f
110365	···	<166	···	>2.7	>0.037	9	>0.35	b,f
115527	···	<140	···	>3.3	>0.11	4.3	>0.16	b,f
117972	367	>283	0.31	<0.87	0.0062	23	>19	d,e

Note. — The columns list blackbody temperatures of thermal excesses, inferred seperations from the star and fractional bolometric luminosities.
Notes:
a. $W4$-only excess: The $W3$ excess flux in this case was either saturated or $> 3\sigma$ below the photosphere. A limiting temperature and radius for the dust cannot be determined.
b. $W4$-only excess: The $W3$ excess flux is formally negative and an upper limit on the excess flux is used to place a 3σ limit on the dust temperature and radius.
c. $W4$-only excess: Both the $W3$ and the $W4$ excesses were used to calculate a dust temperature and radius. An upper limit on the $W3$ excess flux was used to calculate a 3σ limit on the dust temperature and radius.
d. $W3$-only excess: Both the $W3$ and the $W4$ excesses were used to calculate a dust temperature and radius. An upper limit on the $W4$ excess flux was used to calculate a 3σ limit on the dust temperature and radius.
e. A lower limit on the fractional luminosity was calculated for a blackbody with peak emission at $\lambda = 12\mu m$ as described in Section 3 in PMH14.
f. A lower limit on the fractional luminosity was calculated for a blackbody with peak emission at $\lambda = 22\mu m$ as described in Section 3 in PMH14
g. Significant excesses were found both at $W3$ and $W4$. The dust parameters are calculated exactly using a blackbody for the excess.

Chapter 5

Identification of Warm Debris Disks in the Galactic Plane and Out to 120 pc

The work presented here is a preliminary analysis of the census of warm debris disks in Hipparcos beyond 75 pc, identified from their $W3 - W4$ color excess. This work is built upon the last two chapters, and is done in collaboration with Dr. Stanimir Metchev, Dr. Aren Heinze, and Joseph Trollo

5.1 Introduction

Up until now, we have restricted the identification of excesses to within a 75 pc volume around the Sun. This is because stars within this volume have accurate parallaxes, and make excellent targets for further disk characterization through high-contrast imaging techniques. These stars also have very little to no line-of-sight extinction from interstellar dust, as they located within a structure known as the Local Bubble (Lallement et al., 2003).

However, the nearby solar neighborhood has been heavily scrutinized for debris disks by the last thirty years of disk detections, by missions including *IRAS*, *Spitzer*, and now *WISE*. If one considers the census of debris disks within 120 pc, roughly 80% reside within a volume 75 pc, while only ∼20% are within the volume between 75 and 120 pc. However, by looking at the distribution of *Hipparcos* main-sequence stars within 120 pc, the ratio of stars between 0–75 pc and 75–120 pc is nearly 50/50. In addition, the density of stars increases at lower galactic lattitudes. However, only ∼8% of known debris disks are within the galactic plane. Usually, the galactic plane is avoided because of the density of stars, which can cause source confusion and false detections. But if we are

to believe the incidence rate of disks derived by the last thirty years of disk detections, there are a vast number of new debris disks that have yet to be identified, both beyond 75 pc, and within the galatic plane.

Since we already have the necessary tools in place, and our parent sample of stars (see § 2.2.1 in Chapter 3) already extends out to 120 pc, it may seem like a relatively simple matter to merge the science and parent samples and identify excesses of the entire parent sample. Unfortunately, stars beyond 75 pc are more likely to be affected by line-of-sight extinction. The interstellar dust will decrease the intensity of shorter wavelength light from a star, thereby artificially boosting any measured mid-IR excess flux. Thus, an accurate assessment of an excess beyond 75 pc, for a large sample of stars, requires a priori knowledge of the extinction level for all our stars at the various *WISE* bands.

Nonetheless, one can largely avoid the effects of interstellar extinction, by using the $W3$ and $W4$ bands to search for $W3 - W4$ single color excesses. Interstellar extinction is greater at the $W1$ and $W2$ bands than at $W3$. In addition, the data show a relatively flat slope for the IR extinction curve between 10 and 20μm (Wang et al., 2014). From Kitchin (2004), the extinction from 12 and 25μm is $\frac{A_{[12]}-A_{[25]}}{A_V} = 0.014$ mag. Attributing the $W3$ and $W4$ bands to be analogous to the *Spitzer* IRAC and MIPS bands indicates that the magnitude of the extinction will be small and any extinction felt by $W3$ will be roughly of the same magnitude felt by $W4$, preserving the measured infrared excess flux. In this study, we investigate the presence of warm and faint excesses at $W4$ all the way out to 120 pc, by identifying significant $W3 - W4$ color excesses. In addition, we include stars within the galactic plane by first removing stars contaminated from blended sources by using our astrometric offset analysis, which we introduced in § 4.4.

5.2 Sample Selection

We used a subset of the sample of *Hipparcos* stars used in § 2 of Chapter 3. To summarize, we selected main sequence *Hipparcos* stars with well behaved *WISE* All-Sky photometry in the $W3$ and $W4$ bands. Our parent sample consists of stars within 120 pc with optical Tycho colors constrained to -0.17 mag $< \mathrm{B_T} - \mathrm{V_T} < 1.4$ mag (late B to K spectral types). Since we are only interested in the $W3 - W4$ colors for this study, saturation corrections to the $W1$ and $W2$ photometry were not necessary. Filters from § 2.2.1 in Chapter 3, that are relevant to the $W3$ and $W4$ bands, were placed on our parent sample of stars.

In contrast to the last two studies, here we include stars within the galactic

plane. This adds an additional 766 *Hipparcos* stars with well behaved $W3$ and $W4$ photometry to our parent sample, bringing the number of stars in our $W3-W4$ parent sample to 15199. We would also like to point out that in this study, we increase our science sample out to 120 pc. Since in this study we seek excesses from *Hipparcos* stars out to 120 pc, our science and parent samples are identical.

5.2.1 Culling the Parent Sample via unWISE Images

The higher angular resolution *WISE* images from the unWISE image service Lang (2014) afford us the opportunity to identify sources that are potentially contaminated from blended point sources (e.g., active galactic nuclei, luminous infrared galaxies, other stars, etc.) or extended emission from interstellar IR nebulosity. Contaminated sources will manifest themselves as astrometric offsets, calculated from the centroid positions between the $W3$ and $W4$ images or by using different sized apertures in the $W4$ band to calculate the star's astrometric offset. In Chapter 4, our goal was to identify contaminants amongst the excesses we had already discovered. In contrast, here we aim to reject potentially contaminated stars *prior* to excess identification.

In short, we aimed to identify point source contamination by rejecting stars with significant $W3$-to-$W4$ relative centroid offsets ($\Delta r_{W3,W4} = |\vec{r}_{W3} - \vec{r}_{W4}|$), as well as identify and reject stars contaminated from extend source emission from their $W4$-narrow to $W4$-wide centroid offsets ($\Delta r_{W4} = |\vec{r}_{W4} - \vec{r}_{W4,wide}|$). For this analysis, we extracted centroids for all the stars from their unWISE $W3$ and $W4$ images. A detailed description of these procedures is given in § 4.4.2.

We looked for contaminated sources by identifying stars with statistically significant offsets. The density clouds in Figures 5.1 and 5.2 show the distributions of 15304 stars from our $W3-W4$ parent sample, prior to applying the filters we placed in § 2.2.1 of Chapter 3. The plots show the distribution of our stars' $W4$ SNRs as a function of the $W3$-to-$W4$ relative centroid offsets ($\Delta r_{W3,W4}$) as well as a function of the $W4$-narrow to $W4$-wide centroid offsets (Δr_{W4}). Low $W4$ SNR stars will be larely affected by small scale background variations, thus shifting the distribution at lower SNRs toward larger separations, while the opposite effect will occur for stars at higher SNRs. Thus, a natural upper envelope to the distribution arises, where stars above that envelope will be rejected.

The upper envelopes in both distributions were calculated by fitting an exponential curve to the $\Delta r_{j,max}$ points in log-log space, and using the same techniques outlined in § 4.4.2 to calculate $\Delta r_{j,max}$. We also kept the same fixed 1/3 pixel lower limit for both analyses. In other words, stars are not

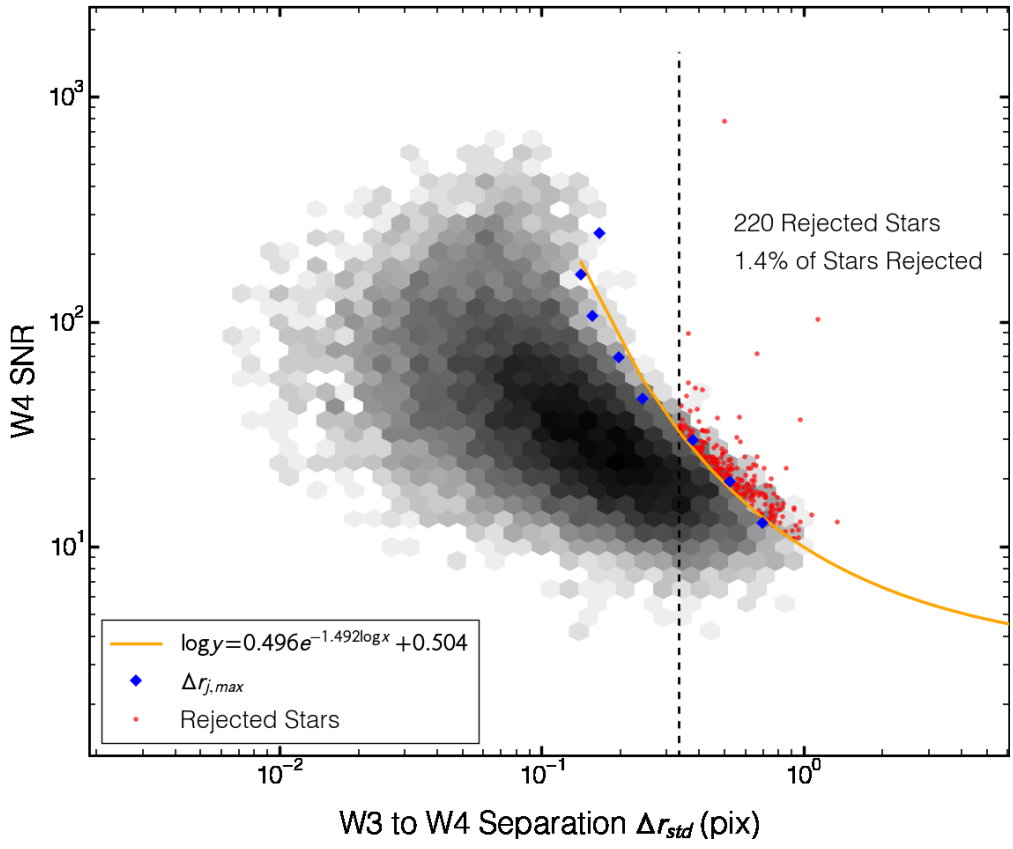

Figure 5.1: Distribution of relative positional offsets of stellar centroids between $W3$ and $W4$ using images from the unWISE image service, plotted with respect to the $W4$ SNR calculated from the unWISE images. The black/gray density cloud represents the density of 15304 Hipparcos stars from the parent 120 pc sample. The black-dotted line represents our separation cut-off (1/3 pixels) below which stars are not rejected. Our rejection threshold (orange dotted line) was fit to $\{\Delta r_{j,max}\}$ (dark-blue diamonds), calculated as described in Section 4.4.2. Rejected stars to the right of the vertical dotted black line and above the orange dotted line are shown as red dots. These are deemed to be contaminated by an unrelated nearby point or extended source seen in projection.

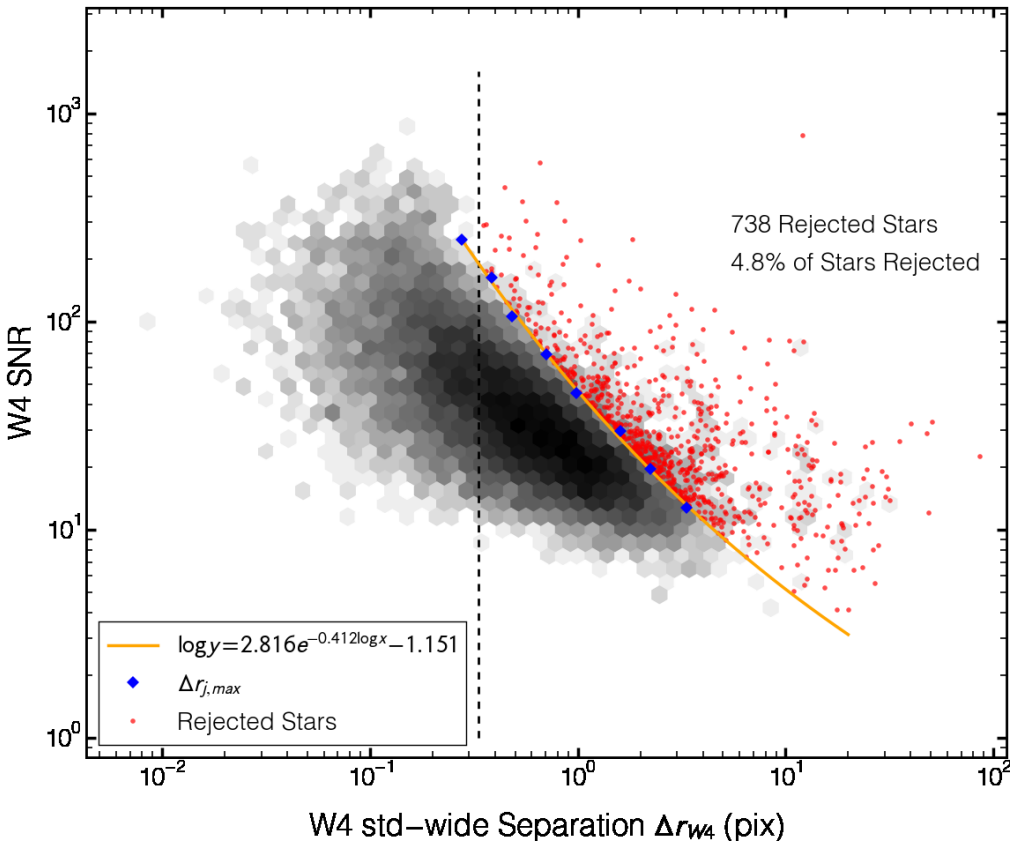

Figure 5.2: Distribution of relative positional offsets of stellar centroids between a narrow 2.5 pixel radius and wide 10 pixel radius apertures, as described in Section 4.4.1. The plot elements are the same as those described in Figure 5.1. Rejected parent sample stars are marked as red dots.

rejected below this separation. The red points in Figures 5.1 and 5.2 show stars from the parent sample that are likely contaminated by blended point sources or extended emission. Two hundred and twenty stars were rejected from the $\Delta r_{W3,W4}$ vs. $W4$ SNR analysis, and 738 stars were rejected from the Δr_{W4} vs. $W4$ SNR analysis. The union of these two sets show that a total of 897 stars should be rejected. Out of the 897 rejected stars, 174 reside in the galactic plane, leaving 592 galactic plane stars in our parent sample. Our final $W3-W4$ parent sample is comprised of 14302 main-sequence *Hipparcos* stars with well behaved $W3$ and $W4$ photometry.

The 897 rejected stars account for 6.27% of the original parent sample. Based on our assumptions, the photometry of all these stars must be contaminated by either extended emission or nearby blended point sources. Although it is difficult to verify this claim, we show in the following section that the distribution of excess significances are much better behaved after removing these stars, implying to some extent that our analysis is doing a good job of cleaning the parent sample of stars.

5.3 IR Excess Identification

Our excesses are selected using the same procedures described in § 2.5 in Chapter 3 and the improved methods for identifying single-color excesses in § 4.3.1. We use Equation 4.1 to determine the significance of the color excess for each star. Since we wish to identify excesses with $W3-W4$ colors only, the excess significance takes on the form of

$$\Sigma_{E[W3-W4]} = \frac{W3-W4-W_{34}(B_T-V_T)}{\sigma_{34}}, \tag{5.1}$$

where $W_{34}(B_T-V_T)$ is the empirically derived $W3-W4$ photospheric color, and σ_{34} is the total error term which includes the photometric and photospheric uncertainties. Both of these quantities are derived in § 2.5 in Chapter 3.

Figure 5.3 shows the distribution of $\Sigma_{E[W3-W4]}$ for our parent sample of stars. We selected excesses such that their $\Sigma_{E[W3-W4]} \geq \Sigma_{E[W3-W4]_{99.5}}$. $\Sigma_{E[W3-W4]_{99.5}}$ is our 99.5% confidence threshold, beyond which 0.5% of stars are false-positive detections. In other words, our analysis is set to identify excesses up to a 0.5% false-discovery rate (FDR). $\Sigma_{E[W3-W4]_{99.5}}$ was calculated using the same procedures that we described in § 4.3. For this analysis, we determined $\Sigma_{E[W3-W4]_{CL}} = 2.894$, marked as the dotted black line in Figure 5.3.

We also performed the same analysis for a subset of the parent sample which contained the stars we rejected due to their astrometric offsets, as described in § 5.2.1. From the Σ_E distribution that included these rejected stars,

we calculated a threshold of $\Sigma_{E[W3-W4]_{CL}} = 3.701$ — a threshold larger than the one obtained when we exclude these rejected stars. The smaller cut off obtained after rejecting the contaminated stars is due to the removal of stars in the uncertainty distribution. This gives us a little bit of an indication that our rejection of astrometric outliers is working to increase our detection to a larger set of real excesses.

Our selection process identified 640 stars with significant $W4$ excesses. Out of the 640, we expect 3.2 (= 640×0.5%) of our excesses to be spurious false-positives. In addition, we still need to remove excesses which may be contaminated from interstellar cirrus clouds. Our astrometric offset rejection in § 5.2.1 does not guarantee rejection of all such contaminated stars, as large patches of extended interstellar cirrus may appear as uniform background emission to our centroiding algorithm. Thus, we visually inspected the four band *WISE* Atlas images and removed 119 sources that appear to be contaminated from interstellar cirrus. This is a significant number of stars which are being rejected from visual screening, even though we are using astrometric offsets to identify similar contaminants. However, the visual checks are quite subjective, and as a result, exclude stars that may not be contaminated. However, such a conservative analysis aids in decreasing the population of false excesses.

Since we are using a subset of the parent sample from Patel et al. (2014a), contaminated excesses we rejected in that study appear in this one as well. Therefore, we list the rejected sources in Table 5.1, excluding those which we listed in Chapters 3 and 4. In total, we identified 522 significant $W3 - W4$ excesses out to 120 pc. Out of these, 210 are within 75 pc and were were identified by our previous two studies in Chapter 3 and 4. This leaves 312 stars, of which 301 are beyond 75 pc. The 11 new <75 pc excess stars are within the galactic plane ($|b| < 5°$).

5.4 Results

From the 522 debris disks we identified in this study, 16 reside within the galactic plane $|b| < 5°$. Out of the 312 $W4$ excesses that we had not identified in our previous studies, 225 stars are new 22μm excesses, previously unreported in the literature. Of these, 222 stars do not have previous detection of an excess at any other wavelength, either. In addition, eight of the 225 new excesses reside within 75 pc, all in the galactic plane.

We also determined the stellar and dust properties of the 522 excess stars, which are listed in Tables 5.2 and 5.3, respectively. We performed the same analysis as in § 4.5 to derive these parameters by performing photospheric model fits. We used NextGen grid models from Hauschildt et al. (1999) to fit

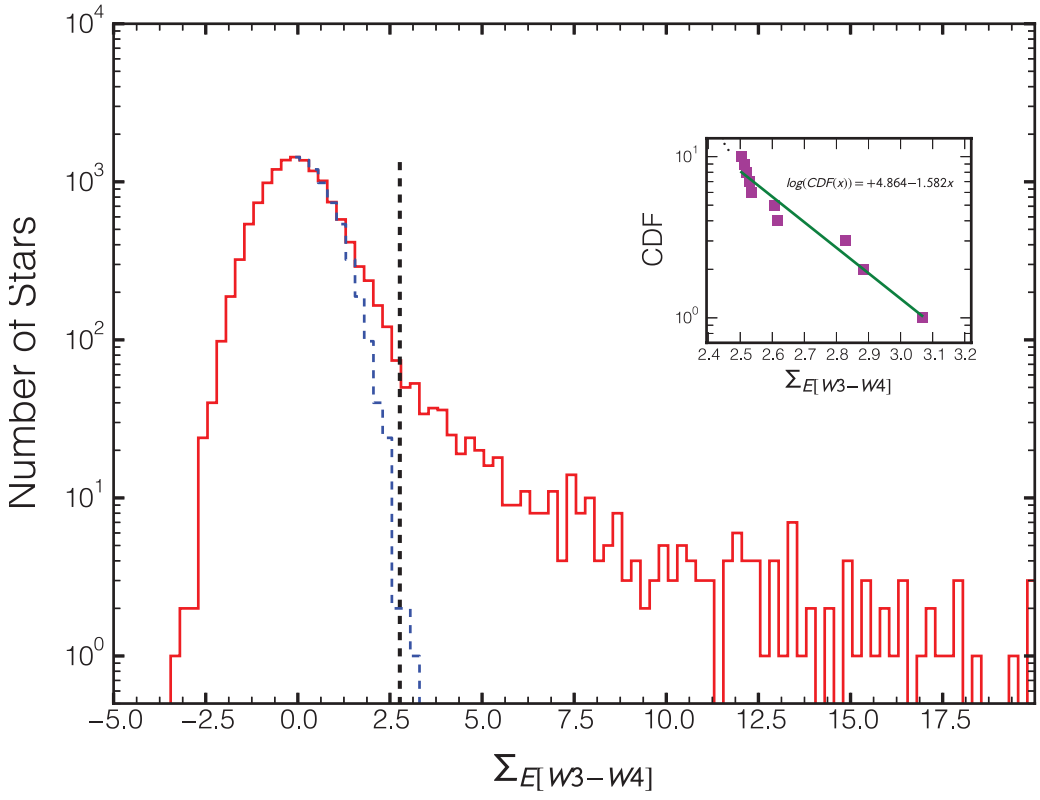

Figure 5.3: Distribution of $\Sigma_{E[W3-W4]}$ for all our stars in the parent sample (solid red histogram). The blue dashed histogram is the uncertainty distribution, created by reflecting all the values of $\Sigma_{E[W3-W4]} < 0$ about the mode of the red distribution. Excesses are selected to the right of our FDR threshold of 0.5% ($\Sigma_{E[W3-W4]_{99.5}}$), denoted by the vertical dashed green line. The inset shows a semi-log fit of a line to the last ten points in the reverse cumulative distribution function of the uncertainties. The fit smoothes over the stochasticity in this sparely populated region of the uncertainty distribution to attain a more accurate estimate of the FDR threshold.

the optical and near-IR photometry from *Hipparcos* and *2MASS*. We scaled the derived photospheric model to the mean of the $W1$, and $W2$ photometry, where we have again applied the saturation corrections determined in § 2.4 in Chapter 3. We used the $W4$ excess flux and $W3$ or 3σ upper limit to the $W3$ excess flux to determine the best fit blackbody temperature for the dust emission. We have also placed upper limits to all of our dust temperature estimates using the 3σ upper limit to the $W3$ excess flux. This allows us to constrain the dust properties to some extent, since we do not have longer wavelength information for all of our stars. Without this information it is difficult to ascertain whether the dust is emitting from warm grains, or whether the excess we measure is the Wien emission of much colder dust.

5.5 Discussion

5.5.1 Survey Sensitivity

A goal of this study was to identify faint warm debris disks with *WISE*, although our detections need to be placed in context to literature excesses. We cannot characterize the full extent of the disk brightness f_d (Equation 1.12) since we only have excess flux information at $W3$ and $W4$. However, we compare the relative flux at $W4$ (R_{22}; Equation 1.11) of the candidate debris disk hosts from our survey to the relative flux of disks detected at similar wavelengths with *Spitzer*. Although it would make sense to compare the relative flux of our disks at 22μm to those detected by *IRAS* at 25μm, the latter sample is rather small given that the majority of *IRAS* disks were detected in the far-IR.

Chen et al. (2014) conducted a study to characterize the SEDs of of 571 stars with archival *Spitzer*/IRS observations, supplemented with data from observations using *Spitzer*/MIPS at 24μm. In addition, Lawler et al. (2009) conducted an unbiased survey to detect Zodiacal light emission from 152 solar type stars in both the *Spitzer*/IRS short (8.5–12μm) and long (30–34μm) bands. We test our sensitivity limits in context to these two surveys: using the relative 24μm flux from Chen et al. (2014) and the relative 32μm flux from Lawler et al. (2009).

Figure 5.4 shows the relative fluxes of the excesses detected from our surveys at 22μm, excesses with *Spitzer*/MIPS24 measurements from Chen et al. (2014), and excesses from Lawler et al. (2009) at 32μm — all of them as a function of *2MASS* K_s magnitude. What is easily evident is that the *Spitzer* surveys are sensitive to fainter mid-IR excesses compared to *WISE*. This does not come as a surprise, because *Spitzer* is a pointed telescope. The *Spitzer*/IRS

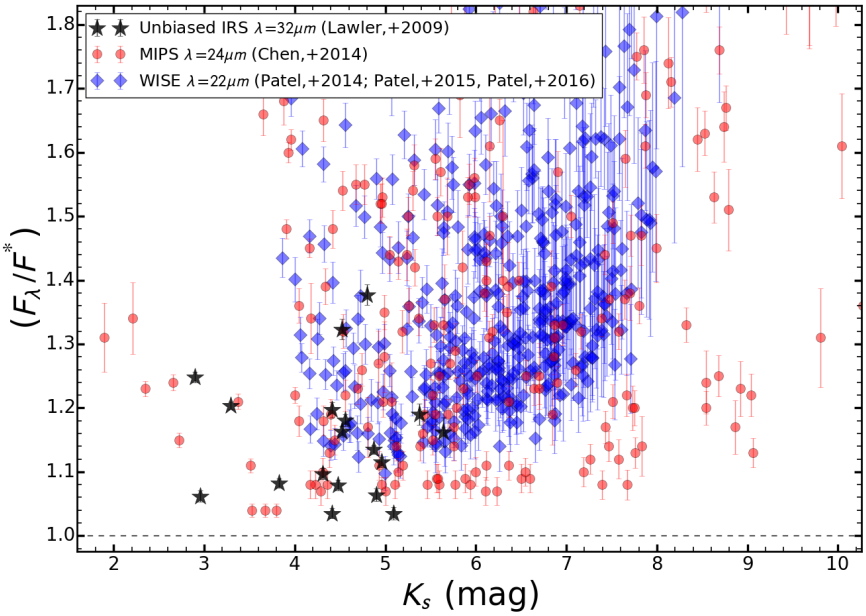

Figure 5.4: The relative fluxes plotted as a function of their *2MASS* K_s magnitudes. The relative fluxes are plotted for our *WISE* excesses from Chapters 3, 4, and this study, in addition to stars with 24μm excesses from Chen et al. (2014), and 32μm *Spitzer*/IRS excesses from Lawler et al. (2009). Data in the figure extend beyond the top of the y-axis boundary. The boundary is set to focus on the faint-excess detections, near the sensitivity limits of each survey.

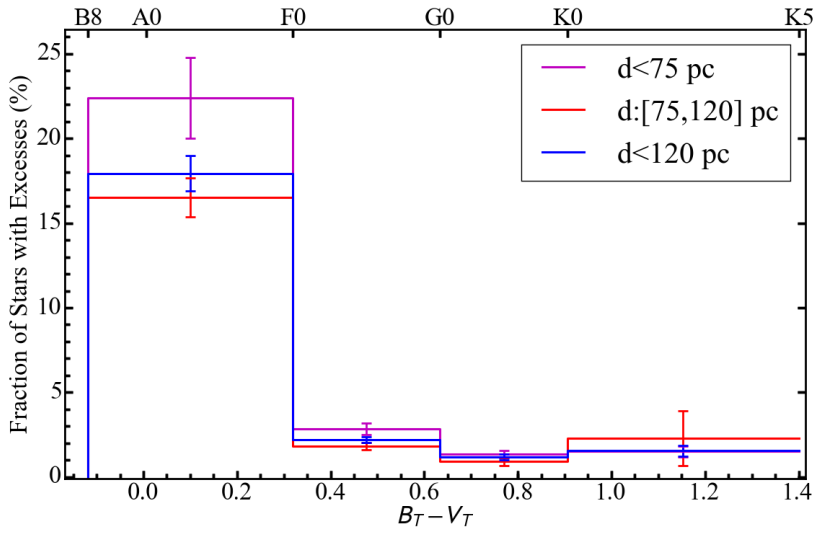

Figure 5.5: Fraction of *WISE W*4 excesses detected as a function of spectral type in different distance volumes.

survey detected dust at levels 1.5× fainter than surveys performed with the *Spitzer*/MIPS instrument (4% and 6% above the photosphere, respectively), mainly because the short wavelength end of the IRS spectra can be used to calibrate the photospheric flux, and the contemporaneously obtained longer wavelength flux can be used to measure the photospheric flux.

Our *WISE* survey, on the other hand, seems to find excesses down to no less than ∼10% of the photospheric emission. This is also only for the brightest stars. At fainter stellar magnitudes, the detection sensitivity deteriorates further. This is mainly due to the fact that *WISE* is a flux limited survey, and for fainter stars, the photometric uncertainties increase, thereby decreasing the significance of any IR excess. Even though our sensitivity with *WISE* is a factor of 2–2.5× poorer than with *Spitzer*, the much larger volume sampled by *WISE* compared to the individual pointed surveys with *Spitzer* allows a much more complete census of solar neighborhood debris disks.

5.5.2 Overall Expansion of Disk Census

With our large sample size, we can robustly determine the incidence rate of 22μm excesses for a given spectral type. Figure 5.5 shows the incidence rate of our excesses as a function of $B_T - V_T$ (spectral type), plotted alongside 1σ error bars. We show three different curves, corresponding to the incidence rates for three different volumes, from which we conclude that there does not seem to

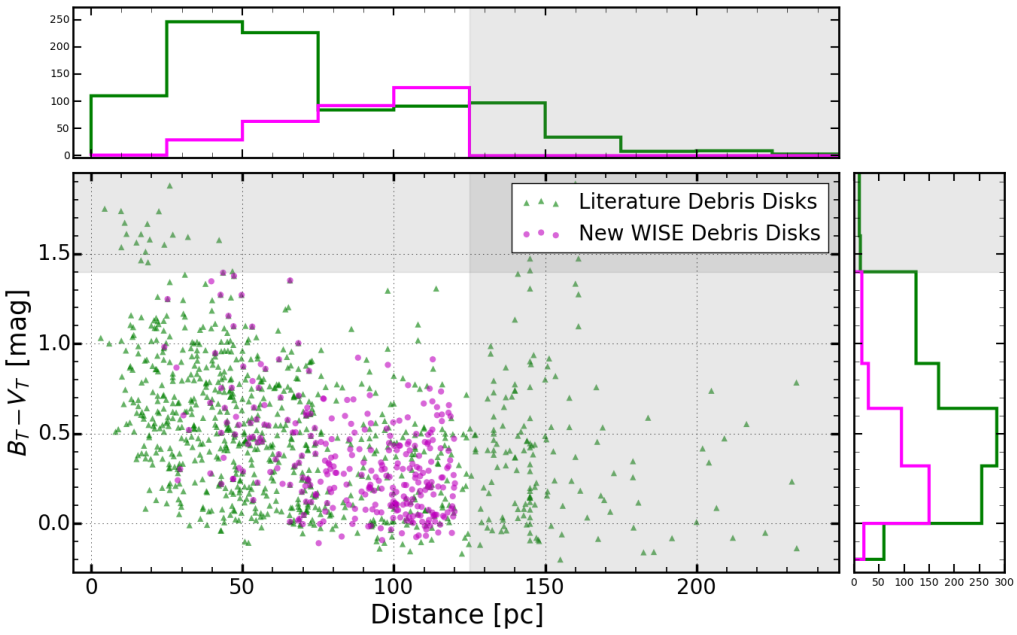

Figure 5.6: $B_T - V_T$ colors as a function of distance for all new $W4$ excesses from our three studies, along with debris disks detected at any wavelength in the literature. Marginalized distributions are also plotted on the top and right for each parameter. The grey shaded areas indicate the regions of the parameter space that our surveys do not explore.

be any statistically significant deviation as a function of distance. We report a $18.0 \pm 1.0\%$ incidence rate of $W4$ excesses for B and A stars, $2.2 \pm 0.2\%$ for F stars, $1.2 \pm 0.2\%$ for G stars and $1.6 \pm 0.3\%$ for K stars.

What is interesting is how this incidence translates into a total census of disks based on expanding our search to a larger volume. In Figure 5.6, we plot the $B_T - V_T$ of our new *WISE* disks alongside those found in literature (detected at any wavelength) as a function of their distances. The collapsed distance distribution are independent of each other. At distances <75 pc, there are clearly a greater number of disks which have been found by other surveys, although our past studies have contributed significantly to the census in this volume. By expanding to 120 pc, we see that within this full volume, we have increased the census of disks by 40%. However, if we only take the volume of space between 75 and 120 pc, we see that our surveys have increased the census of debris disks by 130%.

5.5.3 Excesses at False-Discovery Rates > 0.5%

We select excesses above $\Sigma_{E[W3-W4]_{34}}$, such that 99.5% of our stars are bona-fide IR excesses, and not caused by a statistical fluke. However, below this threshold, there are still a substantial number of potential excesses, even if the FDR is higher than 0.5%. The problem is that one cannot claim with high confidence that any particular star above the 0.5% FDR is a bona-fide excess, give the high rate of contamination. What we can ascertain is how many bona-fide excesses exist below $\Sigma_{E[W3-W4]_{99.5}}$, by calculating the false omission rate (FOR). The FOR is defined as the number of stars in the uncertainty distribution below $\Sigma_{E[W3-W4]_{99.5}}$ over the number of stars in the full Σ_E distribution below $\Sigma_{E[W3-W4]_{99.5}}$, but greater than 0. For this study, the FOR = 89.2%. In other words, 10.8% of the stars below our threshold, but with $\Sigma_{E[W3-W4]} > 0$, likely possess IR excess emission.

The 10.8% FOR corresponds to 724 low-significance excesses, although it is likely that some of these may still suffer from contamination by interstellar cirrus. In § 5.3 we removed 18% of candidate excesses because of cirrus contamination. It is possible that the contaminated fraction among the lower-SNR excesses is higher. Nonetheless, we still expect that a debris disk population of roughly twice the number of our *WISE*/*Hipparcos*-identified disks exists in *WISE*. That is, the overall debris disk occurrence fractions are a factor of ∼2 higher when one accounts for 2–3× fainter, marginal excesses: ∼40% for B and A stars, and ∼4–5% for FGk stars. This conclusion agrees well with the *Spitzer*/MIPS findings on B and A stars by Su et al. (2006) and the *Spitzer*/IRS results on field-aged FGK stars by Carpenter et al. (2009a).

5.6 Conclusion

In this preliminary study, we expanded upon the study done in Chapter 3, and incorporated improvements and verifications techniques in Chapter 4 to identify 22μm excesses around *Hipparcos* main-sequence stars out to 120 pc and within the galactic plane. The relatively low count of disks in the 75–120 pc volume compared with the tally of disks within 75 pc, warrants an investigation of the census of disks beyond 75 pc, which has been left incomplete to date.

We use $W3-W4$ color excesses — mid-IR colors that are minimally affected by interstellar extinction — to search for these excesses. Due to the past calibrations imposed upon our sample of stars, including the astrometric offset rejection of potentially contaminated stars, we identify 522 significant $W3-W4$ excesses at <0.5% FDR, 225 of which are new 10–30μmexcesses. Our study also finds 8 excesses within the galactic plane. The sensitivity of our survey is shown to be clearly dependent on the apparent brightness of the star, and dominated by the $W4$ photometric uncertainties. However, we are able to probe to sensitivities down to ∼10% of the photospheric flux, and have increased the census of disks in the solar neighborhood by 40% within 120 pc and 130% within the volume between 75 and 120 pc.

Table 5.1. Rejected *WISE* Excesses in 75–120 pc Volume

HIP ID	WISE ID	Rejection Reason
HIP58	J000041.57+621032.7	1
HIP2046	J002556.62+035531.2	1
HIP2415	J003047.12+160215.4	3
HIP5333	J010811.69+550920.5	1
HIP7248	J013323.57+713316.0	1
HIP9018	J015607.61+575801.1	1
HIP9278	J015914.97+670236.4	1
HIP10690	J021733.88+580111.4	1
HIP13460	J025318.68+605110.9	1
HIP14592	J030825.93+570045.5	1
HIP15902	J032448.99+283908.6	1
HIP16459	J033201.49+673508.0	3
HIP16612	J033347.74+521716.5	1
HIP16689	J033442.86+065035.5	1
HIP17575	J034550.58+550349.5	1
HIP17675	J034710.70+514222.3	1
HIP17704	J034729.46+241717.7	1
HIP17886	J034932.67+330529.0	1
HIP20861	J042813.46+450244.6	1
HIP21586	J043808.01+511009.9	1
HIP22306	J044815.73+234545.9	1
HIP24403	J051405.75+211325.3	1
HIP25006	J052114.72-072847.9	1
HIP25197	J052327.87+573239.4	1
HIP25419	J052614.03+164153.6	1
HIP25453	J052638.83+065206.9	1
HIP26560	J053852.54+350441.1	1
HIP26588	J053905.54-055351.3	1
HIP28224	J055748.66+020356.4	1
HIP41690	J082955.70-451104.6	1
HIP43701	J085400.46+201349.4	1
HIP48376	J095141.32-543935.9	1
HIP48627	J095457.89-444839.2	1
HIP49131	J100139.00-552905.8	1
HIP54846	J111342.81-632411.3	1
HIP54854	J111350.78-525121.7	1
HIP55069	J111628.56-603403.8	1
HIP55606	J112331.01-091521.3	1
HIP55909	J112735.13-555414.5	1
HIP57022	J114127.88+005701.0	1
HIP57285	J114447.30-581553.3	1
HIP57291	J114450.39-584214.1	1
HIP59502	J121210.23-632714.8	1
HIP59960	J121753.15-555831.9	1
HIP60068	J121903.99-663934.7	1
HIP62026	J124249.72-555649.2	1
HIP62403	J124718.84-661414.7	1
HIP62538	J124853.12-565111.4	1
HIP62576	J124917.39+273308.9	2
HIP63205	J125658.67-600835.0	1
HIP65100	J132030.06-663202.5	1
HIP65783	J132907.80-644032.9	1
HIP66075	J133242.44-554939.4	1
HIP66632	J133928.24-571750.0	1
HIP66963	J134328.49-543643.7	1
HIP67189	J134609.32-683357.2	3
HIP69011	J140740.78-484214.7	3
HIP70035	J141951.26-611623.5	1
HIP70050	J142008.31-280256.6	3
HIP71585	J143824.86-351635.8	3
HIP71645	J143915.59-642456.9	1
HIP74511	J151334.72-625639.0	1
HIP75134	J152112.66-541730.6	1
HIP75778	J152849.17-535536.4	1
HIP76234	J153420.83-392057.4	3
HIP76782	J154037.80-253533.3	1
HIP76801	J154051.88-292403.2	1
HIP77394	J154756.48-255913.0	1
HIP78085	J155639.02-423347.5	1
HIP78532	J160158.33-465414.2	1
HIP78533	J160158.85-373203.9	1

Table 5.1 (cont'd)

HIP ID	WISE ID	Rejection Reason
HIP79026	J160747.76-370036.1	1
HIP80025	J162008.82-361717.1	1
HIP80171	J162155.29-245929.7	1
HIP80770	J162927.55-331913.4	1
HIP80799	J162954.56-245846.5	1
HIP81106	J163355.15-425320.9	1
HIP81467	J163820.66-491334.9	1
HIP81673	J164104.61+361204.1	3
HIP83522	J170409.70-303936.1	1
HIP83711	J170629.53-104823.0	3
HIP84055	J171103.45-313458.7	1
HIP84164	J171221.84-463352.9	3
HIP84359	J171448.66-484229.2	1
HIP84445	J171551.34-301239.1	1
HIP86124	J173604.59-171822.4	3
HIP88460	J180341.50-455145.8	1
HIP88924	J180906.63-092654.7	1
HIP89583	J181649.60-112423.3	1
HIP92973	J185627.75-432104.8	3
HIP94371	J191227.61+165058.4	1
HIP95002	J191953.09+113206.2	1
HIP95696	J192751.84+085811.6	1
HIP95717	J192806.33+175047.7	1
HIP98894	J200455.18+260311.2	1
HIP100767	J202551.22+393753.2	1
HIP101449	J203338.48+532805.6	1
HIP103213	J205439.94+461352.2	1
HIP103269	J205516.80+421756.6	1
HIP103614	J205934.78+611654.4	1
HIP103648	J210000.36+425552.7	1
HIP103994	J210411.92-290855.8	1
HIP104900	J211456.52+642953.3	1
HIP105169	J211816.29-752048.6	1
HIP108414	J215747.44-150724.1	3
HIP108689	J220103.44+555955.3	1
HIP109713	J221323.87+530914.9	1
HIP110214	J221931.54+644718.2	1
HIP110327	J222045.72+560649.6	1
HIP116085	J233123.69+590957.0	1

Note. — Rejection reasons:
1. Contamination by line-of-sight interstellar cirrus based on visual "by-eye" inspection.
2. Rejected on basis of potential spectroscopic component. Warning raised by Wu et al. (2013).
3. Confusion due to nearby *WISE* source.

Table 5.2. Stellar Parameters of $W4$ Excess Hosts within 120 pc

HIP ID	WISE ID	SpT[a]	Dist.[b] (pc)	$T_\star$ (K)	$R_\star$ ($R_\odot$)	F_{W3} (mJy)	$F_{W3,\star}$ (mJy)	F_{W4} (mJy)	$F_{W4,\star}$ (mJy)	$F_{W3}/F_{W3,\star}$[c]	$F_{W4}/F_{W4,\star}$[c]
301	J000344.39-172009.4	B9IVn	83	9840	3.5	437±6	449	170±4	128	0.974	1.32
1829	J002311.98+200509.1	F0	105	7245	1.2	24.5±0.4	24	12.3±0.9	6.88	1.02	1.79
2496	J003140.75-014737.2	A0	107	8762	1.6	54.7±0.8	49.6	39.9±1	14.2	1.1	2.81
2539	J003214.05+345937.8	A5IV	96	8089	1.9	81.7±1	82.4	30.6±1	23.6	0.992	1.3
4303	J005508.13+165435.7	A5	107	7411	1.5	35.3±0.5	36.3	14.3±1	10.4	0.973	1.37
4366	J005558.49+271233.8	A5IV	78	8308	2.0	142±2	144	63.7±2	41.1	0.987	1.55
4630	J005926.25+400918.2	A0	110	8185	1.5	38±0.5	38.2	17.7±0.9	10.9	0.996	1.62
5233	J010655.27+705552.9	A2	113	8238	2.3	85.2±1	86.4	36.1±1	24.8	0.986	1.46
5626	J011217.17+794026.2	A3V	83	9273	2.3	179±2	174	114±2	49.8	1.03	2.29
7051	J013053.11+341026.1	A3	120	7506	1.4	25.1±0.4	24.9	12.6±0.8	7.14	1.01	1.77
7283	J013352.80+890056.0	A3V	103	8632	2.1	90.7±1	90.4	33.8±1	25.9	1.0	1.31
7943	J014203.52+351444.3	B9IV-V	84	10000	2.1	141±2	131	80.6±2	37.6	1.07	2.14
7965	J014220.62+680234.8	A0pSiSr	119	10000	3.0	142±2	141	64.9±2	40.5	1.0	1.6
8250	J014611.92-451728.3	F5V	99	6571	1.4	33.6±0.5	34	12.9±0.9	9.76	0.987	1.32
8417	J014835.89-261513.1	F0V	103	7339	2.1	77±1	78.3	27.9±1	22.4	0.983	1.25
8920	J015450.36+211822.3	G0	96	5792	1.4	655±8	33.2	547±9	9.6	19.7	57
9285	J015919.63-262555.8	A0V	114	9396	1.8	56.5±0.8	58.1	21.8±1	16.6	0.974	1.31
10320	J021254.47-304325.5	A0V	98	9175	3.2	263±4	245	114±3	70	1.07	1.63
10355	J021329.33+404724.6	A3	109	8279	1.6	42.5±0.6	42.9	16.4±1	12.3	0.989	1.33
11522	J022834.46+135235.0	F5	112	6900	1.3	23.8±0.4	24.1	11.6±1	6.92	0.987	1.67
11696	J023050.75+553253.3	F3V	55	6078	1.8	621±9	185	403±9	53.1	3.36	7.59
11821	J023230.04-270010.9	A4V	95	7754	1.5	49.7±0.7	50.7	18.6±0.9	14.5	0.981	1.28
12876	J024532.75-673659.4	A2IV/V	87	8775	3.7	402±5	404	136±3	116	0.995	1.17
13063	J024755.37+553648.5	A0	106	8377	1.8	63.6±0.9	63.8	28.6±1	18.3	0.996	1.57
13394	J025223.08+632434.1	G0	31	6060	1.1	188±2	197	70±2	57	0.953	1.23
13682	J025614.04+040254.3	A0	116	9396	1.2	26.4±0.4	23.9	18.4±1	6.84	1.1	2.68
13872	J025839.71-041231.4	A2	103	7757	1.3	32.1±0.5	32	12.6±0.7	9.16	1.0	1.37
15152	J031517.13-370230.1	F5V	98	6355	1.3	28.6±0.4	28.6	11±0.7	8.22	0.999	1.34
15870	J032426.11+204812.5	A1V	96	10000	1.9	91.7±1	93.5	33.8±1	26.8	0.981	1.26
15922	J032504.59+105835.1	A0	119	8341	1.8	47.2±0.7	44.6	22.2±1	12.8	1.06	1.74
15933	J032512.84-370909.6	A4V	101	8351	1.6	52.4±0.8	52.3	19.2±0.8	15	1.0	1.28
15987	J032555.86-355515.2	A1IV	108	8724	2.2	98.3±1	95.7	48.6±1	27.4	1.03	1.77
16028	J032622.54+370047.3	F2	111	6328	2.0	49.5±0.7	49.1	19.4±1	14.1	1.01	1.38
16322	J033024.45+112011.1	A0Vn	111	10000	3.4	225±3	240	77.1±2	68.6	0.938	1.12
16386	J033103.48+274353.3	B9	120	8980	1.5	34±0.5	34.5	15.3±1	9.88	0.987	1.55
16425	J033130.31+404535.4	A5	116	7517	3.0	127±2	125	47.1±2	35.9	1.01	1.31
16511	J033235.96+092224.0	B9IV	107	10000	2.5	114±2	120	40.6±1	34.2	0.951	1.19
16671	J033433.33+141033.3	F8	118	5610	2.1	43.3±0.7	42.7	20.7±1	12.3	1.01	1.68
16876	J033709.08-294948.5	A1V	119	8982	1.6	39.4±0.5	38.4	18±0.8	11	1.03	1.64
17091	J033941.18+231726.8	G	85	6041	0.7	12.3±0.3	10.4	9.81±1	3	1.18	3.27
17256	J034145.51-474632.3	A4V	100	7865	1.9	72.6±1	74.2	25.6±0.9	21.3	0.978	1.2
17391	J034327.90-333008.1	F2V	112	6787	1.5	30.5±0.4	30.1	13.9±0.7	8.64	1.01	1.61
17707	J034732.19+555518.7	B9Vnn	110	9310	2.4	113±2	115	48.2±1	32.8	0.986	1.47
17900	J034943.54+234242.4	B8V	115	10000	2.2	101±1	87.6	52.2±2	25.1	1.15	2.08
18217	J035343.41+575829.7	A5m	51	8030	1.6	199±3	205	78.3±2	58.6	0.971	1.34
18297	J035445.53+091039.1	A0	119	8736	1.5	37.3±0.6	36.4	16±1	10.4	1.02	1.53
18437	J035629.39-385743.7	A0V	106	9373	1.6	58.6±0.8	49.9	74.7±2	14.3	1.17	5.23

Table 5.2 (cont'd)

HIP ID	WISE ID	SpT[a]	Dist.[b] (pc)	$T_\star$ (K)	$R_\star$ ($R_\odot$)	F_{W3} (mJy)	$F_{W3,\star}$ (mJy)	F_{W4} (mJy)	$F_{W4,\star}$ (mJy)	$F_{W3}/F_{W3,\star}$[c]	$F_{W4}/F_{W4,\star}$[c]
18671	J035954.17-540939.9	F5V	93	6539	1.8	58±0.8	58.9	20.9±0.8	16.9	0.984	1.23
18729	J040043.70-711000.2	A1/A2V	100	8706	1.9	79.2±1	79.3	29.9±1	22.7	0.999	1.31
18863	J040238.47-004803.7	A0	113	9331	1.7	50.8±0.7	51.3	27.6±1	14.7	0.989	1.88
19215	J040707.77+382715.0	F0	118	6959	1.1	17.6±0.3	16	16±1	4.6	1.1	3.49
20171	J041926.12+210831.9	B9IV	83	10000	2.1	152±2	151	56.1±2	43.3	1.0	1.3
20279	J042047.11+645310.2	F5	112	6567	1.5	29.1±0.5	27.9	11.8±0.8	8	1.04	1.48
21238	J043321.63+430154.3	F0	71	7865	1.5	87.6±1	81.6	58.3±2	23.4	1.07	2.49
21618	J043828.81-193827.0	A9IV	101	7473	2.0	72.2±0.9	72.2	28±1	20.7	1.0	1.35
22200	J044628.06-020415.0	G0	114	6065	1.2	17.5±0.3	17.1	23.2±1	4.94	1.02	4.69
22226	J044649.54-261808.9	F3V	80	6754	1.4	50.1±0.7	50.4	31.6±1	14.4	0.995	2.19
22410	J044920.28+301822.9	F8	113	5139	1.6	25.6±0.4	25.4	13.9±1	7.35	1.01	1.89
22776	J045356.21+364526.9	G5	28	5398	0.9	120±2	125	46.1±2	36.2	0.959	1.27
23088	J045809.41+250301.0	A0V	87	9734	2.1	128±2	140	55.2±2	40.1	0.912	1.38
23451	J050227.43+072739.5	A0	112	7594	1.4	48±0.7	25.3	220±5	7.24	1.9	30.4
23621	J050441.80+145132.2	A3p	91	8329	1.7	72.4±1	74.7	31.4±2	21.4	0.97	1.47
25020	J052126.13-452028.0	F3V	102	6646	1.4	31.8±0.4	31.7	14.8±0.7	9.11	1.0	1.62
25608	J052815.34-371350.0	A0V	88	9418	2.4	175±2	179	68±2	51.2	0.977	1.33
25638	J052834.78+134044.3	A4V	94	8032	2.3	118±2	124	43.7±2	35.5	0.953	1.23
25998	J053256.39-474121.3	A3V	109	8248	1.4	33.4±0.5	33.4	35.2±1	9.56	1.0	3.68
26062	J053330.76+243743.3	B8	114	8615	1.9	251±3	55.1	1020±20	15.8	4.55	64.7
26330	J053628.33+253516.3	G0	68	6281	1.0	32.3±0.5	33.2	13.7±1	9.57	0.973	1.43
26621	J053930.48-404102.4	B8V	104	6737	1.7	43.8±0.6	41.9	22.8±0.9	12	1.05	1.9
26625	J053932.56+120013.5	F0	81	6864	1.4	50.8±0.7	50.6	22.1±1	14.5	1.0	1.53
26966	J054321.68-183327.0	A0V	75	9849	1.8	158±2	133	125±3	38.1	1.18	3.27
27259	J054642.09-361353.0	A3V	95	8814	1.6	61.8±0.9	61.5	35.1±1	17.6	1.0	1.99
27698	J055154.31-251309.5	A1V	100	8759	1.5	51.8±0.7	53.3	20±1	15.3	0.971	1.31
27713	J055207.73-090230.4	A2Vn	99	8483	2.6	155±2	151	64.3±2	43.4	1.02	1.48
28230	J055752.60-342834.2	A8IVm...	81	7372	1.3	52±0.7	51.2	43±1	14.7	1.02	2.93
28385	J055945.83+551914.3	A5m	101	7216	3.0	147±2	157	51.6±2	45	0.939	1.15
28778	J060435.05-140157.3	A9V	96	7219	1.6	52±0.8	52	21.9±1	14.9	1.0	1.47
29487	J061244.57-023017.2	A2V	118	9021	2.1	70.7±1	73.2	26.9±1	21	0.965	1.28
29510	J061300.62+272554.2	F2	98	6824	1.3	30.3±0.5	29.4	12.5±1	8.44	1.03	1.48
29606	J061420.39+394022.2	A0	103	8199	1.3	33.1±0.5	33.4	13.6±1	9.57	0.991	1.42
30088	J061957.36-135934.7	B9V	99	9977	1.5	58.1±0.8	58.1	32.7±1	16.6	1.0	1.97
30291	J062218.67-295134.6	F3V	98	6725	1.4	33±0.5	32.8	15.3±0.7	9.41	1.01	1.62
30685	J062653.73-533454.9	F0V	102	6717	1.3	26.3±0.4	26.2	10.6±0.6	7.51	1.0	1.42
30760	J062748.62-620859.5	A0V	84	8639	1.6	79.4±1	80.4	28.7±0.8	23	0.988	1.25
30939	J062936.87+082932.6	F8	48	6137	1.1	83.5±1	85.7	30.1±1	24.7	0.974	1.22
31386	J063446.90-631543.8	A7IV	89	7265	1.4	43.8±0.6	43.8	16.8±0.7	12.5	1.0	1.34
33227	J065450.56+031413.8	F0	86	6952	1.5	53.4±0.7	53.6	23.7±1	15.4	0.997	1.54
33384	J065634.52-792512.7	B9.5V	108	8322	3.8	274±4	281	93.6±2	80.6	0.973	1.16
33476	J065731.89-165321.9	A7V	111	7915	1.9	54.7±0.8	55.6	23±1	15.9	0.984	1.44
33477	J065733.27+194343.0	A5	99	7624	1.6	50.9±0.8	52.2	20.9±1	14.9	0.976	1.4
33788	J070057.19-723338.1	F3/F5V	107	6724	1.8	44.6±0.7	45.6	18.5±0.7	13.1	0.979	1.42
34276	J070620.93-433638.6	A0V	102	9570	1.8	71.2±1	72.1	37±1	20.6	0.989	1.79
35572	J072030.36-063613.1	G5	110	5873	2.6	77.5±1	79.7	27.8±1	23	0.972	1.21
36312	J072830.03-490858.4	F7V	84	6192	1.1	28.3±0.4	27.8	13±0.8	8.02	1.02	1.62

Table 5.2 (cont'd)

HIP ID	WISE ID	SpT[a]	Dist.[b] (pc)	$T_\star$ (K)	$R_\star$ ($R_\odot$)	F_{W3} (mJy)	$F_{W3,\star}$ (mJy)	F_{W4} (mJy)	$F_{W4,\star}$ (mJy)	$F_{W3}/F_{W3,\star}$[c]	$F_{W4}/F_{W4,\star}$[c]
36624	J073155.60+385345.7	A2V	81	8949	1.5	77.4±1	76.6	38.4±2	21.9	1.01	1.75
36837	J073428.83-260701.0	A0V	115	9796	1.8	62.2±0.9	60.6	32.1±1	17.3	1.03	1.85
37411	J074050.88-771614.6	F7V	91	6120	1.2	28.2±0.4	28	10.7±0.6	8.07	1.01	1.32
38403	J075203.83+455558.4	A3	104	7880	2.4	109±2	108	44.9±2	31	1.01	1.45
39510	J080431.37-671229.4	A5V	108	7641	1.6	42.3±0.6	42.3	18±0.6	12.1	0.999	1.49
39535	J080445.28+185031.2	B9V	107	10000	2.0	84.4±1	83.9	36±2	24	1.01	1.5
40706	J081833.23-363932.3	A4m...	29	7760	1.8	770±10	768	289±6	220	1.0	1.31
41765	J083100.44+185806.1	A3	83	7588	1.4	51±0.8	52.3	22.8±2	15	0.975	1.52
41891	J083232.57+222439.9	G0	112	5570	1.7	30.8±0.5	31.3	13.6±1	9.05	0.983	1.51
42090	J083443.86+362510.2	A2Vnn	109	8894	2.9	163±2	169	59.7±2	48.4	0.966	1.23
42197	J083615.57+423447.5	A2	83	7907	1.6	70.8±1	70	30.3±1	20	1.01	1.51
42353	J083805.15+093428.5	A1V	112	9798	1.9	65.9±0.9	66.5	25.8±1	19	0.991	1.36
42637	J084119.45-785747.8	B9IV	95	10000	2.5	215±3	143	147±3	41	1.5	3.58
42928	J084455.13-211004.0	A5V	84	7852	2.4	160±2	167	60.2±2	47.9	0.957	1.26
42994	J084546.93+485243.5	A0	111	8603	1.4	38.1±0.6	37.1	21.1±1	10.6	1.03	1.99
43620	J085303.76-563857.8	A0V	92	9971	1.9	106±1	105	52±1	30.1	1.01	1.73
44078	J085845.37+235800.4	A2	120	7928	1.7	39±0.6	40	16.7±1	11.5	0.974	1.46
44272	J090055.12+090303.9	G0	79	6121	1.0	22.8±0.4	22.7	11.3±1	6.55	1.0	1.73
44393	J090234.51-310103.6	A7V	96	7159	1.5	45.2±0.7	44.2	17.7±0.9	12.7	1.02	1.39
44504	J090400.40+541702.1	A2V	120	9195	3.1	155±2	158	57.9±2	45.4	0.977	1.28
44923	J090904.18-181942.6	A0/A1V	84	9480	2.1	152±2	149	64.3±2	42.7	1.02	1.51
45167	J091212.85+035201.1	A0V	99	9684	2.0	102±1	98.2	54.3±2	28.1	1.04	1.93
45424	J091524.94-150129.7	A0V	112	9433	2.2	86.5±1	87.4	31.9±1	25	0.99	1.27
45511	J091627.51-135002.5	A3V	92	7869	1.9	82.9±1	83.6	29.7±1	23.9	0.992	1.24
45585	J091727.49-744404.1	A0V	82	9636	1.9	147±2	125	132±3	35.8	1.18	3.69
45667	J091831.89-390237.5	A1V	94	9048	1.5	58.7±0.9	54.6	47.6±1	15.6	1.07	3.04
46546	J092933.01-622139.0	A2V	101	8526	2.0	85.9±1	88.1	31.7±1	25.2	0.975	1.26
46679	J093059.85-740911.3	F3V	105	6845	1.5	34.9±0.5	34.2	15.9±0.6	9.82	1.02	1.62
46897	J093326.00-225149.3	B9.5V	80	9264	1.9	129±2	132	51.3±2	37.7	0.975	1.36
47115	J093605.13-645700.5	A2V	80	8534	1.6	89.8±1	86.3	48.3±1	24.7	1.04	1.95
47335	J093845.17-665132.2	A9IV/V	81	7398	1.4	57.7±0.8	57.5	24.6±0.8	16.5	1.0	1.49
47382	J093912.82+252202.8	F0	106	7246	2.1	70.5±1	73.1	25.6±1	21	0.963	1.22
47571	J094201.36-421657.2	A2V	104	8712	1.6	52.2±0.8	52.4	22.6±1	15	0.996	1.51
48164	J094902.83+340506.9	A3	88	7692	1.6	60.9±0.9	62.3	27.9±1	17.9	0.976	1.56
48212	J094946.73+310436.9	A5	76	7727	1.6	85.8±1	86.8	31.7±1	24.9	0.989	1.27
48541	J095359.12+274143.6	A0	107	8037	1.5	40.6±0.6	38.7	30.4±1	11.1	1.05	2.74
48613	J095451.19-501438.1	A0V	93	9665	2.3	153±2	145	126±3	41.4	1.06	3.03
48830	J095739.68-163119.9	F0V	78	7120	2.2	130±2	135	48.7±2	38.8	0.959	1.26
49402	J100507.45-130352.4	B8V	96	10000	3.8	345±5	345	136±4	98.8	0.999	1.38
49582	J100719.82-152718.8	F0V	107	6868	1.6	39.1±0.5	35.9	27±1	10.3	1.09	2.62
50070	J101322.83-511358.7	A7V	52	7528	2.4	398±5	411	139±4	118	0.969	1.18
50605	J102012.94-863324.2	F5IV	78	6649	1.4	53.8±0.7	55.5	19.7±0.9	15.9	0.97	1.24
50658	J102044.25-052255.4	A2	106	8412	1.8	58.1±0.8	59.1	23.4±1	16.9	0.982	1.38
50777	J102207.78-463359.1	G2V	105	5775	1.9	44.1±0.6	44.2	15.8±0.7	12.8	0.997	1.24
51259	J102814.56-361312.9	F3V	77	6720	1.6	72.4±1	74	26.8±1	21.2	0.978	1.26
51556	J103151.39+322246.7	A0IV	78	8265	2.2	171±2	176	59.2±2	50.3	0.973	1.18
52324	J104130.33-354352.0	A0V	114	9216	1.8	56.7±0.8	57.4	22±1	16.4	0.987	1.34

Table 5.2 (cont'd)

HIP ID	WISE ID	SpT[a]	Dist.[b] (pc)	$T_\star$ (K)	$R_\star$ ($R_\odot$)	F_{W3} (mJy)	$F_{W3,\star}$ (mJy)	F_{W4} (mJy)	$F_{W4,\star}$ (mJy)	$F_{W3}/F_{W3,\star}$[c]	$F_{W4}/F_{W4,\star}$[c]
52911	J104915.43+103242.6	A2V	117	8942	3.9	241±3	252	86±2	72.2	0.956	1.19
53484	J105629.47-481955.3	F0V	97	7150	1.4	46.6±0.7	36.9	95.8±2	10.6	1.27	9.06
53605	J105758.95-420221.9	A7V	112	8186	1.9	57.9±0.8	59.1	22.9±1	16.9	0.979	1.36
54778	J111252.43+293216.6	G5	92	5941	1.1	19.2±0.3	19.9	8.61±0.9	5.76	0.961	1.5
55081	J111636.47-035800.4	A3	89	8146	1.8	77.5±1	79.7	27.7±1	22.8	0.973	1.21
55485	J112149.22+570429.7	A7Vn	81	8051	1.9	113±2	112	49.9±2	32.1	1.01	1.55
55570	J112256.99-203731.7	A7V	111	7920	1.6	44.4±0.7	44	20.3±1	12.6	1.01	1.61
55802	J112601.95-203456.5	A5IV/V	104	7955	2.2	87.1±1	88.1	31.4±1	25.2	0.988	1.24
57524	J114724.52-495303.1	G3/G5Vp	92	5670	1.4	31.1±0.4	30.6	13.5±0.7	8.83	1.02	1.53
58361	J115802.26-823124.4	G3V	87	5767	1.4	38.6±0.5	38.2	14.1±0.7	11	1.01	1.28
58580	J120048.14-372844.9	F3V	120	6513	1.8	37.2±0.5	38.4	14.6±1	11	0.968	1.32
58720	J120237.63-691132.2	B9V	106	10000	2.3	120±2	100	124±3	28.7	1.2	4.33
58851	J120412.78+012743.2	Am	112	7884	1.5	36.8±0.6	37.5	15.3±1	10.7	0.982	1.43
59282	J120938.74-582058.8	A3V	104	8080	1.6	50.5±0.8	44.9	27.1±1	12.9	1.12	2.11
59397	J121105.83-562404.9	A2V	113	8281	1.7	50.9±0.7	44.3	42.3±1	12.7	1.15	3.33
59676	J121415.40-054258.3	Am	78	7439	2.0	122±2	125	42.9±2	35.8	0.977	1.2
60561	J122451.85-723614.0	A0V	91	9459	1.5	77.4±1	64.4	50.7±1	18.4	1.2	2.75
60746	J122659.30+264932.6	A4V	85	8475	3.6	383±5	378	140±3	108	1.01	1.29
61240	J123258.83-001623.7	F0	105	6588	1.5	34.9±0.5	35.7	14.7±1	10.3	0.976	1.43
61593	J123715.02-350606.0	A8IV	96	7342	1.4	39.3±0.6	38.4	19.6±0.9	11	1.02	1.78
61782	J123946.17-491155.6	A0V	107	7869	1.3	42.2±0.6	26.7	227±5	7.65	1.58	29.7
62209	J124500.33-690147.7	A3V	99	8590	1.4	40.7±0.6	40.6	17.9±0.9	11.6	1.0	1.54
63013	J125448.23+305955.2	F8	116	5946	1.0	9.72±0.2	9.96	5.64±0.8	2.87	0.976	1.96
63123	J125601.45-312855.5	A0V	104	8664	1.6	54.4±0.8	55.5	21.4±0.9	15.9	0.981	1.35
63236	J125726.12-675738.6	A2IV/V	111	8804	1.9	77.2±1	62.3	57±2	17.8	1.24	3.19
63836	J130459.42-472348.6	F7	107	6385	1.2	21.9±0.3	21.1	9.94±0.8	6.08	1.04	1.63
64574	J131409.22-141655.5	G1V	113	5930	2.5	72.8±1	73.7	25.6±0.9	21.3	0.988	1.2
64837	J131728.92-425558.8	F3V	89	6387	1.4	43.6±0.6	39	24.5±1	11.2	1.12	2.19
64882	J131759.53-732040.8	A1m...	85	7535	1.7	75.2±1	76.4	28.6±1	21.9	0.985	1.31
65089	J132026.79-491325.3	A7/A8V	97	7496	1.3	35.1±0.5	33	22.8±0.9	9.45	1.06	2.42
65678	J132759.52+524443.9	F0	98	7449	2.8	149±2	148	52.9±2	42.3	1.01	1.25
65969	J133133.11-280645.8	A1V	100	8788	2.0	83.7±1	86.3	31.2±1	24.7	0.97	1.26
66198	J133407.30+552054.3	A0V	92	9996	2.3	155±2	152	53.8±2	43.6	1.02	1.23
66837	J134152.75-185905.4	F0V	77	6972	1.4	60.4±0.8	59.3	31.1±1	17	1.02	1.83
67005	J134354.76+520351.9	A1V	96	9591	2.1	110±2	110	45.6±1	31.5	1.0	1.45
67495	J134952.38+131131.3	A2	107	7971	2.3	91.4±1	91.8	37.9±1	26.3	0.995	1.44
67497	J134954.48-501424.0	F0V	107	6816	1.4	32.9±0.5	28.3	93.3±2	8.1	1.16	11.5
67596	J135104.57+344621.0	A5IV	89	8448	1.7	79.1±1	78.8	33.2±1	22.6	1.0	1.47
67714	J135218.43+120954.5	A1V	104	9101	2.3	112±1	113	41.6±1	32.4	0.992	1.29
67970	J135509.97-504443.0	F3V	119	6538	1.5	28.1±0.4	24.9	30.8±1	7.15	1.13	4.3
67973	J135512.12-520939.0	B8V	108	10000	2.6	127±2	125	46.2±1	35.8	1.02	1.29
68764	J140427.32+263605.9	F8	105	6090	0.8	9.46±0.2	8.89	6.49±0.9	2.56	1.06	2.53
68781	J140442.13-500417.2	A2V	113	8419	1.4	34.5±0.5	31.9	17±0.9	9.12	1.08	1.86
68890	J140618.35+232318.3	F5	105	6346	1.6	34.7±0.5	35.3	13.1±0.8	10.1	0.984	1.3
69658	J141524.06-181202.5	A0V	76	9924	2.0	161±2	168	55.9±2	48	0.962	1.17
69758	J141636.16-072800.2	A0	108	7528	1.5	35.1±0.5	35.8	13.9±0.8	10.3	0.98	1.36
69917	J141831.14+520159.9	A2	97	8243	1.7	67±0.9	67.1	26.9±1	19.2	0.999	1.4

Table 5.2 (cont'd)

HIP ID	WISE ID	SpT[a]	Dist.[b] (pc)	$T_\star$ (K)	$R_\star$ ($R_\odot$)	F_{W3} (mJy)	$F_{W3,\star}$ (mJy)	F_{W4} (mJy)	$F_{W4,\star}$ (mJy)	$F_{W3}/F_{W3,\star}$[c]	$F_{W4}/F_{W4,\star}$[c]
70090	J142033.37-375307.1	A0IV	79	10000	4.1	645±9	622	228±4	178	1.04	1.28
70441	J142436.98-471040.0	A1V	110	8946	1.3	36.1±0.6	33.3	26.7±1	9.55	1.08	2.8
70553	J142555.86+005933.5	A2p	106	10000	1.3	37.6±0.5	38.6	15.6±0.8	11.1	0.974	1.41
70790	J142835.44-221605.7	F0V	118	7051	1.6	31.1±0.5	31	12.1±0.8	8.9	1.0	1.36
70894	J142950.53+004944.2	A5IV	79	8177	2.2	163±2	166	57.4±1	47.5	0.983	1.21
71911	J144231.58+601351.4	F0	108	6964	1.6	35.2±0.5	35.6	13±0.7	10.2	0.99	1.28
71933	J144243.53-484758.9	F7/F8V	84	5891	1.5	45.6±0.7	45	17.3±0.9	13	1.01	1.33
72552	J144958.42+283657.1	A4V	98	8781	2.7	167±2	166	79.5±2	47.6	1.0	1.67
73049	J145544.73-335120.7	A0V	78	9002	2.5	236±3	249	80.7±2	71.3	0.947	1.13
73249	J145813.41-110917.1	A1V	109	9440	1.8	67.6±0.9	66.8	26.5±1	19.1	1.01	1.38
73483	J150102.21-643434.4	A9/F0IV/V	118	7129	3.3	138±2	144	55±2	41.2	0.962	1.33
73730	J150417.61+593206.2	A2	100	8030	1.5	46.1±0.6	46.6	18.7±0.8	13.4	0.989	1.4
74144	J150902.28-383203.4	A5m...	81	7578	1.5	62.1±0.8	62.6	28.2±1	17.9	0.992	1.57
74359	J151147.67+101259.8	A0	113	9075	1.8	57.8±0.8	55.2	25.2±1	15.8	1.05	1.59
74499	J151327.94-330850.4	F3/F5V	90	6412	1.1	26.1±0.4	25.3	24.2±1	7.26	1.03	3.33
74553	J151359.16+430253.6	A5	100	7689	2.3	106±1	103	46.6±1	29.5	1.03	1.58
74596	J151429.11+290951.8	A2V	77	8931	2.6	248±3	259	88±2	74.3	0.956	1.18
74923	J151837.62-250001.8	A1/A2V	116	7850	1.6	37.7±0.6	37.6	17.5±1	10.8	1.0	1.62
75164	J152135.29-404458.3	A1V	109	8785	2.4	110±2	112	41±1	32.1	0.984	1.28
75684	J152742.29-152457.3	F6V	92	6252	1.2	26.1±0.5	27.2	11.4±1	7.84	0.959	1.45
75729	J152813.79-112655.8	A0	89	7270	1.4	43.8±0.6	45	18±1	12.9	0.973	1.39
75788	J152856.82+551142.1	A3m	94	8866	1.8	87.1±1	86.2	32.8±1	24.7	1.01	1.33
75848	J152934.70-172627.2	Ap	89	7695	1.9	89±1	89.4	35.3±2	25.6	0.996	1.38
75939	J153036.25-204342.9	A3V	80	8063	2.1	133±2	137	51.4±2	39.4	0.969	1.31
75953	J153046.06+342756.3	A0	108	9143	1.7	59.1±0.8	59.9	30.8±1	17.2	0.986	1.79
76217	J153410.07-331017.1	A0V	102	9550	1.4	46.6±0.7	46.9	19.8±1	13.4	0.994	1.48
76305	J153514.07+651640.2	A2	114	8592	1.5	36.7±0.5	37.1	16.3±0.7	10.6	0.987	1.53
76666	J153921.35-230900.9	B9.5V	100	9244	2.0	89±1	90.8	39.4±2	26	0.981	1.52
76712	J153952.99-343924.5	F3V	115	6659	1.3	20.9±0.4	21.3	9.12±0.9	6.1	0.985	1.5
76736	J154011.47-701340.9	A5V	78	8744	1.6	97.3±1	87	83.6±2	24.9	1.12	3.36
77111	J154442.11+171551.3	A0V	114	9555	2.3	100±1	101	35.1±1	28.9	0.993	1.21
77163	J154523.49+052650.2	A1V	113	9080	3.3	190±2	195	85.6±2	55.8	0.974	1.53
77170	J154526.29-261758.0	G0V	116	5813	1.7	31.9±0.6	32.7	16.6±1	9.44	0.976	1.76
77432	J154824.76-423705.2	F5V	96	6435	1.1	22.8±0.4	21	13.2±0.9	6.03	1.08	2.19
77435	J154826.59-235002.6	A2IV/V	84	8540	1.6	72.2±1	74.7	27.9±2	21.4	0.967	1.3
77910	J155440.27+083449.2	A7Vn	79	7871	2.1	136±2	136	57.9±2	39	1.0	1.48
77979	J155528.15-171523.2	F7V	116	5577	1.2	14.6±0.3	14.9	7.84±1	4.31	0.979	1.82
78359	J155955.04-332307.2	A0V	105	9219	1.6	57.6±0.8	57.1	23.9±1	16.4	1.01	1.46
78596	J160249.37-743344.0	F2/F3V	104	6802	1.4	32±0.4	31.3	18.5±0.9	8.99	1.02	2.05
78975	J160717.41-175230.5	G0	77	5896	0.9	19.1±0.4	19	9.93±1	5.48	1.01	1.81
78996	J160729.92-235702.5	A9V	108	6373	1.7	48±0.8	37.4	41.8±2	10.7	1.28	3.89
79044	J160804.36-361354.8	B9V	103	10000	1.5	46.2±0.7	47.1	17.4±1	13.5	0.98	1.29
79835	J161745.30-374514.6	F3V	79	6508	1.6	66.4±0.9	68.6	25.8±1	19.7	0.967	1.31
80427	J162500.27+514300.0	A3	117	7750	1.9	51.9±0.7	52.3	20.1±0.7	15	0.992	1.34
81160	J163434.90+375944.1	F5	110	6548	1.3	21.9±0.3	21.5	9.11±0.8	6.18	1.02	1.48
81393	J163723.15-172737.9	G5V	88	5005	1.4	29.1±0.5	30.5	13.6±1	8.82	0.954	1.54
81400	J163729.90-115211.6	F2	119	5726	2.4	59.4±0.9	57.3	34.8±2	16.5	1.04	2.11

Table 5.2 (cont'd)

HIP ID	WISE ID	SpT[a]	Dist.[b] (pc)	$T_\star$ (K)	$R_\star$ ($R_\odot$)	F_{W3} (mJy)	$F_{W3,\star}$ (mJy)	F_{W4} (mJy)	$F_{W4,\star}$ (mJy)	$F_{W3}/F_{W3,\star}$[c]	$F_{W4}/F_{W4,\star}$[c]
81560	J163926.07+291306.0	A0	92	7965	1.5	53.6±0.7	53.7	20.9±1	15.4	0.999	1.36
81572	J163935.19-073044.3	F0	92	6713	2.0	74.5±1	73.8	27.9±1	21.2	1.01	1.32
81641	J164038.68+041311.1	A1V	90	9750	2.2	137±2	136	61.6±2	39.1	1.0	1.58
81659	J164051.32+122342.1	A3Vn	96	9076	2.2	117±2	116	41.5±1	33.1	1.01	1.25
81812	J164235.39-111028.9	A2	94	7500	1.6	55.3±1	58.1	24.3±1	16.6	0.952	1.46
81971	J164442.39+021957.9	A2	92	7974	1.4	43.9±0.6	43.9	28.7±1	12.6	1.0	2.28
82069	J164548.44-263858.1	B9.5V	108	9166	1.6	51.8±0.8	47.3	38.3±2	13.5	1.09	2.83
82253	J164824.17+170759.8	A2	111	7223	2.1	62.3±0.9	63.8	23±1	18.3	0.977	1.26
82673	J165400.44+100955.2	B8V	75	10000	3.2	444±6	425	200±4	122	1.05	1.64
83402	J170244.20-543341.1	A3IV	92	8174	1.5	59.3±0.8	57.4	24.7±1	16.5	1.03	1.5
83478	J170339.29+133618.9	A1V	77	9661	1.7	126±2	120	62.7±2	34.4	1.05	1.82
83796	J170730.67+035823.9	F2	90	6472	1.6	47.9±0.7	48.1	18.4±1	13.8	0.995	1.34
83911	J170857.69-235937.3	F3V	87	6420	1.5	46.9±0.7	47.4	18.8±1	13.6	0.99	1.38
83946	J170932.94+304220.1	A2	108	7389	1.3	28.8±0.5	28.8	11.6±0.8	8.26	1.0	1.4
84163	J171221.95+020725.9	G0	86	6040	1.2	31.6±0.4	31.3	12.2±0.9	9.05	1.01	1.34
84299	J171405.23-223439.0	F3/F5V	111	6235	1.5	26.7±0.4	26	12.7±1	7.46	1.03	1.7
84510	J171635.60-743159.2	A0V	106	9764	2.0	87.7±1	89.1	32.2±1	25.5	0.985	1.26
84819	J172007.53+354103.6	F8	100	6708	1.5	35.3±0.5	35	16.1±0.8	10.1	1.01	1.59
84881	J172050.60-452515.3	A0V	118	8287	1.8	150±2	47.6	631±10	13.6	3.15	46.2
85224	J172452.23-185133.4	F5V	107	6313	1.6	35.5±0.6	34.1	62.2±2	9.79	1.04	6.35
85290	J172541.34+600254.5	A1Vn	97	9014	2.7	178±2	177	62.1±2	50.8	1.0	1.22
85721	J173100.34-075648.8	F2	113	6101	1.9	42.5±0.6	42.3	16.2±1	12.2	1.0	1.33
85759	J173126.85+542120.9	A0	109	8201	1.7	51.8±0.7	52	18.6±0.8	14.9	0.996	1.25
85790	J173149.58+282427.2	A1V	82	9604	2.1	157±2	157	66.2±2	44.9	1.0	1.47
86853	J174445.31-395054.6	F0V	115	6586	1.5	39.5±0.7	26.6	49.6±2	7.64	1.48	6.5
87435	J175200.85+064347.3	F2	76	6554	1.6	68.6±0.9	69.7	25±1	20	0.984	1.25
88349	J180230.72+583738.4	A2	89	8438	1.6	65.4±0.9	66.1	29.5±1	18.9	0.99	1.56
89342	J181347.47-461845.7	A1V	113	9216	1.8	57.1±0.8	57.6	24.2±1	16.5	0.991	1.47
90176	J182405.58+202709.1	F0	80	7184	2.0	113±1	115	45.2±1	32.9	0.985	1.37
90563	J182846.77-440520.0	G5V	77	5788	1.0	22.9±0.4	23.2	10.2±0.9	6.69	0.987	1.52
90806	J183126.29-182409.9	B9/B9.5V	68	9524	2.3	259±4	268	130±3	76.8	0.966	1.7
91656	J184126.87+751759.9	F0	90	7001	1.7	61.5±0.8	62.1	23.8±0.9	17.8	0.991	1.34
92346	J184914.27+250247.5	A1V	101	8625	1.8	73±1	71.5	28.6±1	20.5	1.02	1.4
92676	J185302.31-482139.9	A2V	82	8335	2.0	135±2	128	69.5±2	36.8	1.05	1.89
93327	J190031.95+414103.3	F0	86	6704	1.6	58.1±0.7	57.8	22.5±0.9	16.6	1.0	1.35
93743	J190518.54-013043.7	F1V	44	6953	1.3	157±2	158	54.7±2	45.4	0.99	1.21
96440	J193626.08-185110.6	F0V	78	7400	2.5	187±3	193	76.8±2	55.4	0.967	1.39
96610	J193829.18-655451.0	A1/A2V	101	8947	1.7	63.1±0.9	62.4	29.9±1	17.9	1.01	1.67
96718	J193940.22-064231.3	A2	109	7287	1.8	50.7±0.8	51.6	20.2±1	14.8	0.984	1.36
97028	J194309.60+304040.4	A1V	111	9644	2.3	104±1	104	41.3±1	29.8	0.999	1.38
98304	J195825.59-140043.0	F6V	114	5958	1.2	17.3±0.3	17	13.6±1	4.9	1.02	2.78
98579	J200126.79-404851.9	A2/A3V	100	8577	2.2	104±1	106	38.1±1	30.4	0.98	1.26
100464	J202222.86+730903.7	F0	119	7074	1.6	34.6±0.5	30.3	28.3±0.9	8.69	1.14	3.26
102880	J205038.58+224349.4	A2	120	7976	1.7	41.1±0.6	37.6	28.1±1	10.8	1.09	2.6
103224	J205446.99-184733.8	F0V	101	7187	2.7	123±2	124	45±1	35.7	0.99	1.26
103456	J205739.90-242921.2	F5V	113	6340	1.9	41.6±0.7	43.8	16.8±1	12.6	0.95	1.34
103602	J205928.10+791810.0	F8	85	6509	1.3	37.4±0.5	37.6	13.5±0.7	10.9	0.993	1.24

Table 5.2 (cont'd)

HIP ID	WISE ID	SpT[a]	Dist.[b] (pc)	$T_\star$ (K)	$R_\star$ ($R_\odot$)	F_{W3} (mJy)	$F_{W3,\star}$ (mJy)	F_{W4} (mJy)	$F_{W4,\star}$ (mJy)	$F_{W3}/F_{W3,\star}$[c]	$F_{W4}/F_{W4,\star}$[c]
103777	J210145.28-265251.7	A3V	93	9117	2.1	117±2	119	41.5±1	33.9	0.989	1.22
104430	J210916.04-001405.6	A3	101	8078	2.1	92.5±1	89.9	47.2±2	25.8	1.03	1.83
105570	J212253.65+064840.2	A3V	101	8792	3.7	293±4	294	102±3	84.1	0.996	1.21
106313	J213155.33-584500.4	F0V	111	6678	1.6	33.2±0.5	33.7	13.3±0.9	9.65	0.986	1.38
106783	J213743.68+063706.2	A2V	88	9336	1.8	99.1±1	99	41.2±1	28.3	1.0	1.45
107063	J214102.27+050114.3	A5	115	8132	1.8	51±0.7	53	19.4±1	15.2	0.962	1.27
107336	J214423.84-044351.2	A2	111	8625	2.1	78±1	79.4	29.6±1	22.7	0.983	1.3
107517	J214632.11-112157.4	A1V	86	9814	2.2	161±2	164	61.8±2	47	0.979	1.31
107585	J214724.82-043631.2	A2	97	8898	1.6	62.1±0.9	59.4	41±2	17	1.05	2.41
107697	J214858.23-512158.5	A8V	116	7716	1.8	46±0.6	46.4	18.6±1	13.3	0.993	1.4
108570	J215934.54+565316.5	F0	110	7321	2.0	59.9±0.8	60.3	23.1±0.9	17.3	0.993	1.33
109198	J220714.87-740510.7	F7V	100	6258	1.2	22.5±0.4	22.3	9.67±0.8	6.44	1.01	1.5
110739	J222606.81-051040.3	F0	79	7256	1.5	67.3±1	68.6	29.2±1	19.7	0.981	1.48
110786	J222641.68-111341.5	A3	78	7481	1.6	82.2±1	81.7	39±2	23.4	1.01	1.67
111264	J223227.75+291355.9	G5	98	5607	1.2	19.1±0.3	19	8.65±0.9	5.48	1.01	1.58
111822	J223857.61-100607.7	G0	118	5970	2.3	52.5±0.7	54.2	19.9±1	15.7	0.967	1.27
112694	J224917.46-702052.3	A2V	105	8828	2.2	97.7±1	96.8	34.3±1	27.7	1.01	1.24
112835	J225103.84+521605.5	F0	93	7435	1.6	55.4±0.8	56.3	20.4±1	16.1	0.985	1.27
113195	J225524.99+701750.3	A5	79	7209	1.4	57.4±1	58	21.9±1	16.6	0.99	1.31
113981	J230500.76+183752.5	F0	79	6884	1.7	80.6±1	83	29.3±1	23.8	0.972	1.23
114031	J230533.05+145732.6	A0	106	9604	1.6	54±0.8	54.8	29.9±1	15.7	0.985	1.91
114371	J230949.56-143038.0	A0V	104	9432	1.9	81±1	78.3	31.9±2	22.4	1.03	1.42
114802	J231519.30-245106.3	A5IV	111	8079	1.8	49.2±0.7	51.4	19.3±1	14.7	0.958	1.31
114868	J231600.69+352358.2	F0	79	7246	1.9	99.3±1	99.7	35.1±1	28.6	0.996	1.23
115806	J232740.40+251001.9	A0MNp...	111	10000	2.3	99.3±1	96.2	40.5±1	27.5	1.03	1.47
116479	J233605.82+030903.4	F0	101	7106	1.5	40±0.6	40.7	16.8±1	11.7	0.983	1.44
117352	J234739.24-042741.7	A2	107	7599	1.7	44.8±0.7	46.9	17.9±1	13.4	0.956	1.33
118022	J235624.75+560158.5	F8	102	6248	1.7	43.3±0.6	44.9	16.5±0.8	12.9	0.964	1.27
118027	J235628.07+831128.0	A3V	91	8975	1.7	76.8±1	75.6	53.4±1	21.6	1.02	2.47
118133	J235746.21+112827.7	B9V	95	9346	1.6	65.5±1	64.5	30.2±1	18.5	1.02	1.63

Note. — *Hipparcos* stars with detected mid-IR excesses out to 120 pc at $W4$ using $W3 - W4$ colors. The stellar temperature and radius for each stars were obtained from photometric fits as described in § 3 and § 4.5.

Table 5.3. Disk Parameters from Blackbody Fits and Excess Information for Stars within 120 pc

HIP ID	T_d (K)	$T_{d,\mathrm{lim}}$ (K)	R_d (AU)	$R_{d,\mathrm{lim}}$ (AU)	θ ($''$)	f_d ($\times 10^{-5}$)	$f_{d,\mathrm{lim}}$ ($\times 10^{-5}$)	$\Sigma_{E[W3-W4]}$	New?	Notes
301	···	<144	···	>36	>0.43	1.8	>0.061	8.67	N	b
1829	123	<190	9.7	>4.1	0.039–0.092	11	>0.37	6.17	Y	c
2496	162	<190	10	>7.6	0.071–0.098	13	>0.48	22.00	N	c
2539	···	<206	···	>6.8	>0.071	2.8	>0.1	4.52	Y	b
4303	···	<144	···	>9.1	>0.085	4.4	>0.16	3.20	Y	b
4366	···	<150	···	>14	>0.18	4.6	>0.17	12.20	N	b
4630	···	<162	···	>8.7	>0.079	5.3	>0.2	7.87	Y	b
5233	···	<169	···	>13	>0.11	3.9	>0.15	7.79	Y	b
5626	114	<156	33	>18	0.21–0.4	11	>0.29	28.70	N	c
7051	89.8	<169	22	>6.3	0.052–0.19	20	>0.31	7.39	Y	c
7283	97.2	<241	37	>6.1	0.059–0.36	4.4	>0.083	4.65	Y	c
7943	162	<206	16	>9.9	0.12–0.19	5.9	>0.2	21.90	N	c
7965	93.4	<183	70	>18	0.15–0.59	6.7	>0.1	12.40	Y	c
8250	···	<198	···	>3.7	>0.037	5.4	>0.2	3.05	Y	b
8417	···	<198	···	>6.8	>0.066	3	>0.11	3.18	Y	b
8920	403	<419	0.7	>0.65	0.0068–0.0073	3400	>51	48.90	N	c
9285	···	<150	···	>15	>0.14	1.9	>0.067	4.04	Y	b
10320	223	<282	12	>7.5	0.076–0.12	4.6	>0.15	12.00	N	c
10355	···	<198	···	>6.2	>0.057	3	>0.11	3.22	Y	b
11522	···	<162	···	>5.6	>0.05	9.4	>0.37	4.84	Y	b
11696	436	<454	0.87	>0.8	0.015–0.016	400	>5.2	28.40	N	c
11821	···	<190	···	>5.9	>0.062	2.8	>0.11	3.61	Y	b
12876	···	<282	···	>8.1	>0.093	1.8	>0.045	3.30	Y	b
13063	···	<176	···	>9.5	>0.09	4.6	>0.17	7.35	Y	b
13394	131	···	5.5	···	0.180	···	>5.2	5.74	Y	a
13682	169	<198	8	>5.8	0.05–0.069	10	>0.36	13.40	Y	c
13872	97.2	<232	19	>3.4	0.033–0.19	7.1	>0.14	3.90	Y	c
15152	···	<223	···	>2.5	>0.026	6.7	>0.23	3.35	Y	b
15870	···	<183	···	>12	>0.13	1.4	>0.047	3.76	Y	b
15922	183	<241	8.2	>4.7	0.04–0.069	6.2	>0.23	7.97	Y	c
15933	89.8	<251	31	>4	0.04–0.31	5.6	>0.084	3.65	N	c
15987	133	<190	22	>11	0.099–0.2	6.2	>0.21	15.30	Y	c
16028	114	<232	14	>3.4	0.031–0.13	9	>0.26	4.15	Y	c
16322	131	···	43	···	0.389	···	>0.72	2.94	Y	a
16386	···	<162	···	>10	>0.084	3.8	>0.13	4.81	Y	b
16425	150	<271	17	>5.3	0.046–0.15	3.4	>0.13	4.54	Y	c
16511	131	···	30	···	0.274745041	···	>1.1	3.75	Y	a
16671	114	<190	12	>4.2	0.035–0.099	23	>0.68	6.70	Y	c
16876	144	<214	13	>6.1	0.051–0.11	4.5	>0.16	8.61	Y	c
17091	183	<214	1.8	>1.3	0.015–0.021	48	>1.8	7.48	Y	c
17256	···	<198	···	>7	>0.07	2	>0.075	3.37	Y	b
17391	109	<198	13	>4.1	0.036–0.12	13	>0.35	7.38	Y	c
17707	···	<162	···	>18	>0.16	2.9	>0.1	9.23	Y	b
17900	232	<271	8.6	>6.3	0.055–0.075	6.7	>0.19	11.80	Y	c
18217	···	<128	···	>14	>0.29	3.5	>0.12	8.14	N	b
18297	144	<232	13	>4.9	0.041–0.11	4	>0.14	4.53	Y	c
18437	144	<156	14	>12	0.12–0.14	27	>0.92	51.90	N	c
18671	···	<206	···	>4.1	>0.045	4	>0.15	3.72	N	b
18729	···	<223	···	>6.6	>0.065	2.6	>0.085	5.54	Y	b
18863	···	<139	···	>17	>0.15	5.8	>0.19	12.00	Y	b
19215	139	<169	6.6	>4.5	0.038–0.056	37	>1.3	14.80	Y	c
20171	101	<251	43	>7	0.085–0.52	2.7	>0.052	4.73	Y	c
20279	190	<271	4.1	>2	0.018–0.036	8	>0.3	3.78	Y	c
21238	150	<183	9.1	>6.1	0.086–0.13	15	>0.55	22.70	Y	c
21618	86.3	<214	34	>5.6	0.055–0.34	11	>0.15	5.46	N	c
22200	83	<109	15	>8.7	0.076–0.13	240	>2.8	24.80	Y	c
22226	···	<128	···	>9	>0.11	20	>0.69	16.00	N	b
22410	93.4	<169	11	>3.4	0.03–0.099	64	>1.1	7.22	Y	c
22776	131	···	3.4	···	0.121	···	>8.7	5.84	Y	a
23088	131	···	25	···	0.28786817	···	>2.3	9.68	Y	a
23451	123	<128	11	>10	0.093–0.1	410	>12	104.00	N	c
23621	···	<133	···	>15	>0.17	4.2	>0.14	6.49	Y	b
25020	86.3	<176	19	>4.7	0.046–0.19	26	>0.36	7.82	Y	c
25608	···	<156	···	>19	>0.22	2	>0.07	7.48	N	b
25638	131	···	20	···	0.213	···	>2.3	4.41	Y	a
25998	79.7	<105	34	>19	0.18–0.31	85	>0.81	35.40	N	c
26062	156	<162	12	>12	0.1–0.11	530	>18	119.00	N	c
26330	···	<144	···	>4.4	>0.064	8.2	>0.31	4.06	Y	b
26621	156	<206	7.1	>4.1	0.039–0.068	13	>0.53	11.90	N	c
26625	89.8	<183	19	>4.5	0.056–0.23	18	>0.28	5.21	Y	c
26966	183	<206	11	>8.7	0.12–0.15	12	>0.43	32.20	N	c

Table 5.3 (cont'd)

HIP ID	T_d (K)	$T_{d,\lim}$ (K)	R_d (AU)	$R_{d,\lim}$ (AU)	θ ($''$)	f_d ($\times 10^{-5}$)	$f_{d,\lim}$ ($\times 10^{-5}$)	$\Sigma_{E[W3-W4]}$	New?	Notes
27259	86.3	<150	37	>12	0.13–0.39	20	>0.25	16.00	N	c
27698	···	<139	···	>14	>0.14	2.4	>0.082	4.08	Y	b
27713	150	<223	19	>8.7	0.088–0.19	3.8	>0.14	10.00	Y	c
28230	89.8	<128	21	>10	0.13–0.26	53	>0.83	28.90	N	c
28385	131	···	21	···	0.207	···	>2	2.91	Y	a
28778	83	<206	29	>4.7	0.048–0.3	18	>0.21	5.38	Y	c
29487	···	<133	···	>22	>0.18	2.1	>0.068	4.26	Y	b
29510	162	<251	5.3	>2.2	0.023–0.054	7	>0.27	3.40	Y	c
29606	···	<190	···	>5.6	>0.054	3.7	>0.14	3.62	Y	b
30088	83	<144	47	>16	0.16–0.48	16	>0.17	14.90	Y	c
30291	97.2	<183	15	>4.3	0.044–0.16	18	>0.36	7.88	Y	c
30685	89.8	<214	17	>2.9	0.029–0.16	15	>0.24	4.55	Y	c
30760	···	<214	···	>5.9	>0.07	2	>0.068	4.78	N	b
30939	···	<169	···	>3.5	>0.073	4.2	>0.17	3.42	Y	b
31386	86.3	<214	23	>3.7	0.041–0.25	11	>0.15	4.79	N	c
33227	···	<176	···	>5.5	>0.064	7.3	>0.29	6.23	Y	b
33384	···	<190	···	>17	>0.16	1.4	>0.05	3.30	Y	b
33476	···	<162	···	>10	>0.091	4.2	>0.16	5.86	Y	b
33477	···	<150	···	>9.7	>0.098	4.2	>0.16	4.04	Y	b
33788	···	<156	···	>7.6	>0.071	6.2	>0.24	7.19	Y	b
34276	···	<139	···	>19	>0.18	4.9	>0.16	13.80	N	b
35572	···	<176	···	>6.7	>0.061	4.6	>0.18	3.39	Y	b
36312	123	<198	6.6	>2.6	0.031–0.079	14	>0.47	6.50	N	c
36624	101	<176	26	>8.6	0.11–0.32	8.9	>0.18	10.90	N	c
36837	128	<190	23	>10	0.091–0.2	5.3	>0.16	11.20	Y	c
37411	114	<241	8.4	>1.9	0.02–0.091	8.5	>0.25	3.80	Y	c
38403	109	<214	29	>7.5	0.073–0.28	6.2	>0.16	7.46	N	c
39510	···	<183	···	>6.5	>0.06	5.1	>0.2	8.28	Y	b
39535	97.2	<198	45	>11	0.1–0.42	5	>0.087	6.80	N	c
40706	101	<241	24	>4.3	0.15–0.85	5.4	>0.12	7.50	Y	c
41765	···	<133	···	>10	>0.12	6.1	>0.21	5.30	Y	b
41891	···	<169	···	>4.3	>0.038	13	>0.52	3.87	Y	b
42090	···	<118	···	>38	>0.35	2	>0.059	4.37	Y	b
42197	118	<214	16	>4.9	0.059–0.19	6.1	>0.18	6.70	N	c
42353	···	<198	···	>9.8	>0.088	2	>0.068	4.29	Y	b
42637	282	<306	6.2	>5.3	0.055–0.065	20	>0.46	28.70	N	c
42928	131	···	20	···	0.240	···	>2.7	6.64	Y	a
42994	123	<176	16	>7.9	0.071–0.14	9	>0.28	11.20	Y	c
43620	105	<176	37	>13	0.14–0.4	6	>0.13	14.30	Y	c
44078	···	<139	···	>13	>0.11	4.6	>0.16	3.94	Y	b
44272	79.7	<176	13	>2.7	0.035–0.17	54	>0.54	5.55	Y	c
44393	162	<261	6.8	>2.6	0.027–0.071	4.9	>0.19	4.22	Y	c
44504	···	<169	···	>21	>0.17	1.7	>0.063	5.38	Y	b
44923	133	<214	23	>9	0.11–0.28	3.3	>0.11	9.92	N	c
45167	150	<198	18	>10	0.11–0.18	5.3	>0.18	16.10	N	c
45424	···	<223	···	>8.5	>0.076	1.9	>0.058	3.33	Y	b
45511	···	<223	···	>5.4	>0.059	2.6	>0.089	3.56	Y	b
45585	169	<183	13	>11	0.14–0.16	15	>0.54	42.40	N	c
45667	139	<162	14	>10	0.11–0.15	14	>0.49	28.90	Y	c
46546	···	<162	···	>13	>0.13	2	>0.074	4.65	Y	b
46679	128	<198	9.9	>4.1	0.039–0.094	10	>0.34	9.21	Y	c
46897	···	<133	···	>20	>0.25	2.5	>0.081	6.90	N	b
47115	144	<190	13	>7.3	0.091–0.16	7.6	>0.27	18.50	Y	c
47335	93.4	<198	21	>4.6	0.057–0.26	12	>0.21	8.74	Y	c
47382	···	<105	···	>23	>0.22	4.2	>0.1	2.89	Y	b
47571	···	<183	···	>8.2	>0.079	3.8	>0.14	7.06	Y	b
48164	···	<133	···	>12	>0.14	6.2	>0.22	8.33	N	b
48212	···	<198	···	>5.6	>0.074	2.9	>0.11	3.85	Y	b
48541	123	<156	14	>9	0.084–0.14	19	>0.6	20.00	N	c
48613	128	<150	28	>21	0.22–0.3	13	>0.4	36.70	N	c
48830	131	···	15	···	0.188	···	>3.6	5.06	Y	a
49402	···	<214	···	>17	>0.18	2.2	>0.067	7.22	Y	b
49582	156	<183	7	>5.1	0.047–0.065	23	>0.89	17.90	N	c
50070	···	<139	···	>16	>0.32	2	>0.074	3.85	N	b
50605	···	<144	···	>7	>0.09	3.8	>0.14	3.52	Y	b
50658	···	<162	···	>11	>0.1	3.1	>0.12	5.05	Y	b
50777	···	<261	···	>2.1	>0.02	7.4	>0.22	3.16	Y	b
51259	···	<176	···	>5.5	>0.071	3.9	>0.15	3.54	N	b
51556	···	<176	···	>11	>0.15	1.5	>0.056	2.95	Y	b
52324	···	<190	···	>9.4	>0.082	2.2	>0.077	4.17	Y	b
52911	131	···	41	···	0.347	···	>1.5	4.42	Y	a

Table 5.3 (cont'd)

HIP ID	T_d (K)	$T_{d,\mathrm{lim}}$ (K)	R_d (AU)	$R_{d,\mathrm{lim}}$ (AU)	θ ($''$)	f_d ($\times 10^{-5}$)	$f_{d,\mathrm{lim}}$ ($\times 10^{-5}$)	$\Sigma_{E[W3-W4]}$	New?	Notes
53484	133	<139	9.3	>8.6	0.089–0.096	110	>3.9	72.60	Y	c
53605	···	<156	···	>12	>0.11	3.1	>0.12	5.18	Y	b
54778	···	<114	···	>6.8	>0.074	14	>0.42	3.57	Y	b
55081	···	<162	···	>10	>0.11	1.8	>0.07	2.96	Y	b
55485	97.2	<190	30	>7.8	0.097–0.37	9.5	>0.18	9.87	N	c
55570	101	<198	23	>6.1	0.055–0.21	9.8	>0.21	5.83	Y	c
55802	···	<214	···	>6.9	>0.066	2.5	>0.087	3.47	Y	b
57524	133	<214	5.7	>2.2	0.024–0.062	14	>0.52	6.14	N	c
58361	139	<271	5.7	>1.5	0.017–0.066	7	>0.26	3.24	Y	c
58580	···	<123	···	>12	>0.1	6.3	>0.21	3.41	Y	b
58720	162	<176	17	>15	0.14–0.16	18	>0.6	47.50	N	c
58851	···	<176	···	>7.2	>0.064	4.1	>0.16	4.00	Y	b
59282	214	<251	5	>3.7	0.035–0.048	11	>0.38	11.90	N	c
59397	169	<190	9	>7.1	0.063–0.08	19	>0.73	29.80	N	c
59676	···	<198	···	>6.6	>0.085	2.3	>0.086	2.93	Y	b
60561	214	<241	6.4	>5.1	0.056–0.071	12	>0.37	23.90	N	c
60746	144	<271	28	>7.9	0.093–0.33	2.4	>0.086	7.31	Y	c
61240	···	<150	···	>6.9	>0.066	7	>0.27	4.00	Y	b
61593	128	<190	11	>4.8	0.05–0.11	10	>0.35	9.33	Y	c
61782	109	<114	15	>14	0.13–0.14	430	>10	114.00	N	c
62209	86.3	<190	30	>6.3	0.063–0.31	11	>0.15	6.68	Y	c
63013	···	<133	···	>4.4	>0.038	24	>0.82	4.31	Y	b
63123	···	<176	···	>9.1	>0.087	2.6	>0.096	5.44	Y	b
63236	214	<232	7	>6	0.054–0.064	17	>0.57	21.40	N	c
63836	156	<232	4.8	>2.2	0.02–0.045	11	>0.44	4.93	N	c
64574	···	<241	···	>3.6	>0.032	5.3	>0.17	3.45	Y	b
64837	198	<232	3.4	>2.5	0.028–0.038	22	>0.82	13.30	N	c
64882	···	<198	···	>5.7	>0.067	3.4	>0.13	4.85	Y	b
65089	144	<183	8	>5	0.051–0.083	16	>0.6	16.80	N	c
65678	128	<282	21	>4.4	0.045–0.22	3.2	>0.11	4.26	Y	c
65969	···	<128	···	>21	>0.21	2.2	>0.069	4.90	Y	b
66198	169	<331	17	>4.5	0.049–0.19	1.2	>0.042	3.27	Y	c
66837	114	<176	12	>5.2	0.067–0.16	15	>0.43	12.20	Y	c
67005	93.4	<206	48	>9.8	0.1–0.49	5.5	>0.088	7.96	N	c
67495	···	<183	···	>10	>0.093	4.1	>0.16	7.74	N	b
67497	105	<114	14	>12	0.11–0.13	240	>5.8	77.70	N	c
67596	89.8	<198	34	>7.1	0.08–0.39	9	>0.13	7.72	N	c
67714	···	<206	···	>10	>0.097	2	>0.068	5.25	Y	b
67970	139	<156	7.6	>6	0.051–0.064	57	>2.1	35.40	N	c
67973	169	<306	18	>5.6	0.052–0.17	1.5	>0.052	4.81	Y	c
68764	144	<190	3.3	>1.9	0.018–0.032	33	>1.2	5.71	Y	c
68781	198	<251	5.7	>3.5	0.031–0.05	7.3	>0.26	8.75	N	c
68890	···	<198	···	>3.8	>0.036	5.4	>0.21	3.20	Y	b
69658	131	···	24	···	0.322	···	>0.98	3.26	Y	a
69758	···	<169	···	>6.8	>0.063	3.8	>0.15	3.86	Y	b
69917	···	<198	···	>6.9	>0.071	3.5	>0.13	6.51	N	b
70090	232	<358	16	>6.7	0.084–0.2	1.7	>0.05	5.44	N	c
70441	150	<176	11	>7.8	0.07–0.097	13	>0.45	19.90	N	c
70553	···	<133	···	>16	>0.15	2.3	>0.072	5.03	Y	b
70790	86.3	<223	24	>3.6	0.031–0.21	13	>0.18	3.12	Y	c
70894	···	<206	···	>8.1	>0.1	1.9	>0.068	4.57	Y	b
71911	···	<214	···	>3.8	>0.035	4.1	>0.15	2.90	Y	b
71933	133	<261	6.7	>1.7	0.021–0.08	8	>0.29	3.71	Y	c
72552	89.8	<169	58	>16	0.17–0.59	12	>0.17	15.80	N	c
73049	131	···	27	···	0.348	···	>0.99	3.03	N	a
73249	128	<232	22	>6.7	0.061–0.2	2.6	>0.081	4.83	Y	c
73483	···	<114	···	>30	>0.26	5.6	>0.16	6.54	Y	b
73730	···	<183	···	>6.7	>0.067	3.6	>0.14	5.92	N	b
74144	···	<156	···	>8	>0.099	6.1	>0.24	8.68	Y	b
74359	183	<251	9.6	>5.1	0.045–0.085	4	>0.14	8.07	Y	c
74499	97.2	<133	11	>6.1	0.068–0.13	76	>1.5	19.90	N	c
74553	156	<223	13	>6.4	0.063–0.13	5.9	>0.23	10.70	N	c
74596	131	···	27	···	0.352	···	>1.4	4.80	Y	a
74923	83	<176	33	>7.4	0.063–0.28	19	>0.22	6.23	Y	c
75164	···	<190	···	>12	>0.11	2.1	>0.073	5.04	Y	b
75684	···	<114	···	>8.6	>0.093	11	>0.33	3.49	Y	b
75729	···	<144	···	>8.3	>0.092	4.9	>0.18	4.30	Y	b
75788	128	<241	20	>5.6	0.06–0.21	2.6	>0.084	5.84	Y	c
75848	···	<198	···	>6.6	>0.075	4	>0.15	5.18	Y	b
75939	···	<114	···	>24	>0.3	3.7	>0.1	5.43	Y	b
75953	···	<128	···	>20	>0.18	5.9	>0.18	13.50	N	b

Table 5.3 (cont'd)

HIP ID	T_d (K)	$T_{d,\mathrm{lim}}$ (K)	R_d (AU)	$R_{d,\mathrm{lim}}$ (AU)	θ ($''$)	f_d ($\times 10^{-5}$)	$f_{d,\mathrm{lim}}$ ($\times 10^{-5}$)	$\Sigma_{E[W3-W4]}$	New?	Notes
76217	···	<190	···	>7.9	>0.077	2.9	>0.098	4.75	Y	b
76305	···	<156	···	>10	>0.09	4.1	>0.15	8.05	N	b
76666	···	<150	···	>17	>0.17	3.3	>0.12	7.01	Y	b
76712	···	<176	···	>4.4	>0.038	7.8	>0.3	3.17	Y	b
76736	150	<176	12	>8.7	0.11–0.15	18	>0.63	38.30	N	c
77111	···	<241	···	>8	>0.071	1.5	>0.044	3.19	Y	b
77163	···	<114	···	>47	>0.41	4.7	>0.13	12.00	N	b
77170	···	<139	···	>7.1	>0.062	19	>0.69	7.58	Y	b
77432	176	<214	3.4	>2.3	0.024–0.036	20	>0.8	8.42	N	c
77435	···	<118	···	>19	>0.22	3	>0.086	3.86	Y	b
77910	86.3	<190	40	>8.1	0.1–0.5	13	>0.17	7.58	Y	c
77979	···	<144	···	>4.2	>0.036	23	>0.84	4.13	Y	b
78359	109	<214	26	>6.8	0.065–0.25	4.2	>0.1	5.47	Y	c
78596	109	<162	13	>5.8	0.055–0.12	22	>0.59	11.70	Y	c
78975	86.3	<183	9.5	>2.1	0.028–0.12	49	>0.68	4.52	Y	c
78996	198	<214	4	>3.4	0.032–0.037	53	>2	21.50	N	c
79044	···	<183	···	>9.1	>0.089	1.6	>0.052	3.27	Y	b
79835	···	<118	···	>12	>0.14	6.4	>0.2	4.90	Y	b
80427	···	<206	···	>6.2	>0.053	3.6	>0.13	5.68	N	b
81160	139	<232	6.6	>2.4	0.021–0.06	8.2	>0.3	3.25	Y	c
81393	131	···	4.7	···	0.0530	···	>22	5.36	Y	a
81400	133	<176	10	>5.9	0.05–0.086	29	>1.1	13.50	Y	c
81560	···	<214	···	>4.8	>0.052	3.6	>0.13	4.62	Y	b
81572	133	<261	11	>3	0.032–0.12	5.2	>0.19	3.74	Y	c
81641	89.8	<176	55	>14	0.16–0.61	7.7	>0.11	10.50	N	c
81659	123	<282	26	>5	0.052–0.27	2	>0.06	3.78	Y	c
81812	···	<93.4	···	>25	>0.26	11	>0.19	5.63	Y	b
81971	79.7	<133	31	>11	0.12–0.34	44	>0.43	15.10	Y	c
82069	156	<183	12	>8.6	0.08–0.11	12	>0.42	17.30	N	c
82253	···	<183	···	>7.6	>0.068	3.2	>0.12	3.10	Y	b
82673	176	<232	22	>12	0.17–0.29	3.3	>0.12	14.40	Y	c
83402	169	<241	8.2	>4	0.044–0.089	4.3	>0.17	6.37	Y	c
83478	162	<206	13	>8.2	0.11–0.17	4.7	>0.16	13.60	Y	c
83796	···	<214	···	>3.3	>0.037	6.1	>0.22	3.68	Y	b
83911	···	<190	···	>4	>0.046	6.7	>0.26	4.26	Y	b
83946	79.7	<214	27	>3.7	0.034–0.25	17	>0.17	3.32	Y	c
84163	123	<241	7	>1.8	0.021–0.081	8.4	>0.28	3.08	Y	c
84299	144	<214	6.3	>2.9	0.026–0.056	14	>0.52	5.28	Y	c
84510	···	<198	···	>11	>0.1	1.5	>0.05	3.86	Y	b
84819	105	<190	14	>4.2	0.042–0.14	14	>0.35	6.92	Y	c
84881	150	<150	12	>12	0.11–0.11	410	>14	119.00	N	c
85224	86.3	<105	20	>13	0.12–0.18	260	>3.7	48.90	Y	c
85290	97.2	<282	52	>6.2	0.064–0.54	2.8	>0.053	3.59	N	c
85721	93.4	<241	19	>2.8	0.025–0.17	14	>0.25	3.15	Y	c
85759	···	<241	···	>4.6	>0.042	2.6	>0.081	3.35	Y	b
85790	89.8	<198	52	>11	0.13–0.64	6.6	>0.093	10.40	N	c
86853	190	<206	4.1	>3.5	0.03–0.036	91	>3.4	34.80	N	c
87435	···	<190	···	>4.3	>0.057	4.1	>0.16	3.55	Y	b
88349	···	<156	···	>10	>0.12	4.4	>0.17	10.40	N	b
89342	···	<176	···	>11	>0.096	3	>0.11	5.44	Y	b
90176	···	<169	···	>8.5	>0.11	4.6	>0.18	7.49	Y	b
90563	···	<183	···	>2.3	>0.03	12	>0.48	4.10	Y	b
90806	···	<101	···	>45	>0.65	7.1	>0.14	15.60	Y	b
91656	···	<198	···	>4.9	>0.055	4.7	>0.18	5.12	Y	b
92346	156	<251	13	>4.9	0.048–0.12	3	>0.11	6.20	Y	c
92676	156	<206	13	>7.6	0.092–0.16	7.3	>0.27	15.00	N	c
93327	97.2	<223	18	>3.4	0.039–0.21	10	>0.21	4.85	Y	c
93743	···	<251	···	>2.4	>0.054	3.5	>0.11	3.13	Y	b
96440	···	<109	···	>27	>0.34	6.3	>0.17	9.07	Y	b
96610	109	<183	25	>9	0.089–0.25	6.7	>0.17	10.70	Y	c
96718	···	<183	···	>6.7	>0.062	4.4	>0.17	4.17	Y	b
97028	···	<206	···	>11	>0.1	2.3	>0.076	6.34	Y	b
98304	93.4	<144	12	>4.9	0.043–0.1	81	>1.5	10.70	Y	c
98579	···	<162	···	>14	>0.14	2	>0.072	4.14	Y	b
100464	169	<190	6.3	>5	0.042–0.053	29	>1.1	27.10	Y	c
102880	162	<190	9.1	>6.6	0.055–0.076	15	>0.57	18.00	Y	c
103224	···	<223	···	>6.4	>0.063	3.6	>0.13	4.27	Y	b
103456	131	···	10	···	0.091	···	>6.7	3.76	Y	a
103602	···	<241	···	>2.2	>0.026	4.8	>0.16	2.90	Y	b
103777	···	<251	···	>6.2	>0.067	1.9	>0.052	3.62	Y	b
104430	133	<198	18	>8.1	0.08–0.18	8.1	>0.28	12.50	Y	c

Table 5.3 (cont'd)

HIP ID	T_d (K)	$T_{d,\mathrm{lim}}$ (K)	R_d (AU)	$R_{d,\mathrm{lim}}$ (AU)	θ ($''$)	f_d ($\times 10^{-5}$)	$f_{d,\mathrm{lim}}$ ($\times 10^{-5}$)	$\Sigma_{E[W3-W4]}$	New?	Notes
105570	···	<271	···	>8.7	>0.086	2.1	>0.055	3.79	Y	b
106313	···	<190	···	>4.5	>0.041	5.9	>0.23	3.83	Y	b
106783	86.3	<198	47	>8.9	0.1–0.53	7.7	>0.096	7.42	N	c
107063	···	<89.8	···	>35	>0.3	5.8	>0.088	3.50	Y	b
107336	···	<190	···	>9.8	>0.089	2.3	>0.084	4.22	N	b
107517	···	<156	···	>19	>0.22	1.7	>0.059	5.71	Y	b
107585	133	<169	16	>9.8	0.1–0.16	11	>0.36	16.50	N	c
107697	···	<190	···	>6.8	>0.059	4.2	>0.16	4.31	Y	b
108570	···	<206	···	>5.8	>0.053	4.2	>0.15	4.94	Y	b
109198	105	<214	9.9	>2.4	0.024–0.099	15	>0.36	3.80	Y	c
110739	···	<150	···	>8.3	>0.11	5.9	>0.23	6.85	N	b
110786	89.8	<176	26	>6.8	0.087–0.33	18	>0.28	9.45	N	c
111264	97.2	<198	8.9	>2.1	0.022–0.091	28	>0.57	3.64	Y	c
111822	···	<123	···	>12	>0.1	6.9	>0.23	3.17	Y	b
112694	139	<306	20	>4.1	0.039–0.19	1.8	>0.061	3.33	Y	c
112835	···	<206	···	>4.8	>0.052	3.2	>0.12	3.07	Y	b
113195	···	<223	···	>3.4	>0.044	4.3	>0.15	3.44	Y	b
113981	···	<156	···	>7.9	>0.099	3.2	>0.13	3.13	Y	b
114031	···	<128	···	>20	>0.19	6	>0.18	12.00	Y	b
114371	183	<271	11	>5	0.048–0.11	2.6	>0.09	4.50	Y	c
114802	···	<83	···	>38	>0.35	8.8	>0.1	3.67	Y	b
114868	···	<261	···	>3.3	>0.042	3.6	>0.11	3.22	Y	b
115806	169	<251	16	>7.5	0.067–0.15	2.5	>0.085	7.68	Y	c
116479	···	<169	···	>6.3	>0.062	5.6	>0.22	4.31	Y	b
117352	131	···	13	···	0.121	···	>3.8	3.82	Y	a
118022	···	<118	···	>11	>0.11	6.3	>0.2	4.24	Y	b
118027	97.2	<139	32	>16	0.17–0.35	19	>0.35	25.80	Y	c
118133	118	<198	22	>7.7	0.082–0.23	4.9	>0.14	7.94	N	c

Note. — A summary of the calculated disk properties of stars with $W3-W4$ excesses not identified in Chapters 3 and 4. Blackbody temperatures for the dust are listed alongside calculated circumstellar locations, projected angular extent of the dust and the fractional bolometric luminosity. We also list the $W3-W4$ excess significance of each star, along side whether the star is a new detection (Y) or not (N).

a. $W4$-only excess: The W3 excess flux in this case was either saturated or $> 3\sigma$ below the photosphere. A limiting temperature and radius for the dust cannot be determined. Lower limit on the fractional luminosity was calculated for a blackbody with peak emission at $\lambda = 22\mu$m as described in § 3 in Chapter 3.

b.The $W3$ excess flux is formally negative and an upper limit on the excess flux is used to place a 3σ limit on the dust temperature and radius. Lower limit on the fractional luminosity was calculated for a blackbody with peak emission at $\lambda = 22\mu$m as described in § 3 in Chapter 3.

c. Both the $W3$ and the $W4$ excesses were used to calculate a dust temperature and radius. An upper limit on the $W3$ excess flux was used to calculate a 3σ limit on the dust temperature and radius. Lower limit on the fractional luminosity was calculated for a blackbody with peak emission at λ=22μm as described in § 3 in Chapter 3.

Chapter 6

Discussion

6.1 Characterization of Excesses

6.1.1 Evidence of Warm Dust

One of the goals of this study was to ascertain the census of systems which harbor dust at circumstellar distances analogous with the terrestrial planet zone or asteroid belt regions. This means the dust would be located at temperatures between 130–300 K. Because the thermal emission we detect is unresolved, the degeneracies between dust size and temperature make it difficult to correctly ascertain the dust location.

The SED fitting I have conducted allows for an estimate of the dust temperature. Since I use the $W4$ excess flux and any marginal $W3$ excess flux (or 3σ upper limit to the $W3$ excess), I can better constrain the dust temperature, from which an estimate of the dust location can be determined. There is a possibility that dust may exist at colder temperatures in these systems, given the higher incidence of cold dust systems. As such, the excess flux we are detecting at $W4$ for most of our debris disk candidates may be due to the Wien emission from a colder population of dust, at distances analogous to the EKB. The only way to truly lift this degeneracy is to observe these disks in the far-IR. Unfortunately, there is currently no mission which has the capability of performing these observations.

Our analysis in § 4 of Chapter 3 shows that the average of the ratio between the excess $W3$ and $W4$ flux from our newly detected disk candidates within 75 pc, translates to an aggregate temperature of 134 ± 8 K, analogous to the outer edge of the MAB. We also found that this same analysis, when done for the $W4$ detections with previously reported cold and warm disks showed an aggregate temperature of 90 ± 6 K and 154 ± 19 K, respectively. In other words, the aggregate of known cold disks indicates a $W4$ excess flux consistent with

EKB dust, while the aggregate of known warm disks indicates a $W4$ excess flux consistent with asteroid belt dust. This then implies that the average new $W4$ excess detection is likely to be host to asteroid belt dust as well.

This analysis was possible because we were able to accurately measure the $W3$ excess flux, independent of the photospheric fits. This analysis has yet to be undertaken beyond 75 pc, and hence at present I cannot assess the aggregate dust temperature for the entire 120 pc sample. However, if the aggregate of our 75 pc sample of new $W4$ excesses indicates a warm excess (which is on average $T_d \sim$150 K), then we can extrapolate this result to stars beyond 75 pc, and infer that a non-significant fraction of new $W4$ excesses are host to warm dust.

6.2 Comparison To Other *WISE* Surveys

It is important to place our survey of *WISE* debris disks in context with those in the literature to determine whether we are improving upon the design of other studies. In Figure 6.1, I plot the $B_T - V_T$ color for the 222 new disk candidates we identified from this survey alone, as a function of their $W3-W4$ color excess. In addition, I plot the same parameters for *Hipparcos* stars that were identified as $W4$ excesses by Vican & Schneider (2014) or Wu et al. (2013) along with the condition that they pass our selection criteria in § 2.2.1 in Chapter 3. The division in $B_T - V_T$ between these two surveys is inherent to each, as Vican & Schneider (2014) searched for excesses around late F to K stars, while Wu et al. (2013) was sensitive to excesses around bright stars A – F stars.

What is evident is that the excesses we detect are larger in number, and are detected at fainter levels compared to the other surveys. We cannot rely on the survey results from Vican & Schneider (2014), as a number of their stars show negative color excesses or small excesses such that their $\Sigma_{E[W3-W4]}$ are less than our $\Sigma_{E[W3-W4]_{99.5}}$ threshold. Their excesses were detected by subtracting the photospheric flux after fitting near-IR and optical data to photospheric models. As we discussed in § 2.3.1, this introduces biases in measuring the excess, and introduces false-positives into the survey. In contrast, our survey is complementary, though larger in scope, to Wu et al. (2013), as they are preferentially sensitive to brighter excesses.

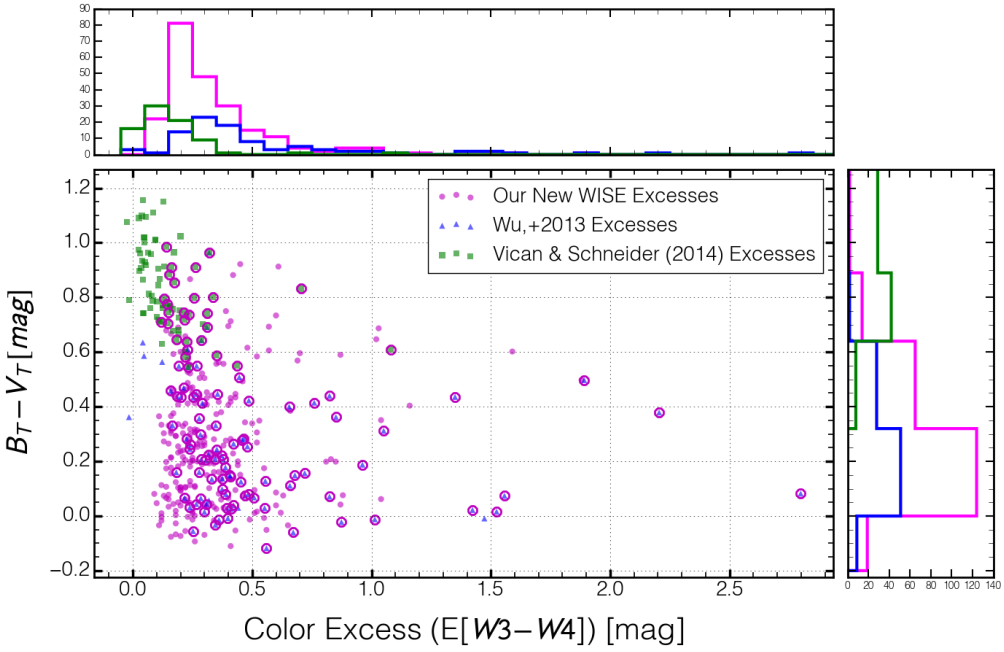

Figure 6.1: Plot of the $B_T - V_T$ colors as a function of the $W3 - W4$ color excess ($E[W3 - W4]$), for all previously unreported *WISE* $W4$ excesses from our survey, the *WISE* survey by Vican & Schneider (2014), and the *WISE* survey by Wu et al. (2013). The top and right panels show the marginalized distributions of both parameters for all three sets of stars. Excesses that our surveys also detect from the other two are indicated by open magenta circles, which are not included in the magenta marginalized distributions.

6.3 Lessons Learned

The success of the surveys I present in this thesis is primarily due to our new methods to filter and calibrate the *WISE* photometry. This includes the plethora of data filters we used to cleanse the sample of contaminants as well as the added sensitivity gained by empirically deriving photospheric colors with which to identify excesses.

The filters we placed on our samples were refined over the course of a couple of years. The struggle to gain a better handle on the *WISE* systematics each time revealed a new quirk in the data, allowing us to increase our understanding on how to better handle the *WISE* data. Caveats such as removing stars contaminated from *WISE* internally inconsistent data, scattered moon light, closely projected companions, etc., became apparent after each iteration of the analysis. These and other filters have been discussed extensively in § 2.2.1 in Chapter 3, and in § 5.2.1. However, the importance of using empirical colors rather than SED fits to identify excesses has not been discussed in great detail. In the following section, I quickly describe these caveats.

6.3.1 Empirical vs. Synthetic *WISE* Colors

When determining the integrated photospheric flux (S) for a broadband filter, one typically convolves the filter's spectral response curve R_λ (similar to the ones in Figure 2.4) with the photospheric emission $F_\star(\lambda)$, typically interpolated from a grid of photospheric models

$$S = \frac{\int \lambda F_*(\lambda)\, R_\lambda\, d\lambda}{\int \lambda R_\lambda\, d\lambda}. \tag{6.1}$$

At times, however, the empirical flux from a particular filter may differ from the filter-convolved "synthetic" flux over a photospheric model. This may be because the filter's band-centered wavelength was misreported, certain systematics are not included in the filter response curves, or perhaps the models do not reflect the true emission spectrum of the observed star.

Whichever the case, if there is any difference between the empirical flux and the synthetic flux, then the latter will misrepresent the former. For excess identification, this difference can introduce false discoveries or even decrease a survey's sensitivity to excesses — if it's primary detection method is SED fit subtraction.

In Figure 6.2, I have plotted the synthetic and empirical *WISE* colors as a function of their $B_T - V_T$ to represent different spectral types. What is immediately clear is that, if one ignores the small scale fluctuations in the empirical trends, there is a significant systematic offset for all *WISE* colors

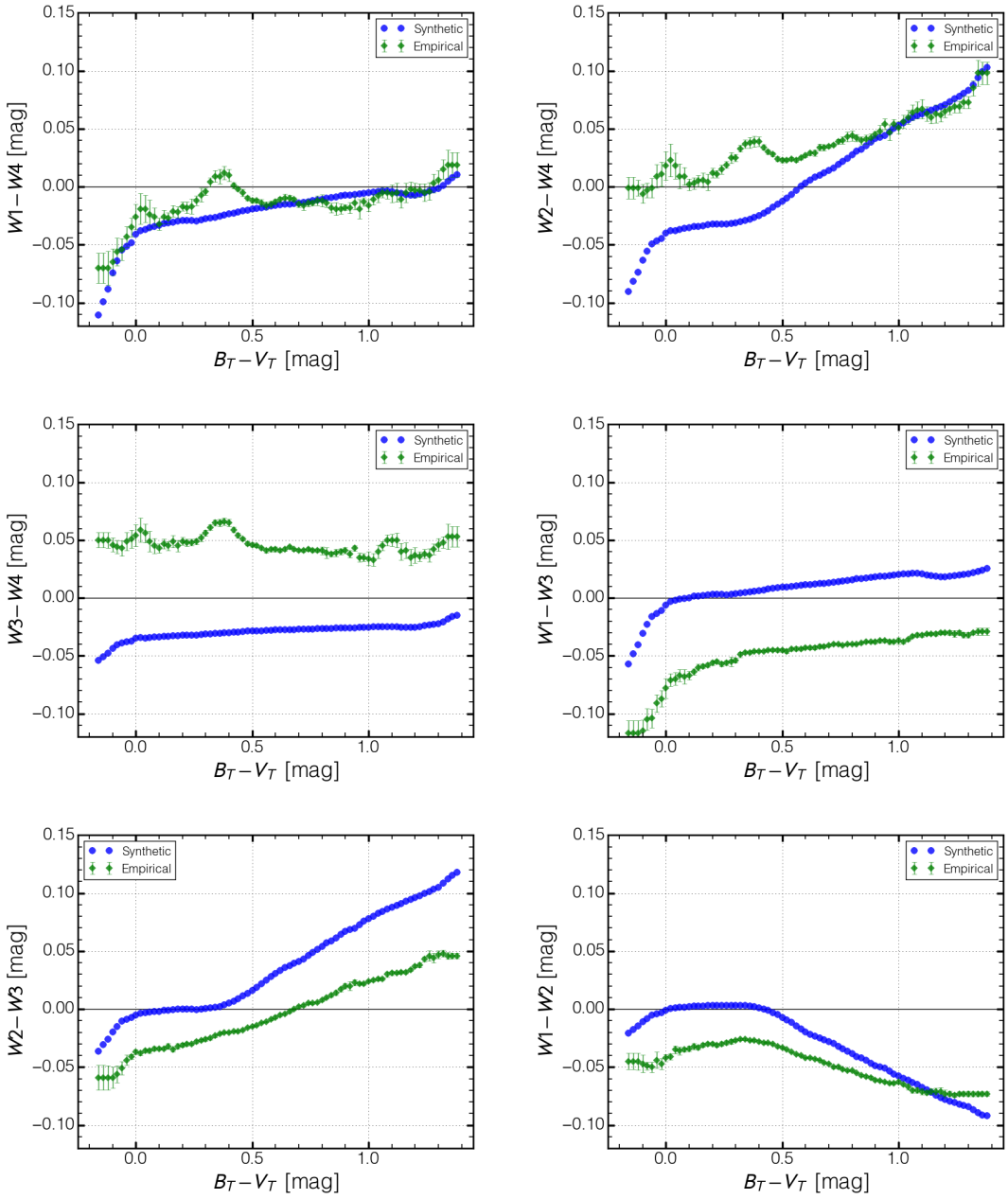

Figure 6.2: Plots of *WISE* photospheric colors. The empirical colors were derived using a running mean approach to the trimmed parent sample of each color described in § 2.5 of Chapter 3. The synthetic colors were derived by convolving the *WISE* filter profiles over a set of models at stellar temperatures corresponding to different $B_T - V_T$ (Pecaut & Mamajek, 2013). All photospheric models were obtained at solar metallicity and log(g)=4.5.

with the exception of $W1 - W4$. From the $W4$ colors, the synthetic colors are underestimated, and are typically negative for the most part. Thus, any excess based on simply deriving the photospheric flux from filter convolution will overestimate the excess flux at $W4$. The opposite is true for the $W3$ colors, which 1) show that the synthetic colors are overestimated and 2) that the empirical $W1 - W3$ colors are primarily negative, systematically offset from the synthetic colors by $+0.06$ mags. In other words, the excess derived from the filter-convolved flux will be underestimated, and there will be too few $W3$ excesses detected by SED fitting — as has been the case before our studies.

To correctly identify an excess using filter-convolved photospheric fluxes, a correction in the star's synthetic colors is required, derived from the empirical ones. Otherwise, studies will always be biased to misidentifying excesses at an alarmingly large rate (seen by the $\sim$60% false-positive rate in Vican & Schneider (2014); see § 5.4 in Chapter 3).

Color corrections would also be needed to properly derive the thermal properties of any circumstellar dust. Our study currently does not use any color corrections when deriving the synthetic fluxes in calculating our dust temperatures. Given the large uncertainties in the temperature determinations from only one or two excess data points, our omission of color-corrections is a second-order effect.

Chapter 7

Conclusion & Future Directions

7.1 Summary

Debris disks play an integral part in understanding the dynamical activity in planetary systems, and how they relate to the evolution of the Solar System. The dust we observe, from both resolved and unresolved thermal emission, can act as a signpost for planetary systems. The majority of the observed dust has been from unresolved thermal emission from space-based observatories performing large surveys to identify debris disks. The advancement in our understanding of how dust evolves is largely due to these surveys over the last thirty years. The majority of disks detected thus far are analogous to EKB, with cold dust detected from their far-IR excess emission.

However, the incidence of systems with warm dust, analogous to the MAB is much smaller in comparison. Since warm dust acts as a signpost for dynamical activity in the terrestrial planet zone, identification and characterization of more of these type of systems will aid in understanding how the inner regions of these systems evolve and determine the ubiquity of solar system analogs.

In this thesis, I presented a set of studies which take advantage of the data products from the *WISE* All-Sky database to search for mid-IR excess flux at 12μm and 22μm. The higher resolution and sensitivity of *WISE* compared to *IRAS*, along with the increased coverage compared to other pointed observatories allow for detection of warm dust around a larger set of stars than previously possible.

Although *WISE* has been previously used to detect mid-IR excesses around nearby stars, our studies take full advantage of the *WISE* sensitivity envelope. We searched for excess flux around main-sequence *Hipparcos* stars, by using the full suite of *WISE*colors for stars within 75 pc, and the $W3-W4$ color for stars out to 120 pc. Our careful removal of contaminants, accurate determination

of the empirical photospheric colors, and improvements made to accurately determine our confidence levels, have yielded 22μm excesses as faint as 8% above the photospheric emission at a false discovery rate of $< 0.5\%$, and $W3$ excesses as low as 6% above the photosphere, at a false-discovery rate of $< 2\%$.

The saturation corrections we implemented to the $W1$ and $W2$ photometry have allowed us to identify excesses around brighter stars in the *WISE* database, while our unWISE rejection analysis allows us to remove astrometrically contaminated sources prior to excess selection. As a result, we have identified a total of 338 new 10–30μm excesses out to 120 pc. This increases the known sample of 10–30μm excesses by 35% for stars within 75 pc, by 130% for stars between 75–120 pc, and by 40% overall.

The large number of new detections presented in this thesis, and the conclusions which can be drawn from the set of studies, not only provide a census of warm disks in the solar neighborhood, but also enhance our understanding of planetary systems that have yet to be discovered and that have already been discovered within the solar neighborhood. Planetary systems that are host to bright debris disks (i.e., HR 8799, β Pic) have been shown to have analogous architecture to the Solar System. Our detection of faint warm dust around the 51 Eridani system, provides context for the newly discovered 51 Eridani b planet (see § A; Macintosh et al., 2015). The architecture of the $2M_{\rm J}$ exoplanet, between a warm and cold belt in this young 20 Myr system, echoes similarities to perhaps a younger Solar System. Hence, the new, fainter population of *WISE* disks that we have provided for the community, can help un understand the ubiquity and evolution of our own Solar System.

7.2 Future Directions

7.2.1 *WISE* Disk Evolution Survey

The next step to this study is to provide an evolutionary analysis of our *WISE* detected disks. Since the excess flux levels we are detecting are relatively faint (down to $\sim$10% above the photosphere, and on average 30% above the photosphere), it would be interesting to know how these systems relate back to the Solar Sytem: are they evolved systems perhaps as old as the solar system, yet able to produce copious amounts of dust? Or are they much younger, at dust levels similar to what was hypothesized for the Solar System in its infancy?

The study we performed was done using an unbiased sample of *Hipparcos* field stars, most of which do not have age information. A quick way to determine ages for stars is to use theoretical isochrones on a color-magnitude

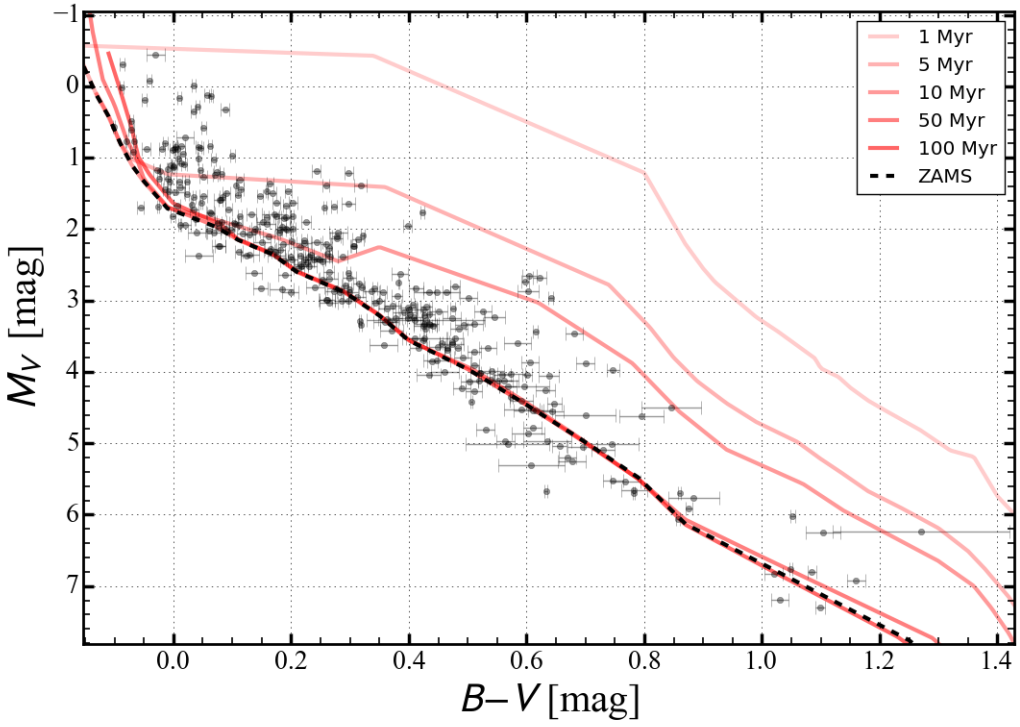

Figure 7.1: A color-magnitude diagram of the newly identified debris disk-host stars from our *Hipparcos-WISE* cross-match. Theoretical isochrones from Siess et al. (2000, 1–100 Myr) have been overplotted. The clustering of stars near the main-sequence, along with the uncertainties in their $B - V$ colors, prevents accurate age determination for stars older than the zero age main-sequence.

diagram (CMD) for stars with known distances. Figure 7.1 hows our excess stars in a CMD overplotted theoretical isochrones.

However, for stars on the zero-age main sequence[1] or older (>10–50 Myr), isochrone fitting becomes very insensitive to age. For FGK stars, chromospheric and coronal activity, and lithium abundance indicators are much better discriminants of stellar age between 0.1–10 Gyr and can be readily measured from high-resolution spectra. A-star ages are more difficult to pin down, but even for these, high-resolution spectra can aid in removing ambiguity in their placement on the CMD.

In an effort to ascertain the ages for our stars, we are undertaking a high-resolution optical spectroscopic survey of our excess host stars. These observations are designed to measure the age-dependent spectroscopic features for the solar type stars in our excess sample, as well as identify any line-of-sight circumstellar Na I absorption, which is evidence of gas in the system (Redfield, 2007).

We have used the echelle spectroscopic instruments on the Mayall 4 m telescope to observe our northern targets ($\delta > -30°$), and the 3.9 m Anglo Australian Telescope for our southern targets. Time was awarded to us for one or both of these telescopes in the 2012B, 2013A, 2013B, 2014A, and 2014B semesters. During this time, we obtained the spectra for 85% of the targets in our sample that did not have archival echelle spectra observations.

The analysis of these data will open a new direction enabled by our excess-search survey: determining the evolution of warm dust around the largest to-date sample of debris disk-host stars in the solar neighborhood.

[1]The location on the CMD when the star reaches the main-sequence; i.e., when the star starts burning hydrogen at its core.

Bibliography

Acke, B. et al. 2012, A&A, 540, A125

Adams, F.C. et al. 2004, ApJ, 611, 360

Allègre, C.J., Manhès, G. and Göpel, C. 2008, Earth and Planetary Science Letters, 267, 386

Andre, P. and Montmerle, T. 1994, ApJ, 420, 837

Aumann, H.H. et al. 1984, ApJL, 278, L23

Avenhaus, H., Schmid, H.M. and Meyer, M.R. 2012, A&A, 548, A105

Backman, D.E. and Paresce, F. 1993, in Protostars and Planets III, ed. E. H. Levy & J. I. Lunine, 1253

Ballering, N.P. et al. 2013, ApJ, 775, 55

Balog, Z. et al. 2014, Experimental Astronomy, 37, 129

Batygin, K. and Brown, M.E. 2010, ApJ, 716, 1323

Beckwith, S.V.W., Henning, T. and Nakagawa, Y. 2000, Protostars and Planets IV, 533

Beckwith, S.V.W. et al. 1990, AJ, 99, 924

Beichman, C.A. et al. 2005, ApJ, 622, 1160

Beichman, C.A. et al. 2006, ApJ, 652, 1674

Bitner, M.A. et al. 2007, ApJL, 661, L69

Bryden, G. et al. 2009, ApJ, 705, 1226

Bryden, G. et al. 2006, ApJ, 636, 1098

Burns, J.A., Lamy, P.L. and Soter, S. 1979, Icarus, 40, 1

Carpenter, J.M. et al. 2009a, ApJS, 181, 197

Carpenter, J.M. et al. 2009b, ApJ, 705, 1646

Cassan, A. et al. 2012, Nature, 481, 167

Chen, C.H. et al. 2005, ApJ, 623, 493

Chen, C.H. et al. 2011, ApJ, 738, 122

Chen, C.H. et al. 2014, ApJS, 211, 25

Chen, C.H. et al. 2012, ApJ, 756, 133

Chen, C.H. et al. 2006, ApJ, 166, 351

Cruz-Saenz de Miera, F. et al. 2014, MNRAS, 437, 391

Currie, T. et al. 2008, ApJ, 672, 558

De Marchi, G. et al. 2013, MNRAS, 435, 3058

De Rosa, R.J. et al. 2014, MNRAS, 437, 1216

de Vries, B.L. et al. 2012, Nature, 490, 74

Dodson-Robinson, S.E. et al. 2011, AJ, 141, 11

Donaldson, J.K. et al. 2012, ApJ, 753, 147

Draine, B.T. 2003, ARA&A, 41, 241

Eiroa, C. et al. 2013, A&A, 555, A11

Fujiwara, H. et al. 2013, A&A, 550, A45

Gomes, R. et al. 2005, Nature, 435, 466

Gorlova, N. et al. 2006, ApJ, 649, 1028

Gray, R.O. et al. 2006, AJ, 132, 161

Hahn, J.M. et al. 2002, Icarus, 158, 360

Hartigan, P., Edwards, S. and Ghandour, L. 1995, ApJ, 452, 736

Hauschildt, P.H., Allard, F. and Baron, E. 1999, ApJ, 512, 377

Heap, S.R. et al. 2000, ApJ, 539, 435

Hillenbrand, L.A. et al. 2008, ApJ, 677, 630

Hunter, J.D. 2007, Computing In Science & Engineering, 9, 90

Kalas, P. et al. 2008, Science, 322, 1345

Kalas, P., Graham, J.R. and Clampin, M. 2005, Nature, 435, 1067

Kalas, P. et al. 2013, ApJ, 775, 56

Kelsall, T. et al. 1998, ApJ, 508, 44

Kennedy, G.M. and Wyatt, M.C. 2013, MNRAS, 433, 2334

Kennedy, G.M. et al. 2012, MNRAS, 2384

Kitchin, C.R. 2004, Astronomy Now, 18, 24

Koerner, D.W. et al. 2010, ApJL, 710, L26

Krivov, A.V. 2010, Research in Astronomy and Astrophysics, 10, 383

Krivov, A.V. et al. 2011, MNRAS, 418, L15

Lagrange, A.M. et al. 2010, Science, 329, 57

Lallement, R. et al. 2003, A&A, 411, 447

Lang, D. 2014, AJ, 147, 108

Latham, D.W. et al. 1989, Nature, 339, 38

Lawler, S.M. et al. 2009, ApJ, 705, 89

Lawler, S.M. and Gladman, B. 2012, ApJ, 752, 53

Liou, J.C. and Zook, H.A. 1999, AJ, 118, 580

Lisse, C.M. et al. 2009, ApJ, 701, 2019

Lisse, C.M. et al. 2012, ApJ, 747, 93

Luhman, K.L. and Mamajek, E.E. 2012, ApJ, 758, 31

Macintosh, B. et al. 2006, in SPIE Conference Series, Vol. 6272, SPIE Conference Series

Macintosh, B. et al. 2015, Science, 350, 64

Maris, M., Burigana, C. and Fogliani, S. 2006, A&A, 452, 685

Marleau, G.D. and Cumming, A. 2014, MNRAS, 437, 1378

Marois, C. et al. 2010, Nature, 468, 1080

Matthews, B.C. et al. 2014, Protostars and Planets VI, 521

Mayor, M. and Queloz, D. 1995, Nature, 378, 355

McDonald, I., Zijlstra, A.A. and Boyer, M.L. 2012, MNRAS, 427, 343

Meyer, M.R. et al. 2008, ApJL, 673, L181

Meyer, M.R. et al. 2006, PASP, 118, 1690

Mizusawa, T.F. et al. 2012, AJ, 144, 135

Moór, A. et al. 2006, ApJ, 644, 525

Moór, A. et al. 2011, ApJS, 193, 4

Morales, F.Y. et al. 2012, ApJ, 757, 7

Morales, F.Y. et al. 2011, ApJL, 730, L29

Morbidelli, A. et al. 2010, AJ, 140, 1391

Nesvold, E.R. and Kuchner, M.J. 2015, ArXiv e-prints

Nesvorný, D. et al. 2010, ApJ, 713, 816

Osterloh, M. and Beckwith, S.V.W. 1995, ApJ, 439, 288

Patel, R.I., Metchev, S.A. and Heinze, A. 2014a, ApJS, 212, 10

Patel, R.I., Metchev, S.A. and Heinze, A. 2014b, ApJS, 214, 14

Patel, R.I., Metchev, S.A. and Heinze, A. 2015, submitted, ApJS

Pecaut, M.J. and Mamajek, E.E. 2013, ApJS, 208, 9

Perryman, M.A.C. et al. 1997, A&A, 323, L49

Planck Collaboration et al. 2014, A&A, 571, A14

Plavchan, P. et al. 2009, ApJ, 698, 1068

Rebull, L.M. et al. 2008, ApJ, 681, 1484

Redfield, S. 2007, ApJL, 656, L97

Rhee, J.H. et al. 2007, ApJ, 660, 1556

Riaz, B. et al. 2012, MNRAS, 420, 2497

Ribas, Á. et al. 2012, A&A, 541, A38

Rieke, G.H. et al. 2005, ApJ, 620, 1010

Rizzuto, A.C., Ireland, M.J. and Zucker, D.B. 2012, MNRAS, 421, L97

Robitaille, T. and Bressert, E. 2012, APLpy: Astronomical Plotting Library in Python, Astrophysics Source Code Library

Rodigas, T.J., Malhotra, R. and Hinz, P.M. 2014, ApJ, 780, 65

Rodigas, T.J. et al. 2015, ApJ, 798, 96

Scicluna, P. et al. 2014, A&A, 566, L3

Siegler, N. et al. 2007, ApJ, 654, 580

Siess, L., Dufour, E. and Forestini, M. 2000, A&A, 358, 593

Skrutskie, M.F. et al. 2006, AJ, 131, 1163

Smith, B.A. and Terrile, R.J. 1984, Science, 226, 1421

Song, I. et al. 2005, Nature, 436, 363

Spangler, C. et al. 2001, ApJ, 555, 932

Su, K.Y.L. et al. 2006, ApJ, 653, 675

Sykes, M.V. 1990, Icarus, 85, 267

Telesco, C.M. et al. 2005, Nature, 433, 133

Terebey, S., Shu, F.H. and Cassen, P. 1984, ApJ, 286, 529

Theissen, C.A. and West, A.A. 2014, ApJ, 794, 146

Thureau, N.D. et al. 2014, MNRAS, 445, 2558

Trilling, D.E. et al. 2008, ApJ, 674, 1086

Trilling, D.E. et al. 2007, ApJ, 658, 1289

Tsiganis, K. et al. 2005, Nature, 435, 459

Urban, L.E. et al. 2012, The Astrophysical Journal, 750, 98

van Leeuwen, F. 2007, A&A, 474, 653

Vican, L. and Schneider, A. 2014, ApJ, 780, 154

Wahhaj, Z. et al. 2015, ArXiv e-prints

Wang, S., Li, A. and Jiang, B.W. 2014, Planet. Space Sci., 100, 32

Williams, J.P. and Cieza, L.A. 2011, ARA&A, 49, 67

Winn, J.N. and Fabrycky, D.C. 2015, ARA&A, 53, null

Wright, E.L. et al. 2010, AJ, 140, 1868

Wu, C.J. et al. 2013, ApJS, 208, 29

Wyatt, M.C. 2005, A&A, 440, 937

Wyatt, M.C. 2008, ARA&A, 46, 339

Wyatt, M.C. et al. 2015, Ap&SS, 357, 103

Wyatt, M.C. et al. 2007, ApJ, 663, 365

Zuckerman, B. 2001, ARA&A, 39, 549

Appendix A

Gemini Planet Imager Exoplanet Survey Detection of 51 Eri b

The Gemini Planet Imager (GPI; Macintosh et al., 2006) is a state of the art high-contrast imaging instrument, currently installed on the 8 m Gemini South Telescope in Chile. GPI was designed primarily to identify and characterize young, faint Jovian mass exoplanets at small angular separations from their host stars.

For the last two years, I have been a part of the Gemini Planet Imager Exoplanet Survey team (GPIES). GPIES' goal is to conduct a survey of ∼300 nearby, young stars to identify young Jovian mass exoplanets. GPIES' first discovery was of the $2M_J$ exoplanet 51 Eridani b (HIP 21547) around its 20 Myr host star. The paper of the discovery was published in the journal Science on August 13$^{\text{th}}$, 2015. In this chapter, I include this paper with the citation of Macintosh et al. (2015). This article has been reprinted here with permission from AAAS. Although my efforts did not lead to this discovery, the system does possess a warm disk which we identified in Chapter 3, which provides context for the discovery and its relationship to the Solar System.

Stanford Synchrotron Radiation Lightsource (SSRL) Beamline 12-2, the National Institute of General Medical Sciences and National Cancer Institute Structural Biology Facility (GM/CA) at the Advanced Photon Source (APS), and the Advanced Light Source (ALS) beamline 8.2.1 for support with x-ray diffraction measurements. We acknowledge the Gordon and Betty Moore Foundation, the Beckman Institute, and the Sanofi-Aventis Bioengineering Research Program for support of the Molecular Observatory at the California Institute of Technology (Caltech). The operations at the SSRL, ALS, and APS are supported by the U.S. Department of Energy and the NIH. GM/CA has been funded in whole or in part with federal funds from the National Cancer Institute (ACB-12002) and the National Institute of General Medical Sciences (AGM-12006). T.S. was supported by a Postdoctoral Fellowship of the Deutsche Forschungsgemeinschaft. S.P. and D.H.L are Amgen Graduate Fellows, supported through the Caltech-Amgen Research Collaboration. F.M.H. was supported by a Ph.D. student fellowship of the Boehringer Ingelheim Fonds. S.K. was supported by NIH Awards R01-GM090324 and U54-GM087519 and by the University of Chicago Comprehensive Cancer Center (P30-CA014599). A.A.K. was supported by NIH awards U01-GM094588 and U54-GM087519 and by Searle Funds at The Chicago Community Trust. A.H. was supported by Caltech startup funds, the Albert Wyrick V Scholar Award of the V Foundation for Cancer Research, the 54th Mallinckrodt Scholar Award of the Edward Mallinckrodt Jr. Foundation, a Kimmel Scholar Award of the Sidney Kimmel Foundation for Cancer Research, a Camille-Dreyfus Teacher Scholar Award of The Camille and Henry Dreyfus Foundation, and NIH grant R01-GM111461. The coordinates and structure factors have been deposited with the Protein Data Bank with accession codes 5CWV (Nup192^{TAIL}), 5CWU (Nup188^{TAIL}), 4JQ5 (*hs*Nup49$^{CCS2+3*}$), 4JNV and 4JNU (*hs*Nup57^{CCS3*}), 5CWT (Nup57^{CCS3*}), 4JO7 (*hs*Nup49$^{CCS2+3*}$•hsNup57^{CCS3*}, 2:2 stoichiometry), 4JO9 (*hs*Nup49$^{CCS2+3*}$•hsNup57^{CCS3*}, 1:2 stoichiometry), 5CWW (Nup82^{NTD}•Nup159^{T}•Nup145N^{APD}), and 5CWS (CNT•Nic96^{R1}•sAB-158). The authors declare no financial conflicts of interest. S.K. and A.K. are inventors on a patent application filed by the University of Chicago that covers a design of monobody libraries (US 13/813,409). Monobodies are available from S.K. under a material transfer agreement with the University of Chicago.

SUPPLEMENTARY MATERIALS

www.sciencemag.org/content/350/6256/56/suppl/DC1
Materials and Methods
Figs. S1 to S38
Tables S1 to S9
Movies S1 to S4
References (*42*–*65*)

29 June 2015; accepted 12 August 2015
Published online 27 August 2015
10.1126/science.aac9176

REPORTS

PLANETARY SCIENCE

Discovery and spectroscopy of the young jovian planet 51 Eri b with the Gemini Planet Imager

B. Macintosh,[1,2]* J. R. Graham,[3] T. Barman,[4] R. J. De Rosa,[3] Q. Konopacky,[5] M. S. Marley,[6] C. Marois,[7,8] E. L. Nielsen,[9,1] L. Pueyo,[10] A. Rajan,[11] J. Rameau,[12] D. Saumon,[13] J. J. Wang,[3] J. Patience,[11] M. Ammons,[2] P. Arriaga,[14] E. Artigau,[12] S. Beckwith,[3] J. Brewster,[9] S. Bruzzone,[15] J. Bulger,[11,16] B. Burningham,[6,17] A. S. Burrows,[18] C. Chen,[10] E. Chiang,[3] J. K. Chilcote,[19] R. I. Dawson,[3] R. Dong,[3] R. Doyon,[12] Z. H. Draper,[8,7] G. Duchêne,[3,20] T. M. Esposito,[14] D. Fabrycky,[21] M. P. Fitzgerald,[14] K. B. Follette,[1] J. J. Fortney,[22] B. Gerard,[8,7] S. Goodsell,[23,24] A. Z. Greenbaum,[25,10] P. Hibon,[24] S. Hinkley,[26] T. H. Cotten,[27] L.-W. Hung,[14] P. Ingraham,[28] M. Johnson-Groh,[8,7] P. Kalas,[3,9] D. Lafreniere,[12] J. E. Larkin,[14] J. Lee,[27] M. Line,[22] D. Long,[10] J. Maire,[19] F. Marchis,[9] B. C. Matthews,[7,8] C. E. Max,[22] S. Metchev,[15,29] M. A. Millar-Blanchaer,[30] T. Mittal,[3] C. V. Morley,[22] K. M. Morzinski,[31] R. Murray-Clay,[32] R. Oppenheimer,[33] D. W. Palmer,[2] R. Patel,[29] M. D. Perrin,[10] L. A. Poyneer,[2] R. R. Rafikov,[18] F. T. Rantakyrö,[24] E. L. Rice,[34,33] P. Rojo,[35] A. R. Rudy,[22] J.-B. Ruffio,[1,9] M. T. Ruiz,[35] N. Sadakuni,[36,24] L. Saddlemyer,[7] M. Salama,[3] D. Savransky,[37] A. C. Schneider,[38] A. Sivaramakrishnan,[10] I. Song,[27] R. Soummer,[10] S. Thomas,[28] G. Vasisht,[39] J. K. Wallace,[39] K. Ward-Duong,[11] S. J. Wiktorowicz,[22] S. G. Wolff,[25,10] B. Zuckerman[14]

Directly detecting thermal emission from young extrasolar planets allows measurement of their atmospheric compositions and luminosities, which are influenced by their formation mechanisms. Using the Gemini Planet Imager, we discovered a planet orbiting the ~20-million-year-old star 51 Eridani at a projected separation of 13 astronomical units. Near-infrared observations show a spectrum with strong methane and water-vapor absorption. Modeling of the spectra and photometry yields a luminosity (normalized by the luminosity of the Sun) of 1.6 to 4.0 × 10^{-6} and an effective temperature of 600 to 750 kelvin. For this age and luminosity, "hot-start" formation models indicate a mass twice that of Jupiter. This planet also has a sufficiently low luminosity to be consistent with the "cold-start" core-accretion process that may have formed Jupiter.

Several young, self-luminous extrasolar planets have been directly imaged at infrared (IR) wavelengths (*1*–*8*). The planets directly imaged to date are massive [(estimated at 5 to 13 Jupiter masses (M_J)] and positioned at large separations [9 to 650 astronomical units (AU)] from their host star, compared with planets in our solar system. Photometry and spectroscopy can be used to probe the atmospheres of these young jovian planets, providing clues about their formation. Several unexpected results have emerged. The near-IR colors of these planets are mostly red, indicating cloudy atmospheres similar to those of brown dwarfs of spectral type L. Methane absorption features are prominent in the near-IR spectra of T dwarfs [effective temperature (T_{eff}) < 1100 K], as well as in the giant planets of our solar system, but such features are weak or absent in the directly imaged exoplanets (*4*, *9*–*11*). Most young planets appear to be methane-free, even at temperatures where equivalent brown dwarfs show evidence of methane, suggesting nonequilibrium chemistry and persistent clouds that are probably age- and mass-dependent (*1*, *12*–*15*).

In spite of uncertainties about their atmospheric properties, the luminosities of these planets are well constrained. Luminosity is a function of age, mass, and initial conditions (*16*, *17*) and hence can provide insights into a planet's formation. Rapid formation (e.g., through global disk instabilities acting on a dynamical time scale) yields high-entropy planets that are bright at young ages ("hot start"). Alternatively, two-stage formation—in which the development of a dense solid core is followed by gas accretion through a shock, as is likely in the case of Jupiter—can produce a range of states, including lower-entropy planets that are cooler and slightly smaller in radius ("cold start"). The young directly imaged planets are almost all too bright for the cold-start model to apply, except for specific accretion shock properties; however, their formation is also difficult to explain by global instability, which should operate preferentially at higher masses and at large semimajor axis separations (*18*, *19*). In addition, these planets are close to the limit of sensitivity for first-generation large-telescope adaptive optics (AO) systems. The goal of the latest generation of surveys, which use dedicated high-contrast AO coronagraphs (*20*–*23*) such as the Gemini Planet Imager (GPI) and its counterparts, is to expand the sample of directly imaged planets to include closer separations, lower masses, and lower temperatures, a crucial empirical step toward investigating the above modes of formation.

The Gemini Planet Imager Exoplanet Survey (GPIES) is targeting 600 young nearby stars with the GPI instrument. The star 51 Eridani (51 Eri) was chosen as an early target for the survey because of its youth and proximity. Its stellar properties are given in Table 1. The star exhibits

weak mid- and far-IR excess emission, indicating low-mass inner (5.5 AU) and outer (82 AU) dust belts (*24*, *25*). It also has two distant (~2000 AU) stellar companions, which constitute the 6-AU–separation M-dwarf binary system GJ 3305 (*26*). 51 Eri and GJ 3305 were classified in 2001 as members of the β Pictoris moving group (*27*), and subsequent measurements support this identification (*28*). The estimated age of the β Pictoris moving group ranges from 12 to 23 million years (My) (*27*, *29*–*32*). Giving strong weight to the group's lithium-depletion boundary age, we adopted an age of 20 ± 6 My for all four components of the 51 Eri system (*28*).

We observed 51 Eri in the H band (1.65 μm) in December 2014, as the 44th target in the GPIES campaign. GPI observations produce spectroscopic cubes with a spectral-resolving power of 45 over the entire field of view. A companion planet designated 51 Eri b, was apparent after subtraction of the point spread function (PSF). The planet is located at a projected separation of 13 AU, and its spectra exhibit distinctive strong methane and water-vapor absorption (Figs. 1 and 2). We observed 51 Eri again in January 2015 to broaden the wavelength coverage, using GPI (J band, 1.25 μm) and the W. M. Keck Observatory's Near Infrared Camera 2 (NIRC2; Lp band, 3.8 μm). The observed spectra are highly similar to those of a field brown dwarf of spectral type T4.5 to T6 (Fig. 2). The J-band spectrum confirmed methane absorption at this wavelength, and the extremely red H-Lp color is similar to that of other cool, low-mass objects (Fig. 3). The signal-to-noise ratio at J-band wavelengths is inferior to that at H-band wavelengths, and extraction introduces additional systematic effects. The J-band detection is reliable (>6σ), but the fluxes in individual spectral channels are less certain. However, the methane feature was robustly detected at both bands (*28*).

Demonstrating common proper motion (*33*), or showing that the probability of a foreground or background contaminant is extremely low, establishes the nature of directly imaged planets. The interval between the December 2014 and January 2015 observations is too brief, given our astrometric accuracy (*28*), to show that 51 Eri b and 51 Eri share proper motion and parallax. However, nondetection of 51 Eri b in archival data from 2003 (*28*) excludes a stationary background source and requires proper motion within ~0.1 arc sec/year of 51 Eri. The strong methane absorption that is evident for 51 Eri b is found only in T-type or later brown dwarfs. We determined the probability of finding a T dwarf in our field by merging the observed T-dwarf luminosity functions (*27*, *28*) and adopting the spectral types and absolute magnitudes for T dwarfs (*34*), from which we calculated a false alarm rate of 1.72×10^{-7} methane objects (i.e., types T0 to T8.5) per GPI field (>5σ). The proper motion constraint eliminates a further 66% of likely background T-dwarf proper motions. The total false alarm probability after observing 44 targets is the probability of a T-spectrum object appearing in 44 Bernoulli trials, given by the binomial distribution, which yields a final probability of 2.4×10^{-6}. Although the occurrence rate of planetary companions is not known with precision, the detection of planetary objects at similar physical separations to 51 Eri b, such as β Pic b and HR8799 e, indicates that the rate is $>10^{-3}$ per star. Hence, with the high-quality spectrum available to us, it is much more likely that 51 Eri b is a bound planetary companion than a chance alignment.

We used planetary atmosphere and evolution models to estimate the properties of 51 Eri b. We first fitted the observed J- and H-band spectra using standard cloud-free equilibrium-chemistry models, with radii constrained based on mass as given by evolutionary tracks, similar to those in (*35*). This constrained fit gives an effective temperature of 750 K, with a radius [0.76 Jupiter radius (R_J)] and surface gravity similar to those of an old (10 billion years), high-mass brown dwarf. A similar, though less extreme, result (small radii and hence high masses and old ages) is associated with several model fits to observations of the HR8799 planets (*13*, *15*, *16*), even though high

Table 1. Properties of 51 Eridani and 51 Eridani b.

51 Eridani	
Spectral type	F0IV
Mass (solar masses)	1.75 ± 0.05
Luminosity ($L/L_\odot$)	7.1 ± 1
Distance (pc)	29.4 ± 0.3
Proper motion (milli-arc sec/year)	44.22 ± 0.34 (east), −64.39 ± 0.27 (north) (*44*)
Age (My)	20 ± 6
Metallicity (metal abundance over hydrogen abundance)	−0.027 (*45*)
J, H, Ks, Lp (magnitudes)	4.74 ± 0.04, 4.77 ± 0.08, 4.54 ± 0.02, 4.54 ± 0.21
Dust luminosity divided by bolometric luminosity	~10^{-6}
51 Eri b	
Projected separation (milli-arc sec)	449 ± 7 (31 January 2015)
Projected separation (AU)	13.2 ± 0.2 (31 January 2015)
Absolute J-band magnitude	16.75 ± 0.40
Absolute H-band magnitude	16.86 ± 0.21
Absolute Lp-band magnitude	13.82 ± 0.27

[1]Kavli Institute for Particle Astrophysics and Cosmology, Stanford University, Stanford, CA 94305, USA. [2]Lawrence Livermore National Laboratory, 7000 East Avenue, Livermore, CA 94040, USA. [3]Department of Astronomy, University of California–Berkeley, Berkeley, CA 94720, USA. [4]Lunar and Planetary Laboratory, University of Arizona, Tucson, AZ 85721, USA. [5]Center for Astrophysics and Space Sciences, University of California–San Diego, 9500 Gilman Drive, La Jolla, CA 92093, USA. [6]NASA Ames Research Center, MS 245-3, Moffett Field, CA 94035, USA. [7]National Research Council of Canada, Herzberg Institute of Astrophysics, 5071 West Saanich Road, Victoria, British Columbia V9E 2E7, Canada. [8]Department of Physics and Astronomy, University of Victoria, 3800 Finnerty Road, Victoria, British Columbia V8P 5C2, Canada. [9]Search for Extraterrestrial Intelligence Institute, Carl Sagan Center, 189 Bernardo Avenue, Mountain View, CA 94043, USA. [10]Space Telescope Science Institute, 3700 San Martin Drive, Baltimore, MD 21218, USA. [11]School of Earth and Space Exploration, Arizona State University, Post Office Box 871404, Tempe, AZ 85287, USA. [12]Institut de Recherche sur les Exoplanètes, Département de Physique, Université de Montréal, Montréal, Québec H3C 3J7, Canada. [13]Los Alamos National Laboratory, Post Office Box 1663, MS F663, Los Alamos, NM 87545, USA. [14]Department of Physics and Astronomy, University of California–Los Angeles, 430 Portola Plaza, Los Angeles, CA 90095, USA. [15]Department of Physics and Astronomy, Centre for Planetary Science and Exploration, The University of Western Ontario, London, Ontario N6A 3K7, Canada. [16]Subaru Telescope, 650 North A'ohoku Place, Hilo, HI 96720, USA. [17]Science and Technology Research Institute, University of Hertfordshire, Hatfield AL10 9AB, UK. [18]Department of Astrophysical Sciences, Princeton University, Princeton, NJ 08544, USA. [19]Dunlap Institute for Astronomy and Astrophysics, University of Toronto, 50 St. George Street, Toronto, Ontario M5S 3H4, Canada. [20]Institut de Planétologie et d'Astrophysique de Grenoble, Université Grenoble Alpes, Centre National de la Recherche Scientifique, 38000 Grenoble, France. [21]Department of Astronomy and Astrophysics, University of Chicago, 5640 South Ellis Avenue, Chicago, IL 60637, USA. [22]Department of Astronomy and Astrophysics, University of California–Santa Cruz, Santa Cruz, CA 95064, USA. [23]Department of Physics, Durham University, Stockton Road, Durham DH1, UK. [24]Gemini Observatory, Casilla 603, La Serena, Chile. [25]Department of Physics and Astronomy, Johns Hopkins University, 3600 North Charles Street, Baltimore, MD 21218, USA. [26]University of Exeter, Astrophysics Group, Physics Building, Stocker Road, Exeter EX4 4QL, UK. [27]Department of Physics and Astronomy, University of Georgia, Athens, GA 30602, USA. [28]Large Synoptic Survey Telescope, 950 North Cherry Avenue, Tucson, AZ 85719, USA. [29]Department of Physics and Astronomy, Stony Brook University, 100 Nicolls Road, Stony Brook, NY 11794-3800, USA. [30]Department of Astronomy and Astrophysics, University of Toronto, Toronto, Ontario M5S 3H4, Canada. [31]Steward Observatory, 933 North Cherry Avenue, University of Arizona, Tucson, AZ 85721, USA. [32]Department of Physics, University of California–Santa Barbara, Broida Hall, Santa Barbara, CA 93106-9530, USA. [33]Department of Astrophysics, American Museum of Natural History, New York, NY 10024, USA. [34]Department of Engineering Science and Physics, College of Staten Island, City University of New York, Staten Island, NY 10314, USA. [35]Departamento de Astronomía, Universidad de Chile, Camino El Observatorio 1515, Casilla 36-D, Las Condes, Santiago, Chile. [36]Stratospheric Observatory for Infrared Astronomy, Universities Space Research Association, NASA Armstrong Flight Research Center, 2825 East Avenue P, Palmdale, CA 93550, USA. [37]Sibley School of Mechanical and Aerospace Engineering, Cornell University, Ithaca, NY 14853, USA. [38]Physics and Astronomy, University of Toledo, 2801 West Bancroft Street, Toledo, OH 43606, USA. [39]Jet Propulsion Laboratory, California Institute of Technology, 4800 Oak Grove Drive, Pasadena, CA 91109, USA.
***Corresponding author. E-mail: bmacintosh@stanford.edu**

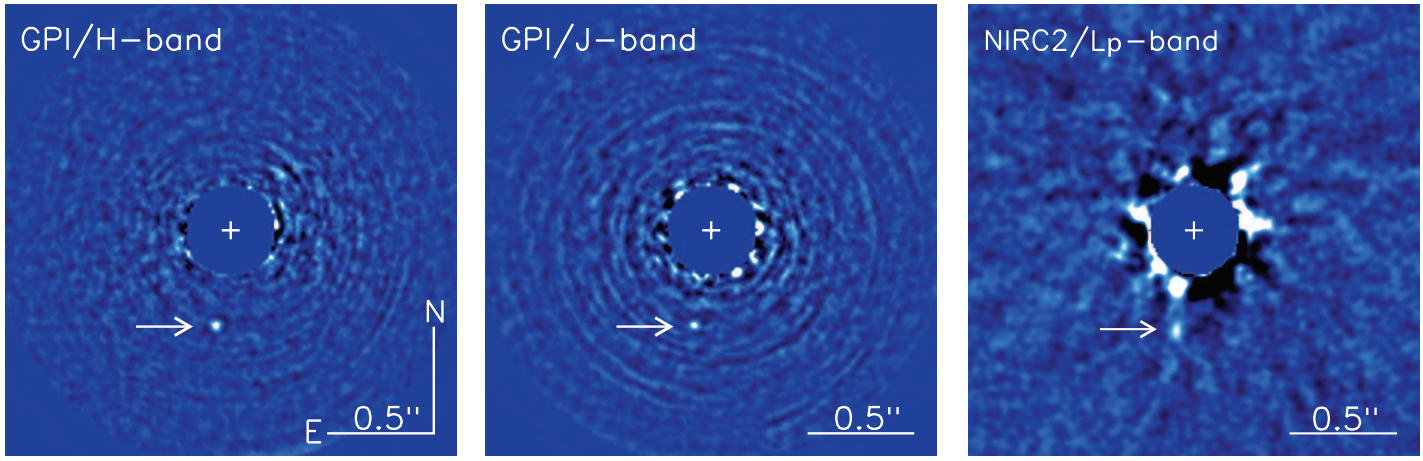

Fig. 1. Images of 51 Eri and 51 Eri b (indicated by the arrow) after PSF subtraction. (**A**) H-band GPI image from December 2014. (**B**) J-band GPI image from January 2015. (**C**) Lp-band NIRC2 image from Januarv 2015.

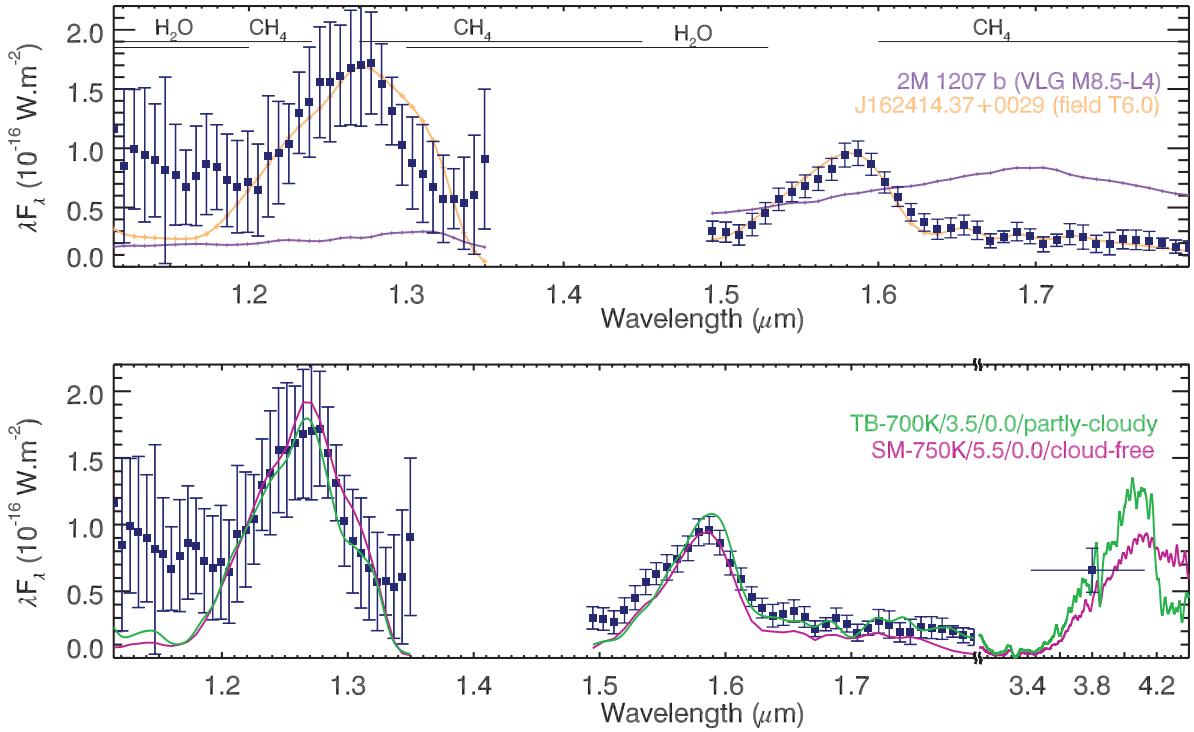

Fig. 2. J- and H-band spectra for 51 Eri b from GPI data, after PSF subtraction. Strong methane absorption, similar to that of Jupiter, is apparent. (**Top**) Spectra for the hotter young planetary object 2M 1207 b (purple) and a high–mass-field T6 brown dwarf from the SpeX library (orange) (*43*) are overplotted. (**Bottom**) Observed J and H spectra and Lp photometry with two model fits overlaid: a young, low-mass, partly cloudy object (TB-700K, green) and a higher-mass cloud-free object (SM-750K, pink). The main source of error in the extracted spectra is residual speckle artifacts, so errors in neighboring spectral channels are strongly correlated; error estimation is discussed in (*28*). λF_λ, flux.

masses are excluded by dynamical stability considerations (*36*). This model was not constrained to fit the Lp-band observation but does so within 1.6σ.

We next fitted a model to the J-H spectra and Lp photometry using a linear combination of cloudy and cloud-free surfaces and nonequilibrium chemistry, and we allowed the planet's radius to vary independently of the radii given by evolutionary tracks. Models of this type generally produce reasonable fits to other directly imaged planets (*11*–*13*, *15*, *37*, *38*). This model produced a slightly lower effective temperature. The spectral shape and colors only weakly constrain gravity but favor lower masses, and the radius (~1 R_J) is consistent with evolutionary tracks, given the age of the system. Table 2 summarizes the results of the modeling. With the spectral and atmospheric uncertainties, a wide range of other models (including those with temperatures as high as ~1000 K) are also broadly consistent with the observations. The low temperature is supported by the evidence of strong methane absorption that is not observed for other planets of similar age.

The value of $\log(L/L_\odot)$, –5.4 to –5.8 (where $L/L_\odot$ is the planet's luminosity normalized by that of the Sun), is similar in all models, regardless of temperature or clouds. Combined with the age, the luminosity can be used to estimate the mass of the planet. For a hot-start model, this corresponds to a mass of ~2 $(t/20\ \mathrm{My})^{0.65}$ $[(L/2\times10^{-6}\ L_\odot)^{0.54}$ M_J, the lowest-mass self-luminous planet directly imaged to date (t, age of the planet). 51 Eri b, unlike other young (<100 million-year-old) planetary-mass companions, has a low enough luminosity to be consistent with cold-start core-accretion scenarios. In cold-start evolution, luminosity at an age of 20 My is nearly independent of mass, so the mass of 51 Eri b would be between 2 and 12 M_J.

51 Eri b and the GJ 3305 binary system form a hierarchical triple configuration (*28*), but the companion pair is far enough away that the planet is expected to be dynamically stable in its current

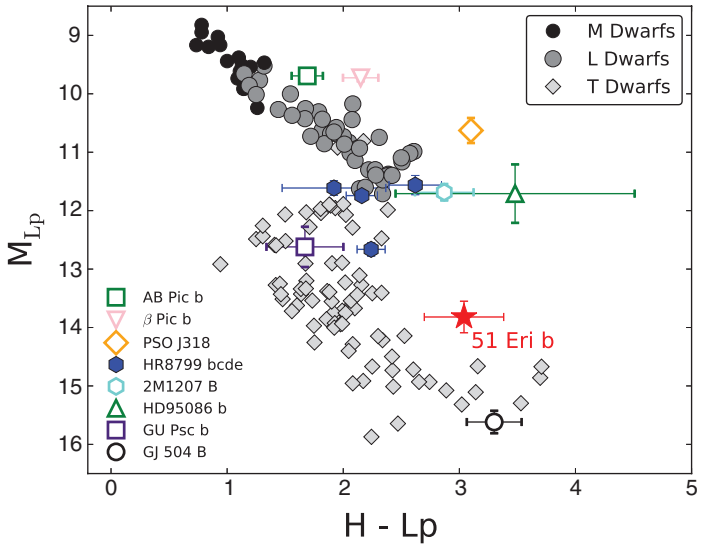

Fig. 3. Color-magnitude diagram of brown dwarfs (gray and black) and planetary-mass objects (colors). 51 Eri b is indicated with a red star, distinct from most other planets in the methane-dominated T-dwarf region of the diagram. The Lp photometry for field brown dwarfs is taken from (*45*, *46*) or converted from the Wide-field Infrared Survey Explorer W1 band (*47*) using an Lp-versus-W1 linear fit. Parallaxes are available for all objects plotted (*46*). M_{Lp}, Lp-band absolute magnitude.

Table 2. Modeling results for 51 Eri b.

	Cloud-free equilibrium model SM-750K	Partial-cloud model TB-700K
Absolute J-band magnitude	16.82	16.64
Absolute H-band magnitude	17.02	16.88
Absolute Lp-band magnitude	14.3	13.96
T_{eff} (K)	750	700
Radius (R_J)	0.76	1
Log($L/L_\odot$)	–5.8	–5.6
Log(surface gravity)	5.5	3.5
Age (My)	10,000	20 (assumed to match stellar age)
Mass (M_J)	67	2 (from luminosity, assuming a high-entropy start)

orbit (*26*). Moreover, the young age of the system suggests that although long-term dynamical effects, such as secular Lidov-Kozai oscillations, might have altered the planet's eccentricity and inclination, it is unlikely that they have had time to produce the extreme eccentricities required for tidal friction to alter the planet's semimajor axis (*39*). The formation of a ~2-M_J planet at an orbital distance of ~15 AU around a Sun-like star can be explained by modest extensions to the core-accretion theory. Early versions of the theory found that accretion of the core at larger orbital distances is in danger of taking too long, failing to capture the natal gas before it dissipates (*40*). 51 Eri b is close enough to the star that this may be less of a problem, and the addition of migration (*41*) or pebbles that experience gas drag (*42*) also helps overcome this time-scale difficulty.

The transition from L-type to T-type planets appears to occur over a narrow range of temperatures, between ~1000 K (HR8799 b and PSO J318.5-22) (*42*) and 700 K (51 Eri b). Direct determination of an object's mass, either through spectral surface gravity indicators or reflex astrometry of the primary star, could determine whether it formed through hot- or cold-start processes. 51 Eri b provides an opportunity to study in detail a planet that is still influenced by the initial conditions of its formation. With a methane-dominated spectrum, low luminosity, and a potentially low-entropy start, 51 Eri b is a bridge between wider-orbit, hotter, more massive planets and planets at Jupiter-like scales.

REFERENCES AND NOTES

1. C. Marois *et al.*, *Science* **322**, 1348–1352 (2008).
2. P. Kalas *et al.*, *Science* **322**, 1345–1348 (2008).
3. A.-M. Lagrange *et al.*, *Science* **329**, 57–59 (2010).
4. M. Kuzuhara *et al.*, *Astrophys. J.* **774**, 11 (2013).
5. J. C. Carson *et al.*, *Astrophys. J.* **763**, L32 (2013).
6. J. Rameau *et al.*, *Astrophys. J.* **772**, L15 (2013).
7. V. Bailey *et al.*, *Astrophys. J.* **780**, L4 (2014).
8. D. Lafrenière, R. Jayawardhana, M. H. van Kerkwijk, *Astrophys. J.* **689**, L153–L156 (2008).
9. M. Janson *et al.*, *Astrophys. J.* **778**, L4 (2013).
10. M.-E. Naud *et al.*, *Astrophys. J.* **787**, 5 (2014).
11. T. S. Barman, Q. M. Konopacky, B. Macintosh, C. Marois, Simultaneous detection of water, methane and carbon monoxide in the atmosphere of exoplanet HR8799b, http://xxx.lanl.gov/abs/1503.03539.
12. T. S. Barman, B. Macintosh, Q. M. Konopacky, C. Marois, *Astrophys. J.* **733**, 65 (2011).
13. A. J. Skemer *et al.*, *Astrophys. J.* **792**, 17 (2014).
14. M. S. Marley *et al.*, *Astrophys. J.* **754**, 135 (2012).
15. N. Madhusudhan, A. Burrows, T. Currie, *Astrophys. J.* **737**, 34 (2011).
16. M. S. Marley, J. J. Fortney, O. Hubickyj, P. Bodenheimer, J. J. Lissauer, *Astrophys. J.* **655**, 541–549 (2007).
17. D. S. Spiegel, A. Burrows, *Astrophys. J.* **745**, 174 (2012).
18. R. R. Rafikov, *Astrophys. J.* **648**, 666–682 (2006).
19. K. M. Kratter, R. Murray-Clay, A. N. Youdin, *Astrophys. J.* **710**, 1375–1386 (2010).
20. J.-L. Beuzit *et al.*, SPHERE Consortium, paper presented at In the Spirit of Lyot 2010: Direct Detection of Exoplanets and Circumstellar Disks, Paris, 25 to 29 October 2010; abstract available at http://adsabs.harvard.edu/abs/2010lyot.confE.44B.
21. N. Jovanovic *et al.*, The Subaru Coronagraphic Extreme Adaptive Optics system: Enabling high-contrast imaging on solar-system scales, http://xxx.lanl.gov/abs/1507.00017.
22. B. R. Oppenheimer *et al.*, *Proc. SPIE* **8447**, 844720 (2012).
23. B. Macintosh *et al.*, *Proc. Natl. Acad. Sci. U.S.A.* **111**, 12661–12666 (2014).
24. R. I. Patel, S. A. Metchev, A. Heinze, *Astrophys. J. Suppl. Ser.* **212**, 10 (2014).
25. P. Riviere-Marichalar *et al.*, *Astron. Astrophys.* **565**, A68 (2014).
26. M. Janson *et al.*, *Astrophys. J. Suppl. Ser.* **214**, 17 (2014).
27. B. Zuckerman, I. Song, M. S. Bessell, R. A. Webb, *Astrophys. J.* **562**, L87–L90 (2001).
28. Material and methods are available as supplementary materials on *Science* Online.
29. M. Simon, G. H. Schaefer, *Astrophys. J.* **743**, 158 (2011).
30. A. S. Binks, R. D. Jeffries, *Mon. Not. R. Astron. Soc. Lett.* **438**, L11–L15 (2014).
31. E. E. Mamajek, C. P. M. Bell, *Mon. Not. R. Astron. Soc.* **445**, 2169–2180 (2014).
32. T. D. Brandt *et al.*, *Astrophys. J.* **786**, 1 (2014).
33. G. Chauvin *et al.*, *Astron. Astrophys.* **438**, L25–L28 (2005).
34. J. D. Kirkpatrick, *et al.*, *Astrophys. J.* **753**, 156 (2012).
35. D. Saumon, M. S. Marley, *Astrophys. J.* **689**, 1327–1344 (2008).
36. D. C. Fabrycky, R. A. Murray-Clay, *Astrophys. J.* **710**, 1408–1421 (2010).
37. J. Chilcote *et al.*, *Astrophys. J.* **798**, L3 (2015).
38. T. Currie *et al.*, *Astrophys. J.* **795**, 133 (2014).
39. D. Fabrycky, S. Tremaine, *Astrophys. J.* **669**, 1298–1315 (2007).
40. J. B. Pollack *et al.*, *Icarus* **124**, 62–85 (1996).
41. Y. Alibert, C. Mordasini, W. Benz, C. Winisdoerffer, *Astron. Astrophys.* **434**, 343–353 (2005).
42. M. Lambrechts, A. Johansen, *Astron. Astrophys.* **544**, A32 (2012).
43. This research has benefitted from the SpeX Prism Spectral Libraries, maintained by A. Burgasser at http://pono.ucsd.edu/~adam/browndwarfs/spexprism.
44. F. van Leeuwen, *Astron. Astrophys.* **474**, 653–664 (2007).
45. E. R. Houdebine, C. J. Butler, D. Garcia-Alvarez, J. Telting, *Mon. Not. R. Astron. Soc.* **426**, 1591–1605 (2012).
46. B. A. Macintosh *et al.*, *Proc. SPIE* **7015**, 701518 (2008).
47. J. K. Chilcote *et al.*, *Proc. SPIE* **8446**, 84468W (2012).

ACKNOWLEDGMENTS

This work is based on observations obtained at the Gemini Observatory, which is operated by the Association of Universities for Research in Astronomy under a cooperative agreement with NSF on behalf of the Gemini partnership, whose membership includes: NSF (United States); the National Research Council (Canada); the Comisión Nacional de Investigación Científica y Tecnológica (Chile); the Australian Research Council (Australia); the Ministério da Ciência, Tecnologia e Inovação (Brazil); and Ministerio de Ciencia, Tecnología e Innovación Productiva (Argentina). The research was supported by grants from NSF, including AST-1411868 (B.M., K.F., J.P., and A.R.), AST-0909188 and AST-1313718 (J.R.G., P.K., R.D.R., and J.W.), AST-1413718 (M.P.F. and G.D.), and AST-1405505 (T.B.). Support was also provided by grants from NASA, including NNX14AJ80G (B.M., F.M., E.N., and M.P.), NNH15AZ591 (D.S. and M.M.), NNX15AD95G (J.R.G. and P.K.), NNX11AD21G (J.R.G. and P.K.), and NNH11ZDA001N (S.M. and R.P.). J.R., R.D., and D.L. acknowledge support from the Fonds de Recherche du Quebec. Support is acknowledged from NSF fellowships DGE-123825 (A.Z.G.), DGE-1311230 (K.W.-D.), DGE-1232825 (S.G.W.), and DGE-1144087 (L.W.H.). Portions of this work were performed under the auspices of the U.S. Department of Energy by Lawrence Livermore National Laboratory under contract DE-AC52-07NA27344. GPI data are archived at the Gemini Science Archive: www.cadc-ccda.hia-iha.nrc-cnrc.gc.ca/en/gsa/.

SUPPLEMENTARY MATERIALS

www.sciencemag.org/content/350/6256/64/suppl/DC1
Materials and Methods
Figs. S1 to S3
Tables S1 to S3
References (*48*–*90*)

17 May 2015; accepted 3 August 2015
Published online 13 August 2015
10.1126/science.aac5891

Discovery and spectroscopy of the young jovian planet 51 Eri b with the Gemini Planet Imager

B. Macintosh *et al.*

Science **350**, 64 (2015);
DOI: 10.1126/science.aac5891

Appendix B

Tables

B.1 Tables for Chapter 1

Table B.1. Major Debris Disk Studies

Study Citation	Primary Instruments	Sample Age (Myr)	Sample Description	Study Summary
Spangler et al. (2001)	ISO60, ISO90	1–630	150 A–K stars	ISO survey to study evolution of dust.
Chen et al. (2005)	SM24, SM70	5–20	40 FG Sco Cen stars	Fourteen 24μm and seven 70μmexcesses detected.
Rieke et al. (2005)	SM24, IRAS25, ISO25	5–850	266 A Stars	Evolution of debris disks around A stars.
Beichman et al. (2006)	SM24, SM70	150–1500	88 FGK Stars	Search for good direct imaging planet targets. 70μm incidence rate of $\sim$13%.
Bryden et al. (2006)	SM70	Median 4000	69 FGK Stars	Low frequency of disks for old solar type stars.
Chen et al. (2006)	SIRS 5.5–35μm	10–10000	50 B–M stars	Spectra suggest multiple dust populations.
Gorlova et al. (2006)	SM24	100–120	54 B8–K6	Survey of Pleiades show 25% of B–A & 10% of F–K3 stars have 24μm excesses.
Su et al. (2006)	SM24, SM70	5–850	160 A stars	Study of dust evolution around A stars ($\sim$33% incidence).
Rhee et al. (2007)	IRAS12, IRAS25, IRAS60, IRAS100	5–5000	622 B–F stars	Study of *IRAS* FSC to study evolution of disks in *Hipparcos*
Siegler et al. (2007)	SM24	50	34 B3–M5	Activity in terrestrial region of FGK stars is common at 50 Myr and decays τ $\sim$100 Myr.
Trilling et al. (2007)	SM24, SM70	50–10000	69 A3–F8 Binaries	Incidence of disks around binaries is higher than for singles.
Currie et al. (2008)	SI 3.6–8μm, SM24	25	209 B–K stars	Survey of disks in NGC 2232. Incidence of 25% at 5 Myr, 50–60% at 20–25%. Results suggest most A stars produce icy planets.
Hillenbrand et al. (2008)	SM70	3–3000	328 FGK stars	>1/3 of disks may have multi-temperature components; $\sim$10% of stars possess 70μm excesses.
Meyer et al. (2008)	SM24	3–3000	309 FGK	30 disks. Incidence of 8.5%–19% for < 300 Myr, < 4% for older stars.
Rebull et al. (2008)	SM24, SM70	22	42 A–K	Study of disks in β Pictoris moving group. Incidence rates of 23% for 24μm excesses and >37% for 70μm excesses.
Trilling et al. (2008)	SM24, SM70	190–11000	350 A–M stars	Incidence of $\sim$4.2% for 24μm, and $\sim$ 16.4% 70μm excesses.
Carpenter et al. (2009b)	SM24, SM70	5–17	205 B0–M5 stars	54 disks identified in Upper Sco. Magnitude of F star 24μm excesses increases from 5–17 Myr with weak confidence.
Bryden et al. (2009)	SM24,SM70	100-12000	104 F–M RV planet hosts	No significant difference between incidence rates of disks around stars with and without planets.
Carpenter et al. (2009a)	SM24, SM70, SI8.6, SIRS 8–35μm	3–3000	314 FGK stars	Dust around solar type stars; 15% incidence at <300Myr down to 2.5% at Gyr for 24μmexcesses. Similar decline for 70μm excess upper envelope.
Lawler et al. (2009)	SIRS 8.5–12μm, SIRS 30–34μm	100–10000	152 FGK stars	11.8% incidence rate for 30–34μm excesses (100× Zodiacal Dust) ;< 1% for 8.5–12μm excesses (1000× Zodiacal Dust).
Plavchan et al. (2009)	SM24, SM70	8–1100	70 A–M stars	70μm incidence rates of $\sim$4% for GK stars, & 21% for FG stars.
Koerner et al. (2010)	SM24, SM70	···	634 B-K stars	4.6% incidence rate at 24μm and 4.8% incidence for 70μm excesses.
Chen et al. (2011)	SM24, SM70, 3500–10500 Å spectra	11–17	182 F–G Sco Cen stars	Incidence of $\sim$30% at 24μm with 41 new discoveries of PPDs and debris disks.
Dodson-Robinson et al. (2011)	SIRS 32μm	···	111 FGKM stars	11 debris disks around planet hosts; planets detected by RV searches formed within 240 AU of their stars.

Table B.1. Major Debris Disk Studies – continued.

Study Citation	Primary Instruments	Sample Age (Myr)	Sample Description	Study Summary
Morales et al. (2011)	SIRS 7.5–35μm, SIRS 5.2–35μm	<1000	69 disk stars (A–K)	Observations of stars with SM data. Common warm dust in stars suggest dust not found at same location around all stars.
Chen et al. (2012)	SM24, SM70	11–17	215 B–A Sco Cen stars	51 new discoveries and fractions of 24–27%.
Donaldson et al. (2012)	HP70, HP100, HP160	30	17 B–M	6 targets show excesses.
Luhman & Mamajek (2012)	SM24, SM70, SI 3.6μm, 4.5μm, 5.8μm, 8.0μm	11	863 B-M USco Stars	50 new transitional, evolved & debris disks. < 10% of B–G stars show inner primordial disks, & ∼25% at earlier than M5. Disk lifetime longer for lower mass stars.
Urban et al. (2012)	SM24	670	122 A–M stars	Study of disks at LHB ages; detection of excesses at 10% of photosphere flux.
Eiroa et al. (2013)	HP70, HP100, HP160, HS250, HS350, HS500	100–10000	133 FGK stars	DUNES Survey; Disks detected at f_d a several times that of EKB dust at ∼20% incidence rates. A number of disks are resolved.
Chen et al. (2014)	SM24, SM70, SIRS 31μm	1-10000	571 B–K	Analysis of SIRS spectra for large disk sample that show double disk temperatures and spectral features for a number of disks.
Thureau et al. (2014)	HP100, HP160	30–1000	86 A stars	DEBRIS Survey; with 24±5%.

Note. — I have tabulated the results from major disk studies over the last couple of decades. Studies with a significant number of detections have been listed > 30, along with those that have had a significant impact on the field.
ISO25, ISO60, ISO90: ISO at 25μm, 60μm, and 90μm, respectively.
SM24, SM70: *Spitzer*/MIPS at 24μm, and 70μm, respectively.
IRAS12, IRAS25, IRAS60, IRAS100: IRAS at 12μm, 25μm, 60μm, 100μm.
SIRS: *Spitzer*/IRS SI8.6: *Spitzer*/IRAC at 8.6μm
HP70, HP100, HP160: *Herschel*/PACS 70μm, 100μm, and 160μm, respectively.
HS250, HS350, HS500: *Herschel*/SPIRES 250μm, 350μm, and 500μm, respectively.

B.2 Tables for Chapter 3

Table B.2. Stellar Parameters of Stars with IR Excesses - Cont. of Table 5 in Chapter 3

HIP ID	WISE ID	SpT[a]	Dist.[b] (pc)	T_* (K)	R_* ($R_\odot$)	χ^2_*	F_{W3} (mJy)	$F_{W3,*}$ (mJy)	F_{W4} (mJy)	$F_{W4,*}$ (mJy)	$\Delta_{F_{W3}}/F_{W3}$[d]	$\Delta_{F_{W4}}/F_{W4}$[d]	$W1_{corr}$[e] (mag)	$W2_{corr}$[e] (mag)
544	J000637.09+290115.4	K0V	14	5493	0.86	3.3	536±7	550	186±4	153	-0.026	0.178	4.260±0.082	4.290±0.051
560	J000650.16-230627.5	F2IV	39	6789	1.5	0.38	234±3	234	130±3	64.7	-0.001	0.501	5.220±0.072	5.240±0.037
682	J000825.79+063700.6	G2V	39	5845	1.1	1.2	106±1	108	41.6±2	29.9	-0.019	0.281	6.050±0.051	6.100±0.022
1473	J001819.60+364706.3	A2V	41	8987	2	0.62	527±7	524	182±3	144	0.006	0.208	4.260±0.097	4.330±0.050
1481	J001826.25-632839.6	F8/G0V	42	6138	1.1	0.73	102±1	102	41.7±1	28.4	-0.003	0.319	6.130±0.048	6.150±0.023
1866	J002338.01-034548.9	K:	47	4527	0.65	1.7	21.1±0.4	21.4	9.22±1	5.99	-0.012	0.350	7.830±0.022	7.910±0.021
2472	J003125.12-484812.7	A0V	53	9489	2.1	1.2	377±6	374	130±4	103	0.010	0.209	4.760±0.075	4.790±0.046
2710	J003427.10-063014.9	F2	41	6428	1.2	1.2	142±2	145	48.3±2	40.0	-0.019	0.171	5.680±0.061	5.740±0.027
3210	J004051.69-531236.1	F7V	45	6197	1.2	1.4	107±1	107	37±1	29.6	0.006	0.200	6.070±0.050	6.090±0.022
3279	J004147.56+554056.2	G5	69	5807	1.2	1.3	41.4±0.6	42.1	14.4±0.6	11.7	-0.015	0.188	7.070±0.030	7.120±0.020
3965	J005057.54+513029.0	F2IV	67	7374	1.9	1.3	150±2	152	54.1±1	41.8	-0.010	0.227	5.630±0.061	5.720±0.028
5462	J010956.58-642133.0	G5V	47	5608	0.81	0.94	42±0.6	41.7	16.6±0.9	11.6	0.006	0.301	7.100±0.031	7.140±0.019
5631	J011219.08+121654.1	F5	34	6267	1.1	3.1	156±2	161	51.3±2	44.4	-0.033	0.133	5.620±0.054	5.630±0.029
5709	J011326.63-393223.9	F3/F5V	55	6627	1.3	0.81	92.7±1	94.5	32±1	26.1	-0.020	0.184	6.190±0.047	6.210±0.023
6490	J012323.64+064427.1	G0	72	6142	1.1	0.97	33.3±0.5	33.5	12.5±1	9.31	-0.008	0.258	7.340±0.028	7.360±0.021
6494	J012326.11-763642.6	G5V	46	5711	0.93	0.25	57.2±0.8	57.5	20.8±0.9	16.0	-0.006	0.233	6.750±0.039	6.800±0.021
6679	J012540.67+025819.4	F0	49	6552	1.3	1.4	124±2	126	47.6±1	34.7	-0.012	0.270	5.830±0.056	5.910±0.026
7345	J013437.83-154034.8	A1V	59	9006	1.7	1.2	213±3	186	265±6	51.3	0.124	0.806	5.440±0.060	5.470±0.028
7576	J013735.57-064538.4	G5	24	5322	0.79	3	142±2	146	48.7±1	40.8	-0.030	0.163	5.720±0.056	5.760±0.028
7699	J013907.72-562546.0	F5V	48	6474	1.3	1.7	121±2	120	54.9±2	33.1	0.007	0.398	5.930±0.054	5.950±0.023
7805	J014024.13-605956.7	F2IV/V	67	6679	1.3	0.46	66.6±0.9	66	31.4±1	18.2	0.009	0.419	6.610±0.040	6.620±0.021
7978	J014229.49-534428.1	F8V	17	6097	1.1	0.82	600±8	622	218±4	173	-0.036	0.207	4.200±0.098	4.180±0.060
8109	J014414.01+545311.1	F8	44	5956	1.3	0.98	134±2	134	47.2±1	37.2	-0.002	0.211	5.910±0.053	5.850±0.027
8122	J014422.85+323056.5	A3	69	7664	1.6	0.72	97.6±1	99.1	45.3±1	27.3	-0.015	0.397	6.110±0.049	6.180±0.021
8241	J014606.39-533118.7	A1V	62	9413	2.2	0.91	295±4	291	120±3	80.2	0.014	0.333	4.970±0.070	4.940±0.041
8987	J015549.61-525026.4	K4/K5V	40	4496	0.81	1.6	45.3±0.6	45.2	15.7±0.9	12.7	0.002	0.192	7.030±0.031	7.100±0.020
9052	J015638.21-812956.9	F3IV/V	72	6797	1.9	0.73	121±2	118	40.5±1	32.7	0.025	0.192	6.020±0.048	5.980±0.025
9141	J015749.04-215405.7	G3/G5V	41	5682	0.95	1.2	77.4±1	77.7	28.5±1	21.6	-0.004	0.241	6.380±0.045	6.450±0.020
9902	J020726.23-594046.1	F8V	44	6156	1.1	1.6	104±1	96.9	53.8±1	26.9	0.072	0.499	6.200±0.046	6.180±0.022
10054	J020925.16+811745.5	A1V	71	8311	1.9	2.3	154±2	152	52.7±2	41.8	0.013	0.208	5.670±0.059	5.700±0.025
10670	J021718.90+335049.4	A1Vnn	34	9430	1.9	0.79	743±10	740	327±5	204	0.004	0.376	3.850±0.109	4.030±0.066
11157	J022332.30+193755.5	G5	55	5648	0.86	1.1	33.8±0.7	34.6	14.1±1	9.63	-0.023	0.316	7.300±0.028	7.340±0.020
11477	J022801.71-334839.5	A2/A3V	47	8925	1.7	1.4	297±4	296	124±3	81.5	0.004	0.345	4.890±0.070	4.960±0.041
11847	J023255.85+372000.6	F0	63	6834	1.3	2.7	73±1	71.3	169±4	19.7	0.024	0.883	6.500±0.040	6.550±0.021
12489	J024041.12+270339.2	A3V	71	8722	2.4	0.92	268±3	269	93.1±3	74.2	-0.004	0.203	4.990±0.073	5.060±0.043
13141	J024901.61-624823.3	A2V	50	8614	1.8	3.3	289±4	289	101±2	79.5	0.002	0.215	4.980±0.074	4.950±0.038
13209	J024959.08+271536.8	B8Vn	51	12190	2.7	0.28	828±10	778	313±7	213	0.060	0.320	3.790±0.094	3.900±0.075
13569	J025449.55-333129.3	A3m...	73	7403	1.6	1.7	95±1	94.7	37±1	26.1	0.004	0.295	6.140±0.047	6.200±0.020
13679	J025613.80+082252.8	F7IV	43	6516	1.9	2.3	318±4	326	109±3	90.6	-0.028	0.168	4.830±0.072	4.900±0.037
14684	J030942.33-093447.6	G0	37	5405	0.81	1.3	62.6±0.9	63.3	21.3±0.9	17.6	-0.010	0.173	6.640±0.038	6.680±0.022
15929	J032510.63-064408.3	F8	73	6346	1.1	1.2	37±0.6	36.8	18.6±1	10.2	0.005	0.451	7.220±0.032	7.230±0.022
16449	J033153.68-253651.0	A3IV/V	72	8508	1.6	0.43	104±1	104	57.9±2	28.8	-0.002	0.503	6.050±0.051	6.120±0.023
16908	J033735.06+212035.2	G5	40	4942	0.75	2	44.2±0.7	44.4	15.9±1	12.4	-0.003	0.225	7.070±0.033	7.080±0.020
17338	J034239.79-203243.3	G8V	50	5211	0.89	3.6	41.3±0.6	41	18±1	11.4	0.007	0.365	7.120±0.032	7.140±0.019
17395	J034333.82-102908.4	A5m	42	7821	1.5	0.73	270±3	268	113±3	74.0	0.006	0.347	5.030±0.071	5.120±0.035
17764	J034811.61-744138.6	F3IV/V	54	6706	1.3	0.41	103±1	103	49.4±1	28.4	0.001	0.425	6.100±0.050	6.140±0.022
18187	J035327.23-411321.1	F6V	41	6225	1.1	1.8	121±2	121	45.8±1	33.5	0.001	0.267	5.930±0.051	5.950±0.024

Table B.2 (cont'd)

HIP ID	WISE ID	SpT[a]	Dist.[b] (pc)	T_* (K)	R_* ($R_\odot$)	χ^2_*	F_{W3} (mJy)	$F_{W3,*}$ (mJy)	F_{W4} (mJy)	$F_{W4,*}$ (mJy)	$\Delta_{F_{W3}}/F_{W3}$[d] $\Delta_{F_{W4}}/F_{W4}$[d]		$W1_{corr}$[e] (mag)	$W2_{corr}$[e] (mag)
18481	J035701.73+060223.3	A2Vn	70	8919	1.6	1.4	127±2	124	52.7±2	34.2	0.024	0.351	5.910±0.051	5.930±0.027
19610[c]	J041208.76-102811.1	G5+G5	61	5660	0.98	4.8	63.7±0.9	59.4	19.3±1	16.5	0.066	0.143	6.740±0.041	6.700±0.023
19793	J041432.39+233429.4	G3V	47	5788	1.1	1.5	70.8±1	72.4	28±1	20.1	-0.021	0.280	6.500±0.039	6.520±0.022
19796	J041434.42+104205.1	F8V	45	6238	1.3	0.69	127±2	134	44±2	37.1	-0.048	0.156	5.820±0.053	5.870±0.025
20261	J042036.38+150543.7	F0V	47	7739	2	2.6	365±5	375	119±3	103	-0.029	0.133	4.710±0.076	4.730±0.047
20693	J042557.39+050900.6	F5	50	6242	1.3	0.81	103±2	105	41.9±1	29.0	-0.017	0.307	6.120±0.049	6.100±0.022
20737	J042638.62-285708.0	K0V	38	5150	0.82	1.3	60.9±0.8	61.1	24.1±1	17.0	-0.004	0.293	6.690±0.039	6.740±0.021
20794	J042722.22+070344.9	F5	74	6771	1.4	3.1	63.1±1	65.5	24±1	18.1	-0.039	0.245	6.570±0.039	6.620±0.020
20901	J042850.24+130251.3	A7V	49	7919	2.3	0.69	433±6	437	160±4	120	-0.008	0.247	4.540±0.079	4.470±0.057
20998	J043011.60-675234.8	G5V	52	5652	1.4	2.4	112±1	111	36.8±1	30.8	0.015	0.163	5.960±0.051	6.060±0.025
21547	J043736.16-022825.2	F0V	29	7416	1.4	2.8	445±6	438	146±3	121	0.015	0.171	4.450±0.081	4.510±0.052
21983	J044331.80+111000.4	K8	47	4610	0.77	1.6	30.2±0.5	30.3	12.2±1	8.48	-0.005	0.307	7.460±0.027	7.540±0.019
22152	J044600.82+763638.4	F7V	32	6327	1.2	1	229±3	230	83.2±2	63.8	-0.005	0.233	5.190±0.068	5.230±0.032
22192	J044625.75-280514.5	A2IV/V	56	7962	1.5	0.64	149±2	150	54±2	41.2	-0.004	0.237	5.750±0.052	5.710±0.028
22295[c]	J044805.35-804645.0	F7V	61	6240	1.3	4.4	54.1±0.7	54.2	19.4±0.8	15.5	-0.002	0.199	6.780±0.038	6.820±0.019
22312	J044819.63+674547.2	F0	69	7186	1.5	0.97	92.1±1	93.2	34.2±1	25.7	-0.012	0.247	6.270±0.045	6.250±0.020
22394[c]	J044913.04+244809.7	K3V	50	4840	0.73	4.4	50.7±0.7	50.7	20.4±1	14.8	0.000	0.275	6.830±0.036	6.920±0.020
22509[c]	J045036.73+085400.5	A1Vn	69	9200	2	4.3	599±9	598	199±4	177	0.001	0.113	4.130±0.101	4.250±0.060
22845	J045453.76+100901.8	A0V	36	8736	1.7	1.7	496±6	492	197±5	135	0.009	0.314	4.370±0.081	4.380±0.058
23443	J050220.30+135435.8	G0	39	5916	1.1	0.75	109±2	110	38.9±2	30.6	-0.007	0.213	6.010±0.051	6.070±0.023
23497	J050305.80+213523.4	A7V	53	8187	2.8	0.59	584±9	582	200±4	161	0.003	0.196	4.180±0.088	4.190±0.057
23871	J050748.35+202505.8	A5V	58	8650	2	0.33	273±4	275	108±3	75.9	-0.009	0.300	5.010±0.074	5.070±0.041
24528	J051543.88-225339.5	A3V	75	8304	1.4	0.57	83.2±1	78.1	48.2±2	21.5	0.061	0.553	6.380±0.043	6.420±0.021
24947	J052038.08-394517.7	F6V	48	6219	1.2	0.97	105±1	105	37.3±1	29.1	0.007	0.222	6.100±0.053	6.110±0.024
25183	J052312.24-314456.3	F3V	72	6530	1.6	2.7	79.3±1	79.5	31.2±1	22.0	-0.002	0.297	6.390±0.043	6.390±0.021
25376	J052542.62-532849.8	F7V	59	6243	1.2	1.4	65.3±0.9	66.3	21.6±0.7	18.3	-0.016	0.153	6.560±0.044	6.600±0.021
26395	J053708.78-114632.0	A2V	63	9033	1.4	1.9	124±2	120	73.4±2	33.0	0.036	0.551	5.910±0.051	5.980±0.022
26453	J053739.64-283734.7	F3V	57	6666	1.3	0.59	94.9±1	93.2	60.7±2	25.7	0.018	0.576	6.230±0.050	6.240±0.023
26563	J053853.07-071246.5	A4V	45	8307	2.1	1.7	492±6	488	181±4	135	0.008	0.255	4.350±0.082	4.450±0.059
26990	J054335.83-395524.6	G0V	55	5971	1.1	1.1	59.7±0.8	59.8	23.1±0.8	16.6	-0.002	0.279	6.710±0.036	6.730±0.019
28498	J060055.38-545704.7	F5V	56	6442	1.3	0.99	90±1	91	30.5±1	25.2	-0.011	0.174	6.200±0.049	6.260±0.021
30252	J062150.07-511415.7	A5V	71	7757	1.6	0.82	97±1	95.1	66±2	26.2	0.019	0.603	6.190±0.047	6.220±0.023
30893	J062905.35+270027.7	K2V	30	5007	0.77	3.1	80.6±1	83.3	23.1±1	23.2	-0.033	-0.005	6.430±0.037	6.400±0.021
32435	J064613.60-835928.8	F5V	56	6396	1.3	0.88	89.5±1	88.8	41.1±1	24.6	0.008	0.403	6.300±0.046	6.300±0.021
33690	J065959.41-612007.5	K0IV-V	18	5396	0.86	1	296±4	300	111±3	83.6	-0.015	0.249	4.950±0.072	4.990±0.041
34334	J070702.53-554614.3	G6/G8V	72	5563	0.98	0.9	26.1±0.4	26.2	9.4±0.6	7.28	-0.004	0.225	7.610±0.026	7.650±0.021
35198	J071625.22+350102.8	G5	36	5389	0.78	0.84	63.9±0.9	64.1	23.7±1	17.8	-0.003	0.248	6.670±0.036	6.690±0.022
35567	J072022.92-561740.1	A1V	71	8515	1.4	2.5	98±1	87.7	103±2	24.2	0.105	0.765	6.220±0.048	6.260±0.022
36515[c]	J073042.45-372021.1	G3V	22	5794	0.92	4	265±4	261	87.5±2	72.5	0.015	0.171	5.020±0.075	5.100±0.038
36827	J073426.11-065348.5	K2V	25	5067	0.74	2.8	113±2	116	40.7±1	32.3	-0.024	0.206	5.950±0.041	6.040±0.022
36927	J073526.70-522630.4	K3IV-V	25	4714	0.71	2.7	90.3±1	92.7	30.5±1	25.9	-0.027	0.151	6.220±0.045	6.300±0.021
36948	J073547.42-321213.3	G3/G5V	35	5453	0.85	0.84	78.4±1	78.6	44.3±2	21.9	-0.002	0.506	6.430±0.042	6.450±0.022
38369	J075139.41-400414.7	F5V	65	6199	1.1	1.5	45.2±0.7	46.1	17±0.8	12.8	-0.022	0.249	6.980±0.035	7.010±0.020
38538	J075329.80+264556.5	A3V	68	8533	2.8	1.5	382±5	383	127±3	105	-0.002	0.167	4.640±0.082	4.750±0.041
40693	J081824.16-123805.9	K0V	12	5398	0.88	0.87	671±9	667	278±5	186	0.006	0.332	4.080±0.094	4.130±0.069
41081	J082255.15-520725.2	A0V	70	9610	1.6	0.067	143±2	129	75.1±2	35.5	0.097	0.528	5.870±0.054	5.880±0.026
41152	J082348.49+531310.1	A3V	50	8509	1.6	1.1	227±3	230	95.4±2	63.4	-0.012	0.336	5.200±0.073	5.250±0.033

Table B.2 (cont'd)

HIP ID	WISE ID	SpT[a]	Dist.[b] (pc)	T_* (K)	R_* ($R_\odot$)	χ^2_*	F_{W3} (mJy)	$F_{W3,*}$ (mJy)	F_{W4} (mJy)	$F_{W4,*}$ (mJy)	$\Delta_{F_{W3}}/F_{W3}$[d]	$\Delta_{F_{W4}}/F_{W4}$[d]	$W1_{corr}$[e] (mag)	$W2_{corr}$[e] (mag)
41277[c]	J082516.86+041511.7	K8	44	3970	0.58	13	32.1±0.6	32	12.9±1	9.52	0.002	0.261	7.410±0.026	7.440±0.021
41307	J082539.61-035423.2	A0V	38	9752	2.1	1.3	794±10	786	353±6	217	0.010	0.386	3.820±0.104	3.890±0.080
41373	J082625.17-524827.0	A0V	69	8945	1.6	0.58	129±2	128	62.8±2	35.2	0.012	0.439	5.850±0.054	5.890±0.025
43121	J084655.98+120635.4	A1V	54	8342	1.5	1.9	174±2	173	78.7±2	47.7	0.005	0.393	5.490±0.059	5.540±0.031
43414	J085034.99-664733.7	F5IV	52	6575	3	0.9	579±8	571	225±4	158	0.013	0.300	4.190±0.096	4.290±0.058
46843	J093243.65+265916.4	K0	18	5311	0.79	2.8	256±3	262	85.2±2	73.1	-0.024	0.143	5.130±0.063	5.150±0.036
47135	J093617.61-782041.1	G2V	68	5924	1.1	0.75	41±0.6	40.9	14.4±0.7	11.4	0.002	0.210	7.120±0.032	7.160±0.020
47792	J094436.47-621442.0	K3/4V	58	4620	0.82	1.2	23.2±0.4	23.1	8.48±0.7	6.46	0.002	0.238	7.750±0.023	7.830±0.021
47990	J094653.90-041753.3	K0	69	5738	1.2	1.6	41.2±0.6	41.8	14.9±0.9	11.6	-0.013	0.220	7.090±0.031	7.110±0.020
48423	J095216.55+491126.2	G5	33	5607	0.91	1.2	107±1	109	43.1±2	30.3	-0.018	0.297	6.110±0.044	6.110±0.023
49593	J100725.82+351441.5	A7V	28	8006	1.6	1.2	692±10	695	251±6	191	-0.003	0.236	4.040±0.108	4.120±0.064
49809	J101005.80-124858.2	F2/F3IV/V	28	6901	1.5	0.9	497±6	505	166±3	139	-0.016	0.161	4.390±0.089	4.350±0.059
50155	J101419.21+150418.4	G5	53	5187	0.85	1.6	32.3±0.5	33	12.2±1	9.19	-0.020	0.248	7.350±0.028	7.430±0.020
50860	J102306.33+335429.4	A6V	74	8201	2.2	1.3	180±2	180	60.7±2	49.7	-0.003	0.180	5.420±0.072	5.490±0.032
51194	J102725.15-654216.5	A2V	68	8752	1.7	0.67	139±2	139	47.5±1	38.4	-0.004	0.192	5.740±0.059	5.780±0.028
51793	J103455.79-742141.0	K2/3V	55	4584	0.72	3.4	20.3±0.3	19.4	6.54±0.5	5.41	0.045	0.172	7.950±0.023	7.990±0.020
52457	J104324.88+231118.3	A3Vn	70	9070	2.5	1.8	301±4	305	107±2	84.0	-0.014	0.212	4.900±0.066	4.980±0.036
52709	J104637.16-431134.2	A4IV	72	7952	1.9	1.1	133±2	135	47.2±1	37.2	-0.010	0.213	5.820±0.055	5.800±0.029
52947	J104941.85-713914.7	F0/F2V	74	6850	1.4	1.5	64.1±0.9	64.7	25.3±0.9	17.9	-0.009	0.294	6.600±0.042	6.620±0.021
53954	J110219.79+201047.8	A1m	39	9064	1.9	0.45	560±8	556	253±4	153	0.007	0.394	4.280±0.101	4.240±0.062
55057	J111616.56-034541.8	K0	55	5554	0.91	1.2	37.3±0.6	37.5	14.2±1	10.4	-0.006	0.262	7.200±0.028	7.270±0.020
55130	J111711.95-380051.5	A1V	73	8637	1.6	0.86	115±2	115	39.7±1	31.7	0.004	0.202	5.930±0.048	6.010±0.024
56253	J113149.95+810738.4	A2m	59	7671	1.7	1.3	168±2	172	55.2±1	47.4	-0.022	0.141	5.520±0.060	5.560±0.030
57971	J115326.75-350400.2	A2V	74	8794	1.7	0.32	117±2	118	48±1	32.5	-0.003	0.323	5.930±0.056	5.970±0.023
59394	J121103.79-233608.9	A1V	59	9077	1.8	0.28	216±3	215	94.5±2	59.2	0.003	0.374	5.290±0.065	5.320±0.034
59422	J121121.74-034644.4	F5	50	6597	1.4	1.6	123±2	126	51.3±2	34.9	-0.023	0.320	5.810±0.055	5.910±0.025
59608	J121325.88+101544.4	A2m	50	7580	1.7	1.1	228±3	229	83.7±2	63.3	-0.007	0.244	5.230±0.063	5.260±0.030
59893	J121702.77-041503.9	K2	68	5058	0.86	0.77	19.9±0.4	20	8.87±1	5.57	-0.004	0.372	7.910±0.023	7.960±0.020
60074	J121906.38+163252.4	G2V	27	5853	0.96	1.6	176±2	179	69.5±2	49.8	-0.016	0.283	5.520±0.064	5.520±0.030
61558	J123647.35-054954.9	A3V	69	8927	1.7	1.1	151±2	149	69.9±2	41.2	0.008	0.411	5.660±0.057	5.740±0.028
61960	J124153.12+101407.6	A0V	36	8919	1.5	1.7	383±5	376	163±3	103	0.018	0.364	4.700±0.077	4.660±0.047
62492	J124821.96+304602.1	F7V	68	6390	1.2	1	52.1±0.7	52.8	20.9±1	14.7	-0.014	0.297	6.830±0.036	6.860±0.019
63076	J125528.55+652618.3	A5n	29	7175	1.5	2.4	476±6	482	154±3	133	-0.012	0.138	4.380±0.092	4.550±0.049
63286	J125809.71-230318.5	F2V	61	6971	1.5	0.64	106±1	108	38.9±1	29.7	-0.015	0.236	6.030±0.053	6.060±0.024
63404	J125932.76-381313.2	K3V	43	4676	0.93	3.6	53.3±0.7	54.6	18.8±0.8	15.2	-0.024	0.190	6.800±0.037	6.870±0.020
63973	J130634.58-494111.0	K0V	33	5267	0.78	1.2	73.4±1	72.1	27.6±1	20.1	0.018	0.271	6.500±0.042	6.560±0.022
64461	J131246.24+343140.8	F5	62	6102	1.2	1.6	57.2±0.8	58.5	20.9±0.9	16.2	-0.023	0.227	6.730±0.039	6.750±0.020
65728	J132827.00+595645.3	A1Vn	71	10000	2	0.64	185±3	189	63.7±2	52.0	-0.021	0.184	5.460±0.064	5.460±0.032
66065	J133235.83-284134.0	A0/A1V	72	9279	1.9	1.5	165±2	165	55.7±2	45.4	-0.001	0.186	5.530±0.063	5.580±0.025
66234[c]	J133427.12+490058.0	A5V	55	8080	1.9	4.1	546±8	476	182±3	132	0.128	0.277	4.320±0.089	4.420±0.052
66257	J133447.91+371056.5	F2IVSB	46	6553	3.3	3.4	1300±10	866	399±7	239	0.332	0.400	3.350±0.132	3.580±0.074
66634	J133930.29+525517.0	A3Vn	54	8498	1.8	0.86	242±3	245	82.3±2	67.6	-0.012	0.179	5.110±0.067	5.150±0.039
66765	J134104.34-342752.6	K1V	16	5209	0.77	2.1	311±4	316	104±2	88.1	-0.018	0.153	4.870±0.075	4.950±0.042
66901	J134235.62-120512.9	F5	52	6548	1.2	1.1	80.7±1	82.6	28.1±1	22.8	-0.023	0.189	6.300±0.046	6.370±0.021
67682[c]	J135155.64-363725.4	F8	63	6150	1.3	5.8	54.4±0.8	54.4	18.7±0.9	15.9	0.000	0.149	6.820±0.036	6.840±0.020
67782	J135310.20+283853.6	A7V	66	7977	2	0.28	189±3	189	61.9±2	52.2	-0.004	0.156	5.450±0.059	5.450±0.032
68593	J140231.57+313939.3	F8	39	6159	1.1	1.5	129±2	131	42.7±1	36.4	-0.015	0.149	5.820±0.055	5.880±0.027

Table B.2 (cont'd)

HIP ID	WISE ID	SpT[a]	Dist.[b] (pc)	T_* (K)	R_* ($R_\odot$)	χ^2_*	F_{W3} (mJy)	$F_{W3,*}$ (mJy)	F_{W4} (mJy)	$F_{W4,*}$ (mJy)	$\Delta_{F_{W3}}/F_{W3}$[d]	$\Delta_{F_{W4}}/F_{W4}$[d]	$W1_{corr}$[e] (mag)	$W2_{corr}$[e] (mag)
68755	J140422.98-032804.6	K0	64	4930	0.78	1.1	17.5±0.3	18.0	7.44±0.8	5.00	-0.023	0.328	8.010±0.022	8.090±0.019
69281	J141055.71+151255.2	G0	60	5584	1.3	1.1	67.9±0.9	68.4	26.9±1	19.0	-0.007	0.292	6.570±0.037	6.610±0.019
69508	J141346.12-363716.1	F2V	70	6917	1.5	0.58	80±1	80.9	28.3±1	22.3	-0.011	0.211	6.370±0.044	6.380±0.021
69682	J141549.85-272055.1	G5V	63	5641	1	1.5	37±0.5	37.4	16.3±0.9	10.4	-0.011	0.364	7.200±0.031	7.240±0.021
70239	J142216.75-690507.3	F5V	56	6510	1.3	2.1	91.4±1	91.9	31.3±1	25.4	-0.006	0.188	6.190±0.044	6.260±0.019
71602	J143837.42+545111.5	F2	66	6606	1.5	0.97	79.7±1	80.3	29±1	22.2	-0.007	0.235	6.350±0.043	6.400±0.020
71718	J144010.46+574247.6	F8	53	6168	1.1	0.63	68±0.9	68.7	24.5±0.9	19.1	-0.010	0.220	6.530±0.042	6.590±0.021
72104	J144459.20-351130.5	A0V	66	9183	2.5	2.1	347±5	346	127±3	95.4	0.002	0.248	4.720±0.082	4.790±0.044
73798	J150458.06-325053.9	G3V	71	5557	0.75	1.8	15.4±0.3	15.7	7.5±1	4.37	-0.023	0.417	8.160±0.022	8.190±0.020
74235	J151012.39-162321.6	K2VFe-0.8	29	5176	0.55	3.4	46.9±0.7	47.1	13.6±1	13.1	-0.003	0.036	6.940±0.032	6.910±0.019
74926	J151839.87-183739.3	K5p	25	4281	0.49	6	43±0.6	42.5	13.3±1	13.6	0.011	-0.021	7.130±0.031	7.090±0.021
75158	J152132.63-064936.0	F8	74	6434	1.7	0.5	87.6±1	87.7	35.4±1	24.4	-0.001	0.312	6.330±0.042	6.330±0.020
76280	J153450.17+064812.2	G5	43	5633	1	1.7	81±1	82.9	27.6±1	23.1	-0.023	0.163	6.340±0.044	6.380±0.022
76757	J154022.95+545734.9	G5	70	5928	1.1	1.7	36.5±0.5	37.1	13.3±0.7	10.3	-0.017	0.225	7.210±0.032	7.250±0.019
77094	J154430.16+032211.6	F5	59	6723	1.4	1.4	88.4±1	89.5	33.5±1	24.7	-0.013	0.261	6.240±0.039	6.260±0.020
77464	J154856.78-034906.5	A5IV	54	8547	1.7	0.87	221±3	225	87±2	62.1	-0.019	0.286	5.250±0.060	5.230±0.030
78010	J155546.22-150933.9	F6V	63	6138	1.4	0.74	75.2±1	76.6	27.3±1	21.3	-0.018	0.220	6.440±0.045	6.460±0.022
78045	J155605.87-602857.6	A3V	66	8925	1.8	0.85	165±2	166	68.7±2	45.7	-0.007	0.335	5.640±0.054	5.600±0.030
78979	J160719.43-302457.4	K1V	62	5175	0.88	0.37	26.1±0.4	26.3	10.2±0.9	7.33	-0.007	0.279	7.610±0.026	7.670±0.023
79797	J161705.32-675629.3	A4V	52	8306	1.4	2.1	167±2	163	61.5±2	44.9	0.026	0.270	5.600±0.058	5.620±0.023
79881	J161817.88-283651.5	A0V:	41	9658	1.6	3.1	345±5	348	124±3	95.9	-0.010	0.224	4.730±0.069	4.830±0.039
80781[c]	J162939.90+620512.9	K2	68	4744	0.76	13	16.3±0.3	15.9	4.6±0.5	4.44	0.026	0.035	8.170±0.023	8.190±0.020
81800	J164227.97+495610.0	F8V	29	6114	1.2	1	249±3	255	80.7±2	71.0	-0.025	0.120	5.140±0.063	5.140±0.036
82587	J165257.98+314205.9	F0V	29	7100	1.5	0.63	449±6	449	158±4	124	0.000	0.218	4.530±0.076	4.500±0.054
82887	J165619.23+690028.5	K2	64	5058	1	0.34	33.3±0.5	33.6	11.1±0.5	9.36	-0.007	0.156	7.340±0.028	7.410±0.022
83494	J170353.52+344724.8	A5V	55	7904	1.6	1.2	166±2	167	57.2±2	46.0	-0.005	0.195	5.620±0.057	5.610±0.028
84183	J171232.61+625228.1	F0IV	43	7846	1.6	0.5	278±4	278	95.7±2	76.8	-0.003	0.198	5.020±0.078	5.060±0.039
85157	J172406.55+225736.6	F0IV	43	7740	1.5	0.89	249±3	250	205±4	68.9	-0.002	0.664	5.090±0.067	5.170±0.034
85523[c]	J172840.55-465351.6	K5	4.5	4450	0.71	5.5	459±6	457	152±3	139	0.005	0.082	4.680±0.077	4.580±0.048
85537[c]	J172849.61+001950.5	A8V	60	7500	1.8	4.7	350±5	374	120±3	107	-0.067	0.108	4.700±0.076	4.720±0.041
85699	J173048.14+865805.0	A2m	47	7818	1.6	1.3	220±3	224	75.3±2	61.8	-0.018	0.180	5.220±0.070	5.290±0.031
85922	J173329.81-054442.1	A5V	48	7954	1.7	2.2	259±4	254	102±3	70.0	0.020	0.311	5.200±0.070	5.130±0.038
86178	J173636.77+304706.6	A5V	70	8229	1.9	1.6	152±2	155	52.2±1	42.7	-0.020	0.182	5.640±0.059	5.670±0.030
86305	J173805.44-543002.9	A7V	45	7923	1.9	3.9	369±5	356	223±5	98.1	0.036	0.561	4.740±0.070	4.720±0.042
86598	J174149.04-504328.6	F8/G0V	72	6050	1.3	1.5	48±0.7	47.6	17.7±1	13.2	0.009	0.252	6.930±0.033	6.980±0.019
87108	J174753.48+024226.0	A0V	32	9368	2	0.087	1070±10	960	470±9	264	0.100	0.437	3.610±0.084	3.700±0.071
87558	J175314.09+060605.9	F4IV-V	31	6603	1.5	2.1	379±5	378	123±3	104	0.003	0.150	4.720±0.087	4.660±0.042
89770	J181908.10+713104.6	F5	53	6557	1.7	0.56	172±2	167	103±2	46.0	0.033	0.553	5.620±0.061	5.610±0.030
92858	J185518.92-372957.5	K1V	24	5050	0.81	2.9	142±2	142	48.4±2	39.7	-0.001	0.180	5.730±0.056	5.770±0.027
93412	J190128.68-342235.9	F5V	64	6286	1.1	0.9	45.7±0.7	45.5	18.1±1	12.6	0.003	0.304	7.020±0.033	7.020±0.020
93542[c]	J190306.92-420542.7	A0Vn	59	9700	2.1	33	376±5	375	251±6	111	0.002	0.559	4.690±0.084	4.760±0.045
94184	J191027.67-300026.1	F5V	53	6523	1.8	2	190±3	195	70.1±2	53.9	-0.024	0.230	5.370±0.071	5.400±0.034
94491[c]	J191356.34-265235.1	F3V	62	6720	1.6	6.2	107±2	107	57.7±2	31.6	0.002	0.453	6.010±0.050	6.120±0.020
95261	J192251.21-542527.0	A0Vn	48	9640	1.6	2.6	371±5	282	414±7	77.7	0.240	0.812	4.940±0.069	4.950±0.036
95270	J192258.97-543217.8	F5/F6V	52	6432	1.5	0.96	128±2	128	217±5	35.5	-0.001	0.836	5.860±0.053	5.880±0.024
95619[c]	J192656.49-294436.1	B8/B9V	70	12500	2.8	47	165±2	165	122±3	49.7	0.004	0.592	5.550±0.062	5.680±0.029
95793	J192900.97+015701.3	A0V	61	8629	1.7	1.1	175±2	176	58.9±2	48.4	-0.003	0.178	5.470±0.067	5.530±0.032

Table B.2 (cont'd)

HIP ID	WISE ID	SpT[a]	Dist.[b] (pc)	T_* (K)	R_* ($R_\odot$)	χ^2_*	F_{W3} (mJy)	$F_{W3,*}$ (mJy)	F_{W4} (mJy)	$F_{W4,*}$ (mJy)	$\Delta_{F_{W3}}/F_{W3}$[d]	$\Delta_{F_{W4}}/F_{W4}$[d]	$W1_{corr}$[e] (mag)	$W2_{corr}$[e] (mag)
95938	J193040.05+350610.0	F5	55	6104	1.2	1.3	74.7±1	74.5	35±1	20.6	0.003	0.411	6.430±0.043	6.500±0.021
96562	J193751.77-301743.3	F2V	65	···	···	···	50.7±0.7	50.6	17.4±1	14	0.001	0.195	6.940±0.032	6.870±0.020
99273	J200905.24-261327.1	F5V	52	6406	1.4	1.2	116±2	113	196±4	31.3	0.025	0.840	6.030±0.051	6.050±0.025
99742	J201416.65+151152.0	A2V	46	8889	1.8	0.36	359±5	359	153±3	99.0	0.001	0.351	4.690±0.078	4.750±0.041
100526	J202301.40+544022.3	A2	72	7863	1.6	0.33	96.3±1	97	41.2±1	26.7	-0.007	0.351	6.160±0.047	6.200±0.021
101070	J202921.13+200515.8	A3m	70	7725	1.7	0.72	111±2	112	43.8±2	30.8	-0.008	0.297	6.040±0.052	6.040±0.023
101163[c]	J203018.89+544052.6	F5	57	6510	1.5	4.2	90.4±1	90.7	31.3±1	25.8	-0.003	0.174	6.190±0.049	6.250±0.022
101800	J203749.14+112239.5	A2V	58	9266	1.7	2	212±3	210	85.9±2	57.9	0.007	0.326	5.310±0.065	5.340±0.036
102238[c]	J204300.07+264831.1	K3	65	4840	0.73	8.4	23.9±0.4	22.1	7.05±0.9	6.21	0.075	0.120	7.820±0.024	7.830±0.021
102419	J204515.03-154753.6	F2/F3IV/V	59	6985	1.4	0.77	102±1	103	39.8±2	28.4	-0.013	0.285	6.080±0.046	6.120±0.022
102655	J204810.79-060122.0	G0	54	5872	0.97	2.8	47.9±0.7	48.3	21±1	13.4	-0.009	0.360	6.880±0.034	6.950±0.020
102727	J204857.35+610707.1	F8	67	6373	1.3	1	58.1±0.9	58.9	20.1±0.7	16.4	-0.014	0.185	6.710±0.038	6.750±0.020
103048	J205241.66-531624.7	F5/F6V	70	6430	1.5	0.82	70.1±1	70.2	31.5±1	19.4	-0.001	0.383	6.540±0.043	6.550±0.021
103131	J205341.67+360747.0	G5IV-V	58	5550	1.6	0.86	109±1	109	36.3±1	30.3	0.004	0.166	6.060±0.048	6.130±0.023
105388[c]	J212049.98-530204.0	G5V	43	5660	0.98	4.3	52.9±0.8	52.9	19.8±1	15.5	0.000	0.220	6.810±0.035	6.870±0.020
105819	J212551.61+003203.9	A1IV	74	7955	1.8	2	118±2	118	39.8±2	32.5	0.001	0.184	5.910±0.055	5.960±0.025
105966	J212740.08+273631.2	A1V	58	9311	1.7	1.6	212±3	214	68.4±2	59.0	-0.012	0.137	5.290±0.065	5.370±0.031
106741	J213721.15-182629.2	F3/F5IV	52	6686	1.2	0.86	97.5±1	98.7	35.2±1	27.3	-0.012	0.225	6.170±0.047	6.170±0.023
106914	J213910.33+711831.0	F5	66	6432	1.8	1.3	118±2	118	38.4±0.9	32.7	-0.001	0.150	5.920±0.051	5.950±0.025
107457	J214552.88+702053.8	G5	39	5672	0.92	3	80.6±1	80.8	27.3±0.8	22.5	-0.003	0.175	6.350±0.045	6.390±0.019
107596	J214738.27-055500.2	A7V	70	7686	2	1.1	164±2	166	67.5±3	45.7	-0.011	0.324	5.530±0.058	5.550±0.030
107919	J215151.96+110528.8	A5	70	7557	1.7	0.89	109±1	109	49.8±2	30.1	-0.005	0.396	6.000±0.049	6.070±0.023
107947	J215209.76-620309.4	F6V	45	6350	1.2	2.5	111±2	112	37.4±1	31.2	-0.008	0.168	6.000±0.052	6.020±0.024
109656	J221250.94-105533.1	K3	72	4814	0.79	1.3	15.1±0.3	14.1	5.42±0.8	3.93	0.067	0.274	8.280±0.023	8.350±0.021
109941	J221600.66-141101.8	K5V	56	4439	0.96	6.4	33.1±0.5	32.7	10.5±1	10.5	0.012	-0.005	7.400±0.027	7.400±0.019
111188	J223130.35-322046.1	A1V	44	9638	2.1	0.28	576±8	561	204±5	154	0.026	0.242	4.190±0.099	4.270±0.055
113477	J225854.95+690153.2	K0V	41	5304	0.83	1.1	53.6±0.7	54.5	18.3±0.6	15.2	-0.017	0.170	6.790±0.037	6.870±0.020
114189	J230728.78+210802.8	A5V	39	7308	1.4	1.1	237±3	233	93.8±3	64.2	0.016	0.315	5.170±0.068	5.230±0.035
114822	J231534.23-032946.8	A3V	71	9019	2.1	0.63	195±3	197	75.7±2	54.2	-0.007	0.284	5.400±0.067	5.390±0.028
114948	J231657.93-620004.5	F7V	21	6281	1.2	1.2	500±6	501	164±3	139	-0.001	0.151	4.390±0.088	4.390±0.063
115738	J232656.02+011519.5	A0p	47	9623	1.7	2.5	304±4	302	128±3	83.3	0.005	0.351	4.920±0.079	4.970±0.039
115819[c]	J232748.68+045125.8	K7V:	66	4050	0.61	13	38.8±0.6	38.6	14.9±1	11.7	0.004	0.218	7.220±0.029	7.260±0.020
116431	J233536.19+082257.0	F0	68	6776	1.5	2.1	79.2±1	80.9	82.3±2	22.3	-0.021	0.729	6.360±0.040	6.400±0.023
116973	J234243.63-195300.1	K3/K4	45	4574	0.79	3.9	33.3±0.5	33.8	13.5±1	9.44	-0.015	0.302	7.310±0.025	7.390±0.020
117481	J234919.44-275115.8	F6/F7V	34	6282	1	0.63	150±2	151	55.2±2	41.9	-0.003	0.241	5.710±0.051	5.730±0.028
117915[c]	J235504.53+283801.5	K0VSB	40	5280	0.82	51	520±7	515	170±4	162	0.009	0.049	4.520±0.088	4.490±0.054
118008	J235610.84-390310.2	K3V	22	4868	0.72	1.2	127±2	130	43.8±1	36.2	-0.021	0.174	5.850±0.051	5.940±0.023

Note. — *Hipparcos* stars with detected mid-IR excesses at either $W2$, $W3$ and/or $W4$. Unless otherwise noted, the stellar temperature and radius were obtained from photometric fits as described in § 3 in Chapter 3. The χ^2_* column gives the goodness of the photospheric fit.

[a]Spectral types for stars downloaded from *Hipparcos* database. Stars marked with asterisks had their spectral types estimated from their $B_T - V_T$ colors using empirical color relations from Pecaut & Mamajek (2013).

[b]Parallactic distances from *Hipparcos*.

[c]Stellar temperature and radius were estimated from empirical color relations from Pecaut & Mamajek (2013) using the listed *Hipparcos* spectral type.

[d]The quoted fractional excesses in $W3$ and $W4$ represent the ratios of the measured excess and the estimated stellar photospheric flux in these bands. They have not been color-corrected for the filter response, although such corrections have been applied to the estimates of the fractional bolometric luminosities f_d of the dust (§ 3 in Chapter 3), Table B.4).

[e]Saturation corrected $W1$ and $W2$ photometry (see § 2.4 in Chapter 3)

Table B.3. IR Excess Information - Cont. of Table 6 in Chapter 3

HIP ID	Excess Flag	New? (12|22μm)	Excess Significance ($\Sigma_{\overline{F}}$)					
			$W1-W4$	$W2-W4$	$W3-W4$	$W1-W3$	$W2-W3$	$W1-W2$
544	UNYUNU	-N	···	2.26	6.47	···	-1.16	···
560	YYYNNN	-N	9.22	15.98	24.30	0.47	0.77	0.08
682	YYYNNN	-N	4.67	6.46	6.81	-0.24	-0.18	-0.06
1473	UYYUNU	-N	···	3.29	6.70	···	0.20	···
1481	YYYNNN	-N	6.97	9.63	10.17	0.72	0.57	0.48
1866	YYYNNN	-Y	3.43	3.48	3.16	0.43	1.03	-0.27
2472	YYYNNN	-Y	3.29	4.64	4.17	1.46	2.24	0.12
2710	NNYNNN	-N	1.51	2.96	3.61	-0.78	-0.54	-0.43
3210	YYYNNN	-Y	3.28	4.43	4.05	0.53	0.83	0.20
3279	NYYNNN	-Y	3.19	3.61	3.43	-0.27	0.27	-0.26
3965	NYYNNN	-Y	2.43	5.80	6.28	-0.62	0.86	-0.96
5462	YYYNNN	-N	5.66	6.03	5.31	1.03	1.6	0.08
5631	NNYNNN	-N	1.69	2.08	3.20	-0.31	-0.97	0.27
5709	NNYNNN	-Y	2.48	3.13	3.42	-0.18	-0.31	0.04
6490	YNNNNN	-Y	3.26	3.08	2.87	1.05	0.57	0.69
6494	YYYNNN	-Y	4.46	5.15	4.67	0.70	1.08	0.17
6679	YYYNNN	-N	3.54	6.77	7.62	-0.81	0.22	-0.82
7345	YYYNYN	NN	26.76	47.78	56.35	2.73	5.33	0.06
7576	NNYNNN	-N	2.43	3.22	4.58	-0.39	-1.13	0.26
7699	YYYNNN	-Y	7.93	12.40	13.25	0.36	0.44	0.19
7805	YYYNNN	-N	10.24	12.80	12.45	1.28	1.54	0.40
7978	UUYUUU	-N	···	···	9.06	···	···	···
8109	YYYNNN	-Y	4.92	4.80	5.09	2.04	0.33	1.80
8122	YYYNNN	-N	7.75	12.25	12.60	-0.33	0.78	-0.68
8241	UUYUUU	-N	···	···	11.62	···	···	···
8987	YYNNNN	-Y	3.21	3.35	2.60	1.34	1.73	0.10
9052	YYUUUN	-Y	4.00	4.09	···	···	···	1.17
9141	YYYNNN	-N	3.90	5.56	5.39	-0.27	0.43	-0.36
9902	UUYUUU	-N	···	···	17.89	···	···	···
10054	NYYNNN	-Y	3.12	5.10	4.56	0.67	1.38	0.11
10670	UYYUNU	-N	···	7.28	17.77	···	1.30	···
11157	YYYNNN	-Y	4.01	3.94	3.87	0.15	-0.07	0.39
11477	YYYNNN	-N	4.89	8.56	13.56	-0.27	0.47	-0.48
11847	YYYNNN	-N	47.57	70.28	72.89	1.02	2.50	-0.46
12489	UUYUUU	-N	···	···	4.78	···	···	···
13141	UUYUUU	-Y	···	···	6.13	···	···	···
13209	UUYUUU	-Y	···	···	9.42	···	···	···
13569	YYYNNN	-N	4.55	7.57	7.61	-0.48	0.46	-0.70
13679	NYYNNN	-Y	1.80	3.73	4.72	-0.36	0.36	-0.47
14684	NYYNNN	-N	3.14	3.37	3.26	0.26	-0.04	0.35
15929	YYYNNN	-Y	7.98	8.10	8.00	0.73	0.41	0.48
16449	YYYNNN	-N	11.62	19.04	20.18	-0.01	1.39	-0.60
16908	YNNNNN	-Y	3.51	3.19	2.69	1.76	1.31	0.96
17338	YYYNNN	-Y	6.76	6.60	6.37	1.20	0.23	1.10
17395	YYYNNN	-N	5.11	10.17	12.19	0.11	1.86	-0.70
17764	YYYNNN	-N	9.29	14.85	15.51	0.38	1.15	-0.16
18187	YYYNNN	-N	5.12	7.65	8.71	0.34	0.23	0.29
18481	YYYNNN	-N	7.25	9.72	9.78	1.55	2.05	0.37
19610	NNNYNN	Y-	2.2	1.13	0.39	2.93	1.63	1.92
19793	YYYNNN	-N	5.32	5.61	5.96	0.26	-0.48	0.66
19796	UUYUUU	-Y	···	···	3.94	···	···	···
20261	NNYNNN	-Y	1.55	2.13	3.53	0.20	0.19	0.10
20693	YYYNNN	-N	6.36	7.90	8.50	0.71	-0.30	0.93
20737	YYYNNN	-N	5.85	6.50	6.24	0.77	0.65	0.42
20794	YYYNNN	-Y	3.21	3.95	4.33	-1.05	-0.93	-0.41
20901	YNYNNN	-N	3.27	2.65	7.85	0.41	-1.16	1.07
20998	UUYUUU	-Y	···	···	3.27	···	···	···
21547	UUYUUU	-Y	···	···	3.76	···	···	···
21983	YYNNNN	-Y	3.36	3.37	3.08	0.96	1.19	-0.07
22152	NYYNNN	-Y	2.76	5.02	6.91	-0.41	-0.46	-0.13
22192	YYYNNN	-N	4.92	5.61	6.16	1.42	0.50	1.14
22295	YYYNNN	-N	3.83	4.64	4.45	0.07	0.34	-0.01
22312	UUYUUU	-Y	···	···	5.12	···	···	···
22394	YUYNUU	-Y	3.99	···	4.82	-0.92	···	···
22509	UNYUNU	-Y	···	2.80	4.12	···	1.16	···
22845	UYYUNU	-N	···	4.88	10.99	···	-0.14	···
23443	NYYNNN	-Y	2.77	4.02	3.86	-0.25	0.43	-0.38
23497	UNYUNU	-Y	···	2.20	5.28	···	-0.31	···
23871	YYYNNN	-N	4.14	7.41	10.40	0.05	0.81	-0.35

Table B.3 (cont'd)

HIP ID	Excess Flag	New? (12|22μm)	Excess Significance ($\Sigma_{\overline{E}}$)					
			$W1-W4$	$W2-W4$	$W3-W4$	$W1-W3$	$W2-W3$	$W1-W2$
24528	YYYNYN	NN	14.16	19.33	17.82	1.67	3.74	-0.32
24947	YYYNNN	-N	3.95	5.29	5.38	0.75	0.59	0.50
25183	UUYUUU	-N	···	···	7.52	···	···	···
25376	NNYNNN	-Y	2.02	2.90	3.17	-0.43	-0.4	-0.11
26395	YYYNNN	-Y	13.35	21.74	21.20	0.99	3.30	-0.59
26453	YYYNNN	-N	14.80	21.69	22.73	1.06	1.70	0.20
26563	UYUUUU	-Y	···	4.49	···	···	···	···
26990	YYYNNN	-N	6.21	7.02	6.72	0.99	0.63	0.69
28498	UUYUUU	-Y	···	···	3.77	···	···	···
30252	YYYNNN	-Y	17.32	25.68	27.42	1.15	2.09	0.04
30893	NNNNNY	–	0.70	-0.65	-0.38	1.87	-0.82	2.35
32435	YUYNUU	-N	10.05	···	14.29	1.44	···	···
33690	YYYNNN	-N	3.77	5.49	8.96	0.08	-0.26	0.26
34334	YNNNNN	-Y	3.42	3.25	2.93	0.96	0.69	0.49
35198	YYYNNN	-Y	5.18	5.11	4.49	1.65	1.25	0.90
35567	UUYUUU	-Y	···	···	48.21	···	···	···
36515	UUYUUU	-N	···	···	3.86	···	···	···
36827	YYYNNN	-N	3.47	4.74	5.14	-0.73	-0.38	-0.44
36927	UYYUNU	-Y	···	3.41	3.52	···	-0.29	···
36948	YYYNNN	-N	13.42	16.73	17.23	0.95	0.66	0.64
38369	YYYNNN	-Y	4.35	4.67	4.70	0.09	-0.12	0.28
38538	NYYNNN	-N	1.46	3.98	3.48	0.02	1.74	-0.79
40693	UYYUNU	-N	···	5.54	15.07	···	0.26	···
41081	YUYYUU	NN	13.06	···	21.28	2.89	···	···
41152	YYYNNN	-N	4.85	9.77	13.03	-0.16	0.55	-0.33
41277	YNNNNN	-Y	3.40	2.97	2.96	1.49	0.04	1.33
41307	UYYUNU	-Y	···	5.41	17.52	···	0.26	···
41373	YYYNNN	-N	8.73	12.87	13.09	0.68	1.42	0.02
43121	YYYNNN	-N	6.76	10.79	12.94	-0.1	0.45	-0.29
43414	UYYUNU	-Y	···	5.58	11.01	···	0.93	···
46843	NNYNNN	-Y	2.55	2.95	3.9	0.46	-0.17	0.55
47135	YYYNNN	-N	3.57	3.86	3.23	0.96	1.33	0.14
47792	NYNNNN	-Y	3.19	3.31	2.69	1.30	1.59	-0.28
47990	YNYNNN	-N	3.47	3.16	3.36	0.28	-0.65	0.87
48423	YYYNNN	-N	7.04	8.06	8.27	1.36	0.70	0.98
49593	UYYUNU	-N	···	4.51	6.80	···	1.48	···
49809	UNYUNU	-N	···	1.06	4.06	···	-0.76	···
50155	YYNNNN	-Y	3.24	3.57	3.04	0.29	1.50	-0.73
50860	NNYNNN	-Y	1.32	3.08	3.56	-0.52	0.07	-0.43
51194	UUYUUU	-Y	···	···	4.81	···	···	···
51793	NNNYNN	Y-	2.15	1.90	1.02	3.39	2.97	0.79
52457	NYYNNN	-Y	2.73	5.57	6.80	0.09	1.45	-0.63
52709	YYYNNN	-Y	3.60	4.19	5.27	0.58	-0.39	0.83
52947	YYYNNN	-Y	5.17	6.66	6.86	0.04	0.00	0.06
53954	UYYUNU	-Y	···	6.83	18.03	···	-0.17	···
55057	YYYNNN	-Y	3.45	3.69	3.24	0.46	1.31	-0.41
55130	NYYNNN	-Y	2.56	4.45	3.64	-0.11	1.42	-0.83
56253	NNYNNN	-Y	1.25	2.20	3.17	-0.34	-0.35	-0.16
57971	UUYUUU	-Y	···	···	10.17	···	···	···
59394	YYYNNN	-Y	6.53	10.44	13.48	0.55	0.86	0.13
59422	YYYNNN	-N	4.22	7.56	8.32	-1.35	-0.16	-1.15
59608	YYYNNN	-Y	3.50	5.60	6.37	0.33	0.67	-0.01
59893	YYYNNN	-Y	4.15	4.02	3.74	1.29	0.94	0.46
60074	YYYNNN	-N	4.80	7.08	9.21	0.29	-0.58	0.60
61558	YYYNNN	-N	7.45	12.05	12.37	0.29	2.02	-0.70
61960	UUYUUU	-N	···	···	14.07	···	···	···
62492	YYYNNN	-Y	5.27	5.91	5.77	0.17	0.24	0.09
63076	UYYUNU	-N	···	3.62	3.27	···	2.15	···
63286	NYYNNN	-Y	2.94	4.28	4.97	-0.41	-0.59	-0.08
63404	NYYNNN	-Y	3.07	3.49	3.72	-0.21	-0.76	0.20
63973	YYYNNN	-Y	5.75	7.29	6.34	1.07	1.85	0.08
64461	YYYNNN	-N	3.94	4.30	4.45	0.16	-0.35	0.47
65728	NYYNNN	-Y	2.87	3.74	4.85	0.73	0.25	0.55
66065	NNYNNN	-Y	1.64	2.95	3.47	-0.27	-0.20	-0.15
66234	UUYUUU	-N	···	···	4.84	···	···	···
66257	UYUUUU	-N	···	3.32	···	···	···	···
66634	NNYNNN	-Y	1.77	2.93	4.49	-0.33	-0.32	-0.09
66765	NNYNNN	-N	1.57	3.02	4.75	-0.31	0.09	-0.29
66901	NYYNNN	-Y	2.26	3.68	3.91	-0.88	-0.30	-0.63

Table B.3 (cont'd)

HIP ID	Excess Flag	New? (12|22μm)	Excess Significance ($\Sigma_{\overline{E}}$)					
			$W1-W4$	$W2-W4$	$W3-W4$	$W1-W3$	$W2-W3$	$W1-W2$
67682	UYNUNU	-Y	···	3.52	3.09	···	0.82	···
67782	UNYUNU	-Y	···	2.73	3.19	···	0.23	···
68593	NNYNNN	-Y	1.82	3.19	3.27	-0.28	0.29	-0.33
68755	YYYNNN	-Y	3.51	3.60	3.51	-0.22	0.13	-0.11
69281	YYYNNN	-N	6.30	7.21	6.78	0.84	0.97	0.40
69508	NYYNNN	-Y	3.07	3.68	3.76	0.25	-0.07	0.30
69682	YYYNNN	-N	6.88	7.23	7.34	-0.03	0.02	0.14
70239	NYYNNN	-Y	2.30	3.99	3.46	-0.45	1.04	-0.89
71602	YYYNNN	-N	3.63	5.20	4.98	-0.22	0.58	-0.46
71718	YYYNNN	-Y	3.87	5.34	4.95	0.02	0.84	-0.32
72104	NYYNNN	-Y	2.38	4.63	6.99	-0.13	0.51	-0.37
73798	YYYNNN	-Y	3.82	3.77	3.68	0.34	0.17	0.35
74235	NNNNNY	–	-0.05	-1.11	-0.26	-0.08	-3.63	2.48
74926	NNNNNY	–	1.37	0.23	0.43	2.48	-1.11	2.96
75158	YYYNNN	-Y	7.06	8.16	7.51	1.62	1.54	0.82
76280	NNYNNN	-N	2.68	3.14	3.37	-0.05	-0.30	0.23
76757	YYYNNN	-N	3.67	4.10	3.93	-0.01	0.21	-0.03
77094	YYYNNN	-N	4.31	4.97	5.51	-0.24	-0.73	0.24
77464	YYYNNN	-N	5.02	7.25	10.34	0.21	-0.86	0.70
78010	YYYNNN	-Y	3.52	3.93	3.80	0.41	0.26	0.35
78045	YYYNNN	-N	7.22	8.66	9.89	1.62	0.64	1.16
78979	YYNNNN	-Y	3.40	3.33	2.92	1.13	1.18	0.16
79797	YUYNUU	-Y	4.66	···	7.42	1.03	···	···
79881	NYYNNN	-Y	2.50	5.00	5.74	-0.12	1.37	-0.73
80781	UUUYNN	Y-	···	···	···	2.90	2.09	1.09
81800	NNYNNN	-Y	1.89	2.06	3.37	0.30	-0.37	0.53
82587	NNYNNN	-N	2.72	2.74	5.54	0.58	-0.1	0.56
82887	NYNNNN	-Y	3.13	3.32	2.57	0.94	1.38	-0.10
83494	YYYNNN	-Y	3.49	4.37	4.28	1.09	0.91	0.66
84183	NYYNNN	-Y	2.42	4.63	6.06	0.35	1.00	-0.09
85157	YYYNNN	-N	15.32	27.92	40.11	-0.31	0.88	-0.68
85523	YNYNNN	-Y	4.03	3.09	3.87	2.60	0.68	1.82
85537	UUYUUU	-N	···	···	5.44	···	···	···
85699	NYYNNN	-Y	1.73	4.15	4.93	-0.39	0.51	-0.55
85922	YYYNNN	-N	5.69	6.99	8.73	1.77	0.82	1.25
86178	NYYNNN	-Y	2.43	3.91	4.65	-0.08	0.03	-0.03
86305	YYYNNN	-N	11.32	16.33	28.52	0.79	0.27	0.62
86598	YYYNNN	-Y	3.46	3.77	3.25	0.63	1.33	-0.12
87108	UYUUUU	-Y	···	7.70	···	···	···	···
87558	UUYUUU	-Y	···	···	3.16	···	···	···
89770	UUYUUU	-N	···	···	27.40	···	···	···
92858	NNYNNN	-Y	2.39	3.04	3.99	-0.11	-0.77	0.33
93412	UYYUNU	-N	···	5.30	4.96	···	0.73	···
93542	YYYNNN	-N	10.47	18.19	28.98	0.60	1.64	-0.26
94184	NYYNNN	-Y	2.45	3.98	5.94	-0.64	-1.11	-0.02
94491	YYYNNN	-Y	9.78	16.32	15.50	-0.44	2.22	-1.47
95261	YYYYYN	NN	23.82	41.60	59.95	3.93	6.61	0.39
95270	YYYNNN	-N	33.06	57.44	68.85	0.28	0.03	0.31
95619	YYYNNN	-Y	14.77	27.74	32.36	0.32	3.24	-1.23
95793	NYYNNN	-N	1.76	3.44	3.75	-0.17	0.42	-0.34
95938	YYYNNN	-Y	8.40	11.50	11.15	-0.07	1.31	-0.66
96562	NNNNNY	–	3.04	1.87	1.94	2.47	-0.42	2.71
99273	YYYNNN	-N	35.23	57.17	68.53	1.54	2.38	0.26
99742	YYYNNN	-N	4.62	8.32	13.59	-0.14	0.23	-0.23
100526	YYYNNN	-Y	7.44	11.45	11.71	0.32	0.99	-0.14
101070	YYYNNN	-Y	5.39	6.89	6.86	0.93	0.84	0.48
101163	NYYNNN	-Y	2.33	4.03	4.25	-0.71	-0.09	-0.55
101800	YYYNNN	-N	5.33	8.23	11.08	0.51	0.71	0.15
102238	NUNYUU	Y-	1.03	···	0.00	4.49	···	···
102419	YYYNNN	-N	4.15	5.53	5.70	-0.32	-0.03	-0.27
102655	YYYNNN	-Y	5.80	6.83	6.82	-0.88	-0.06	-0.69
102727	YYYNNN	-Y	3.37	4.33	3.96	0.15	0.59	-0.13
103048	YYYNNN	-N	7.88	9.34	9.22	0.84	0.67	0.52
103131	NYYNNN	-Y	3.13	4.51	3.36	0.79	1.88	-0.10
105388	YYYNNN	-N	4.14	4.72	4.47	0.05	0.58	-0.19
105819	NYNNNN	-Y	1.92	3.27	2.99	-0.19	0.66	-0.39
105966	NYNNNN	-Y	1.51	3.58	2.56	0.24	1.89	-0.61
106741	YYYNNN	-N	3.64	4.03	4.16	0.59	0.06	0.57
106914	NNYNNN	-Y	1.66	2.40	3.18	-0.23	-0.52	0.11

Table B.3 (cont'd)

HIP ID	Excess Flag	New? (12|22μm)	Excess Significance ($\Sigma_{\overline{E}}$)					
			$W1-W4$	$W2-W4$	$W3-W4$	$W1-W3$	$W2-W3$	$W1-W2$
107457	NYYNNN	-N	2.84	3.93	4.17	-0.02	-0.16	0.20
107596	YYYNNN	-N	4.55	6.04	7.89	-0.55	-1.36	0.23
107919	YYYNNN	-N	7.33	11.33	11.84	-0.34	1.18	-0.91
107947	NNYNNN	-N	2.42	3.00	3.48	0.08	-0.44	0.37
109656	UUUYYN	Y-	···	···	···	3.60	4.12	-0.23
109941	NNNNNY	–	1.29	0.69	0.51	2.32	0.21	2.37
111188	UUYUUU	-Y	···	···	5.90	···	···	···
113477	UUYUUU	-Y	···	···	3.78	···	···	···
114189	UUYUUU	-N	···	···	8.64	···	···	···
114822	YYYNNN	-N	4.37	6.76	8.25	0.47	-0.17	0.58
114948	UNYUNU	-N	···	1.51	3.97	···	-0.19	···
115738	YYYNNN	-N	5.13	9.72	14.11	0.46	1.26	-0.12
115819	YYYNNN	-Y	3.91	3.53	3.29	1.78	0.84	1.00
116431	YYYNNN	-N	26.56	35.19	39.69	-0.21	0.33	-0.33
116973	YYYNNN	-Y	3.52	3.69	3.57	-0.42	0.19	-0.30
117481	YYYNNN	-N	4.40	5.83	5.84	0.65	1.01	0.13
117915	YYYNNN	-N	3.23	3.41	3.59	1.98	1.55	0.93
118008	NYYNNN	-N	2.57	4.45	4.16	-0.39	0.42	-0.40

Note. — Summary of the properties of the IR excesses attributed to circumstellar excess disks at $W2, W3$ and/or $W4$ for the stars in our science sample. The *WISE* Excess Flag indicates the combination of detections from the various colors. Each flag is a six character string that identifies whether the star has a statistically probable (Y) or insignificant (N) excess based on the order of the color analyses: $W1-W4$, $W2-W4$,$W3-W4$,$W1-W3$, $W2-W3$ and $W1-W2$. Any stars can have unlisted (U) values, indicating that the star was rejected by the selection criteria for that particular color (§ 2.2 in Chapter 3). 'U' entires correspond to null entries in the corresponding $Wi-Wj$ $\Sigma_{\overline{E}}$ column. Column 3 lists whether or not the star is a new detection at the $W3$ and/or $W4$ bands (12 or 22μm). The last six columns lists the significance of the excess $\Sigma_{\overline{E}}$ for each color.

Table B.4. Disk Parameters from Blackbody Fits - Cont. of Table 7 in Chapter 3

HIP ID	T_{BB} (K)	$T_{BB_{lim}}$ (K)	R_{BB} (AU)	$R_{BB_{lim}}$ (AU)	θ ($''$)	f_d (10^{-5})	$f_{d_{lim}}$ (10^{-5})	Notes
544	···	<162	···	>2.3	>0.17	6.0	>0.23	b,e
560	···	<138	···	>8.1	>0.21	16	>0.57	b,e
682	···	<160	···	>3.2	>0.083	9.1	>0.35	b,e
1473	112	<263	28	>5.1	0.12–0.68	2.5	>0.064	c,e
1481	···	<185	···	>2.7	>0.065	9.6	>0.36	b,e
1866	···	<177	···	>0.99	>0.021	27	>1.0	b,e
2472	137	<311	22	>4.2	0.08–0.42	1.7	>0.055	c,e
2710	···	<208	···	>2.7	>0.065	3.9	>0.14	b,e
3210	117	<276	7.6	>1.3	0.03–0.17	6.3	>0.19	c,e
3279	···	<215	···	>1.9	>0.028	6.0	>0.21	b,e
3965	···	<207	···	>5.5	>0.082	3.7	>0.13	b,e
5462	101	<216	5.7	>1.2	0.027–0.12	19	>0.43	c,e
5631	···	<134	···	>5.4	>0.16	3.1	>0.11	b,e
5709	···	<199	···	>3.3	>0.06	3.8	>0.14	b,e
6490	···	<205	···	>2.2	>0.03	7.5	>0.27	b,e
6494	···	<217	···	>1.5	>0.032	8.4	>0.29	b,e
6679	···	<175	···	>4.3	>0.088	6.1	>0.24	b,e
7345	**133**	···	**17**	···	**0.29**	**31**	···	**g**
7576	···	<146	···	>2.4	>0.1	6.1	>0.23	b,e
7699	97.5	<183	13	>3.7	0.078–0.27	21	>0.43	c,e
7805	98.2	<174	14	>4.5	0.067–0.21	21	>0.42	c,e
7978	···	<96.7	···	>10	>0.58	10	>0.20	b,e
8109	···	<244	···	>1.8	>0.041	7.3	>0.23	b,e
8122	···	<140	···	>11	>0.15	7.3	>0.26	b,e
8241	123	<213	28	>9.3	0.15–0.45	3.6	>0.11	c,e
8987	94.4	<269	4.2	>0.52	0.013–0.11	24	>0.46	c,e
9052	210	<374	4.5	>1.4	0.02–0.063	3.8	>0.14	c,e
9141	···	<217	···	>1.5	>0.037	8.9	>0.31	b,e
9902	181	<221	2.9	>2	0.045–0.066	20	>0.77	c,e
10054	155	<288	12	>3.5	0.05–0.17	2.2	>0.082	c,e
10670	94.4	<175	42	>12	0.35–1.2	7.5	>0.13	c,e
11157	···	<182	···	>1.9	>0.034	12	>0.46	b,e
11477	95.2	<190	33	>8.2	0.18–0.7	7.4	>0.13	c,e
11847	78.9	<91.7	22	>16	0.26–0.35	430	>4.0	c,e
12489	···	<225	···	>8.2	>0.12	2.2	>0.069	b,e
13141	95.2	<245	33	>5	0.1–0.66	4.2	>0.075	c,e
13209	234	<314	14	>7.8	0.15–0.27	1.8	>0.046	c,e
13569	94.4	<210	23	>4.7	0.064–0.31	10	>0.18	c,e
13679	···	<170	···	>6.4	>0.15	3.4	>0.13	b,e
14684	···	<242	···	>0.92	>0.025	7.5	>0.24	b,e
15929	86.6	<167	14	>3.7	0.05–0.19	41	>0.55	c,e
16449	···	<140	···	>13	>0.18	8.4	>0.29	b,e
16908	···	<244	···	>0.71	>0.018	13	>0.43	b,e
17338	96.7	<192	5.9	>1.5	0.03–0.12	36	>0.71	c,e
17395	99	<189	22	>6	0.14–0.52	9.6	>0.19	c,e
17764	87.3	<161	18	>5.3	0.098–0.33	30	>0.42	c,e
18187	90.8	<210	12	>2.3	0.056–0.3	16	>0.26	c,e
18481	146	<218	14	>6.1	0.087–0.19	3.9	>0.14	c,e
19610	522	>274	0.27	<0.97	0.0044–0.016	25	>0.078	d,f
19793	···	<152	···	>3.5	>0.074	9.5	>0.36	b,e
19796	131	···	6.8	···	0.15	···	>0.14	a,e
20261	···	<169	···	>9.8	>0.21	1.6	>0.059	b,e
20693	···	<163	···	>4.3	>0.086	8.4	>0.33	b,e
20737	···	<194	···	>1.3	>0.035	15	>0.54	b,e
20794	···	<119	···	>11	>0.15	6.1	>0.19	b,e
20901	···	<196	···	>8.4	>0.17	3.3	>0.12	b,e
20998	181	<353	3.2	>0.84	0.016–0.062	5.0	>0.19	c,e
21547	180	<344	5.5	>1.5	0.051–0.19	2.4	>0.091	c,e
21983	···	<202	···	>0.93	>0.02	22	>0.81	b,e
22152	···	<219	···	>2.4	>0.073	6.2	>0.21	b,e
22192	···	<220	···	>4.5	>0.08	3.3	>0.11	b,e
22295	···	<246	···	>1.9	>0.032	4.5	>0.18	b,e
22312	···	<200	···	>4.6	>0.066	4.3	>0.16	b,e
22394	82	<212	5.9	>0.89	0.018–0.12	110	>0.57	c,e
22509	99	<410	40	>2.3	0.034–0.58	4.7	>0.029	c,e
22845	110	<207	24	>6.6	0.19–0.66	4.9	>0.12	c,e
23443	···	<224	···	>1.7	>0.044	6.9	>0.23	b,e
23497	99	<282	43	>5.3	0.1–0.82	3.9	>0.078	c,e
23871	···	<178	···	>11	>0.19	3.3	>0.12	b,e
24528	**156**	···	**9.1**	···	**0.12**	**10**	···	**g**
24947	119	<254	7.7	>1.7	0.035–0.16	6.9	>0.21	c,e

Table B.4 (cont'd)

HIP ID	T_{BB} (K)	$T_{BB_{lim}}$ (K)	R_{BB} (AU)	$R_{BB_{lim}}$ (AU)	θ ($''$)	f_d (10^{-5})	$f_{d_{lim}}$ (10^{-5})	Notes
25183	···	<191	···	>4.2	>0.059	7.2	>0.27	b,e
25376	···	<236	···	>1.9	>0.033	4.1	>0.13	b,e
26395	128	<173	16	>8.7	0.14–0.25	9.4	>0.30	c,e
26453	99.8	<146	14	>6.4	0.11–0.24	38	>0.80	c,e
26563	118	<235	24	>6	0.14–0.54	3.7	>0.11	c,e
26990	···	<205	···	>2.1	>0.039	9.0	>0.32	b,e
28498	···	<227	···	>2.4	>0.044	4.2	>0.14	b,e
30252	99.8	<142	22	>11	0.15–0.3	27	>0.57	c,e
32435	97.5	<178	13	>3.9	0.07–0.23	23	>0.45	c,e
33690	···	<182	···	>1.7	>0.094	9.9	>0.38	b,e
34334	···	<234	···	>1.3	>0.018	9.2	>0.30	b,e
35198	···	<215	···	>1.1	>0.031	11	>0.38	b,e
35567	135	<153	13	>9.9	0.14–0.18	28	>0.94	c,e
36515	177	<351	2.3	>0.58	0.026–0.1	4.9	>0.19	c,e
36827	···	<180	···	>1.4	>0.055	9.2	>0.36	b,e
36927	···	<194	···	>0.97	>0.038	7.9	>0.30	b,e
36948	···	<139	···	>3	>0.085	31	>1.1	b,e
38369	···	<170	···	>3.4	>0.052	6.5	>0.25	b,e
38538	···	<283	···	>5.8	>0.085	2.3	>0.058	b,e
40693	101	<199	5.8	>1.5	0.12–0.46	26	>0.55	c,e
41081	**199**	···	**8.2**	···	**0.12**	**6.7**	···	**g**
41152	···	<155	···	>11	>0.22	4.0	>0.15	b,e
41277	86.6	<238	2.8	>0.38	0.0086–0.065	140	>0.97	c,e
41307	104	<186	41	>13	0.34–1.1	5.7	>0.12	c,e
41373	103	<176	28	>9.4	0.14–0.4	9.0	>0.19	c,e
43121	93	<171	28	>8.2	0.15–0.52	12	>0.19	c,e
43414	128	<229	18	>5.8	0.11–0.35	7.9	>0.27	c,e
46843	···	<190	···	>1.4	>0.08	5.3	>0.20	b,e
47135	88.7	<254	11	>1.4	0.021–0.17	15	>0.22	c,e
47792	88.7	<249	5.2	>0.66	0.011–0.089	36	>0.55	c,e
47990	···	<210	···	>2	>0.029	7.5	>0.27	b,e
48423	···	<150	···	>2.9	>0.089	11	>0.43	b,e
49593	···	<224	···	>4.8	>0.17	3.3	>0.11	b,e
49809	···	<219	···	>3.4	>0.12	3.0	>0.10	b,e
50155	···	<190	···	>1.5	>0.027	11	>0.42	b,e
50860	···	<266	···	>4.7	>0.063	2.6	>0.071	b,e
51194	···	<244	···	>4.9	>0.072	2.2	>0.063	b,e
51793	301	>196	0.38	<0.9	0.007–0.017	15	>0.10	d,f
52457	···	<184	···	>14	>0.2	1.8	>0.065	b,e
52709	···	<217	···	>5.7	>0.079	2.9	>0.096	b,e
52947	···	<181	···	>4.7	>0.063	6.1	>0.23	b,e
53954	98.2	<183	36	>10	0.27–0.93	8.1	>0.15	c,e
55057	···	<215	···	>1.4	>0.025	11	>0.37	b,e
55130	104	<278	26	>3.6	0.049–0.35	3.1	>0.069	c,e
56253	···	<215	···	>5.1	>0.086	1.9	>0.065	b,e
57971	···	<178	···	>9.2	>0.12	3.5	>0.13	b,e
59394	92.2	<179	38	>10	0.17–0.65	8.8	>0.14	c,e
59422	···	<140	···	>7	>0.14	8.0	>0.29	b,e
59608	···	<200	···	>5.6	>0.11	3.7	>0.13	b,e
59893	···	<188	···	>1.4	>0.021	22	>0.82	b,e
60074	···	<167	···	>2.7	>0.098	9.1	>0.35	b,e
61558	97.5	<175	33	>10	0.15–0.48	9.2	>0.17	c,e
61960	130	<209	15	>6	0.16–0.42	4.5	>0.14	c,e
62492	···	<167	···	>4.1	>0.06	7.5	>0.29	b,e
63076	···	<258	···	>2.7	>0.091	2.7	>0.077	b,e
63286	···	<188	···	>4.7	>0.077	4.3	>0.16	b,e
63404	···	<177	···	>1.5	>0.035	10	>0.41	b,e
63973	150	<254	2.2	>0.77	0.023–0.066	12	>0.45	c,e
64461	···	<175	···	>3.3	>0.054	6.0	>0.23	b,e
65728	···	<194	···	>11	>0.16	1.2	>0.04	b,e
66065	···	<258	···	>5.4	>0.076	1.9	>0.051	b,e
66234	464	<633	1.4	>0.73	0.013–0.025	23	>0.13	c,e
66257	131	···	19	···	0.41	···	>0.42	a,e
66634	···	<231	···	>5.5	>0.1	2.0	>0.063	b,e
66765	···	<227	···	>0.93	>0.059	6.9	>0.23	b,e
66901	···	<182	···	>3.4	>0.066	3.9	>0.15	b,e
67682	86	<305	15	>1.2	0.019–0.24	8.6	>0.13	c,e
67782	···	<288	···	>3.5	>0.053	2.6	>0.065	b,e
68593	···	<244	···	>1.7	>0.042	4.3	>0.13	b,e
68755	···	<150	···	>1.9	>0.03	20	>0.73	b,e
69281	···	<187	···	>2.7	>0.045	11	>0.42	b,e

Table B.4 (cont'd)

HIP ID	T_{BB} (K)	$T_{BB_{lim}}$ (K)	R_{BB} (AU)	$R_{BB_{lim}}$ (AU)	θ ($''$)	f_d (10^{-5})	$f_{d_{lim}}$ (10^{-5})	Notes
69508	···	<212	···	>3.7	>0.052	4.1	>0.14	b,e
69682	···	<160	···	>2.9	>0.046	15	>0.57	b,e
70239	···	<238	···	>2.3	>0.04	4.7	>0.15	b,e
71602	···	<212	···	>3.2	>0.049	5.4	>0.19	b,e
71718	···	<210	···	>2.2	>0.042	6.1	>0.22	b,e
72104	95.2	<238	52	>8.3	0.13–0.79	4.3	>0.074	c,e
73798	···	<149	···	>2.4	>0.034	21	>0.74	b,e
75158	···	<191	···	>4.5	>0.06	8.1	>0.30	b,e
76280	···	<193	···	>2	>0.047	5.2	>0.20	b,e
76757	···	<196	···	>2.3	>0.033	6.7	>0.25	b,e
77094	···	<175	···	>4.6	>0.077	5.4	>0.21	b,e
77464	···	<160	···	>11	>0.21	3.1	>0.11	b,e
78010	···	<193	···	>3.2	>0.052	5.9	>0.22	b,e
78045	···	<171	···	>11	>0.16	3.5	>0.13	b,e
78979	···	<208	···	>1.2	>0.02	14	>0.50	b,e
79797	177	<271	7.2	>3.1	0.059–0.14	3.1	>0.12	c,e
79881	···	<210	···	>7.2	>0.17	1.8	>0.057	b,e
80781	272	>174	6.4	<1.5	0.094–0.022	0.15	>0.039	d,f,h
81800	···	<219	···	>2.1	>0.073	3.1	>0.11	b,e
82587	···	<244	···	>2.8	>0.097	4.5	>0.14	b,e
82887	···	<272	···	>0.82	>0.013	9.2	>0.26	b,e
83494	···	<234	···	>4.1	>0.074	2.8	>0.088	b,e
84183	···	<242	···	>3.8	>0.089	3.0	>0.091	b,e
85157	···	<112	···	>16	>0.38	28	>0.76	b,e
85523	160	<590	1.3	>0.094	0.021–0.28	0.84	>0.18	c,e
85537	131	···	14	···	0.23	···	>0.051	a,e
85699	···	<197	···	>5.6	>0.12	2.3	>0.082	b,e
85922	146	<242	11	>4.2	0.087–0.24	4.4	>0.16	c,e
86178	···	<185	···	>8.4	>0.12	1.9	>0.071	b,e
86305	126	<164	17	>9.9	0.22–0.37	14	>0.46	c,e
86598	122	<249	7.2	>1.7	0.024–0.099	8.6	>0.27	c,e
87108	131	···	22	···	0.71	···	>0.17	a,e
87558	109	<334	13	>1.3	0.043–0.4	4.2	>0.11	c,e
89770	123	<165	11	>6.1	0.11–0.21	24	>0.78	c,e
92858	···	<272	···	>0.64	>0.027	11	>0.30	b,e
93412	90.8	<216	12	>2.1	0.033–0.19	19	>0.31	c,e
93542	109	<130	62	>27	0.45–1	12	>0.24	c,e
94184	···	<169	···	>6.3	>0.12	5.0	>0.19	b,e
94491	85.3	<155	23	>6.9	0.11–0.37	360	>0.47	c,e
95261	**177**	···	**11**	···	**0.22**	**25**	···	**g**
95270	···	<88.7	···	>18	>0.34	220	>3.3	b,e
95619	86	<126	140	>65	0.92–2	12	>0.13	c,e
95793	···	<266	···	>4.1	>0.067	2.3	>0.06	b,e
95938	86.6	<167	14	>3.7	0.068–0.25	39	>0.53	c,e
99273	83.3	<99.1	19	>13	0.25–0.36	290	>3.4	c,e
99742	90.8	<181	39	>9.8	0.21–0.85	8.9	>0.13	c,e
100526	···	<166	···	>8	>0.11	5.3	>0.20	b,e
101070	···	<182	···	>6.8	>0.097	4.4	>0.16	b,e
101163	···	<266	···	>2	>0.036	4.1	>0.14	b,e
101800	103	<204	31	>7.9	0.14–0.53	5.0	>0.11	c,e
102238	500	>235	0.17	<0.72	0.0026–0.011	33	>0.14	d,f
102419	···	<181	···	>4.8	>0.082	5.5	>0.21	b,e
102655	···	<170	···	>2.7	>0.049	13	>0.50	b,e
102727	···	<227	···	>2.3	>0.034	4.7	>0.16	b,e
103048	···	<169	···	>4.8	>0.069	11	>0.42	b,e
103131	111	<299	9.1	>1.3	0.022–0.16	7.6	>0.21	c,e
105388	84.6	<244	10	>1.2	0.029–0.24	16	>0.27	c,e
105819	90.8	<276	31	>3.4	0.045–0.42	5.0	>0.078	c,e
105966	···	<272	···	>4.5	>0.078	1.4	>0.035	b,e
106741	···	<202	···	>3.1	>0.061	4.8	>0.17	b,e
106914	···	<313	···	>1.7	>0.026	5.3	>0.12	b,e
107457	···	<270	···	>0.93	>0.024	7.5	>0.21	b,e
107596	···	<167	···	>9.7	>0.14	5.0	>0.19	b,e
107919	···	<150	···	>9.6	>0.14	7.3	>0.27	b,e
107947	···	<258	···	>1.7	>0.037	4.8	>0.14	b,e
109656	268	>175	0.59	<1.4	0.0081–0.019	21	>0.13	d,f,h
111188	188	<303	12	>4.6	0.11–0.27	1.9	>0.064	c,e
113477	···	<219	···	>1.1	>0.027	7.1	>0.24	b,e
114189	134	<225	9.4	>3.3	0.085–0.24	6.0	>0.21	c,e
114822	···	<188	···	>11	>0.15	2.7	>0.097	b,e
114948	···	<297	···	>1.2	>0.058	5.3	>0.13	b,e

Table B.4 (cont'd)

HIP ID	T_{BB} (K)	$T_{BB_{lim}}$ (K)	R_{BB} (AU)	$R_{BB_{lim}}$ (AU)	θ ($''$)	f_d (10^{-5})	$f_{d_{lim}}$ (10^{-5})	Notes
115738	96.7	<189	36	>9.4	0.2–0.76	6.0	>0.11	c,e
115819	102	<258	2.2	>0.35	0.0054–0.034	160	>0.74	c,e
116431	···	<86	···	>21	>0.31	110	>1.5	b,e
116973	···	<169	···	>1.3	>0.029	21	>0.81	b,e
117481	···	<212	···	>2.1	>0.062	6.5	>0.23	b,e
117915	248	<1000	0.86	>0.053	0.0013–0.022	21	>0.063	c,e
118008	···	<197	···	>1	>0.046	8.7	>0.33	b,e

Note. — A summary of the calculated disk properties of stars with $W2$, $W3$ and $W4$ excesses. Blackbody temperatures for the dust are listed **alongside** the calculated circumstellar location, projected angular extent of the dust and the fractional bolometric luminosity.
Notes:
a. $W4$-only excess: The $W3$ excess flux in this case was either saturated or $> 3\sigma$ below the photosphere. A limiting temperature and radius for the dust cannot be determined.
b. $W4$-only excess: The $W3$ excess flux is formally negative and an upper limit to the excess flux is used to place a 3σ limit to the dust temperature and radius.
c. $W4$-only excess: The $W3$ positive excess flux in this case was used to calculate a dust temperature and radius. An upper limit to the $W3$ excess flux was used to calculate a 3σ limit to the dust temperature and radius.
d. $W3$-only excess: The $W4$ positive excess flux in this case was used to calculate a dust temperature and radius. An upper limit to the $W4$ excess flux was used to calculate a 3σ limit to the dust temperature and radius.
e. Lower limit to the fractional luminosity was calculated for a blackbody with peak emission at $\lambda = 12\mu m$ as described in § 3 in chapter 3.
f. Lower limit to the fractional luminosity was calculated for a blackbody with peak emission at $\lambda = 22\mu m$ as described in § 3 in chapter 3.
g. Significant $W3$ and $W4$ excess found in these stars. Dust parameters are exact calculations
h. $W3$-only excess: The $W4$ excess significance in this case was undetermined as the measurement was ignored in all $W4$ analyses as its ASC measurement was $> 2\sigma$ discrepant from the mean Single Frame measurement.

Appendix C

Derivations

C.1 The Weighted Excess Metric

We present the full derivation of $\Sigma_{\overline{E[Wj]}}$ for a star at a *WISE* mid-IR band Wj, where $j = 3$ or 4. Starting with Equation 4.2, we arrive at a general form for the weighted excess by adding the individual color excess terms, and multiplying by weights a_i

$$\overline{E[Wj]} = \sum_{i=1}^{j-1} a_i E[Wi - Wj] \tag{C.1}$$

$$= \sum_{i=1}^{j-1} a_i \left(Wi - Wj - W_{ij}(B_T - V_T)\right). \tag{C.2}$$

The weights a_i are normalized and are unknown:

$$\sum_{i=1}^{j-1} a_i \equiv 1. \tag{C.3}$$

Our general form for the S/N of the weighted average of the excess at Wj is calculated by dividing equation C.1 by the uncertainty in the weighted average, $\sigma_{\overline{E[Wj]}}$. The uncertainty is defined as the quadrature sum of each entry of the Jacobian matrix of $\overline{E[Wj]}$ weighted by its respective uncertainty. The variance of the weighted average is

$$\sigma^2_{\overline{E[Wj]}} = \sum_\alpha \sigma^2_\alpha \left(\frac{\partial \overline{E[Wj]}}{\partial \alpha} \right)^2 + O\left(\sigma_{Wi,Wij}\right) + O(\sigma_{Wi,Wj}), \tag{C.4}$$

where $\alpha \in \{Wi, Wj, Wij(B_T - V_T)\}$ are the terms on the right hand side of Equation C.2. The cross terms in the Jacobian matrix, $O(\sigma_{Wi,Wij})$ and $O(\sigma_{Wi,Wj})$ are proportional to the covariance of the uncertainties in the *WISE* photometry and the mean *WISE* colors. We ignore the first term, $O(\sigma_{Wi,Wij})$, because $\sigma_{Wij} \sim 0.1\sigma_{Wi}$ and W_{ij} is only a shallow function of $B_T - V_T$. We also ignore $O(\sigma_{Wi,Wj})$ because the errors on Wi and Wj are not correlated and hence $\sigma_{Wi,Wj} \sim 0$. Thus, Equation C.4 reduces to

$$\sigma^2_{\overline{E[Wj]}} \simeq \sum_\alpha \sigma^2_\alpha \left(\frac{\partial \overline{E[Wj]}}{\partial \alpha} \right)^2, \tag{C.5}$$

where $\alpha \in \{Wi, Wj\}$, after removing the photospheric uncertainties from the calculation. We define the significance of the weighted excess at Wj in the same form as in Equation 4.4:

$$\Sigma_{\overline{E[Wj]}} = \frac{\overline{E[Wj]}}{\sigma_{\overline{E[Wj]}}}. \tag{C.6}$$

We proceed with solving for the weights in equation C.1. Using $j = 4$ as an example, we can expand equation C.1 as

$$\begin{aligned} \overline{E[W4]} &= a_1 E[W1 - W4] + a_2 E[W2 - W4] + a_3 E[W3 - W4] && \text{(C.7)} \\ &= a_1(W1 - W4 - W_{14}) + a_2(W2 - W4 - W_{24}) + a_3(W3 - W4 - W_{34}), && \text{(C.8)} \end{aligned}$$

Inserting $a_3 = 1 - a_1 - a_2$ into Equation C.7 produces

$$\overline{E[W4]} = a_1 W1 - a_1 W_{14} + a_2 W2 - a_2 W_{24} + W3 - W4 - W_{34} - a_1 W3 + a_1 W_{34} - a_2 W3 + a_2 W_{34}. \tag{C.9}$$

The variance of $\overline{E[W4]}$ is calculated using Equation C.5,

$$\sigma^2_{\overline{E[W4]}} = a_1^2 \sigma^2_{W1} + a_2^2 \sigma^2_{W2} + (1 - a_1 - a_2)^2 \sigma^2_{W3} + \sigma^2_{W4}. \tag{C.10}$$

Next we seek solutions for a_1 and a_2 that minimize the dependence of $\sigma^2_{\overline{E[W4]}}$ on these weights. Thus, by calculating

$$\left(\frac{\partial\sigma^2_{\overline{E[W4]}}}{\partial a_1}\right) = 0 = 2a_1\sigma^2_{W1} - 2\sigma^2_{W3} + 2a_2\sigma^2_{W3} + 2a_1\sigma^2_{W3}, \tag{C.11}$$

$$\left(\frac{\partial\sigma^2_{\overline{E[W4]}}}{\partial a_2}\right) = 0 = 2a_2\sigma^2_{W2} - 2\sigma^2_{W3} + 2a_2\sigma^2_{W3} + 2a_1\sigma^2_{W3} \tag{C.12}$$

We solve for a_1 and a_2

$$a_1 = \frac{\sigma^2_{W3}\sigma^2_{W2}}{\sigma^2_{W2}\sigma^2_{W1} + \sigma^2_{W2}\sigma^2_{W3} + \sigma^2_{W3}\sigma^2_{W1}}, \tag{C.13}$$

$$a_2 = \frac{\sigma^2_{W3}\sigma^2_{W1}}{\sigma^2_{W2}\sigma^2_{W1} + \sigma^2_{W2}\sigma^2_{W3} + \sigma^2_{W3}\sigma^2_{W1}}. \tag{C.14}$$

Now, using Equations C.13 and C.14, we recover a_3,

$$a_3 = \frac{\sigma^2_{W2}\sigma^2_{W1}}{\sigma^2_{W2}\sigma^2_{W1} + \sigma^2_{W2}\sigma^2_{W3} + \sigma^2_{W3}\sigma^2_{W1}}. \tag{C.15}$$

To reduce the form of these weights, we multiply and divide each by $\sigma^2_{W1}\sigma^2_{W2}\sigma^2_{W3}$, to finally obtain the general form for each weight

$$a_i = \frac{1/\sigma^2_{Wi}}{\sum_{i=1}^{j-1} 1/\sigma^2_{Wi}}. \tag{C.16}$$

This is valid for either weighted $W3$ ($j = 3$) or weighted $W4$ ($j = 4$) excesses. We then set $A = \sum_{i=1}^{j-1} 1/\sigma^2_{Wi}$, substitute equation C.16 into equation C.10 to obtain a reduced expression for the variance of the excess ($\sigma_{\overline{E[W4]}}$), and then place that expression into Equation C.6. This gives us the final form for the significance of the weighted excess, which when generalized for $j = 3$ or $j = 4$ is

$$\Sigma_{\overline{E[Wj]}} = \frac{\frac{1}{A}\sum_{i=1}^{j-1}\frac{E[Wi-Wj]}{\sigma_i^2}}{\sqrt{\sigma_j^2 + 1/A}}. \tag{C.17}$$

Equation C.17 is the same result for $\Sigma_{\overline{E[Wj]}}$ as presented in equation 4.4.

Appendix D

Figures

D.1 Extended Figures in Chapter 3

In chapter 3, we showed an example plot of the SEDs (Figure 6) for all the excess stars we identified within 75 pc. Here, I show the SEDs for all the excess stars within this sample.

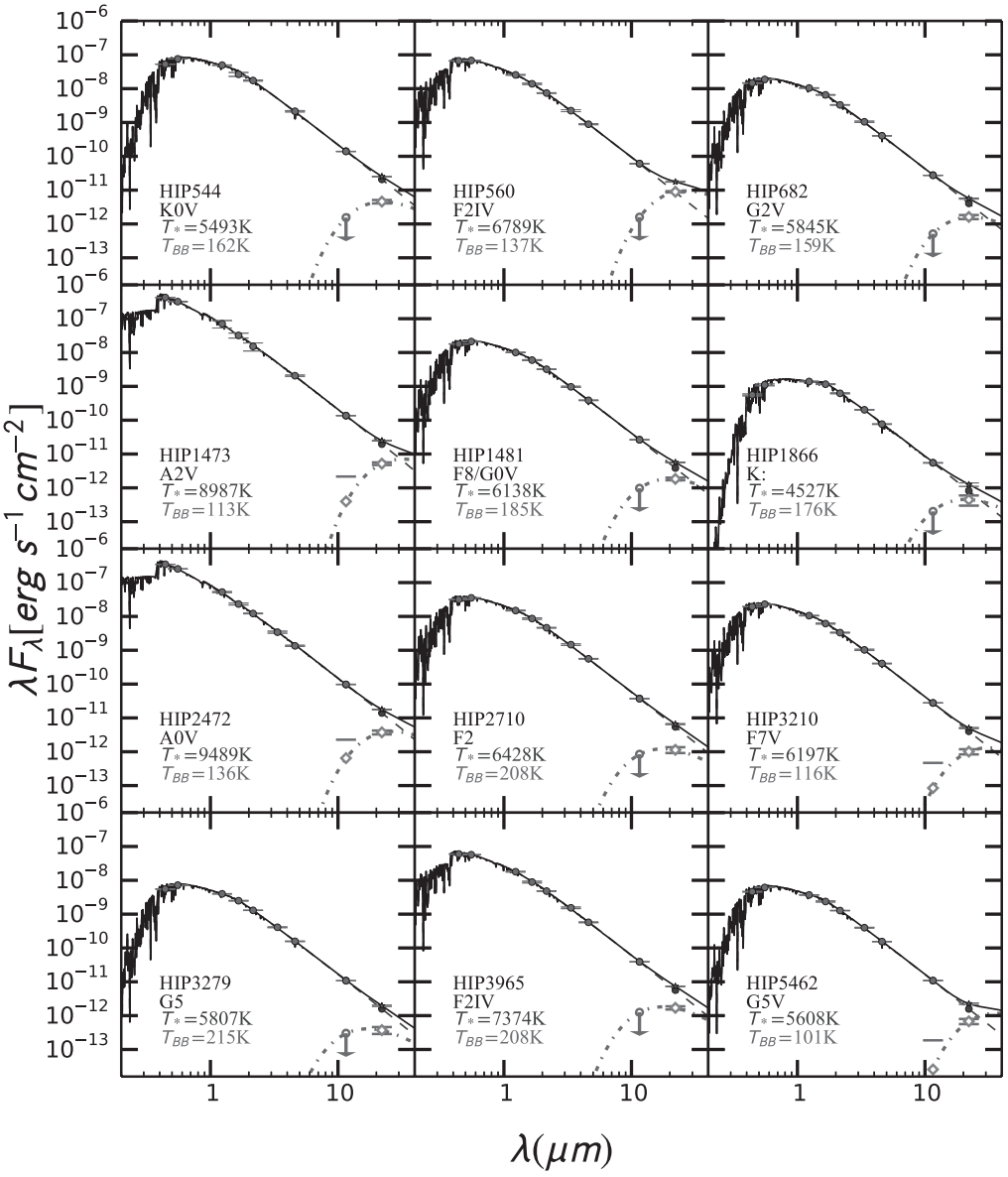

Figure D.1: SEDs of probable debris disk-host stars in our science sample. The dashed lines and solid data points correspond to the fitted model NextGen photosphere and to $BVJHK_s$ photometry from the *Hipparcos* Catalogue and *2MASS* Point Source Catalog. Fluxes plotted as closed circles were used in the fit, and fluxes plotted as stars—excesses above the photosphere—were not used in the fit. Cool blackbody curves (dash-dotted line) were fitted to the excess fluxes (open diamonds) at the $W3$ and/or $W4$ wavelengths. The combined photosphere and excess emission for each star is plotted as a solid black line.

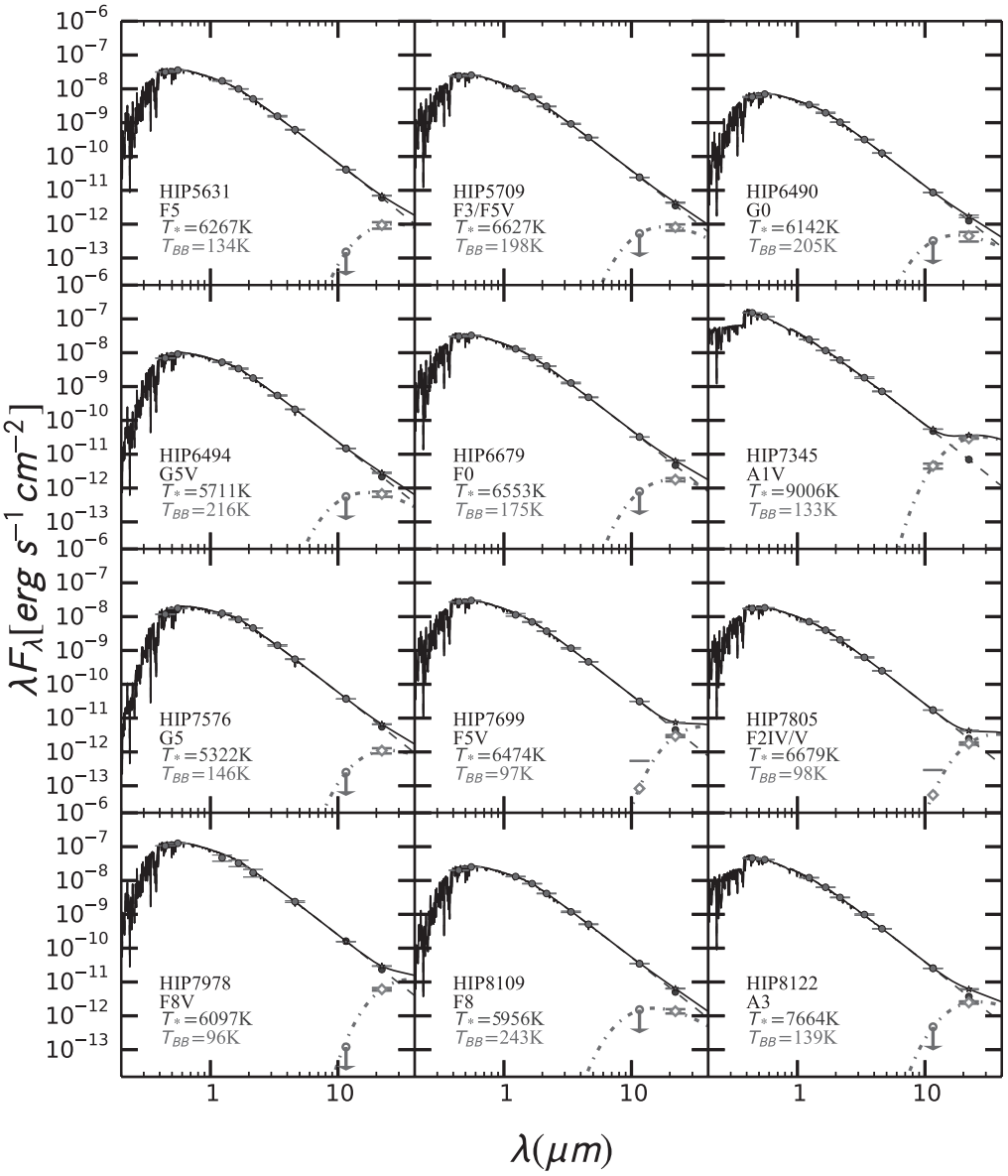

Figure D.2: continued.

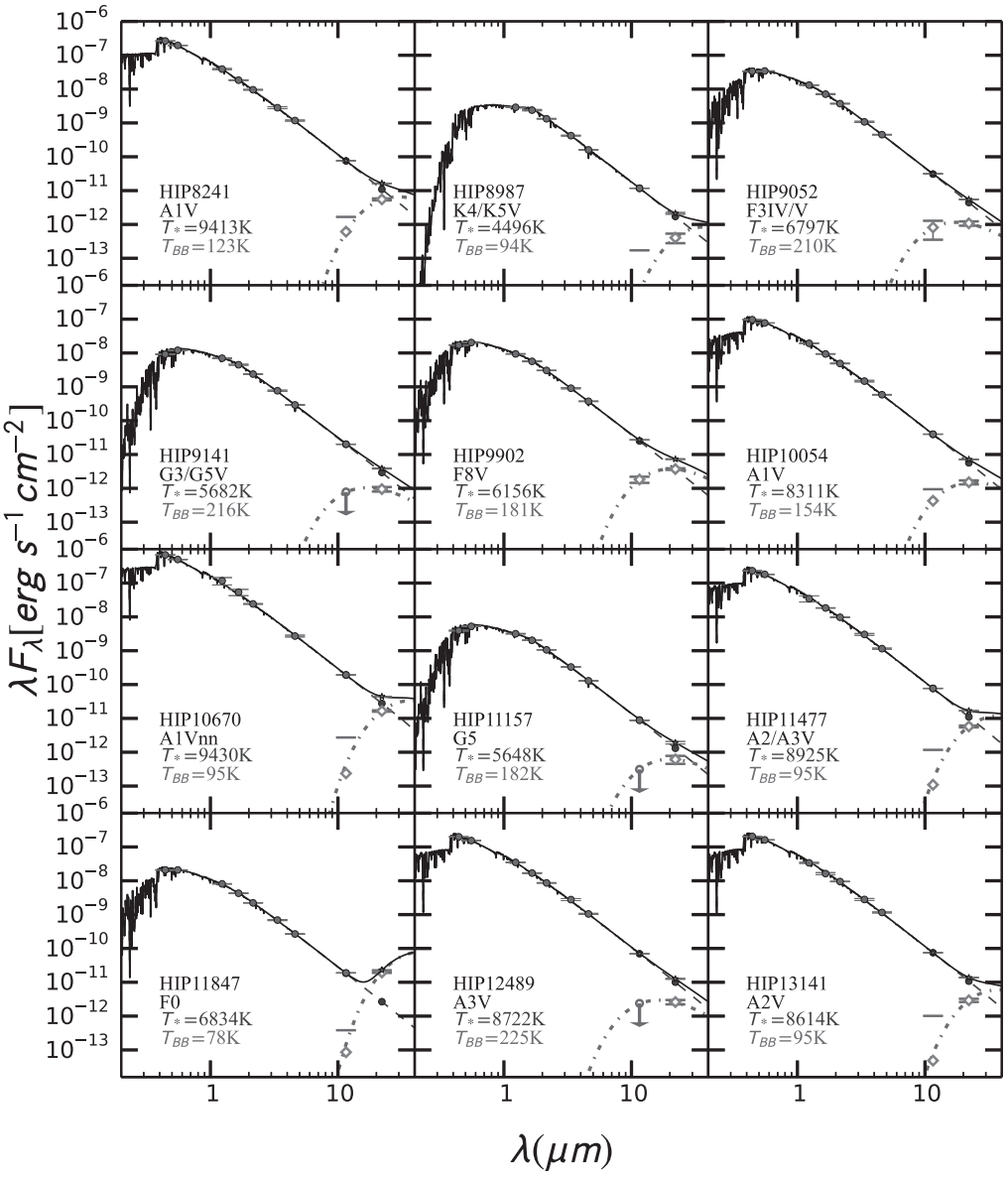

Figure D.2: continued.

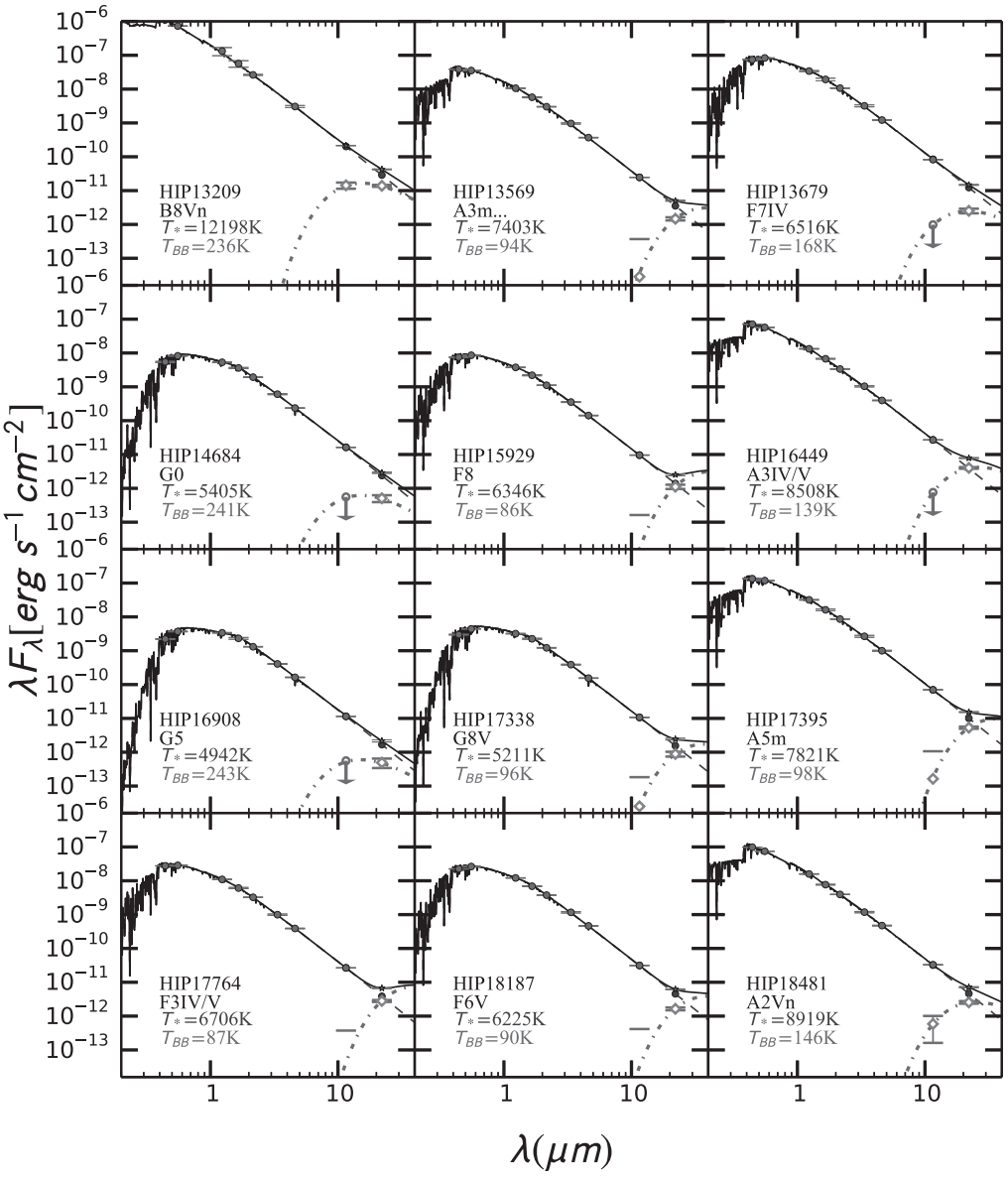

Figure D.2: continued.

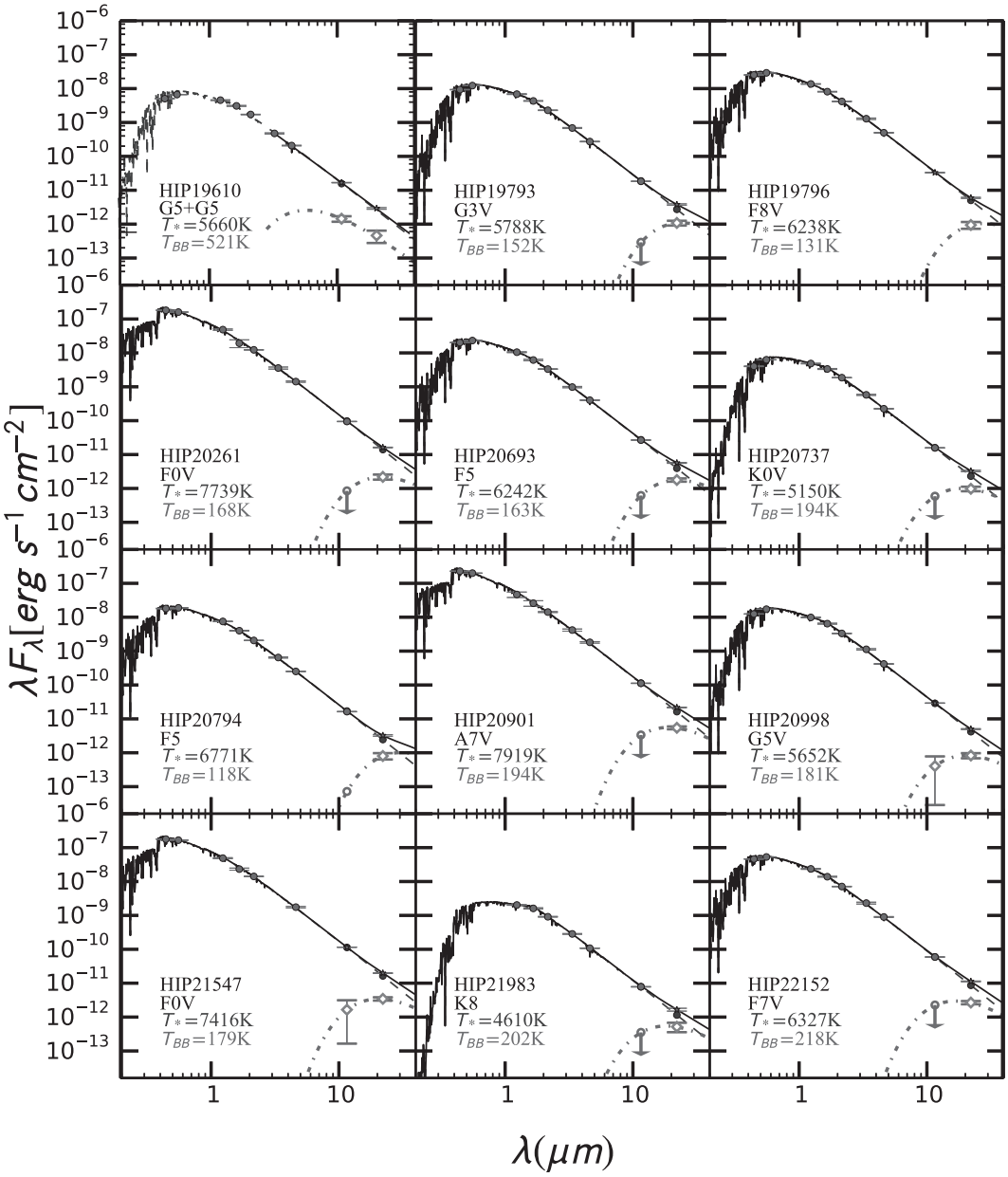

Figure D.2: continued.

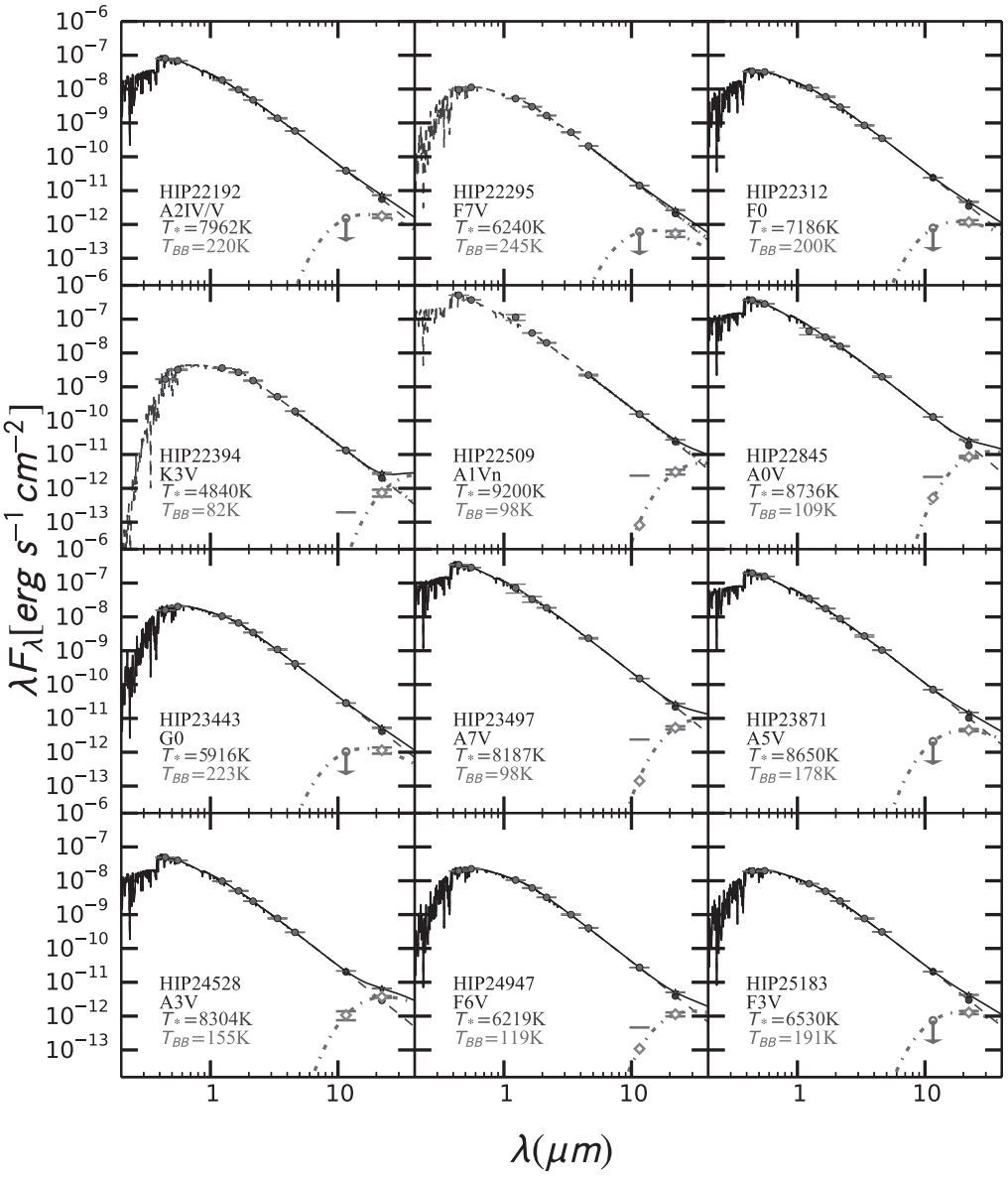

Figure D.2: continued.

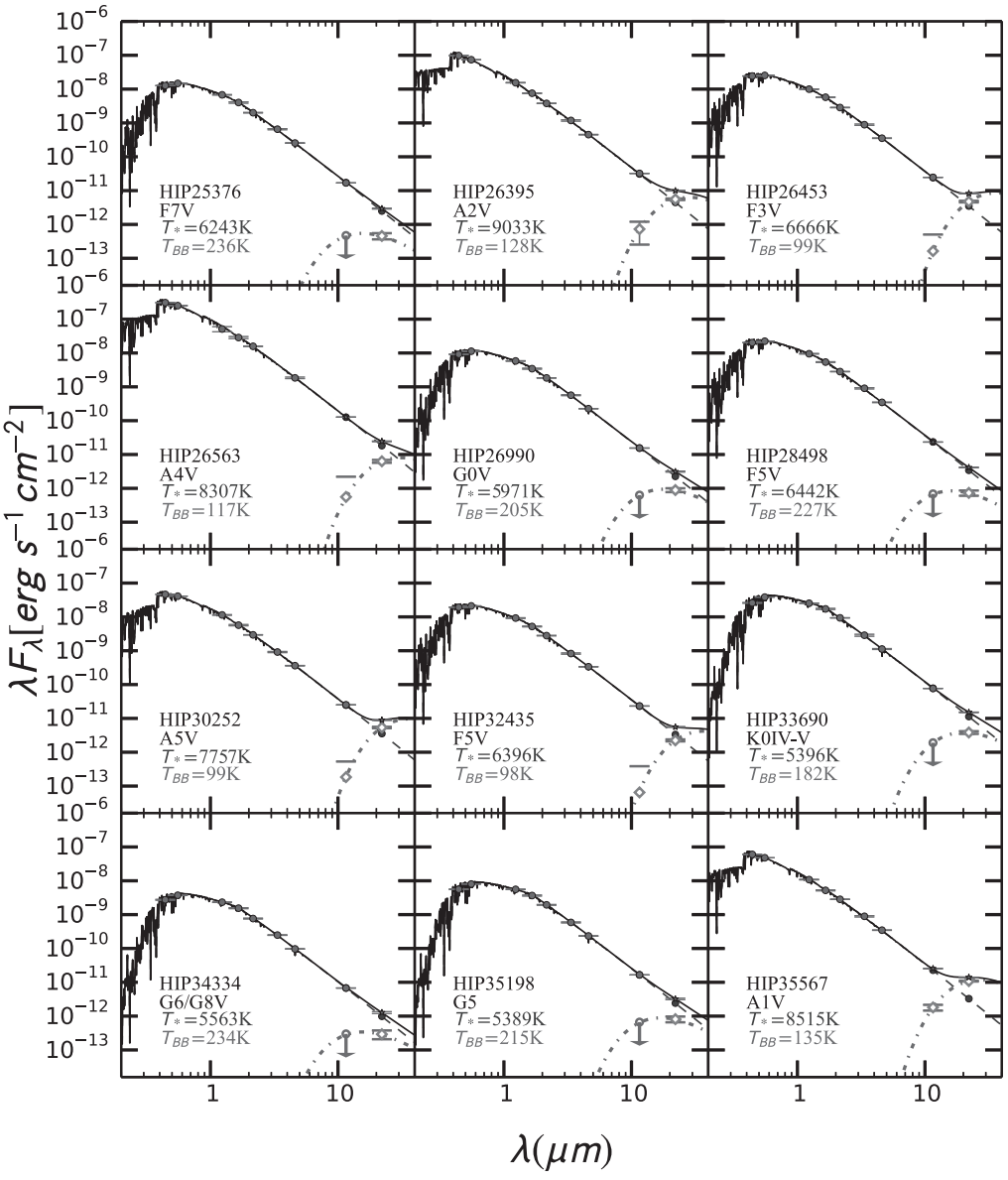

Figure D.2: continued.

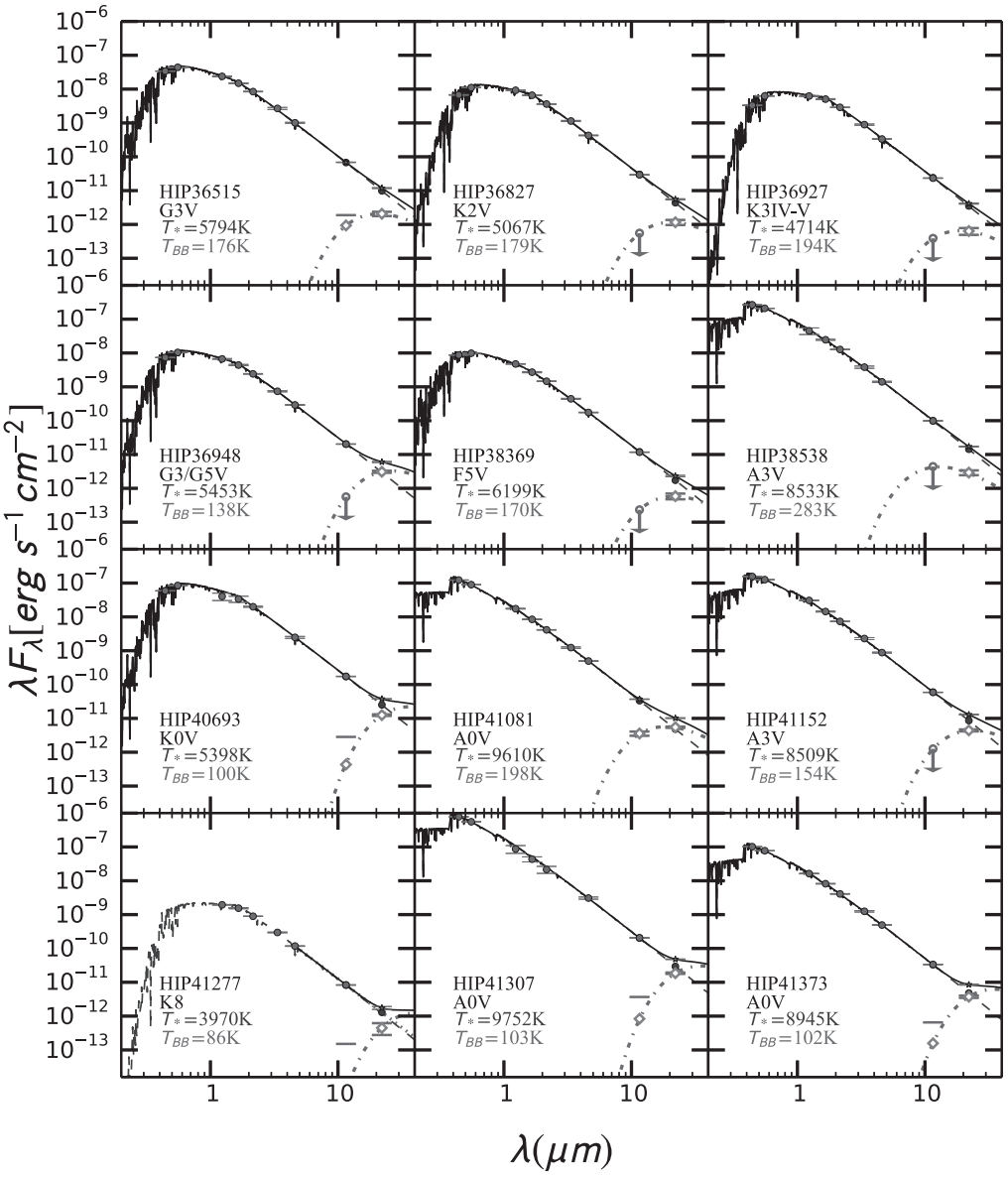

Figure D.2: continued.

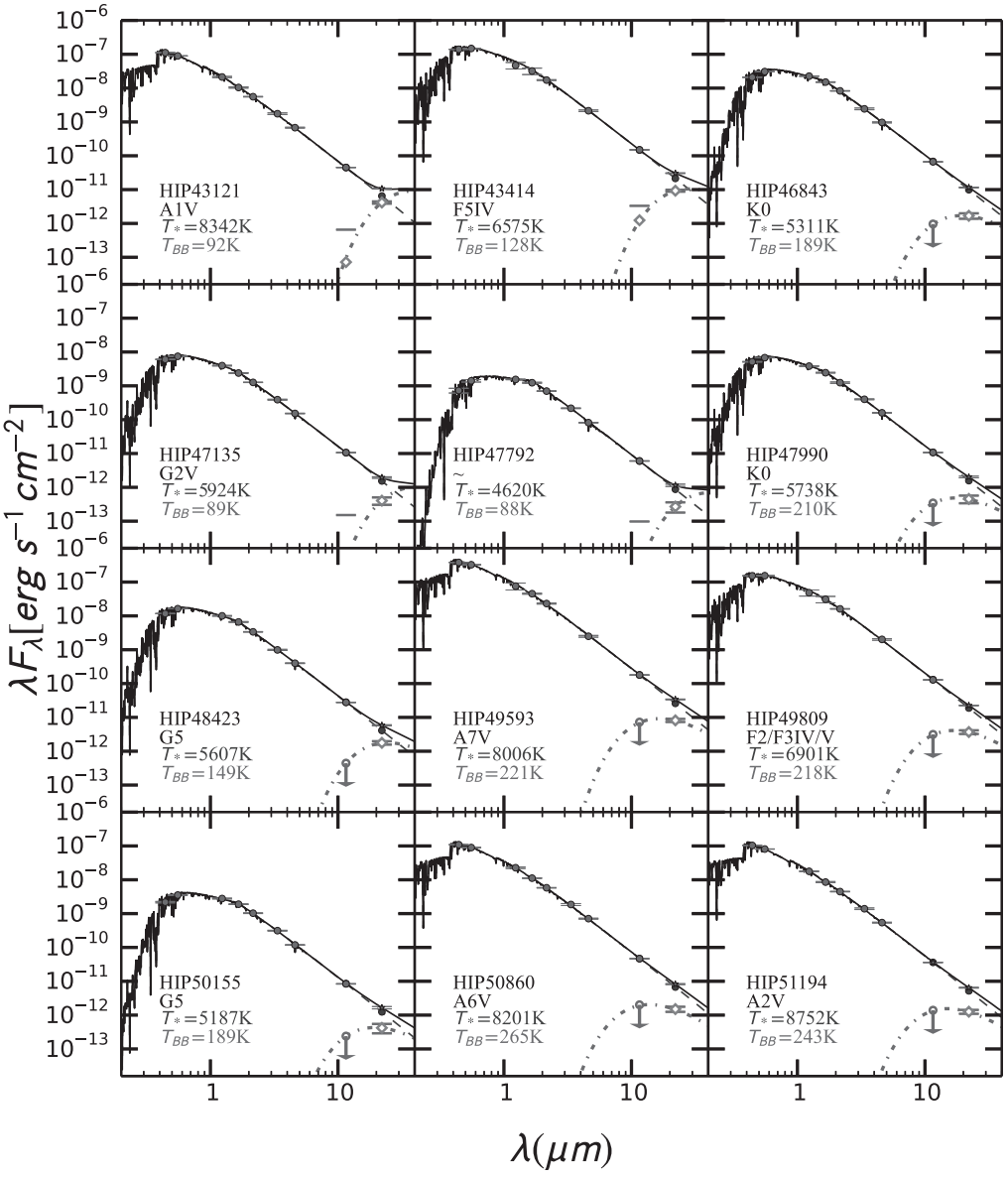

Figure D.2: continued.

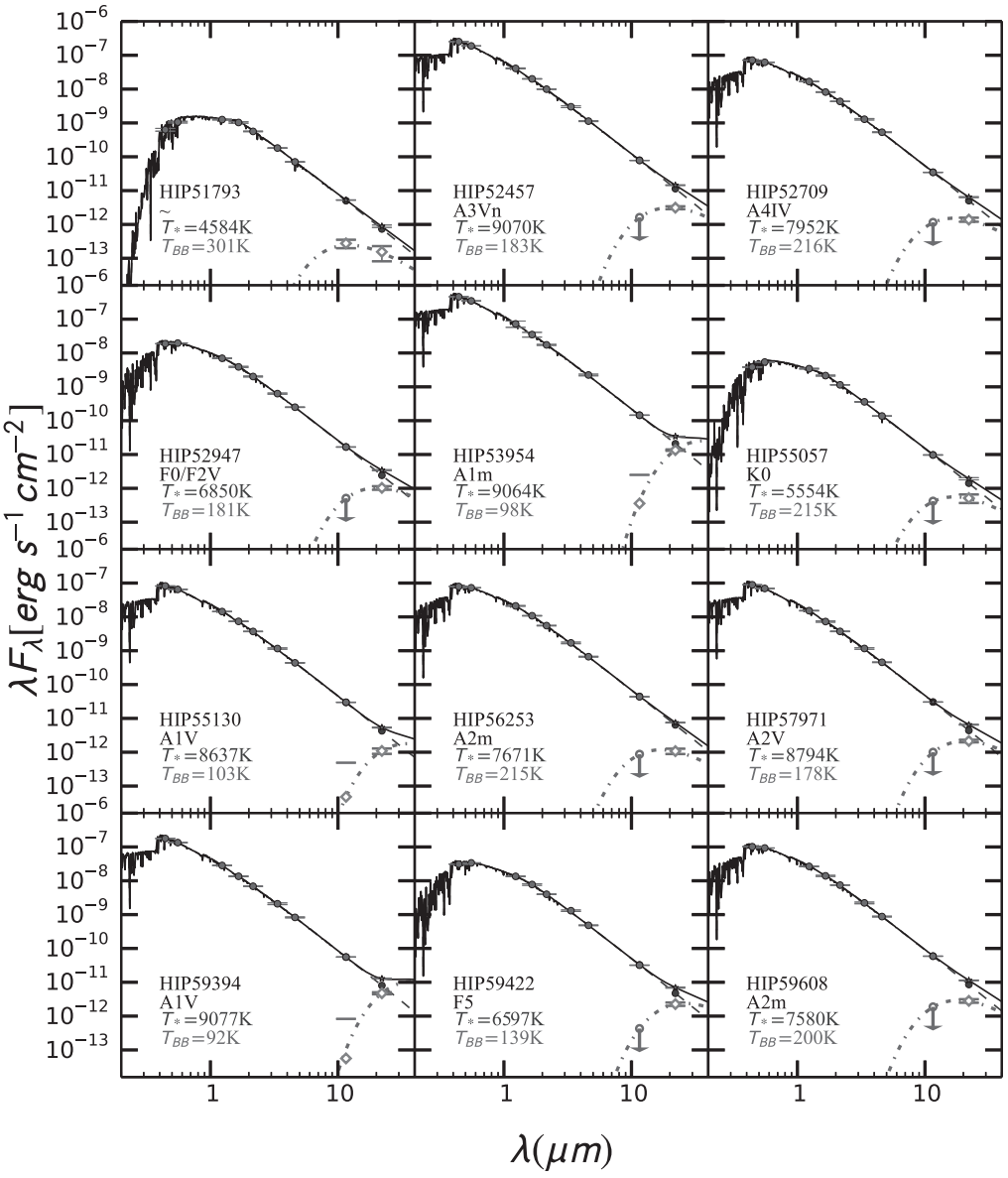

Figure D.2: continued.

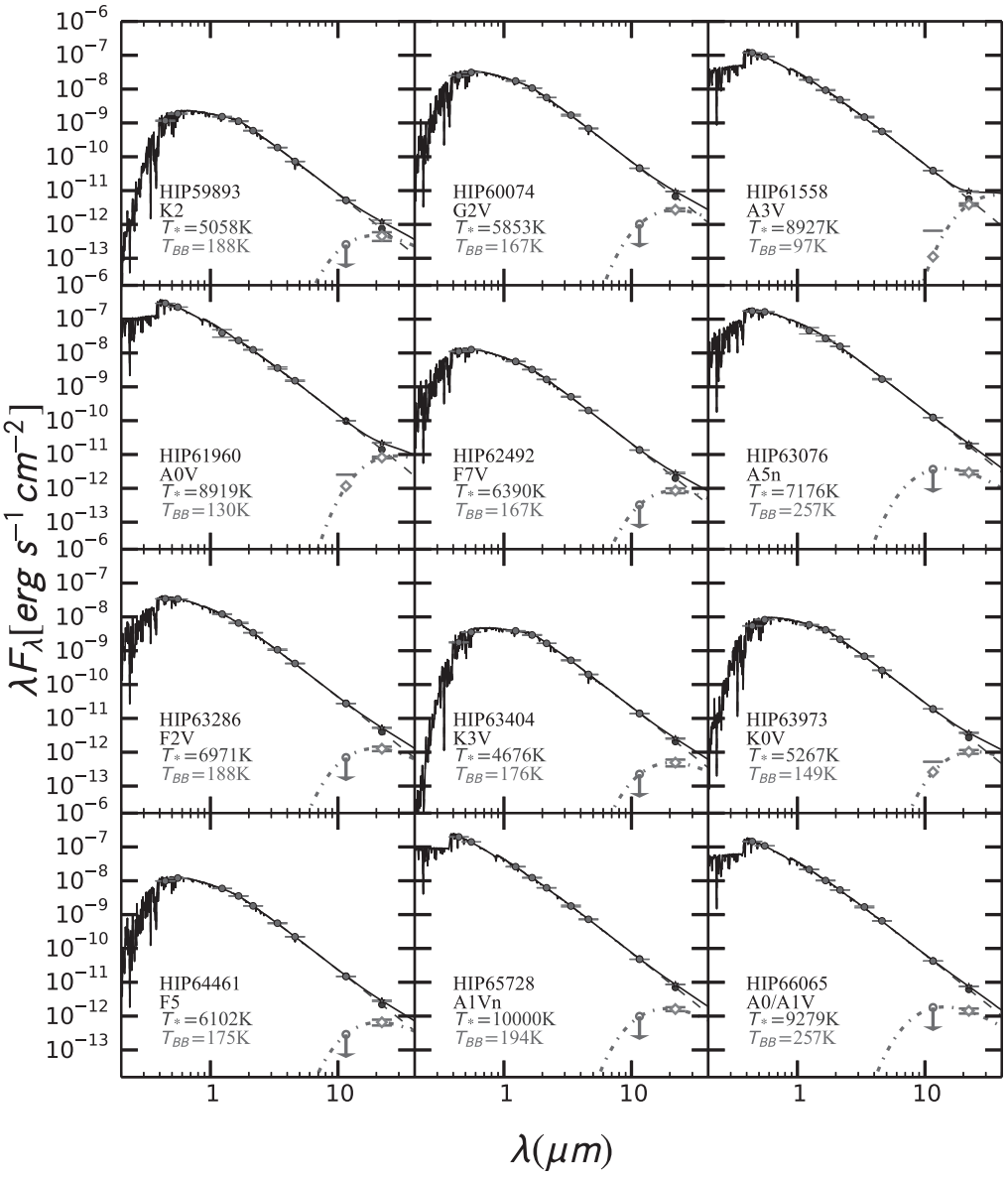

Figure D.2: continued.

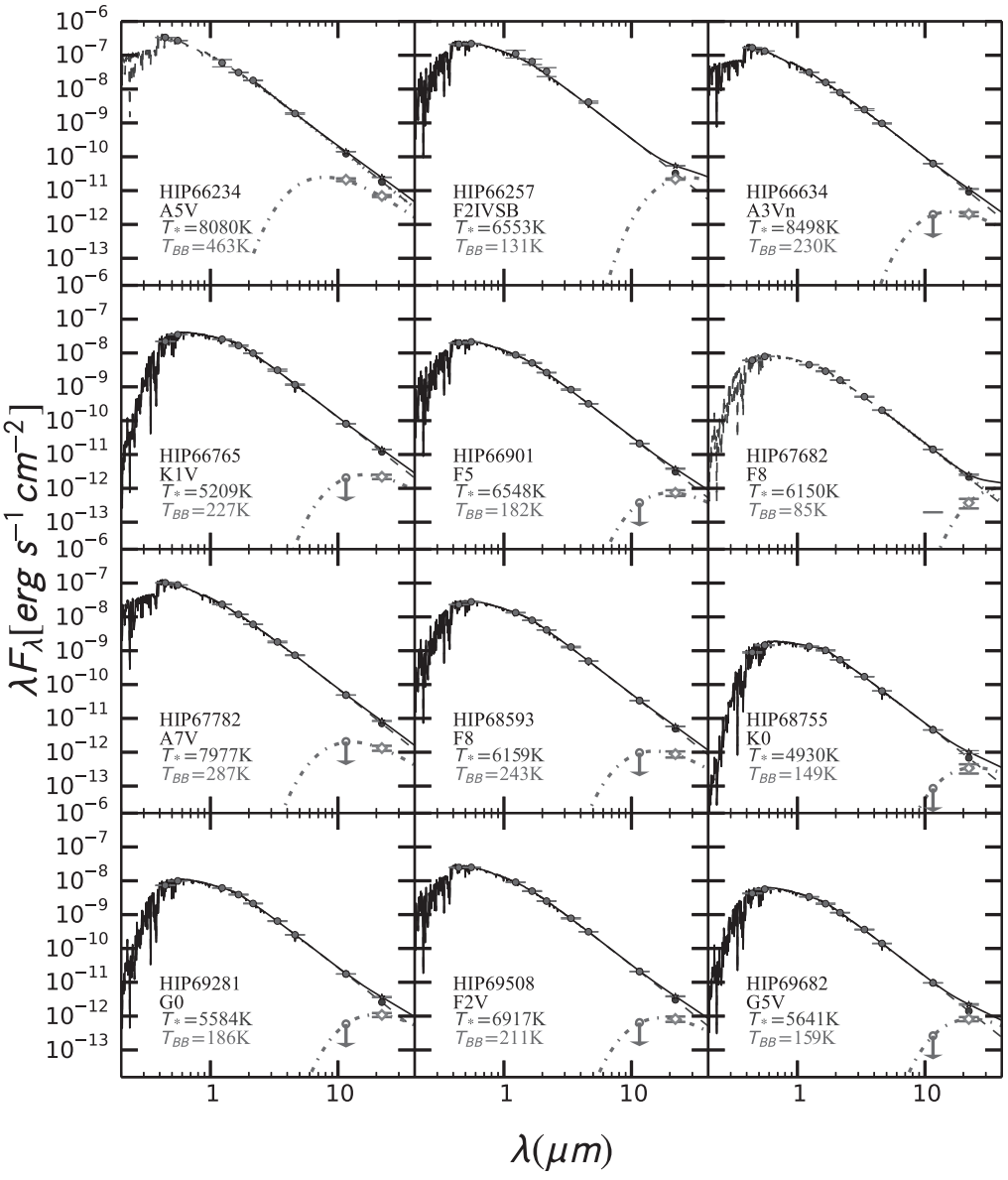

Figure D.2: continued.

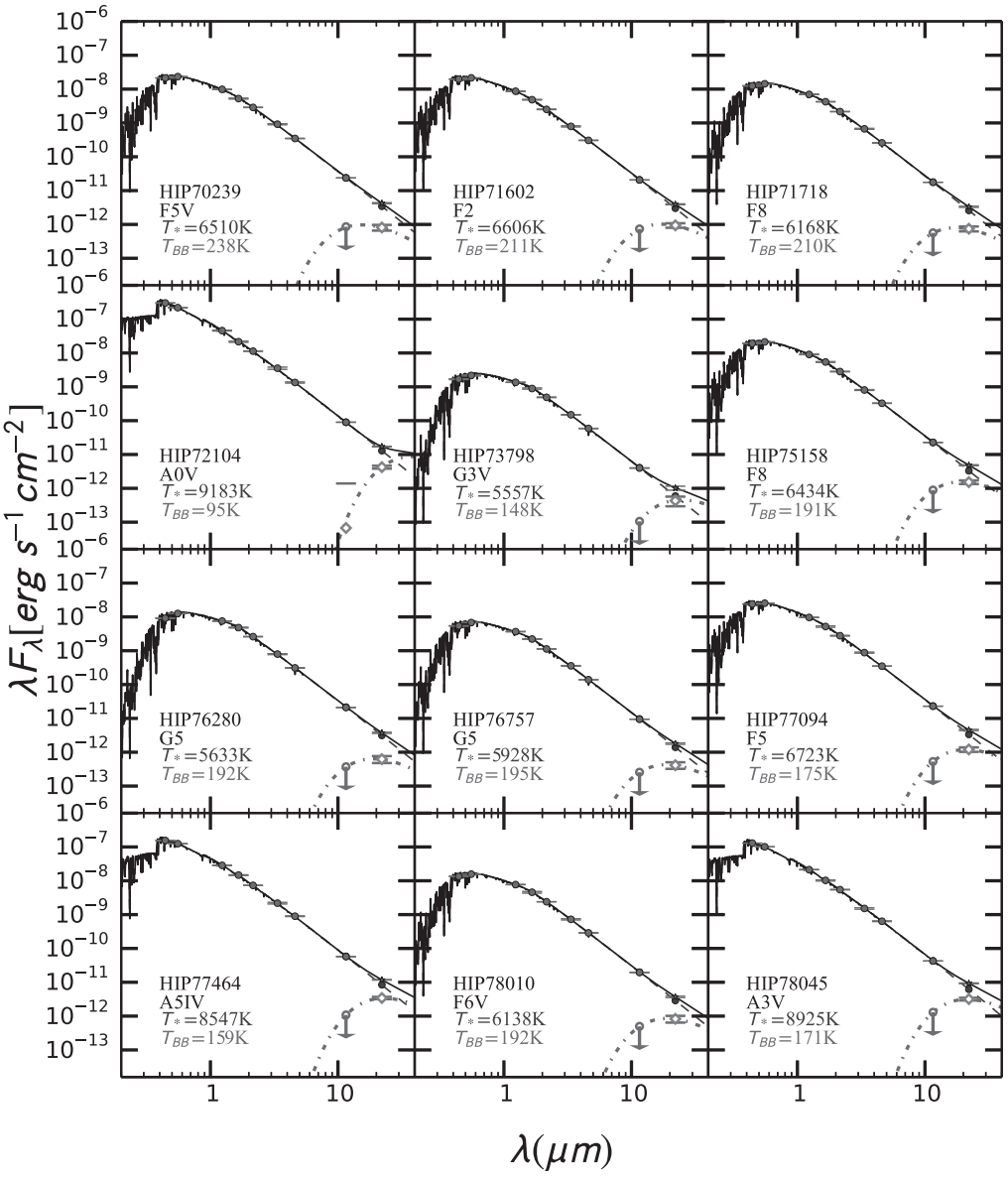

Figure D.2: continued.

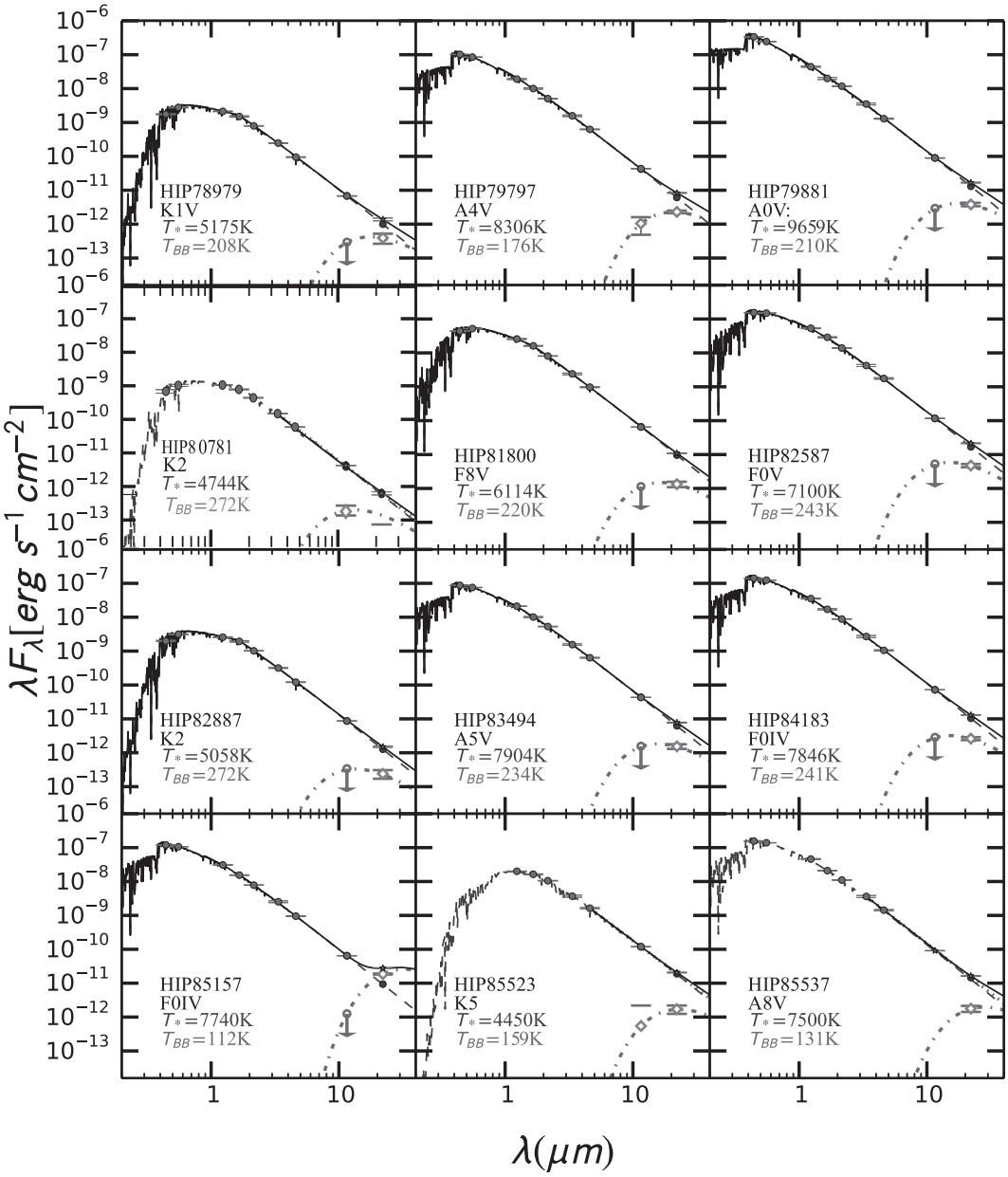

Figure D.2: continued.

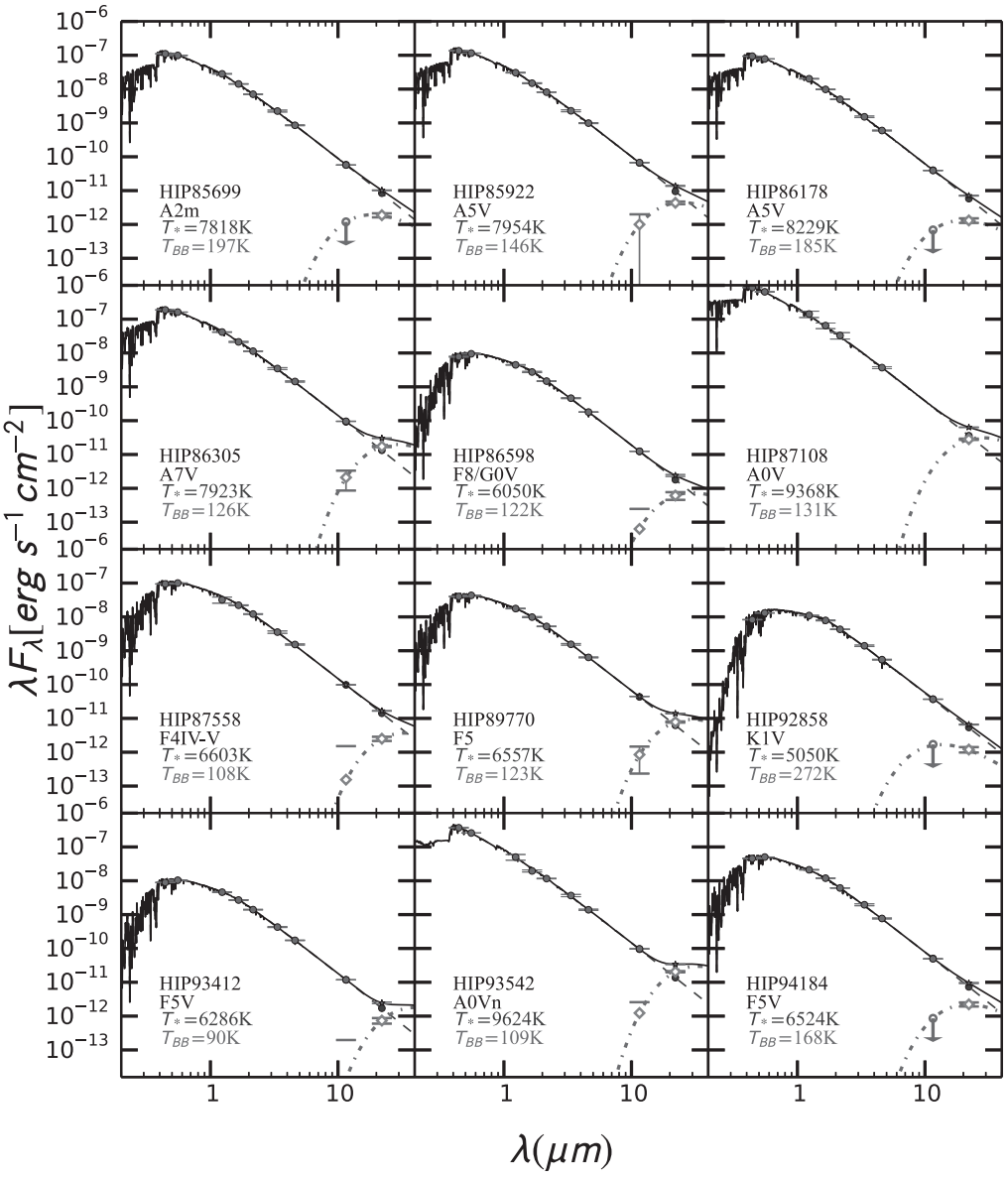

Figure D.2: continued.

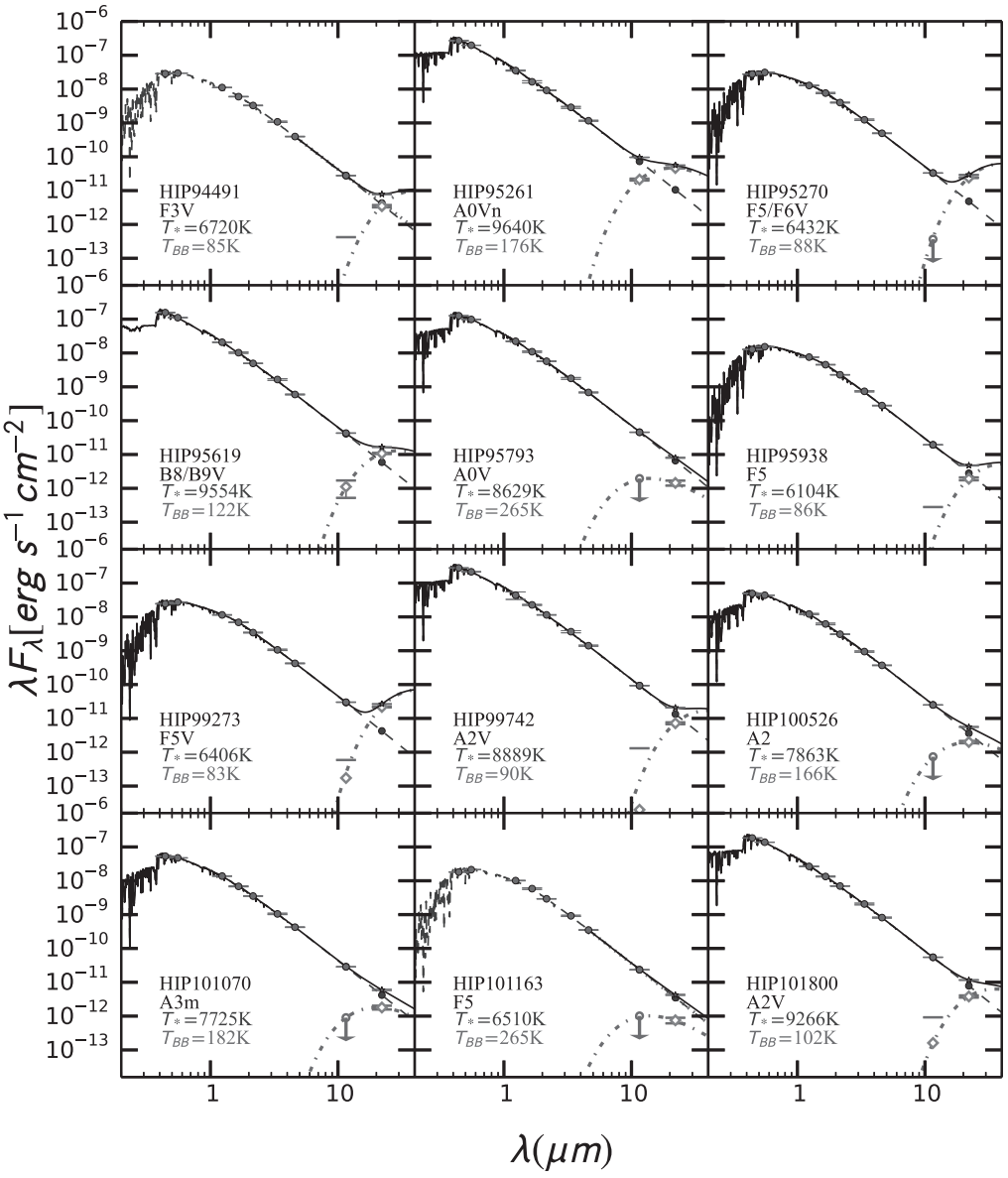

Figure D.2: continued.

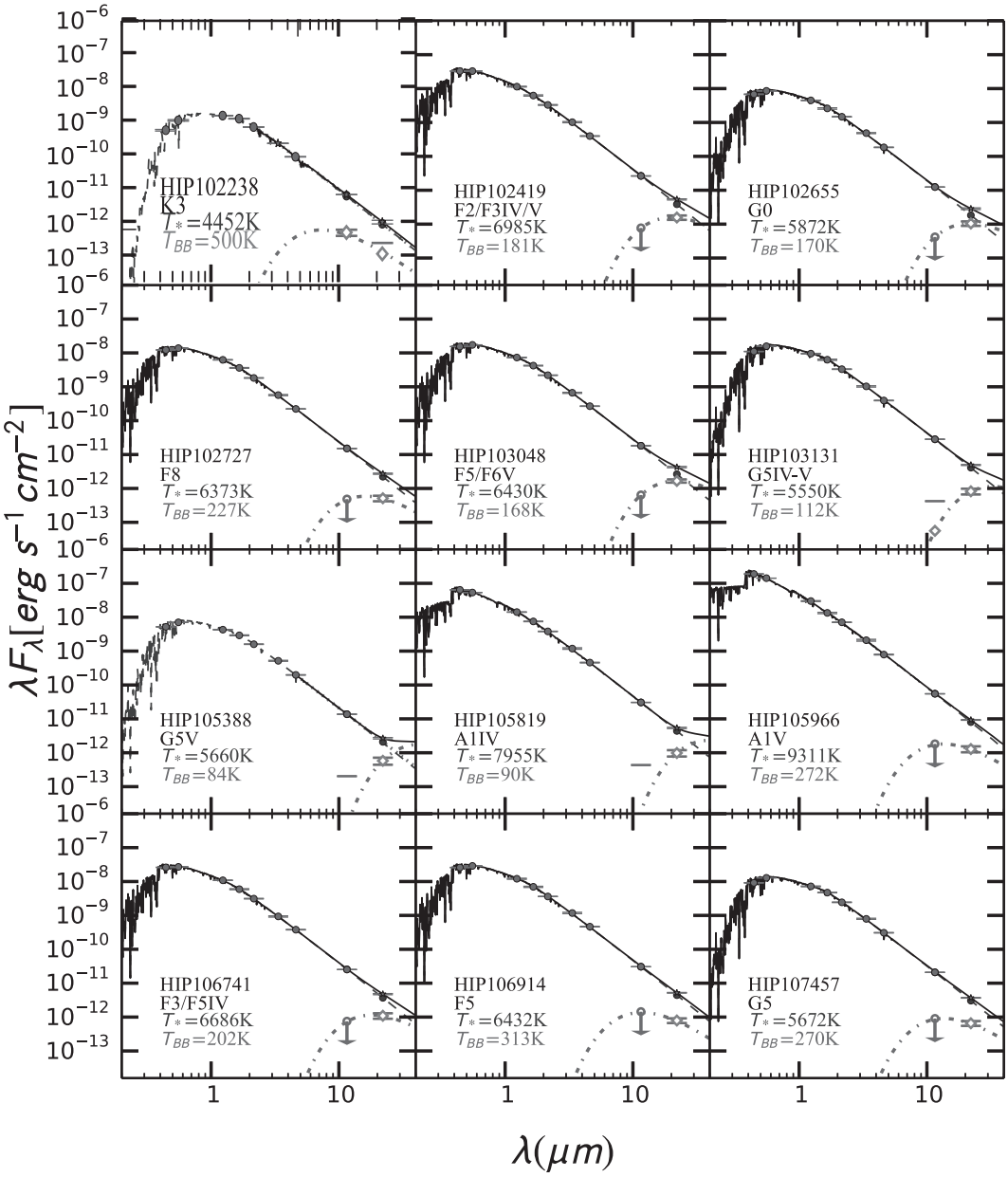

Figure D.2: continued.

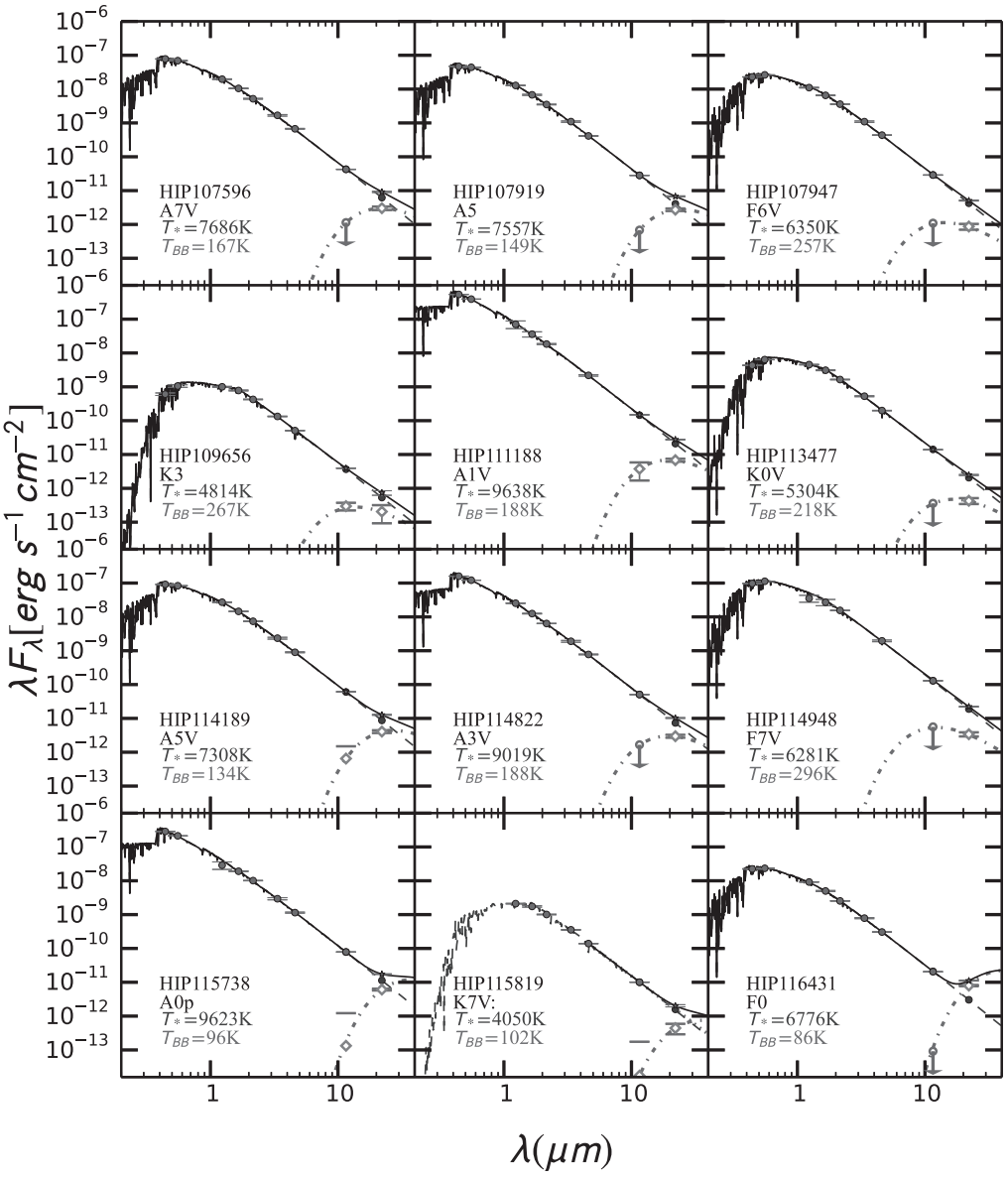

Figure D.2: continued.

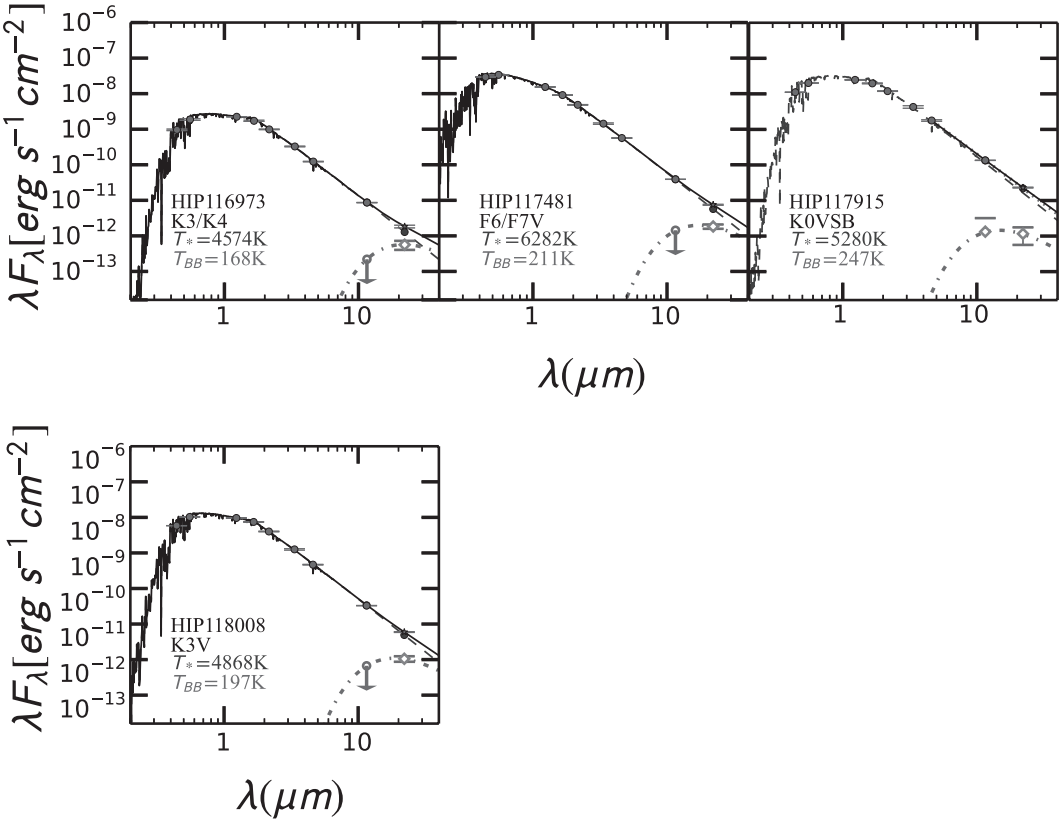

Figure D.2: continued.

D.2 Extended Figures of Chapter 5

In chapter 5, I identified 312 $W3-W4$ excesses, that were not reported from our surveys in Chapters 3 and 4. Here, I plot the SEDs of all these stars.

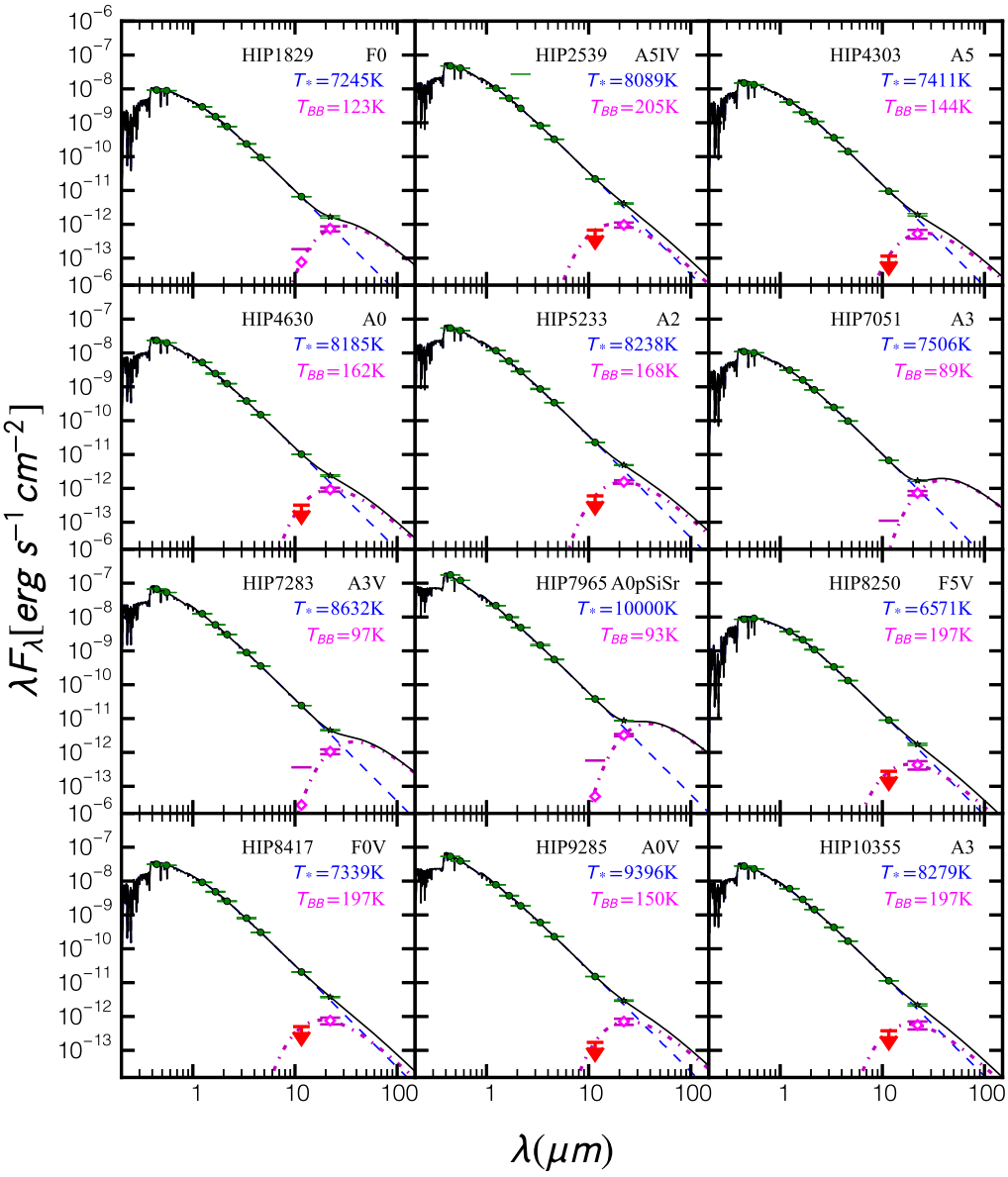

Figure D.3: SEDs of probable debris disk-host stars within 120 pc, identified via their $W3-W4$ excess color. The dashed lines and solid data points correspond to the fitted model NextGen photosphere and to $BVJHK_s$ photometry from the *Hipparcos* Catalogue and *2MASS* Point Source Catalog. Fluxes plotted as closed circles were used in the fit, and fluxes plotted as stars—excesses above the photosphere—were not used in the fit. Cool blackbody curves (dash-dotted line) were fitted to the excess fluxes (open diamonds) at the $W3$ and/or $W4$ wavelengths. The combined photosphere and excess emission for each star is plotted as a solid black line. Upper limits are shown as red arrows pointing down.

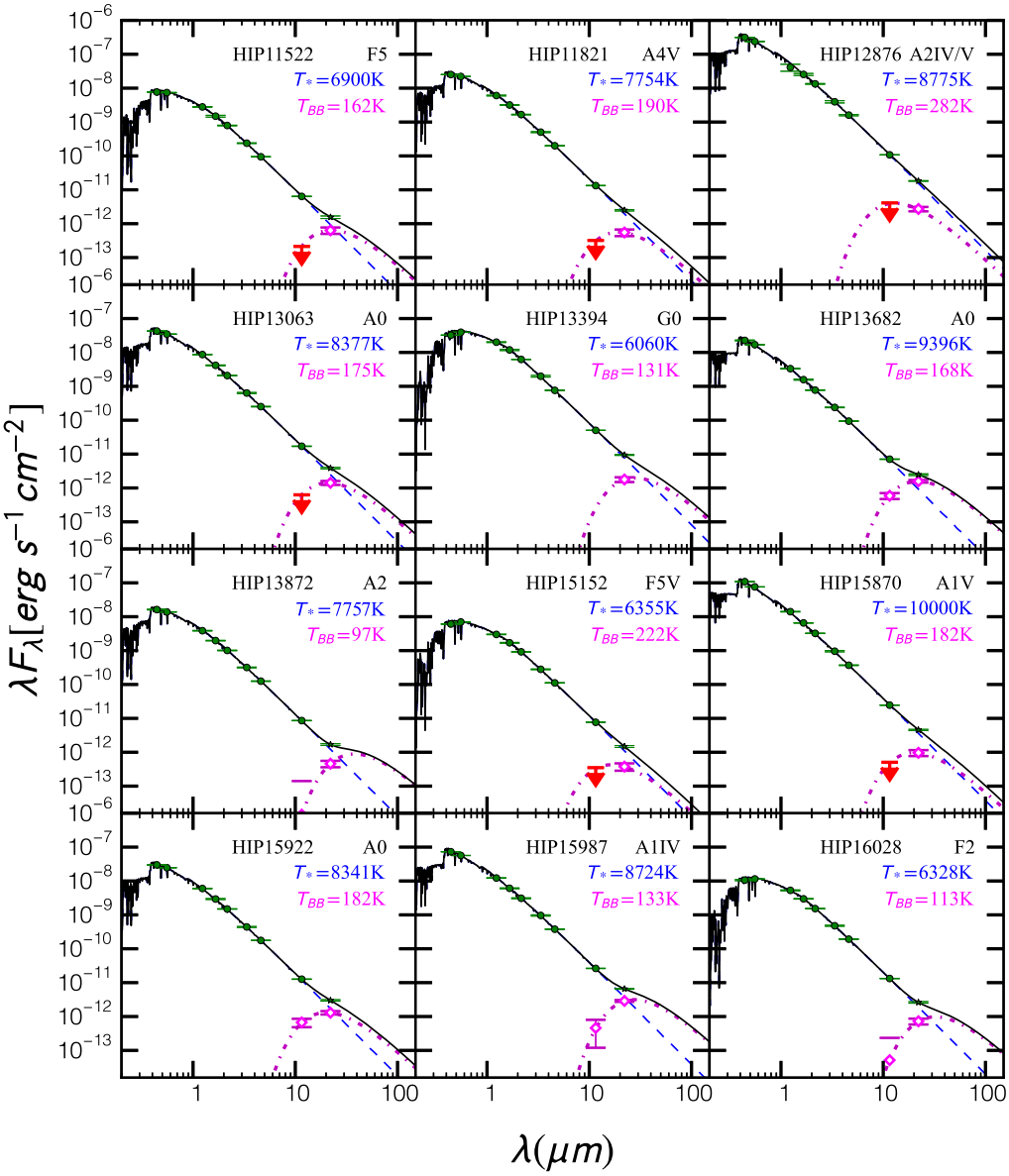

Figure D.3: continued.

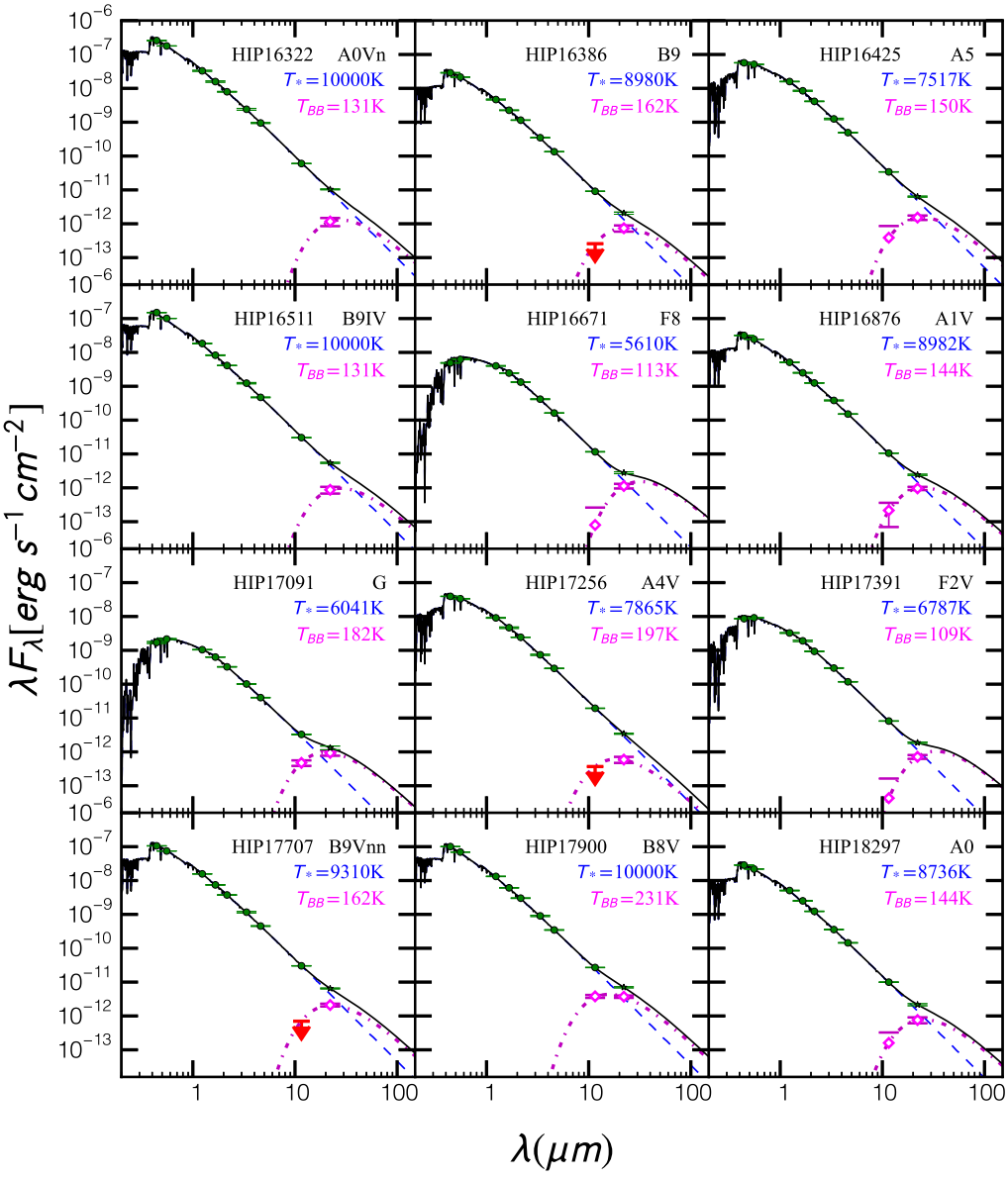

Figure D.3: continued.

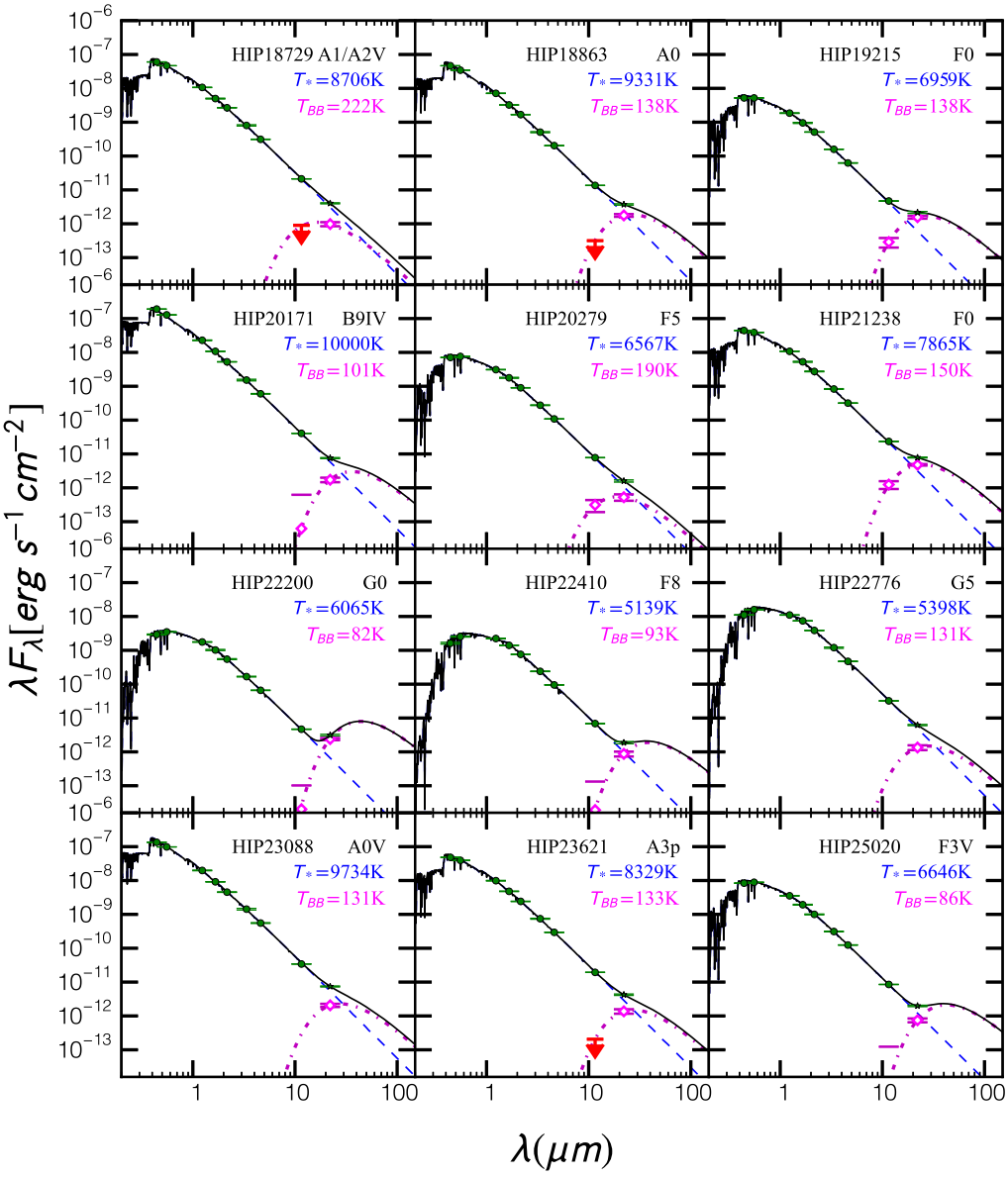

Figure D.3: continued.

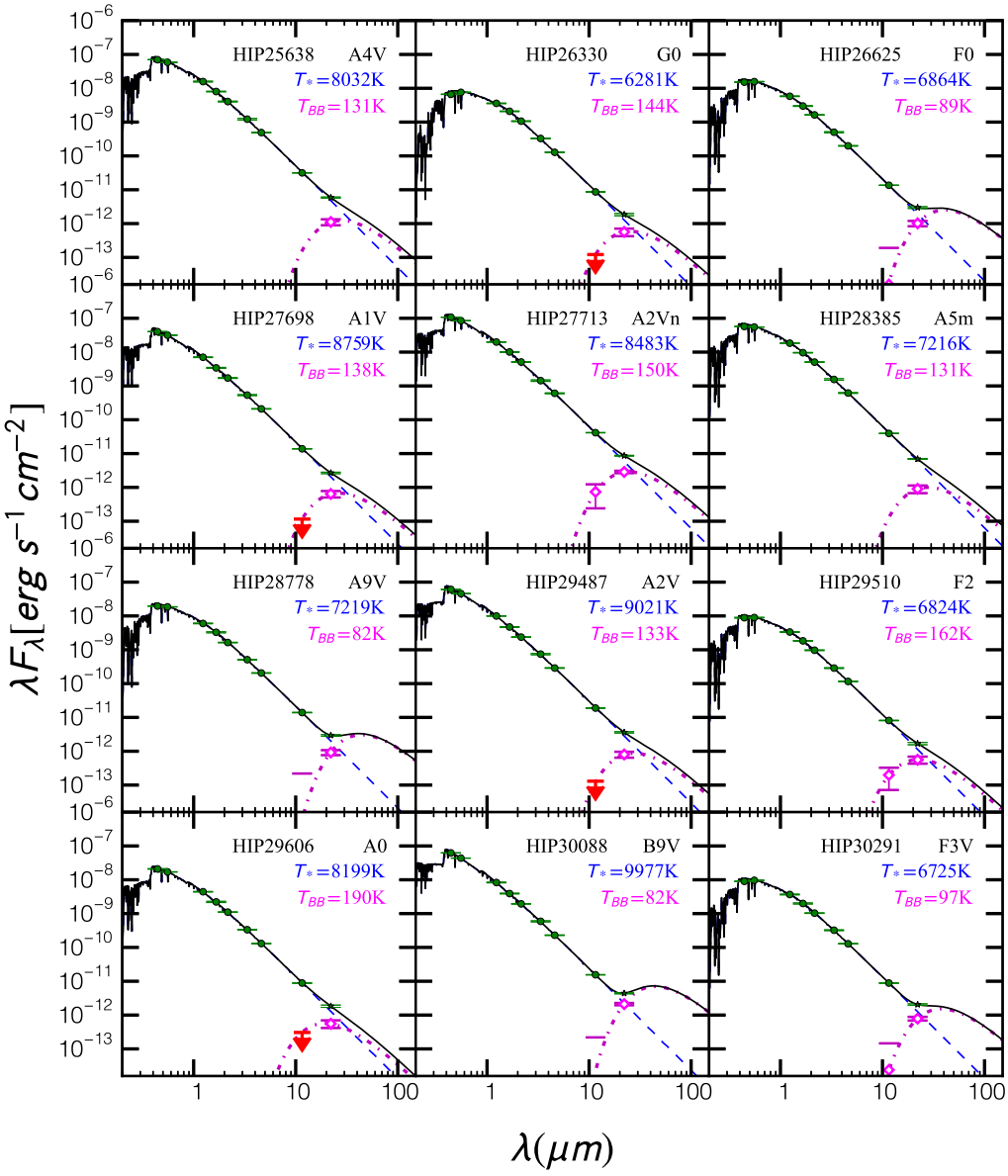

Figure D.3: continued.

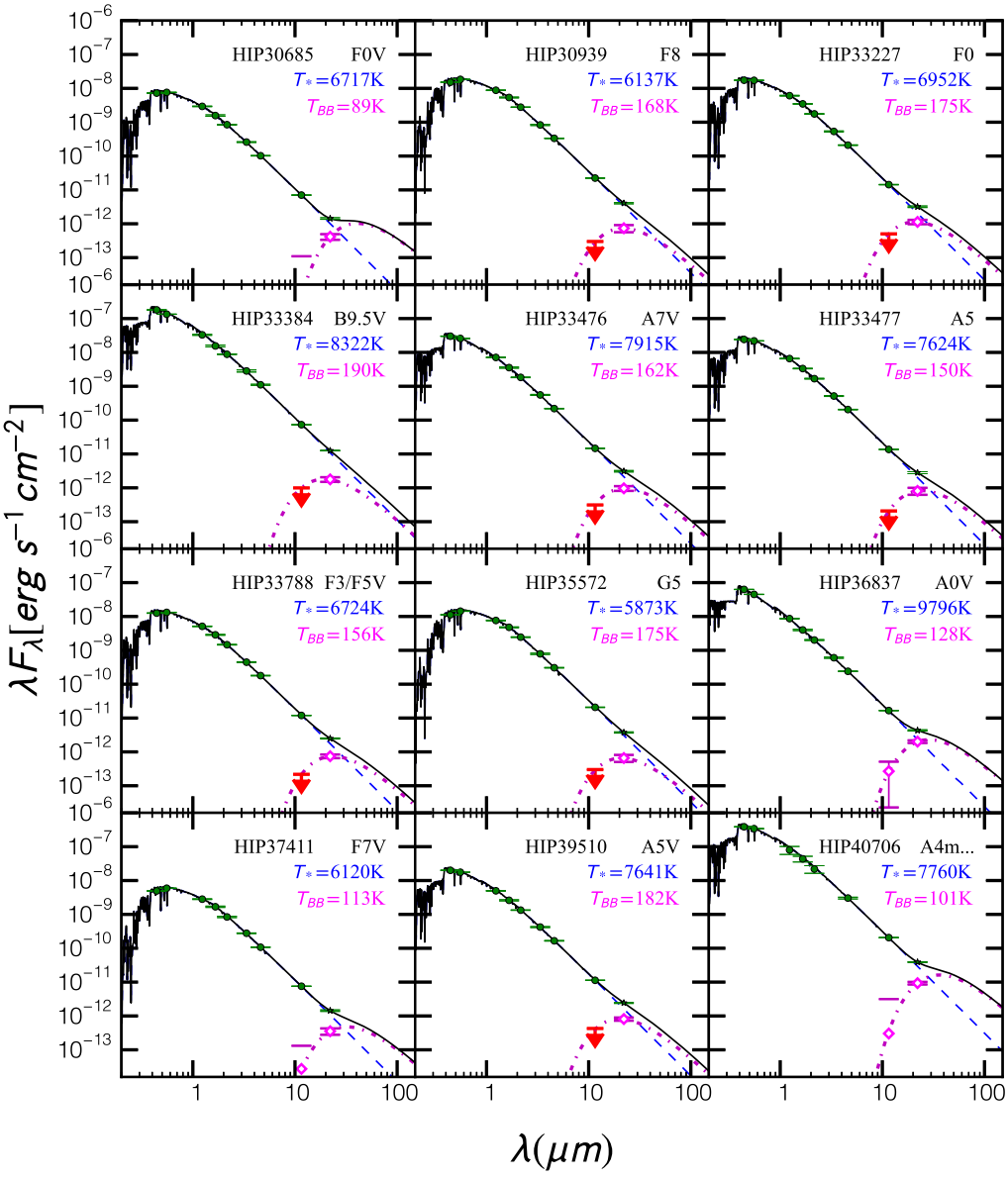

Figure D.3: continued.

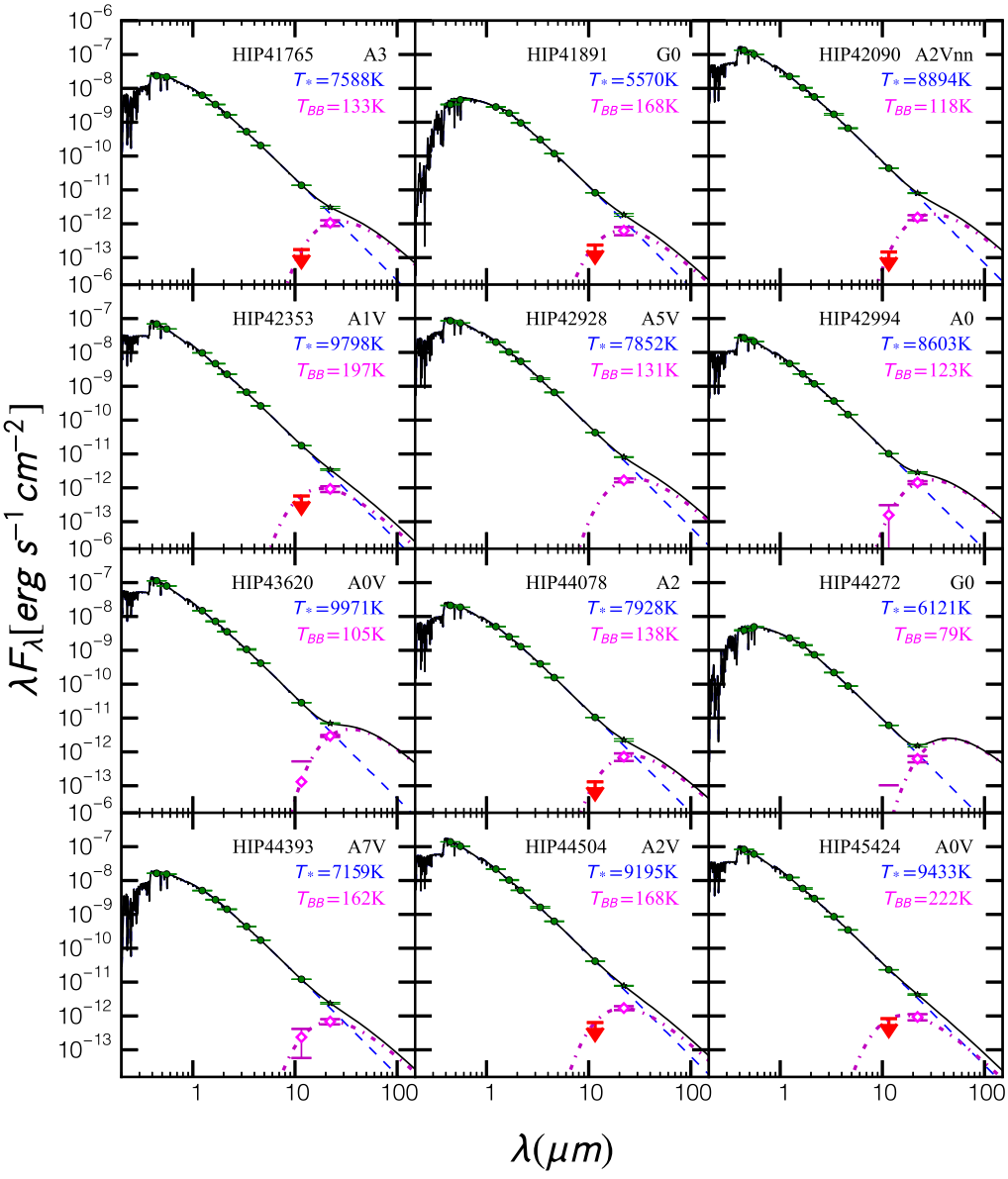

Figure D.3: continued.

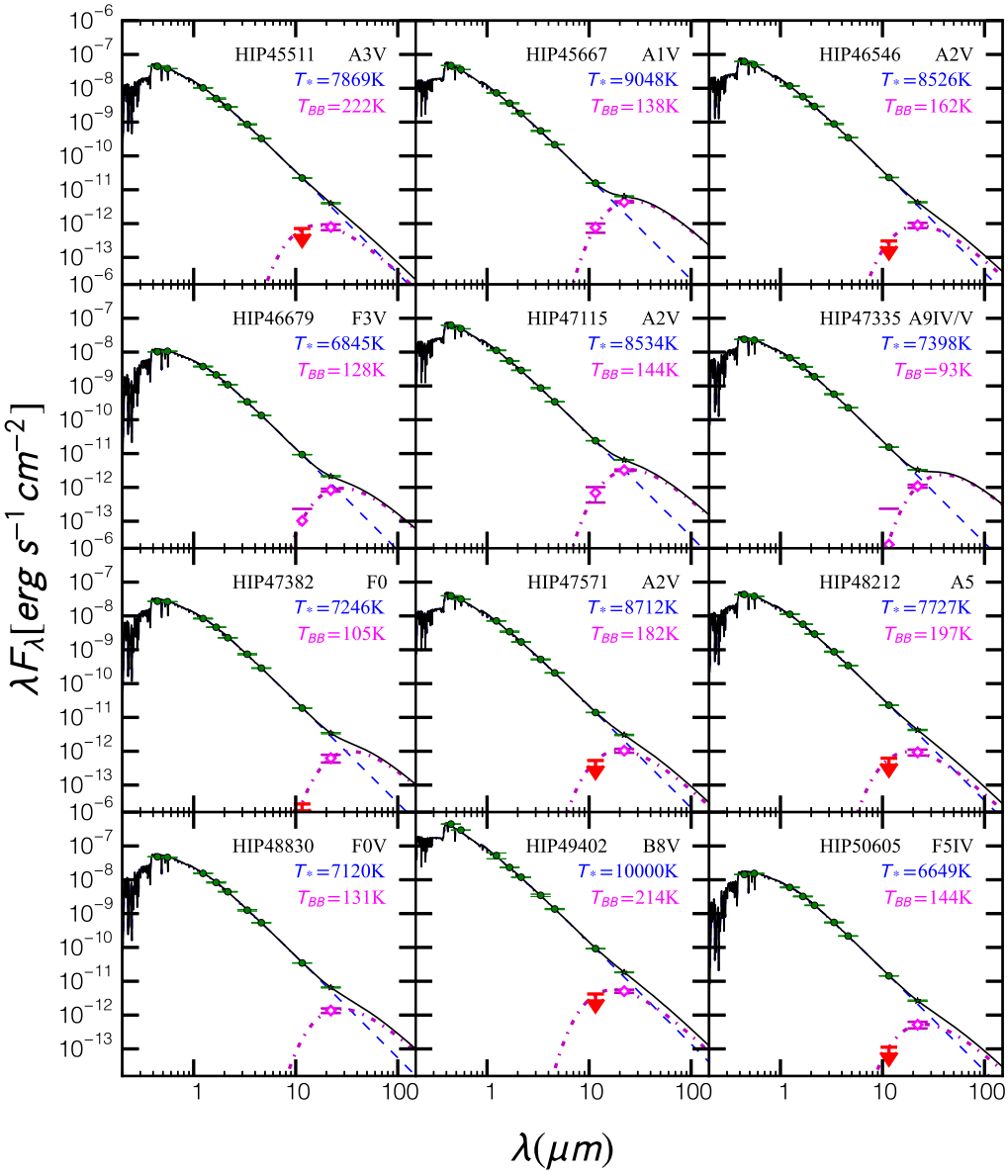

Figure D.3: continued.

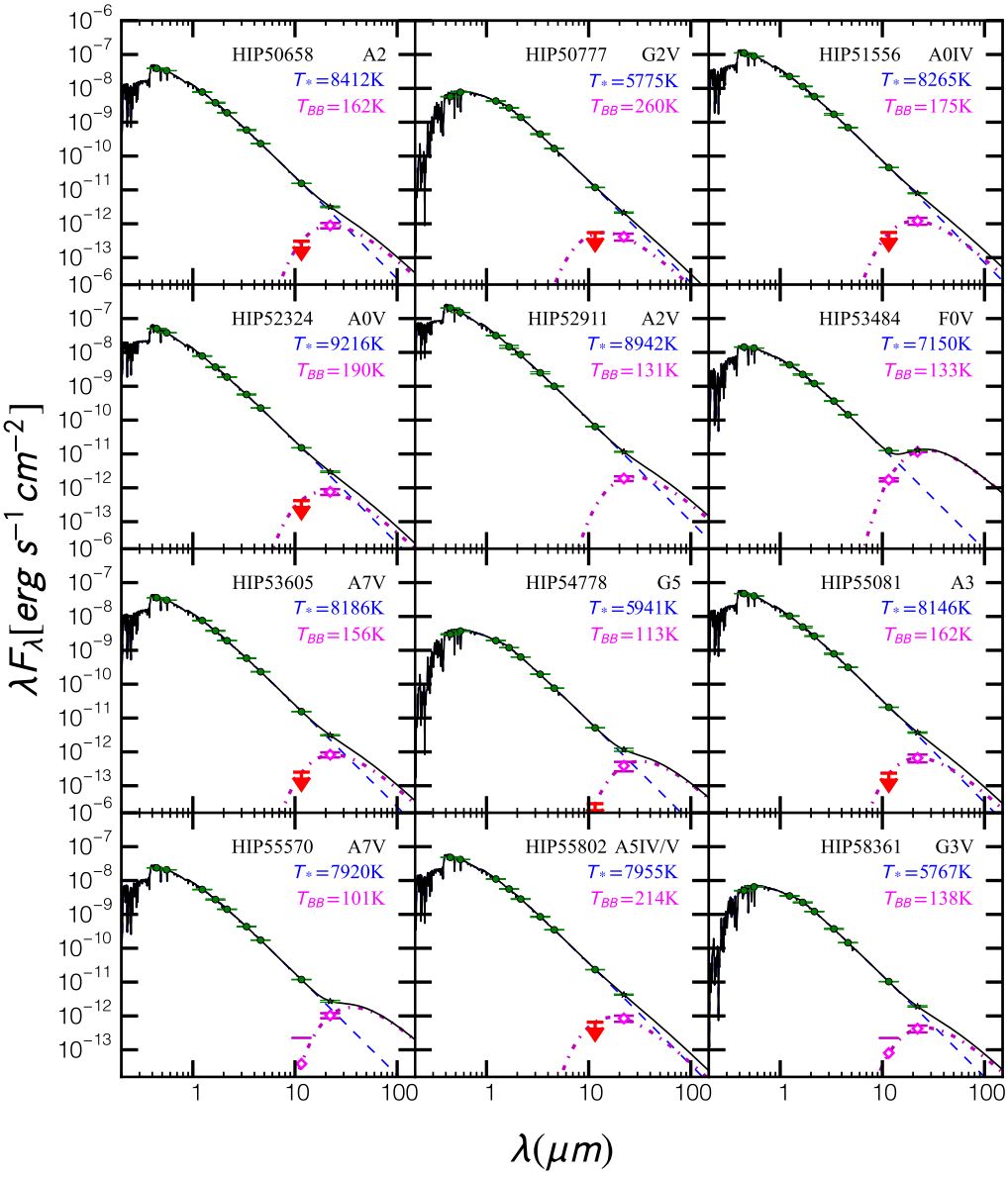

Figure D.3: continued.

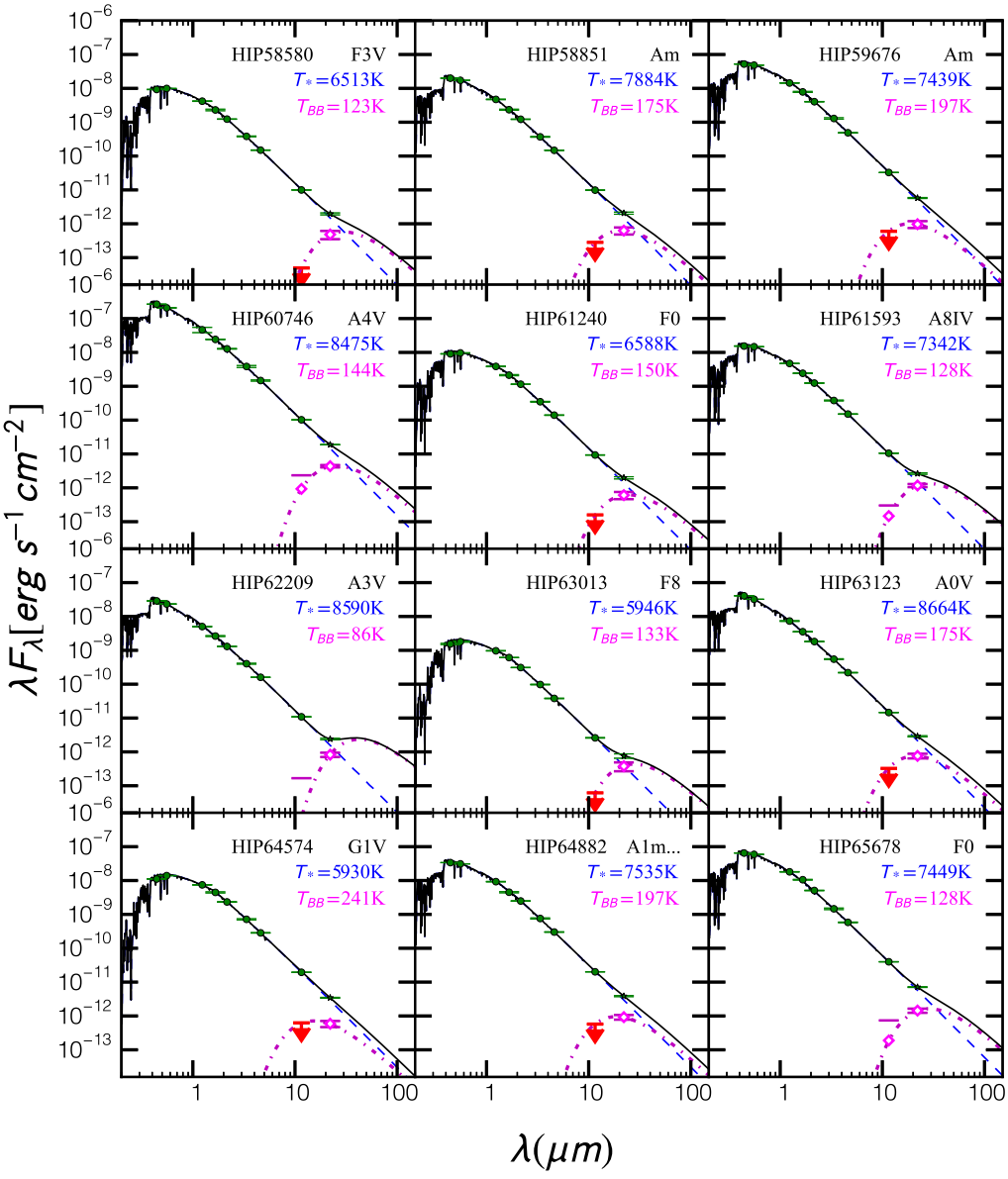

Figure D.3: continued.

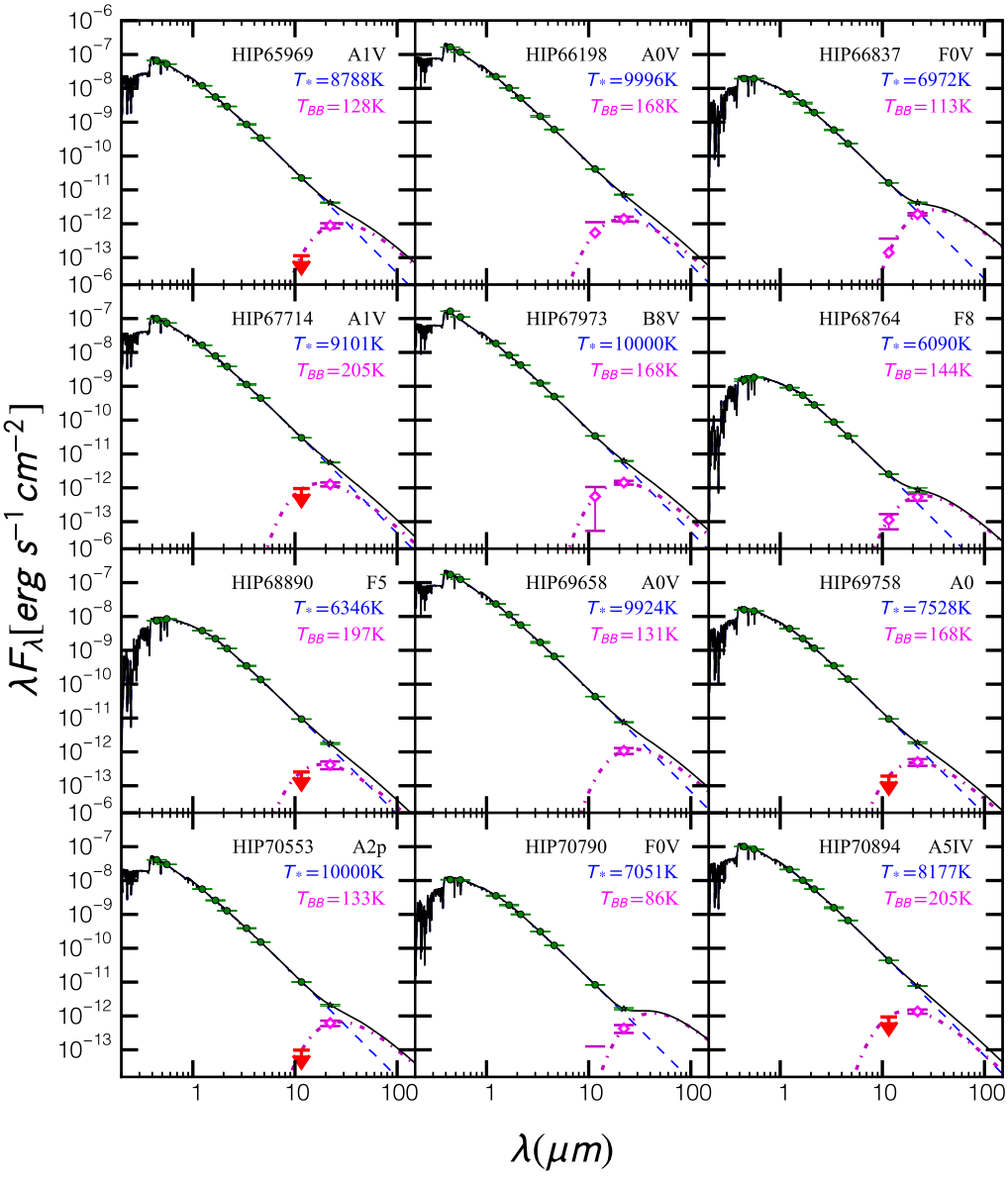

Figure D.3: continued.

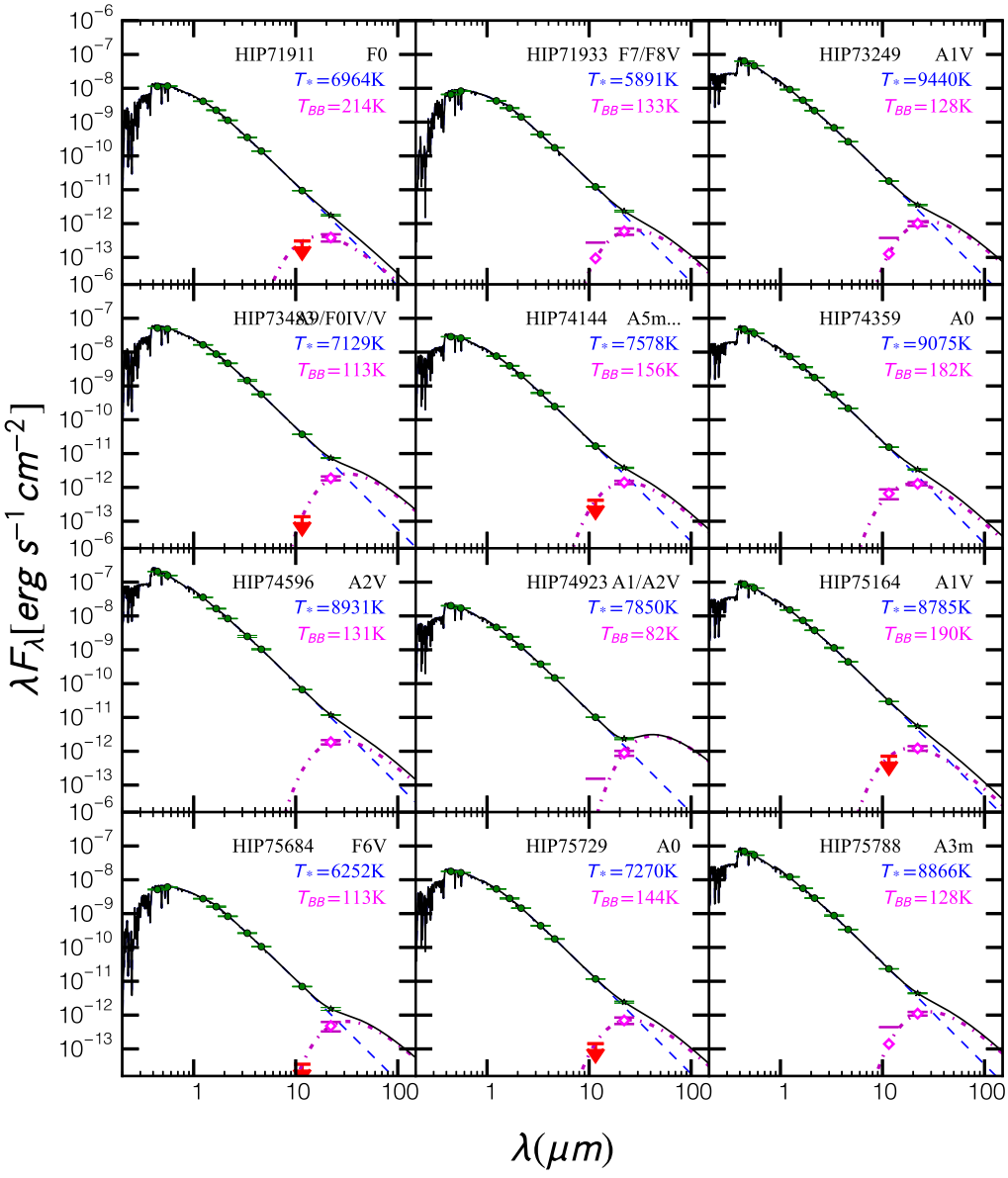

Figure D.3: continued.

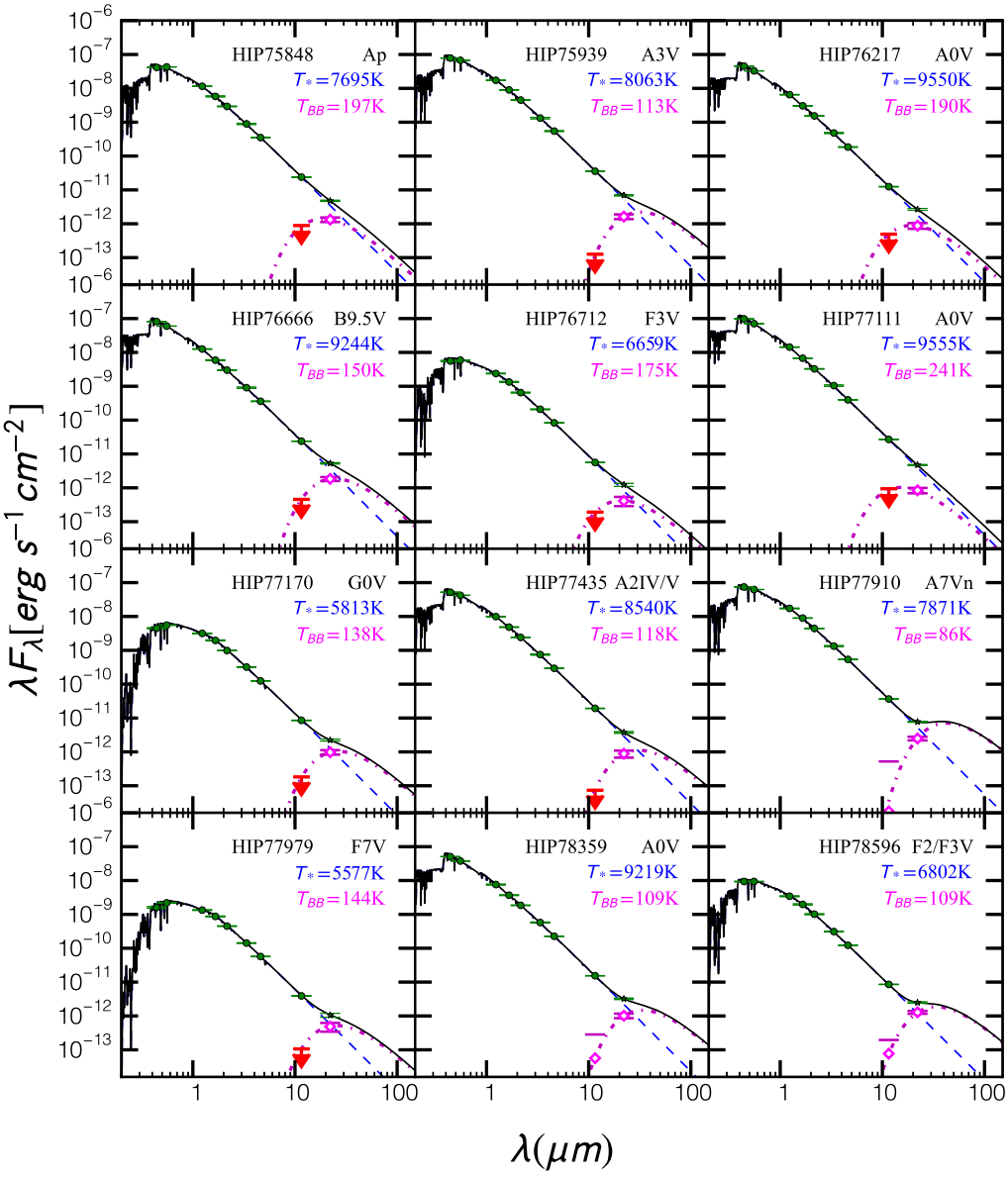

Figure D.3: continued.

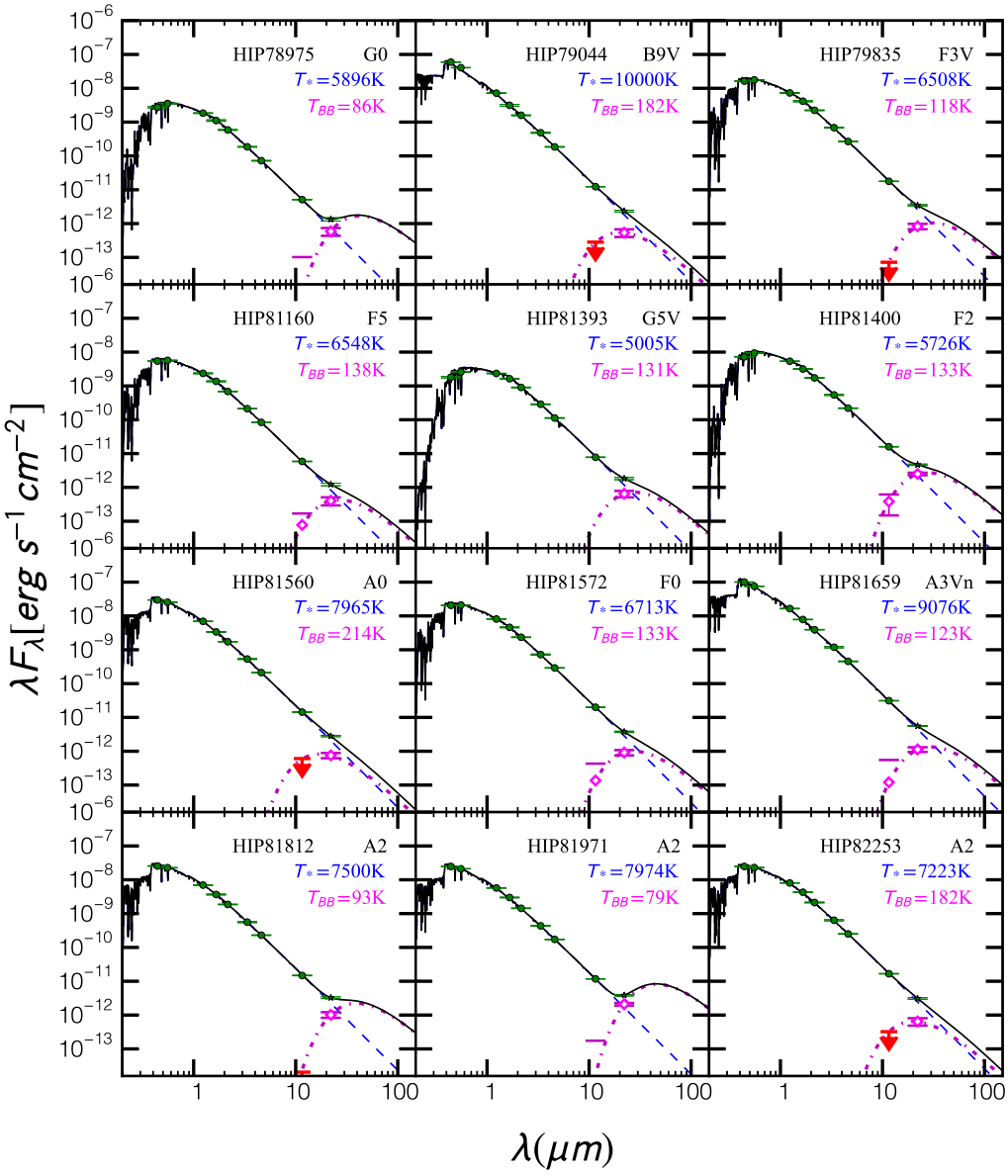

Figure D.3: continued.

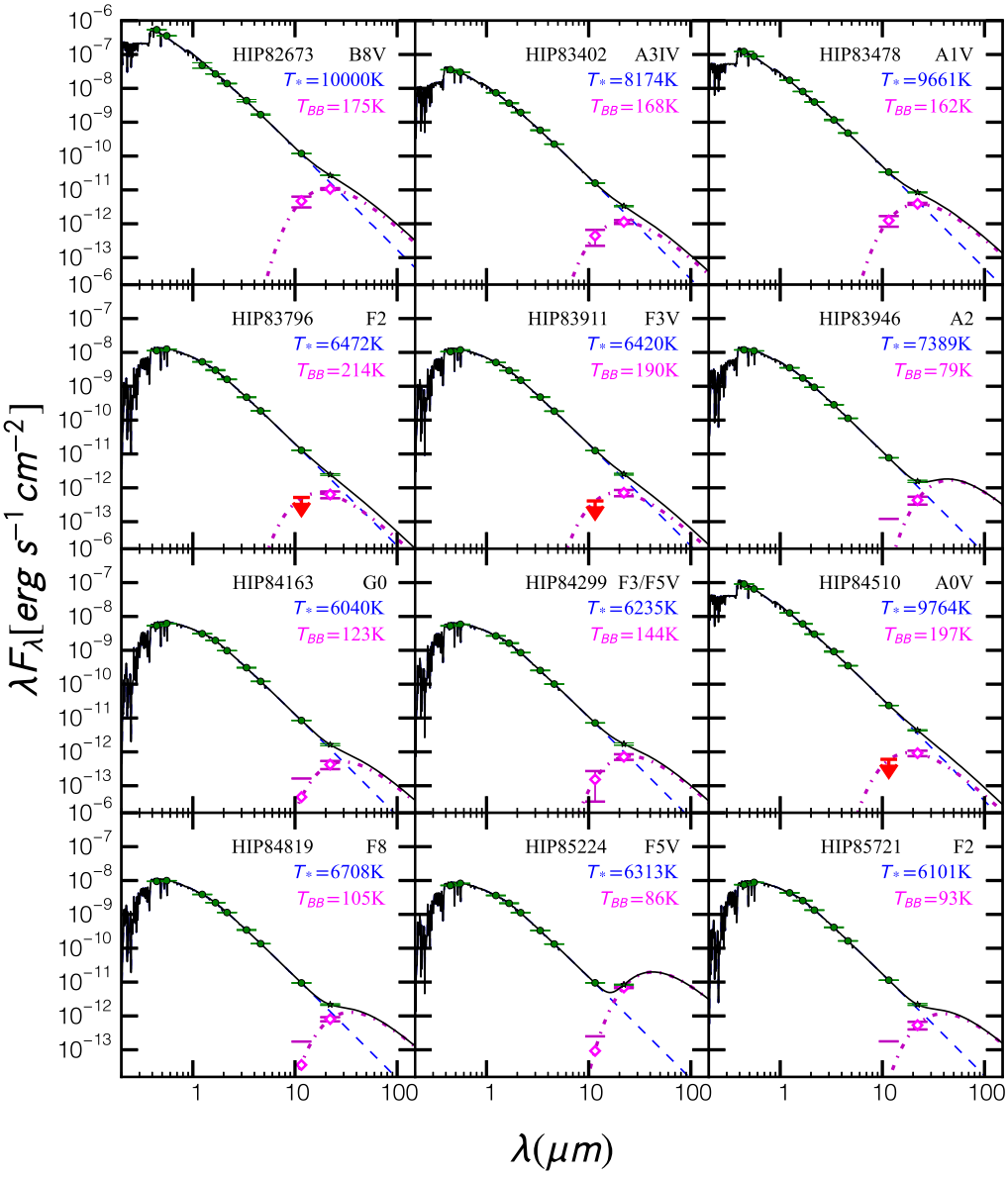

Figure D.3: continued.

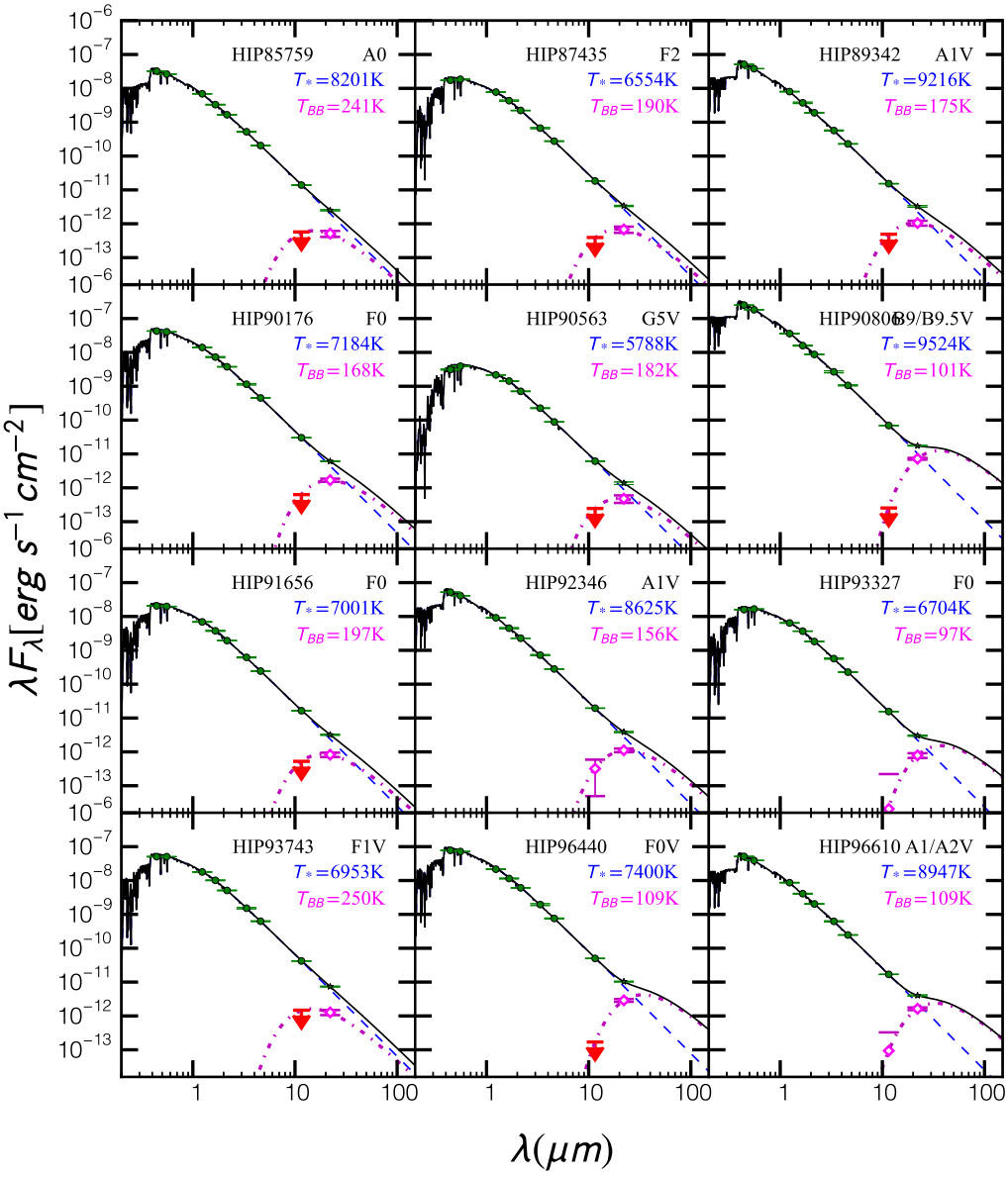

Figure D.3: continued.

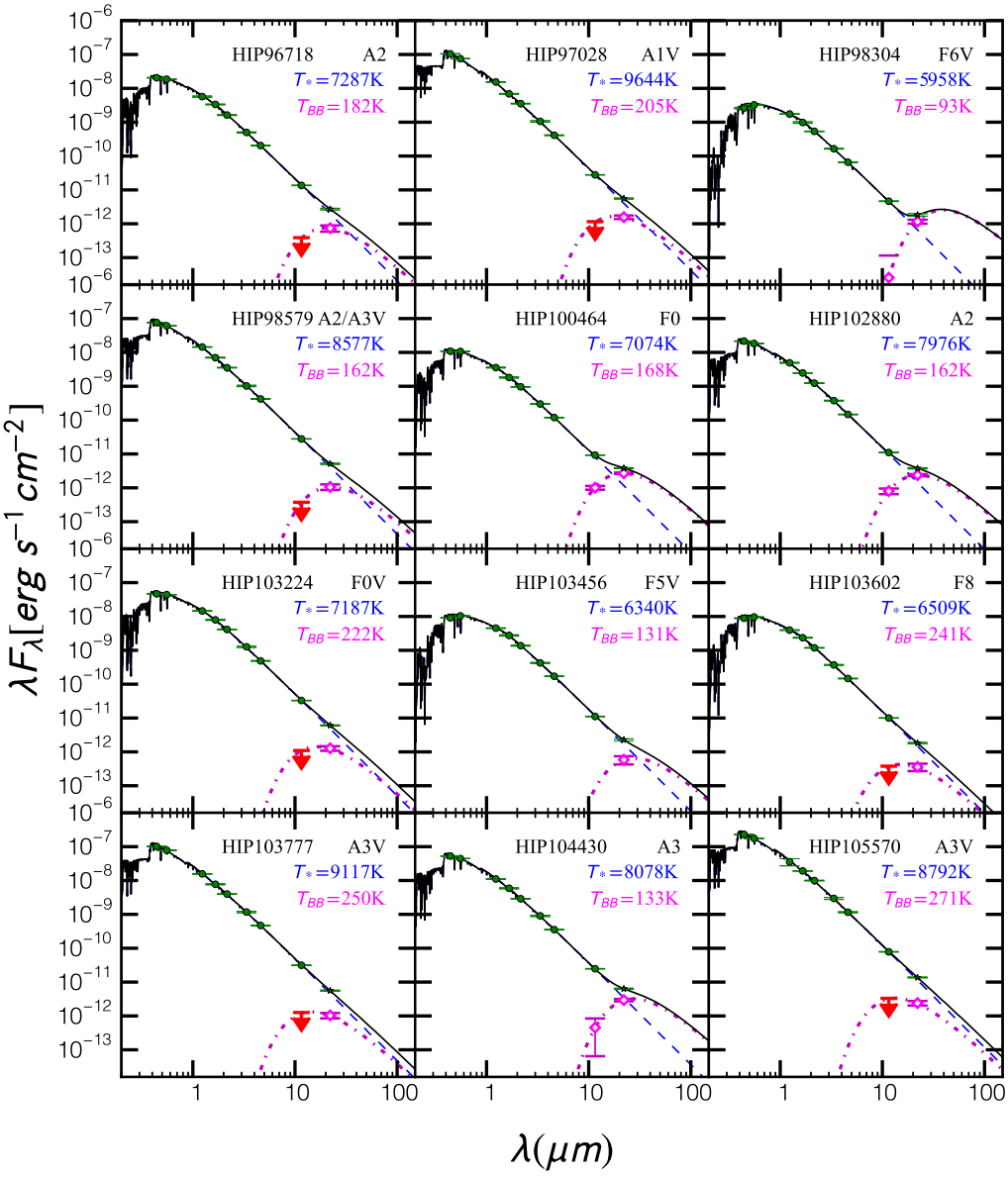

Figure D.3: continued.

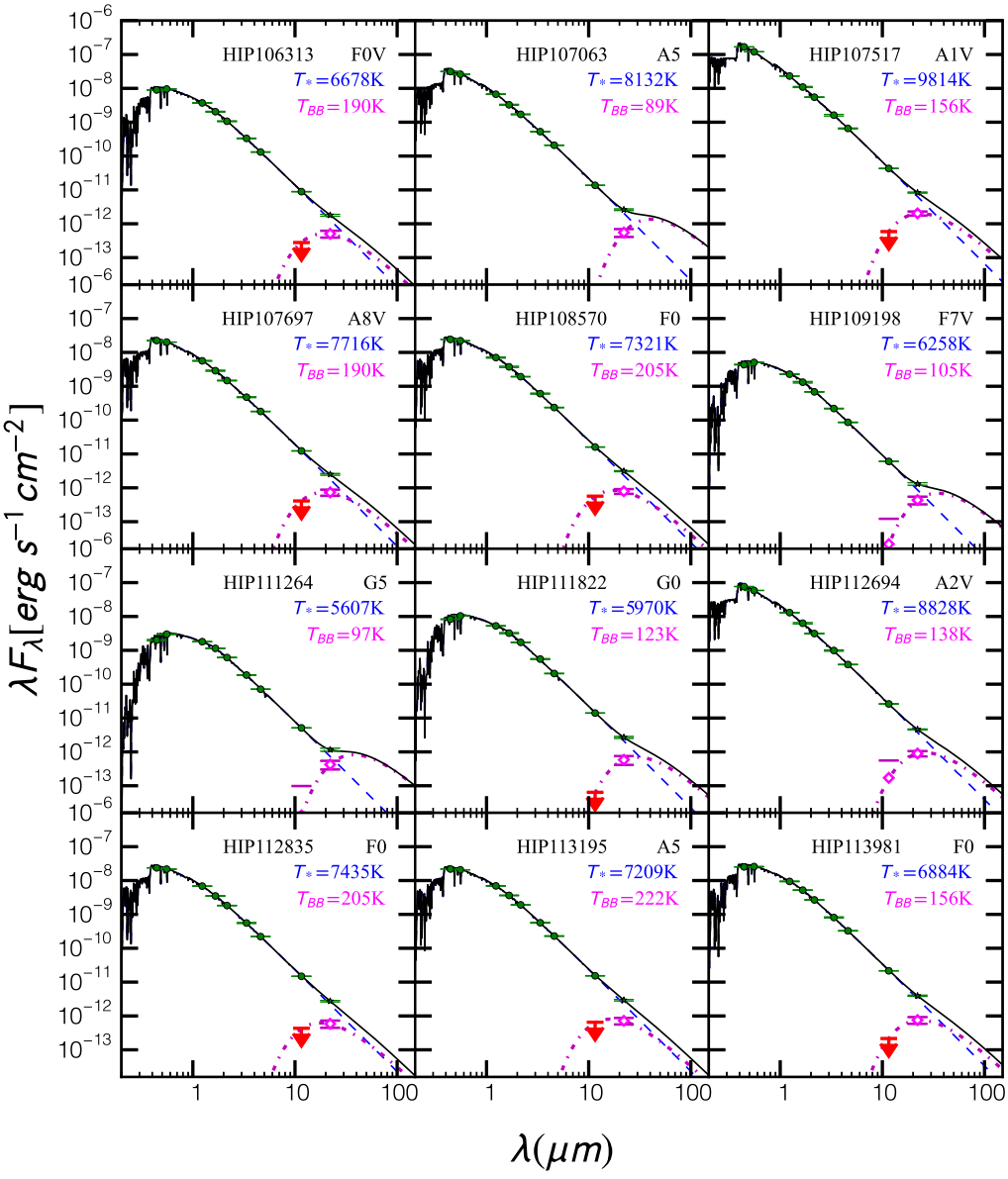

Figure D.3: continued.

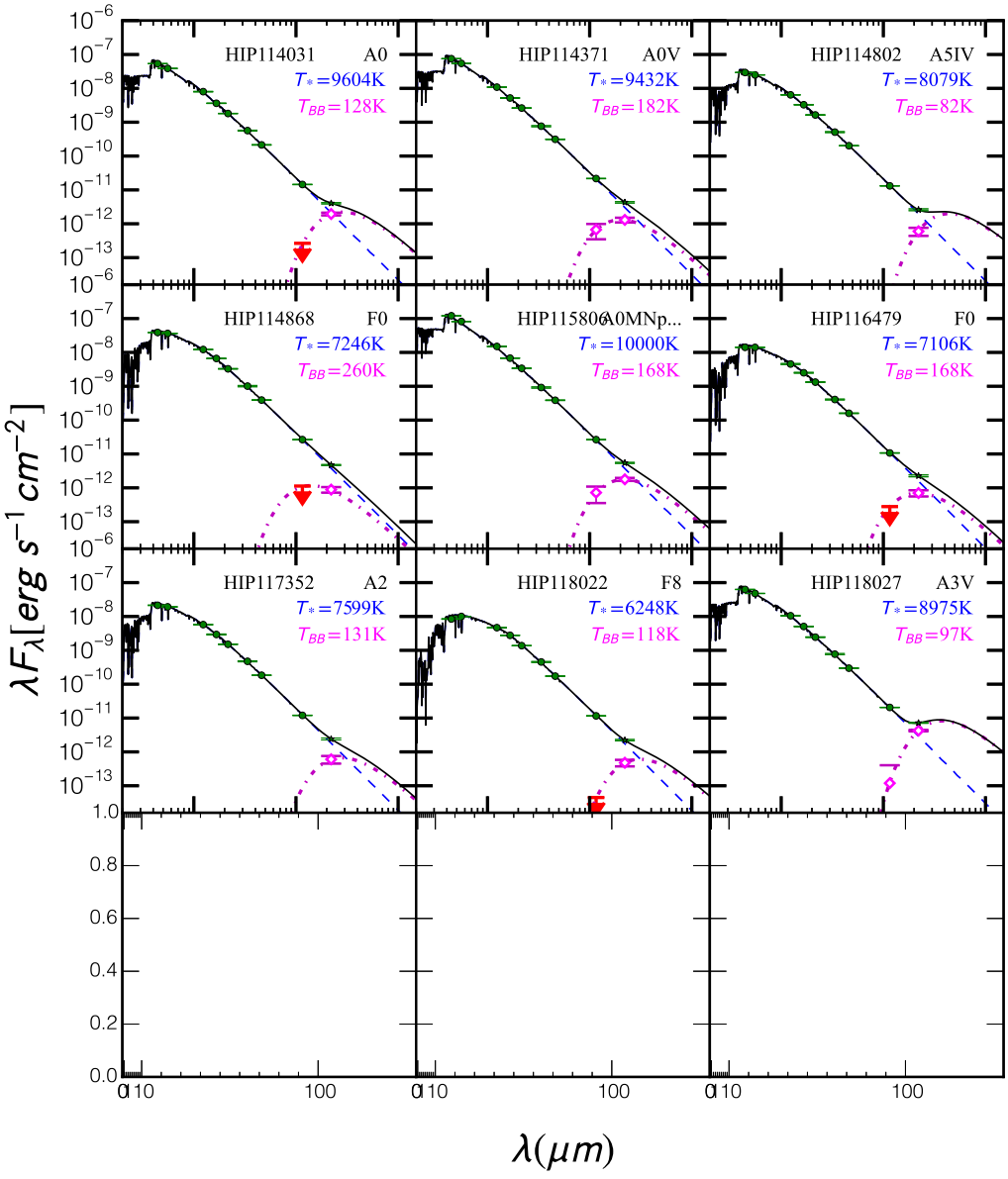

Figure D.3: continued.